VII

Strong-Motion Seismology

This Page Intentionally Left Blank

57

Strong-Motion Seismology

John G. Anderson
University of Nevada, Reno, Nevada, USA

1. Introduction

Strong-motion seismology is concerned with the measurement, interpretation, and estimation of strong shaking generated by potentially damaging earthquakes. Measurements of strong shaking generated by large earthquakes provide a principal research tool. First, these data are essential to understand the high-frequency nature of crustal seismogenic failure processes, the nature of seismic radiation from the source, and the nature of crustal wave-propagation phenomena near the source, all of which have a first order effect on the seismic loads applied to the physical environment. Second, these measurements are a principal tool used to develop empirical descriptions of the character of strong shaking. Principal goals of strong-motion seismology are to improve the scientific understanding of the physical processes that control strong shaking and to develop reliable estimates of seismic hazards for the reduction of loss of life and property during future earthquakes through improved earthquake-resistant design and retrofit.

The strongest earthquake motions that have been recorded to date have peak accelerations between $1g$ and $3g$, where $1g$ ($=980$ cm/sec^2) is the acceleration of the Earth's gravity field, although records with such large peak values are rare. It is less clear what threshold of ground motion needs to be exceeded to be considered "strong motion." Probably a logical level to choose would be about 10 cm/sec^2, as the older strong-motion instruments (accelerographs) that traditionally defined the field are not able to resolve ground accelerations with amplitudes smaller than this. Modern digital accelerographs are much more sensitive, able to resolve peak accelerations to 0.1 cm/sec^2 or smaller. People at rest are able to feel motions as small as 1 cm/sec^2. In moderate magnitude earthquakes, damage to structures that are not designed for earthquake resistance appears at accelerations of about 100 cm/sec^2.

Earthquakes with magnitude less than 5 are of minor concern for strong-motion seismology. They are not known to damage structures of modern construction. Only a tiny fraction of such small events has caused deaths, and the number of deaths is small except in extraordinary circumstances of extremely poor construction and faulting directly under a population center. As the magnitude grows, both the destructive capability and average number of deaths per event also grows. Events with magnitudes between 6 and 7.5 are most commonly responsible for significant disasters. Globally, on average, there are 130 earthquakes per year with magnitude in the range 6.0–6.9, and 15 earthquakes per year with magnitude in the range 7.0–7.9 (see Chapter 41 by Engdahl and Villasenor). Many of these, of course, are in remote locations and have little impact. Events with magnitude of 8 or above, with their immense destructive potential, fortunately occur at an average rate of only about 0.7 per year, with some in remote locations, so disasters caused by such events are less frequent.

Observation of strong motion is more difficult than observation in other fields of seismology due to the infrequency of large earthquakes and the difficulty of anticipating areas of strong shaking for instrumentation. Weak motions from an earthquake with magnitude greater than 6 can be recorded worldwide. Thus, a seismologist who studies teleseisms can record over 100 earthquakes per year, for interpretations of earth structure or tectonics. Similarly, local networks are generally set to the most sensitive level possible to detect and locate the smallest earthquakes, which are much more abundant. The sensitive instruments used for these two branches of earthquake studies are driven off scale by strong shaking, and thus their records cannot be used. A specialized instrument, the strong-motion accelerograph, was developed in the 1930s to record strong motion. A network of these specialized instruments must have the good fortune to be located close to the earthquake, and must be maintained, often for decades, in a state of readiness to record the rare strong shaking. In the 1990s, the situation changed somewhat with improvements in digital recording technology. A strong-motion accelerograph manufactured in the second half of the 1990s has

INTERNATIONAL HANDBOOK OF EARTHQUAKE AND ENGINEERING SEISMOLOGY, VOLUME 81B *ISBN: 0-12-440658-0*

an analog-to-digital converter with resolution of at least 16, and typically 19, bits, allowing it to record nearby earthquakes with magnitude as small as 2–3 with a useful signal-to-noise ratio, without sacrificing the ability to faithfully record the strongest shaking. With that capability, it can make a meaningful contribution to network seismology and, consequently, is worth including as part of the real-time networks in seismic areas. This overlap in instrumental capabilities promises a significant increase in the amount and quality of data that is useful for the objectives of strong-motion seismology.

Useful reviews of strong-motion seismology can be found in Kramer (1996) and Campbell (2002).

2. Strong-Motion Measurements

2.1 Instruments

The founding father of the strong-motion instrumentation program in the United States is John R. Freeman. After the Tokyo, Japan, earthquake of 1923, and the Santa Barbara, California, and Montreal, Quebec, earthquakes of 1925, he stimulated important early interactions between US and Japanese institutions on earthquake engineering and wrote the first significant book in the English language on earthquake engineering, *Earthquake Damage and Earthquake Insurance* (Freeman, 1932). He particularly recognized the urgent need for an instrument to record the strong shaking during earthquakes, and the result of his lobbying efforts was that the Coast and Geodetic Survey was authorized to develop and install such instruments in 1932. Nine months after the first instruments were installed, the first significant strong-motion records were obtained from the March 10, 1933, Long Beach, California, earthquake. Chapter 2 (G. Housner) gives a more complete review of the early history of strong-motion seismology.

Strong-motion seismology requires a specialized instrument called the strong-motion accelerograph. The instrument is a self-contained unit in as compact a container as possible, e.g., a box smaller than one foot (∼30 cm) on each side. The sensor (accelerometer) is typically a damped spring-mass system. The spring is stiff, giving the system a high natural frequency (typically 25–50 Hz), with the parameters selected so that accelerations of 1–2g (typically) will cause a deflection corresponding to full scale of the recording system. Some of the stiffness may be introduced electronically in a force-balance feedback loop that seeks to keep the seismic mass motionless relative to the frame of the instrument. The instrument is called an accelerometer because when the ground vibrates with frequencies less than the natural frequency of the sensor (and these frequencies usually predominate), the deflection of the sensor is proportional to the acceleration. Every accelerograph contains three accelerometers to measure the one vertical and two perpendicular horizontal components of acceleration.

In accelerographs designed in the United States through the late 1970s, the recording medium was usually photographic film. The enclosure was thus made into a light-proof box. A Japanese design used a pen to mechanically scratch a waxed paper. Newer designs convert an electrical signal to a digital format, which is recorded in a digital memory within the unit. However, probably half of the accelerographs in operation in the year 2000 still used the film recording. To record frequencies of ground motion above 20 Hz, the film must move through the camera at a fairly high rate, 1 cm/sec being typical. Digital accelerographs record 100 to 200 samples per second. To conserve recording medium, the accelerographs are built to activate the recorder when strong motion above some threshold is detected, and turn it off when the strong shaking has stopped. Trigger mechanisms in old instruments were mechanical or electromechanical sensors installed separately from the accelerometers. Digital systems monitor the signal amplitude coming from the sensors themselves. Usually, internal batteries operate the system, so that power failure will not cause a loss of data, and the batteries are kept fully charged by a trickle charging system to maintain readiness. Timing systems were not used in many of the early analog accelerographs, but they became more important as the analysis became more sophisticated. High-precision time, usually from satellite systems, is now essential with the digital accelerographs that provide records of aftershocks and other small events in large numbers. Precision time together with pre-event memory allow digital accelerographs to pinpoint earthquake locations beyond what is possible using only the traditional high-gain seismic networks.

2.2 Networks

The first network of strong-motion instruments, totaling 51 instruments, was installed by the US Coast and Geodetic Survey by the end of 1935. The total number of instruments deployed worldwide remained low until the mid-1960s, when commercially produced accelerographs became available and building ordinances began to require their installation in tall structures. In 2000, there were between 10,000 and 20,000 strong-motion instruments operating worldwide.

Any effort to identify all of the active accelerograph networks in the world is certain to be incomplete. However, an attempt, which succeeds in including at least most of the major networks, is made in Chapter 87 by Lahr and van Eck. Most seismically active countries have at least a few accelerographs in operation. Industrial nations with high seismic hazards have extensive programs. Countries with the most extensive strong-motion networks are Japan (see Chapter 63 by Kinoshita for a review of the largest Japanese network) and Taiwan (see Chapter 64 by Shin *et al.*). The United States has networks operated by the US Geological Survey (Borcherdt, 1997), the California Division of Mines and Geology (Shakal, 1997), the US Bureau of Reclamation (Viksne *et al.*, 1997), the US Army Corps of Engineers (Franklin, 1997), and other organizations, several of which are identified in the US Geological Survey (1999). Other countries whose networks have produced data from major earthquakes in recent years are Mexico (Anderson *et al.*, 1994; Quaas, 1997)

and Turkey (Inan *et al*., 1996). Ambraseys (1997) estimated that there are 2000 strong-motion instruments operating in Europe, and that these have produced over 2500 recordings. Unfortunately, it is still possible for large earthquakes to occur in populated regions of the world but not be recorded by any local strong-motion instruments (e.g., Gujarat, India, January 26, 2001, $M_w = 7.6$). Every such earthquake is both a tragedy and a lost opportunity, because there is still a critical shortage of recordings of ground motions from close distances to large earthquakes. Confident knowledge of ground motions in those circumstances can only be obtained from empirical observations.

2.3 Processing Data

Significant accelerograms recorded on film formats are eventually digitized and distributed. A great deal of effort has been devoted to this process because of the importance of accurate information for earthquake-resistant design. Although the instruments record acceleration, estimates of the ground velocity and displacement are also important for both engineering and geophysical research. Thus numerical integration of the records is important. The challenge in doing this accurately is determining exactly where the true zero level of acceleration is located on the accelerograms, both on the film record and on digital recordings (since an accelerograph is sensitive to a static field, e.g., a tilt). From film recordings, ground motions can generally be recovered for frequencies greater than about 0.2 Hz; this lower limit depends strongly on the size of the earthquake and the type of instrument. At high frequencies, data is reliable to 10 to 25 Hz on analog accelerographs and to 50 Hz or more on modern digital accelerographs. The history and current methods for data processing are discussed in Chapter 58 by Shakal *et al*.

2.4 Archiving of Accelerograms

With so many different organizations operating strong-motion accelerograph networks, a single global system of access to strong-motion data has never been completely achieved. Various systems for data recovery have been put in place. Perhaps the most thorough for the late 1900s was the World Data Center, which sought to compile and reproduce various tapes or computer disks. Seekins *et al.* (1992) prepared a CD-ROM with much of the data gathered in North America through 1986. Other CD-ROM data sets have been prepared by Alcantara *et al.* (1997), Cousins (1998), Ambraseys *et al*. (2000), Lee (2001), and Celebi *et al*. (2001). Distribution over the Internet also began in the late 1990s. In 2000, many strong-motion programs operated active Web sites for data distribution. A particularly useful US program for distribution of strong-motion data was established by the Southern California Earthquake Center (SCEC) for southern California data, and expanded with support from the Consortium of Organizations for Strong-Motion Observation Systems (COSMOS) to other data sets. The database could be accessed through the World Wide Web operated COSMOS (*http://db.cosmos-eq.org*). Data from large and small earthquakes recorded on the extensive Kyoshin Net and Kiban-Kyoshin Net in Japan can be accessed through their excellent Web sites (*http://www.k-net.bosai.go.jp/* and *http://www.kik.bosai.go.jp/*, respectively). The content of the European data is also available online (*http://www.isesd.cv.ic.ac.uk/esd/frameset.htm*, Ambraseys *et al*., 2001).

3. Empirical Descriptions of Strong Ground Motion

Empirical descriptions of strong motion invariably incorporate a dependence on the earthquake size and distance to the active faulting. The challenge of developing empirical descriptions is discussed by both Bolt and Abrahamson in Chapter 59 and by Campbell in Chapter 60, and thus the current chapter is confined to discussion of elementary material and definitions that are fundamental to those detailed discussions.

Earthquake size is measured using a variety of magnitude scales. Important magnitudes in the United States include the moment magnitude (discussed below), the local magnitude (M_L) originally defined by Richter using an instrument with a natural period of 0.8 seconds (see Richter, 1958), the body wave magnitude (m_b) determined from short-period teleseismic P waves measured on instruments with a natural period of 1.0 seconds, the surface wave magnitude (M_S) determined from teleseismic 20-second Rayleigh waves, and the coda duration magnitude (determined by the duration of the S-wave coda on short-period seismic networks using instruments with natural periods of a fraction of a second). While all of these scales are calibrated to give similar numbers at the magnitudes of overlap, it is impossible, due to the different methods of their determination, for them to all agree at every magnitude. The average relationship among these scales and the reasons for their differences are discussed by Heaton *et al*. (1986), and in Chapter 44 by Utsu (see also Chapter 60 by Campbell). The moment magnitude is at present the preferred scale for correlation with ground-motion characteristics, even though it is the last one to have been developed.

3.1 Parameters to Describe Strong Ground Motion

Because of the importance of strong-motion recordings for earthquake engineering, a number of different parameters have come into use to represent various characteristics of strong-motion recordings. To illustrate these, it is convenient to consider an example drawn from the collection of significant strong-motion records. Figure 1 shows four of the strong-motion accelerograms that were obtained in the September 19, 1985, Michoacan, Mexico, earthquake ($M_w = 8.0$). A report on these data is given by Anderson *et al*. (1986). Figure 2 shows the velocity at one of those stations, Caleta de Campos, integrated from the

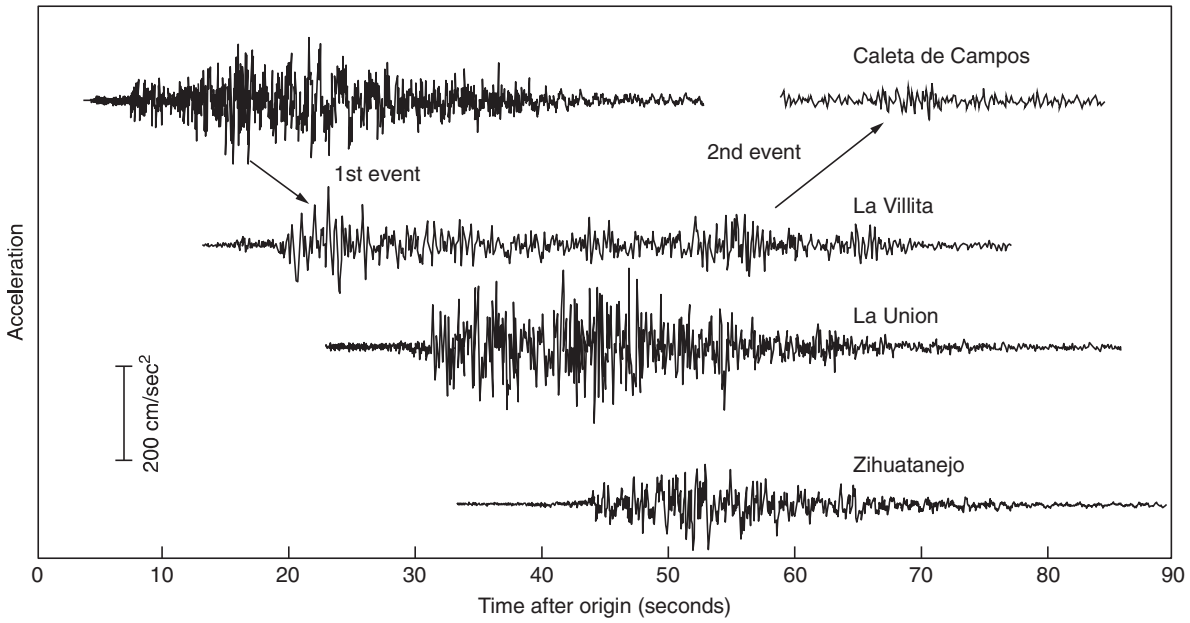

FIGURE 1 North–south component of acceleration at four strong-motion stations that recorded the September 19, 1985, Michoacan, Mexico, earthquake ($M_w = 8.0$). The Caleta de Campos station is almost directly above the hypocenter, the Zihuatanejo station is near the end of the rupture, 146 km east-southeast of Caleta de Campos, and the other stations are approximately along a line between Caleta de Campos and Zihuatanejo. The vertical separation of the traces is proportional to the separation of the stations on a projection along the strike of the causative fault. All records are aligned in absolute time after the origin of the earthquake (from Anderson *et al*., 1986).

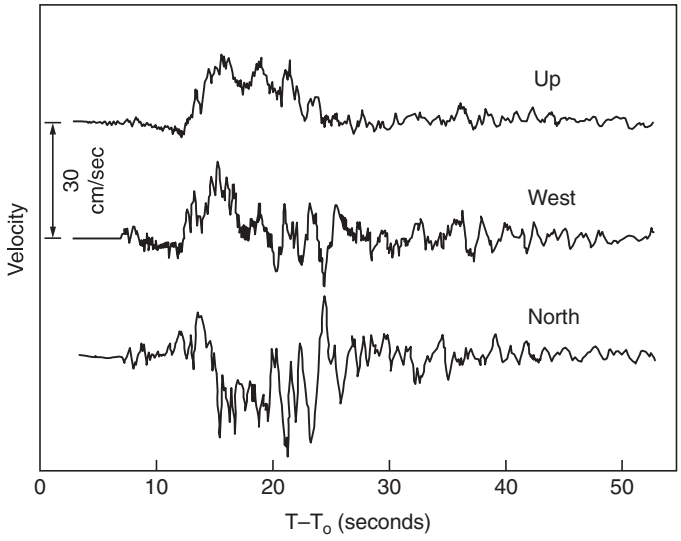

FIGURE 2 Three components of velocity at Caleta de Campos during the September 19, 1985, Michoacan earthquake (from Anderson *et al*., 1986).

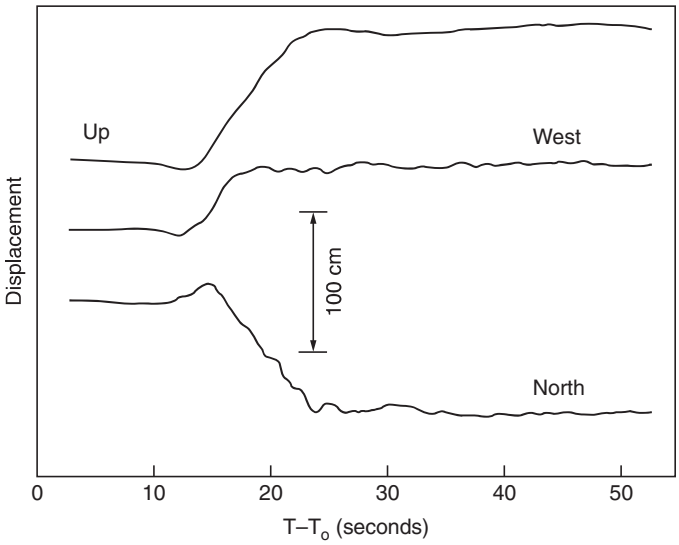

FIGURE 3 Three components of displacement at Caleta de Campos during the September 19, 1985, Michoacan earthquake (from Anderson *et al*., 1986).

accelerograms. Figure 3 shows the corresponding displacement, integrated from the velocities given in Figure 2. The Caleta de Campos station is sited on rock above the fault plane; the fault is between 15 and 25 km below the station, dipping at about 15°. Figure 4 shows the integral of acceleration-squared from the record. Figure 5 shows the Fourier amplitude spectrum for the north component of the Caleta de Campos accelerogram, and Figure 6 shows the corresponding response spectrum.

Figures 1–6 illustrate the set of parameters typically used to characterize strong-motion records. The simplest of these is peak acceleration, which is easily obtained from the unprocessed accelerogram (Figure 1). After records are digitized, it is common

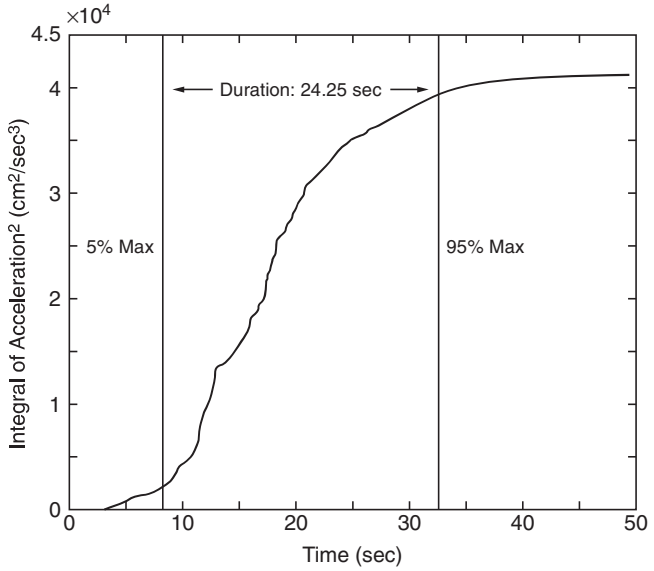

FIGURE 4 Integral of acceleration-squared determined from the north–south component of acceleration recorded at Caleta de Campos during the September 19, 1985, Michoacan earthquake. This integration is used as one method to measure the duration of the strong ground motions.

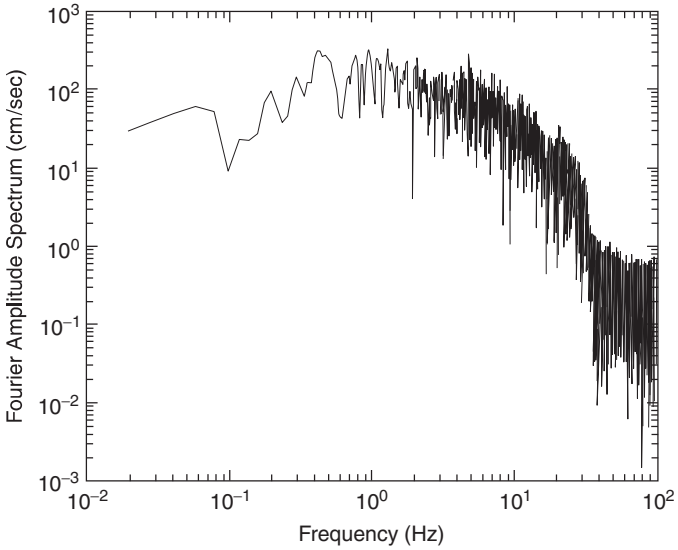

FIGURE 5 Fourier spectrum of the north–south component of acceleration recorded at Caleta de Campos during the September 19, 1985, Michoacan earthquake.

to obtain several additional parameters. Time-domain parameters often include peak velocity (Figure 2) and peak displacement (Figure 3, although it should be noted that records from which a static offset is recovered are extremely rare). Duration of the strong shaking is generally considered important, but there is not a unique definition of duration. One simple approach is to measure the interval between the times when the peak acceleration first and last exceeds some threshold, usually $0.05g$ (Bolt, 1969; Kramer, 1996). Figure 4 shows the alternative approach that was used by Trifunac and Brady (1975), namely to define the amount of time in which 90% of the integral of the acceleration-squared takes place. These two definitions lead to opposite results as distance increases. At large distances the peak ground motions decrease so that the interval duration goes to zero even though the ground was moving. On the other hand, the energy becomes dispersed, resulting in an increase in the time interval over which 90% of the total energy in the seismogram arrives. In the frequency domain, the Fourier amplitude spectrum (Figure 5) and a class of spectra known as response spectra (one of which is shown in Figure 6) are generally determined.

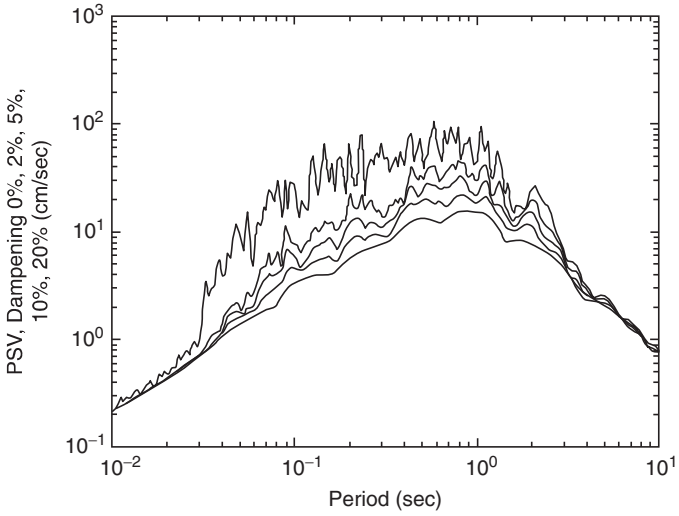

FIGURE 6 Pseudo-relative velocity response spectrum determined from the north–south component of acceleration recorded at Caleta de Campos during the September 19, 1985, Michoacan earthquake.

Response spectra describe peak time–domain response of a suite of single degree of freedom oscillators to the seismic excitation. Five types of response spectra are defined: relative displacement (*Sd*), relative velocity (*Sv*), absolute acceleration (*Sa*), pseudo-relative velocity (*PSV*), and pseudo-relative acceleration (*PSA*) (e.g., Hudson, 1979). Response spectra play an important role in the development of engineering designs. Consider a damped oscillator, which operates on the same principle as an inertial seismograph. Let the undamped natural period of this oscillator be T_o and let the fraction of critical damping be h. When the base of this oscillator is subjected to an accelerogram, there is relative motion between the seismic mass and the base. The maximum value of the relative displacement is the value of the relative displacement spectrum (*Sd*) at the period and damping of the oscillator. Thus to calculate a relative displacement spectrum, it is necessary to calculate the response to the accelerogram of a suite of oscillators with a range of T_o. The relative velocity response (*Sv*) has the value of the peak relative velocity between the seismic mass and the base. The absolute acceleration response (*Sa*) is the maximum acceleration of the seismic mass in an inertial reference frame. The pseudo-relative velocity, *PSV*, is obtained from *Sd* by $PSV = (2\pi/T_o)\, Sd$. The pseudo-relative

acceleration, *PSA*, is obtained from *Sd* by $PSA = (2\pi/T_o)^2 Sd$. In general, $PSA \approx Sa$ and $PSV \approx Sv$, although these different spectra can have different asymptotic properties at high and low frequencies. The spectra are usually computed for a range of damping, from $h = 0\%$ (undamped) to $h = 20\%$ of critical. This range is used because most manmade structures are similarly lightly damped. A damping of $h = 5\%$ is the most likely to be reported. Newmark and Hall (1982), Kramer (1996), and Jennings in Chapter 67 present a review of response spectra and their applications.

Figure 6 gives *PSV* for a 5% damped oscillator for one of the accelerograms shown in Figure 1. Comparison of Figures 5 and 6 shows that in the central frequency ranges, *PSV* takes values that are comparable to a smoothed Fourier spectrum of acceleration. This is expected, as the Fourier spectral integral is in fact closely related to the Duhamel integral, which is one method used to compute the response spectra (Udwadia and Trifunac, 1973).

3.2 Ground-Motion Prediction Equations

Based on past recordings of strong earthquake motion, consisting of data such as those in Figures 1–6, the peak acceleration and other peak parameters can be described by a "ground-motion prediction equation" as a function of the earthquake magnitude, distance from the fault to the site, general site condition parameter, and sometimes other parameters. Figure 7 shows an example of one such relationship, developed by Abrahamson and Silva (1997) for crustal earthquakes in tectonically active areas. Naturally the ground-motion prediction equations do not exactly describe peaks of past earthquake ground motions. The deviation of a datum from the predicted mean peak acceleration (the "residual") is treated as a random variable, and it is consistent with a lognormal distribution function out to two standard deviations at least. The standard deviation for Figure 7 depends on magnitude. Abrahamson and Silva estimate that it is 0.7 natural (i.e., base e) logarithm units for $M < 5$, 0.43 for $M > 7$, and a linearly decreasing function of magnitude in between. For reference, a standard deviation of 0.5 corresponds to a multiplicative factor of 1.6 (times the mean value) to obtain the value that exceeds 84% of the data. Peak acceleration is a commonly employed parameter for these regressions, but peak velocity, peak displacement, spectral amplitudes, and duration have also been modeled in this manner. Recent ground-motion prediction equations are reviewed thoroughly by Campbell in Chapter 60, and also discussed by Bolt and Abrahamson in Chapter 59, and Faccioli and Pessina in Chapter 62.

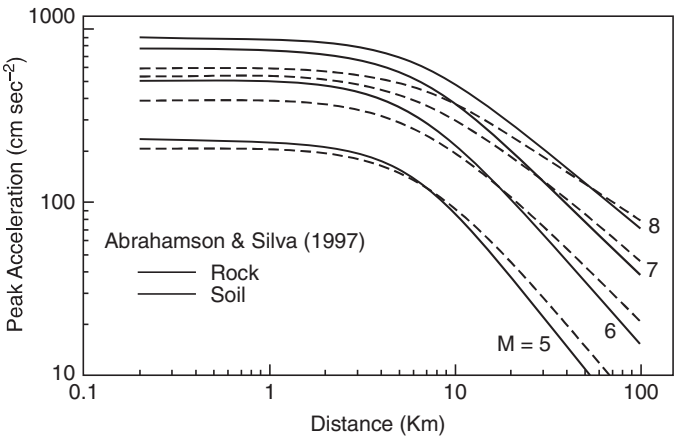

FIGURE 7 Peak acceleration as a function of magnitude and distance from the fault, as given by the ground-motion prediction equation of Abrahamson and Silva (1997).

Because ground-motion prediction equations are a key component of probabilistic seismic hazard analyses, it is clear that their development will be an important part of seismological research for some time to come. Until 1999, the estimates from these equations for large magnitudes and short distances were based more on extrapolation than on extensive amounts of data. In 1999, there were two significant earthquakes that contributed very important data at short distances. One was the Izmit, Turkey, earthquake (August 17, 1999, $M_w = 7.6$), for which Anderson *et al*. (2000a) found the peak accelerations on rock at near-fault distances to be significantly below four different ground-motion prediction equations. The other was the Chi-Chi, Taiwan, earthquake (September 20, 1999, $M_w = 7.6$), for which peak accelerations were significantly below three different recent ground-motion prediction equations developed primarily from North American data but presumed to apply to the same tectonic environment (Tsai and Huang, 2000). The discrepancy could be caused by any of several factors. Faults with a large total slip tend to be smooth and devoid of asperities, thus radiating less high-frequency energy than a fault with less total slip (Anderson *et al*., 2000a). Faults with a high slip rate have less time to heal between earthquakes, and thus earthquakes on these faults may have lower stress drops and less high-frequency energy. Differences could arise from differing lithology in the rocks cut by the fault. The nature of the regional stress field (e.g., extensional vs. compressional) could affect the high-frequency generation (Spudich *et al*., 1999). Somerville (2000) suggested that the discrepancy could be related to whether or not the earthquake ruptured the surface. Finally, the discrepancy could be due to the dynamics of rupture, which under some models can change when the slip becomes large enough. This issue illustrates that considerably more data, research, and basic physical understanding will be needed to reduce the uncertainties inherent in the present generation of ground-motion prediction equations.

4. Physics Contributing to the Nature of Strong-Motion Seismograms

A major goal of strong-motion seismology is to be able to synthesize strong-motion seismograms suitable for use in engineering analyses (Aki, 1980). The ability to synthesize observations

depends on understanding of the physical phenomena affecting the ground motions at a site of interest when a fault identified by the geologists breaks.

In the last part of the 20th century, there was major progress toward this goal. A full understanding requires input from two disciplines. One is earthquake source physics, where the minimum requirement is a kinematical description of the slip function on the fault. The other is wave propagation, across the entire frequency band, from the fault to the station. The following sections discuss each of these fields.

4.1 Mathematical Framework for Ground-Motion Modeling

Earthquakes are caused when the rocks on opposite sides of a fault slip suddenly. The characteristics of strong ground motions that result from this instability are strongly affected by the geometrical and dynamic characteristics of the faulting. The geometrical characteristics include the size, shape, depth, and orientation of the fault area that slipped during the earthquake and the amount and direction of slip. The orientation of the fault and the amount and direction of offset may be variable over the fault surface. The important dynamic parameters include where on the fault the rupture initiated (hypocenter), how rapidly it spread over the fault (rupture velocity), how quickly (rise time) and how smoothly the slip took place at each point on the fault, and how coherently adjacent points on the fault moved. These dynamic parameters are functions of the stresses acting on the fault, the physical properties of the rock surrounding the fault, and the strength of the fault itself, and are variables over the dimension of a large fault during major earthquakes.

The process is generally expressed mathematically using a representation theorem. Using the notation of Aki and Richards (1980, p. 39), one form for the representation theorem is

$$u_n(\mathbf{x}, t) = \int_{-\infty}^{\infty} d\tau \iint_{\Sigma} [u_i(\boldsymbol{\xi}, \tau)] c_{ijpq} \nu_j \frac{\partial G_{np}(\mathbf{x}, t-\tau; \boldsymbol{\xi}, 0)}{\partial \xi_q} d\Sigma \tag{1}$$

In this equation, $u_n(\mathbf{x}, t)$ gives the n^{th} component of the displacement of the ground at an arbitrary location $\mathbf{x}$ and at time t. The vector $\mathbf{v}$ is normal to the fault, and the positive direction of the normal defines the positive side of the fault for defining the slip discontinuity. The i^{th} component of the discontinuity in the slip across the fault is given by

$$[u_i(\boldsymbol{\xi}, \tau)] = u_i^+(\boldsymbol{\xi}, \tau) - u_i^-(\boldsymbol{\xi}, \tau) \tag{2}$$

where $\boldsymbol{\xi}$ represents a location on the fault surface Σ and τ is the time that this displacement occurs. Because the fault is represented by the surface Σ, $d\Sigma$ represents two spatial dimensions. The Green's function is given by $G_{np}(\mathbf{x}, t; \boldsymbol{\xi}, \tau)$. This gives the motion in the n direction at location $\mathbf{x}$ and time t caused by a point force acting in the p direction at location ξ and time τ. Finally, c_{ijpq} gives the elastic constants of the medium. For an isotropic medium,

$$c_{ijpq} = \lambda \delta_{ij} \delta_{kl} + \mu(\delta_{ik}\delta_{jl} + \delta_{il}\delta_{jk}), \tag{3}$$

where λ and μ are the Lame constants. The constant μ is the familiar shear modulus; there is no similarly simple experiment by which λ can be measured. By convention, in Eq. (1) summation takes place over repeated indices.

Equation (1) represents the ground motion at the site as the linear combination, through the integral over space, of the contributions from each point on the fault surface. The convolution over time incorporates the effect of the rupture at each point taking a finite amount of time to reach its final value. Through the representation theorem, the problem of predicting ground motions requires specification of the offset on the fault as a function of location and time, which incorporates earthquake source physics, and a specification of the Green's function, which incorporates wave propagation. Spudich and Archuleta (1987) discuss several techniques that are used for evaluation of Eq. (1).

Equation (1) has certain limitations. For large amplitudes of seismic waves, the stress–strain relationship in the Earth, especially near the surface, becomes nonlinear. In this case, the assumed linear superposition of waves from different parts of the fault does not apply. A common approximation for this case is to predict the motion in "rock" at some depth beneath the surface, where linearity is assumed to apply, and then treat the wave propagation from that depth to the surface as a vertical propagation problem through the nonlinear medium. On the earthquake source side, writing the time dependence in the Green's function as $(t - \tau)$ assumes that the Green's function is independent of time. This assumption can break down if the faulting process affects the propagation of the seismic waves from the source to the station. For instance, if seismic shear waves are not transmitted through the fault where it is slipping, but they are transmitted through the fault where it is not slipping, then Eq. (1) would not hold exactly. In spite of these limitations, Eq. (1) forms the mathematical basis for nearly all model-based ground-motion predictions and has enabled the inversion of strong ground-motion records to obtain models of the slip function for numerous earthquakes.

4.2 Effects of the Earthquake Source

4.2.1 Source Effects in the Far-Field

Some understanding of seismic radiation in the far-field is important for strong-motion seismology. The far-field spectrum is important because most places shaken by an earthquake are in the far-field region. For the eastern United States, models of strong motion have focused primarily on estimation of far-field ground motions. In addition, nearly all determinations of the seismic

moment are made in the far-field region. In the near-field region, we expect that we cannot disregard the contributions of the far-field Green's function terms to the ground-motion spectrum, nor can we disregard the effects of spatial variation of the far-field radiation pattern for waves originating at different locations along the fault. Source effects on the far-field seismogram are discussed by Aki and Richards (1980, Chapter 14).

The seismic moment, M_0, is generally regarded as the best available single number to describe the size of an earthquake. A rigorous definition starts with the seismic moment density, which represents the internal stresses necessary to cancel the strain produced by the internal nonlinear processes that cause the earthquake. These stresses can be interpreted as a double-couple force, and the seismic moment is the magnitude of one of these couples integrated over the fault (e.g., Aki and Richards, 1980; Madariaga, 1983). The magnitude of the forces controls the amplitudes of radiated seismic waves, and thus seismic moment can be determined from seismograms. In an infinite, homogeneous, isotropic medium, seismic moment is also given by the equation

$$M_0 = \mu A D \tag{4}$$

where A is the fault area (e.g., length, L, times width, W), D is the average slip, and μ is the shear modulus. This links seismic observations with the magnitude of geological deformations. The moment magnitude, usually designated as M_w, is essentially a change of variable from seismic moment,

$$M_w = \frac{2}{3}\log M_0 - 10.73, \tag{5}$$

when the units of M_0 are dyne cm. Notation and terminology are a little confusing, as common usage differs slightly from the original literature (see Chapter 44 by Utsu). Kanamori (1977) defined an energy magnitude M_w such that

$$\log(M_0) = 1.5 M_w + 16.1, \tag{6}$$

and Hanks and Kanamori (1979) defined a moment magnitude **M** such that

$$\log(M_0) = 1.5\,\mathbf{M} + 16.1. \tag{7}$$

Harvard University, in their project to determine seismic moments for all large earthquakes worldwide, uses Eq. (5), which differs slightly from both of these definitions. The Harvard catalog is available online at *http://www.seismology.harvard.edu/projects/CMT/*.

A couple of examples of the way seismic moment can be used are in order. According to the Harvard CMT solution, the September 19, 1985, Michoacan, Mexico, earthquake had a seismic moment of 1.1×10^{28} dyne cm and $M_w = 8.0$. Based on the aftershock area (Anderson *et al*., 1986) the fault was about $L = 170$ km long and $W = 50$ km wide. Assuming a shear modulus of 4.0×10^{11} dyne/cm^2, Eq. (4) implies $D = 320$ cm. The fault could not be examined in this case, but the static offsets inferred from the accelerograms (e.g., Figure 3) are consistent with this estimate of the slip to within a factor of less than two. A second example is the Northridge, California, earthquake of January 17, 1994. This event had a Harvard moment of 1.18×10^{26} dyne cm and $M_w = 6.7$. The fault dimension, according to Wald *et al*. (1996) was 15 km along strike and 20 km along the dip. The source was shallower than the Michoacan earthquake, so the shear modulus can be taken to be 3.3×10^{11} dyne/cm^2, implying an average slip $D = 120$ cm. Because slip of more than ~10 m has practically never been observed, it becomes clear that a large seismic moment and consequently a large moment magnitude requires a very large fault area. Increasing fault dimensions have a fundamental impact on the characteristics of strong motions, as will be described following.

Because of the relationship of the moment to the size of the fault that caused the earthquake (length, width, dip, and the slip distribution), and because the fault size and slip may in some cases be estimated from geological studies, these geometrical characteristics can be used to estimate the seismic moment of anticipated earthquakes. Alternatively, when the geometry is not completely known, regression equations, such as those given by Wells and Coppersmith (1994), can relate moment magnitudes to the fault dimensions. Scatter of data relative to regression equations arises because the ratios of fault length to width to slip vary, perhaps, in part, correlated with the slip rate and/or repeat time on the fault (Kanamori and Allen, 1986; Scholz *et al*., 1986; Anderson *et al*., 1996).

Theoretically, the moment has a fundamental effect on strong ground motion in determining the spectral amplitudes of low-frequency ground motions. To see this, we begin with an expression for the complete vector displacement field from a point source in an infinite, homogeneous, isotropic solid. This expression, derivable from Eq. (1) (Aki and Richards, 1980, p. 81), is

$$\begin{aligned}\mathbf{u}(\mathbf{x},t) = {} & \frac{1}{4\pi\rho}\mathbf{A}^N\frac{1}{r^4}\int_{r/\alpha}^{r/\beta}\tau M_0(t-\tau)\,d\tau \\ & + \frac{1}{4\pi\rho\alpha^2}\mathbf{A}^{IP}\frac{1}{r^2}M_0\left(t-\frac{r}{\alpha}\right) \\ & + \frac{1}{4\pi\rho\beta^2}\mathbf{A}^{IS}\frac{1}{r^2}M_0\left(t-\frac{r}{\beta}\right) \\ & + \frac{1}{4\pi\rho\alpha^3}\mathbf{A}^{FP}\frac{1}{r}\dot{M}_0\left(t-\frac{r}{\alpha}\right) \\ & + \frac{1}{4\pi\rho\beta^3}\mathbf{A}^{FS}\frac{1}{r}\dot{M}_0\left(t-\frac{r}{\beta}\right),\end{aligned} \tag{8}$$

where the radiation pattern terms are

$$\begin{aligned}\mathbf{A}^N &= 9\sin 2\theta\,\cos\varphi\hat{\mathbf{r}} \quad - 6(\cos 2\theta\,\cos\varphi\hat{\boldsymbol{\theta}} - \cos\theta\,\sin\varphi\hat{\boldsymbol{\varphi}}) \\ \mathbf{A}^{IP} &= 4\sin 2\theta\,\cos\varphi\hat{\mathbf{r}} \quad - 2(\cos 2\theta\,\cos\varphi\hat{\boldsymbol{\theta}} - \cos\theta\,\sin\varphi\hat{\boldsymbol{\varphi}}) \\ \mathbf{A}^{IS} &= -3\sin 2\theta\,\cos\varphi\hat{\mathbf{r}} + 3(\cos 2\theta\,\cos\varphi\hat{\boldsymbol{\theta}} - \cos\theta\,\sin\varphi\hat{\boldsymbol{\varphi}}) \\ \mathbf{A}^{FP} &= \sin 2\theta\,\cos\varphi\hat{\mathbf{r}} \\ \mathbf{A}^{FS} &= \qquad\qquad (\cos 2\theta\,\cos\varphi\hat{\boldsymbol{\theta}} - \cos\theta\,\sin\varphi\hat{\boldsymbol{\varphi}}).\end{aligned} \tag{9}$$

In Eq. (8), **u** is the displacement due to the earthquake. The earthquake is assumed to be a point source located at the origin, and $\mathbf{x} = (r, \theta, \varphi)$ is the location of the observer in spherical coordinates. The observation point is a distance r from the earthquake. $\hat{\mathbf{r}}$, $\hat{\boldsymbol{\theta}}$, and $\hat{\boldsymbol{\varphi}}$ are unit vectors in the direction of r, θ, and φ, increasing (respectively), so that the radial direction is along $\hat{\mathbf{r}}$ away from the source toward the site, and $\hat{\boldsymbol{\theta}}$ and $\hat{\boldsymbol{\varphi}}$ are both transverse directions. The angle θ is a co-latitudinal polar angle, measured between the direction that is normal to the fault and the direction to the station. The angle φ is measured in the plane containing the fault, between the direction of slip on the fault and the normal projection of the observation point into the plane. The vectors **A** are radiation patterns, which give the relative amplitudes of the different components of motion at location **x**. The superscripts on the components of **A** correspond to the types of waves: *N* to near-field waves, *IP* to intermediate-field *P*-waves, *IS* to intermediate-field *S*-waves, *FP* to far-field *P*-waves, and *FS* to far-field *S*-waves. $\dot{M}_0(t)$ is the moment rate. The constants in the equation are ρ, the material density, and α and β, the compressional and shear velocities in the medium.

From Eq. (8), the *P*-waves arrive at the location **x** after a delay of duration $\frac{r}{\alpha}$. The *S*-waves arrive at the location **x** after a delay of duration $\frac{r}{\beta}$. The first three terms in Eq. (8), the near- and intermediate-field motions, carry a permanent offset of the ground. The intermediate-field offsets arrive with the *P*-wave and the *S*-wave velocities, and the near-field offset arrives continuously between the *P*- and the *S*-waves. The amplitude of the near-field term decreases as r^{-4} while the intermediate-field terms decrease as r^{-2}. Thus these first three terms diminish rapidly and do not carry any energy into the far-field, but they are seen on some strong-motion records after integration to displacement. The far-field radiation terms decrease in amplitude as r^{-1}. Because the energy content of the wave is proportional to the amplitude squared, and the surface of a sphere with radius r increases as r^2, the energy carried by these waves is the same through a sphere of any radius (neglecting anelastic losses), and these terms do carry energy into the far-field.

The moment rate, $\dot{M}_0(t)$, reflects the fact that the slip on the fault is not instantaneous. Rather, it takes some time for rupture to spread from the hypocenter to the entire extent of the fault, and also it takes some time for the slip at each point to be completed. This equation treats the fault as a point source, in which the effects of these phenomena must be concentrated into a single effective moment rate. Thus it is a far-field approximation when it is applied to the interpretation of seismograms. Aki and Richards (1980, p. 805) suggest that a conservative criterion under which this approximation is strictly valid is when the wavelength λ satisfies the criteria $\lambda \gg \frac{2L^2}{r}$. For a station 30 km from a fault with length $L = 10$ km, this condition is met for frequencies substantially less than 0.5 Hz. At higher frequencies, the apparent moment rate that one would infer from the seismogram would be affected by the source finiteness, and show an azimuthal dependence. When fault finiteness is a factor, it may be possible to treat the fault as a set of several point sources, with each source radiating as in Eq. (8). Several studies have shown that the far-field moment-rate function is the Radon transform of the slip-rate function as a function of space and time (e.g., Kostrov, 1970; Ruff, 1984), and some have inverted seismograms to recover source behavior. Good examples of the source pulses seen for small earthquakes at differing azimuths are Frankel *et al*. (1986) and Fletcher and Spudich (1998).

Much can be learned from the relationship between seismic moment and the far-field *P*- and *S*-waves. We focus on the far-field *S* wave in Eq. (8), given by

$$\mathbf{u}^{FS}(\mathbf{x}, t) = \frac{\mathbf{A}^{FS}(\theta, \varphi)}{4\pi\rho\beta^3 r}\dot{M}_0\left(t - \frac{r}{\beta}\right), \tag{10}$$

recognizing that the application to the far-field *P*-wave is largely the same. The amplitude of the displacement pulse of *S*-waves in an infinite homogeneous medium is proportional to the moment rate. The integral of that displacement pulse over time is proportional to M_0, because

$$M_0 = \int_0^\infty \dot{M}_0(t)\, dt. \tag{11}$$

The limit of integration is written here as infinity, but the intent is that it be only long enough to include the duration of actual slip on the fault, and thus typically totals a few seconds. Consequently, moment can be estimated from the low frequencies of ground motion observations at large distances from the fault, with appropriate corrections for geometrical spreading, radiation pattern, and complexities of wave propagation.

As recognized by Aki (1967), spectral properties of the source spectrum follow from properties of the Fourier transform and from the far-field terms in Eq. (8). The far-field displacement pulse predicted by Eq. (8) is, in general, a one-sided pulse. A property of the amplitude of the Fourier transform of any one-sided pulse is that at low frequencies, it is asymptotic to the area under the pulse. Thus, M_0 can be estimated from the low-frequency asymptote of the Fourier transform of the displacement seismogram.

The Fourier transform of any one-sided pulse also has a corner frequency, f_C, say, that is inversely proportional to the duration of the pulse, with the amplitude of the transform decreasing for frequencies above the corner frequency. For example, for a boxcar function [$b(t) = 1$ for $0 \le t \le T_b$ and 0 otherwise] with a duration of T_b, the corner frequency is $f_C = 1/(2T_b)$. At the fault, the duration of faulting is controlled by the time it takes rupture to cross the fault, usually using a rupture velocity of about 90% of the shear velocity. Thus by measuring the corner frequency from the Fourier amplitude spectrum, it is possible to estimate the apparent duration of faulting at the source and the fault dimension. A relationship between corner frequency and fault dimension (radius, r_f) that is commonly used for small earthquakes was proposed by Brune (1970, 1971): $r_f = 2.34\,\beta/(2\,\pi f_C)$. Geometrical uncertainties (e.g., is rupture unilateral or bilateral, etc.) contribute about a factor of two to overall uncertainty.

Aki and Richards (1980) discuss additional relations and considerations for relating the corner frequency to the fault dimension. For very small events, the corner frequency can be obscured by attenuation. For larger earthquakes, strong-motion accelerograms cannot generally be assumed to be in the far-field, and the finite fault size and source-station geometry have a significant impact on the records. Nonetheless, the general prediction is that a larger earthquake, with a larger fault dimension, will generally have a smaller corner frequency. It was recognized by Aki (1967) that if $D \propto L \propto W$, implying that the stress drop is constant (e.g., Kanamori and Anderson, 1975), then $M_0 \propto L^3$, $f_C \propto L^{-1}$ and $f_C \propto M_0^{-1/3}$.

Figures 8–10 illustrate the way accelerograms recorded 25 km from the epicenter depend on magnitude, and can be used to illustrate several of these predictions. Figure 8 shows accelerograms from several earthquakes, of different magnitudes, plotted on a common scale. As the magnitude of the earthquake increases, the amplitudes of ground acceleration generally increase, and the duration increases dramatically. The increase in duration follows from the increase in the dimension of the fault. Figure 9 shows Fourier amplitude spectra corresponding to each of the accelerograms in Figure 8, and Figure 10 shows the *PSV* response spectra. The response spectra, in this case, are shown on tripartite axes. This is a common type of presentation that allows one to read the values of *PSA* and *Sd* also directly from the figure. The shape of the Fourier spectrum of acceleration can be generalized as in Figure 11. Figures 9 and 10 show that as

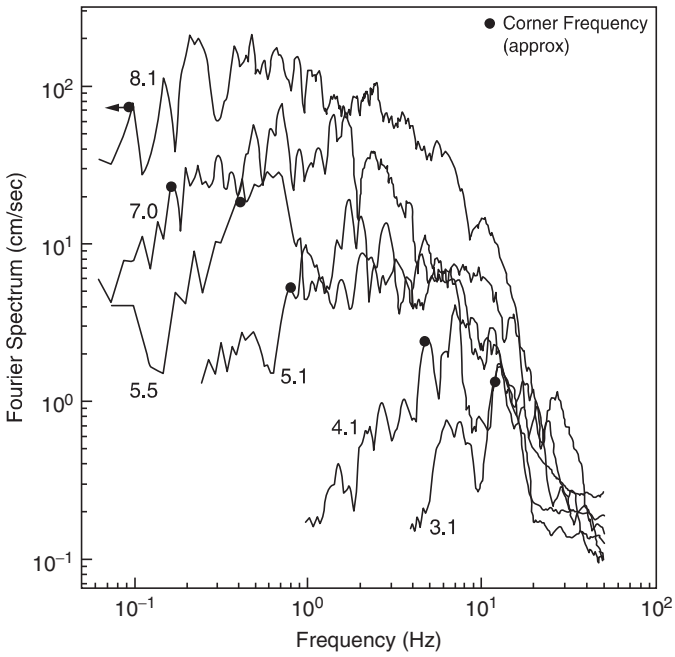

FIGURE 9 Smoothed Fourier amplitude spectra for the accelerograms shown in Figure 8 (modified from Anderson and Quaas, 1988). Circles identify approximate corner frequency on each spectrum.

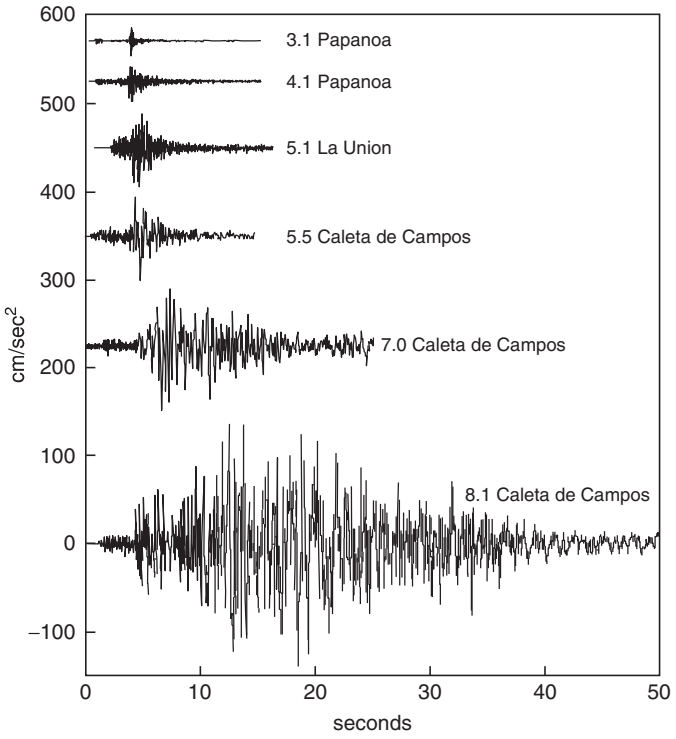

FIGURE 8 Accelerograms recorded in Guerrero, Mexico, from earthquakes of several magnitudes (from Anderson and Quaas, 1988).

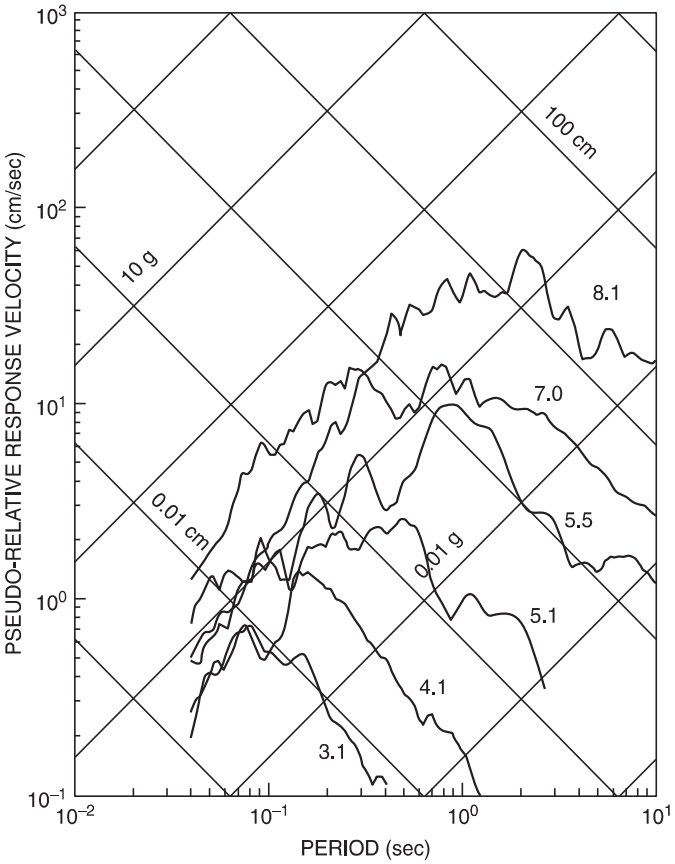

FIGURE 10 Pseudo-relative velocity response spectra of the accelerograms shown in Figure 8 (from Anderson and Quaas, 1988).

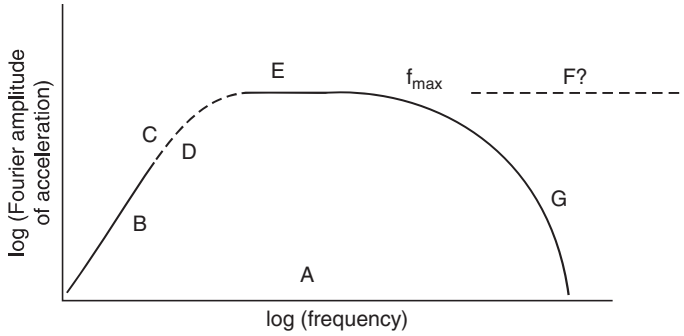

FIGURE 11 Qualitative illustration of the far-field Fourier amplitude spectrum of a strong-motion accelerogram. The overall level (A) is controlled by the distance from the seismic source. At low frequencies (B), the spectrum increases proportional to f^2, where f is the frequency. The corner frequency (C) is controlled by the fault dimension and directivity, and occurs at the frequency where this asymptotic behavior is replaced with a lower slope. The shape of the spectrum immediately above the corner frequency (D) is controlled by large-scale complexity of the fault slip as a function of space and time. The flat portion (E) is characteristic of an ω–*square* source model, meaning that the source displacement spectrum has a high-frequency rolloff of ω^{-2}. The spectrum rolls off at high frequencies (G), i.e., frequencies greater than f_{max}. It is not known to what extent the spectrum at the fault is flat (F) with the rolloff due to attenuation, and to what extent the rolloff occurs due to processes at the earthquake source.

the magnitude increases, the amplitudes of the low-frequency waves increase dramatically, while the amplitudes of the high frequencies increase slowly. This change in spectral shape as the moment of the earthquake increases is the reason different magnitude scales cannot be calibrated to be identical: Different magnitudes are measured at different frequencies depending on the characteristics of the instruments, and spectral amplitudes at different frequencies do not change with the same ratio as earthquake size increases.

The spectra in Figures 5, 9, and 11 are Fourier spectra of the acceleration of the ground, not of the displacement. The relationship of the two at each frequency is

$$|\tilde{a}(f)| = (2\pi f)^2 |\tilde{u}(f)|, \tag{12}$$

where $\tilde{u}(f)$ is the Fourier transform of the displacement pulse. Thus, where the displacement spectrum is predicted to be constant at low frequencies, the acceleration spectrum $[\tilde{a}(f)]$ is predicted to increase proportional to f^2. The corner frequency is recognized at the transition from this rapid increase to a more nearly flat spectrum in the higher frequency band (Figure 11); it clearly decreases as magnitude increases (Figure 9). The magnitude dependence of the corner frequency introduces the magnitude dependence into the frequency band within which the accelerograph signal is above the instrumental noise level.

Above the corner frequency, a spectrum that falls off proportional to f^{-2} is called an ω–*square* (or ω^{-2}) model, and one that falls off proportional to f^{-3} is an ω–*cube* (or ω^{-3}) model ($\omega = 2\pi f$). In a frequency band where the displacement spectrum is proportional to f^{-2}, the acceleration spectrum is independent of frequency. In Figure 5, as is typical with strong-motion accelerograms (Hanks, 1979, 1982), this is the approximate spectral behavior above the corner frequency and up to a frequency of 5–10 Hz (f_{max}, Figure 11). This approximately flat acceleration spectrum over a sizeable frequency band in strong-motion records for larger magnitude earthquakes has motivated models of strong motion as band-limited white noise (e.g., Hanks, 1979). The amplitude of this flat part increases gradually with magnitude (Figure 9). Below the corner frequency, the spectrum increases by a factor of 10–30 for each increase of a unit magnitude. These overall trends of the acceleration spectra at low to intermediate frequencies (e.g., below several Hz) are consistent with the ω–*square* model for the earthquake spectrum.

From a signal processing perspective, the rate of falloff of the spectrum of a general one-sided pulse is controlled by the sharpness of discontinuities in the displacement time series. The spectrum of the boxcar falls off proportional to f^{-1}. If the steps at the start and end of the boxcar are replaced with ramps, the falloff is proportional to f^{-2} instead. In the asymptotic limit at high frequencies, it is necessary for the seismic spectrum to fall off at least as fast as $f^{-1.5}$, because the radiated energy is finite. The more interesting interpretations, however, are in terms of the earthquake source time functions, summarized by Aki and Richards (1980). They suggest that the ω–*square* spectral shape is the result of dominance of stopping phases (i.e., signals from the edge of the expanding fault as it is arrested) in the seismic spectrum, as models for the spectrum from the start of rupture are predicted to have an ω–*cube* behavior. Indeed, some studies of strong motions from well-recorded earthquakes find evidence that high-frequency radiation is released preferentially from the margins of the areas with the largest slip, rather than from the areas that slipped the most (e.g., Zeng *et al*., 1993b; Kakehi and Irikura, 1996, 1997; Kakehi *et al*., 1996; Nakahara, 1998; Nakahara *et al*., 1999).

The fine structure on most spectra make it difficult to determine shapes definitively. Many spectra seem to show a spectral fall-off closer to f^{-1} in a limited frequency band immediately above the corner frequency (e.g., Tucker and Brune, 1973); consider also the frequencies above the corner frequency in Figure 9 for the $M \sim$ 7–8 earthquakes. Brune (1970) proposed a physical interpretation of the high-frequency falloff: that f^{-2} follows from an earthquake with complete stress drop, whereas f^{-1} is an indication of partial stress drop (i.e., rupture is arrested before all of the stress driving the earthquake has been relieved).

4.2.2 Finite Source Models

While the characteristics of ground motions in the far-field are informative for strong-motion seismology, several phenomena observed in strong motion can only be understood in the context of finite source models. These include directivity, near-source pulse motions, and static offsets.

Description of the spatial distribution of slip is feasible for earthquakes that rupture a sufficiently large fault surface. Models can be developed using teleseismic data, but models that

are also constrained by strong-motion data are most interesting as the strong-motion data is significantly less affected by attenuation and thus includes a much broader frequency band than teleseismic waves. These models are generally kinematic models, in that they describe a slip function as a function of location and time on the fault without assuring that this function satisfies all known physics of earthquake rupture. Some dynamic models that are consistent with known earthquake physics have also been developed recently (e.g., Mikumo and Miyatake, 1995; Olsen *et al*., 1997, Belardinelli *et al*., 1999). Dynamic rupture of earthquakes is reviewed by Madariaga and Olsen in Chapter 12.

Haskell (1964) proposed that a propagating ramp was a useful description of an earthquake slip function. In this model, rupture starts at one edge of a rectangular fault and propagates to the opposite edge with a constant velocity, the rupture velocity. When the rupture front reaches a point on the fault, slip begins and one side of the fault slips past the other with a constant slip velocity until a final offset is reached. The time required to reach this final offset is the rise time. Current models make use of the same concepts, but generally allow the rupture velocity, rise time, slip direction, and final offset all to be variables over the fault surface. These additional variables can be thought of as adding roughness to the propagating ramp model. Many of the earthquakes for which slip functions are available are listed in Table 1. A representative slip function, for the Landers earthquake, is given in Chapter 12 by Madariaga and Olsen. Most of these events have been modeled with a rupture velocity less than the shear velocity, in the range of 2.4–3.0 km/sec, with no evidence of a dependence of rupture velocity on seismic moment (Somerville *et al*., 1999). Supershear rupture velocity has been observed in three crustal earthquakes; the 1979 Imperial Valley earthquake (Olson and Apsel, 1982; Archuleta, 1984; Spudich and Cranswick, 1984), the 1999 Izmit/Kocaeli, Turkey, earthquake (Ellsworth and Celebi, 1999; Anderson *et al*., 2000b; Bouchon *et al*., 2000; Sekiguchi and Iwata, 2002), and the 1999 Duzce, Turkey, earthquake (Bouchon *et al*., 2000).

Heaton (1990) attempted to generalize the results of these inversions. His important conclusion, which has been supported in subsequent studies (e.g., Somerville *et al*., 1999), is that the rise time on the fault appears to be short, implying that the rupture can be approximated as a slip pulse that is propagating along the fault (e.g., Figure 13 of Chapter 12 by Madariaga and Olsen), like the propagating ramp of Haskell (1964). Horton (1996) concluded that in the 1989 Loma Prieta earthquake, the duration of the slip pulse was approximately as expected if it is controlled by the fault width. If the duration of the rise time is shorter than this, as Heaton (1990) suggests, there are significant implications for earthquake rupture mechanics. From the practical viewpoint, a short rise time introduces a constraint on the approach to developing scenario source functions for possible future earthquakes, for the purposes of simulating plausible future ground motions.

At the same distance from the fault, directivity has a first order effect on the ground motion, in addition to its effect on the radiation pattern [Eq. (8)]. Directivity is the effect on the seismograms of rupture propagation along the fault. It impacts both high-frequency and low-frequency seismograms. To illustrate

TABLE 1 Earthquake Slip Models

Earthquake	Date	Reference
Parkfield ($M = 5.5$)	June 28, 1966	Aki (1968); Trifunac and Udwadia (1974)
San Fernando ($M_w = 6.5$)	Feb 9, 1971	Heaton (1982)
Coyote Lake ($M_w = 5.7$)	June 8, 1979	Liu and Helmberger (1983)
Tabas ($M_w = 7.1$)	Sep 16, 1978	Hartzell and Mendoza (1991)
Imperial Valley ($M_w = 6.4$)	Oct 15, 1979	Olson and Apsel (1982); Hartzell and Heaton (1983); Archuleta (1984)
Borah Peak ($M_w = 6.9$)	Oct 28, 1983	Mendoza and Hartzell (1988)
Morgan Hill ($M_w = 6.2$)	April 24, 1984	Hartzell and Heaton (1986); Beroza and Spudich (1988)
Nahanni ($M_w = 6.8$)	Oct 5, 1985	Hartzell *et al.* (1994)
Michoacan, Mexico ($M_w = 8.0$)	Sep 19, 1985	Mendoza and Hartzell (1988, 1989); Mendez and Anderson (1991); Wald *et al.* (1991)
North Palm Springs ($M_w = 6.1$)	Aug 7, 1986	Mendoza and Hartzell (1988); Hartzell (1989)
Whittier Narrows ($M_w = 6.0$)	Oct 1, 1987	Hartzell and Iida (1990); Zeng *et al*. (1993a)
Superstition Hills ($M_w = 6.3$)	Nov 24, 1987	Wald *et al*. (1990)
Loma Prieta ($M_w = 7.0$)	Oct 17, 1989	Beroza (1991); Steidl *et al.* (1991); Wald *et al*. (1991); Horton *et al*. (1994); Horton (1996)
Landers ($M_w = 7.3$)	June 28, 1992	Campillo and Archuleta (1993); Wald and Heaton (1994); Cohee and Beroza (1994); Cotton and Campillo (1995); Wald *et al*. (1996); Olsen *et al.* (1997); Hernandez *et al.* (1999)
Northridge ($M_w = 6.7$)	Jan 17, 1994	Hartzell *et al.* (1996); Wald *et al.* (1996); Zeng and Anderson (1996)
Hyogo-ken Nanbu (Kobe) ($M_w = 6.9$)	Jan 17, 1995	Sekiguchi *et al.* (1996); Horikawa *et al*. (1996); Kakehi *et al.* (1996); Wald (1996); Ide *et al.* (1996); Yoshida *et al.* (1996); Kamae and Irikura (1998); Cho and Nakanishi (2000)
Kocaeli, Turkey ($M_w = 7.6$)	Aug 17, 1999	Yagi and Kikuchi (2000)
Chi-Chi, Taiwan ($M_w = 7.6$)	Sep 20, 1999	Ma *et al*. (2001); Zeng and Chen (2001); Oglesby and Day (2001)

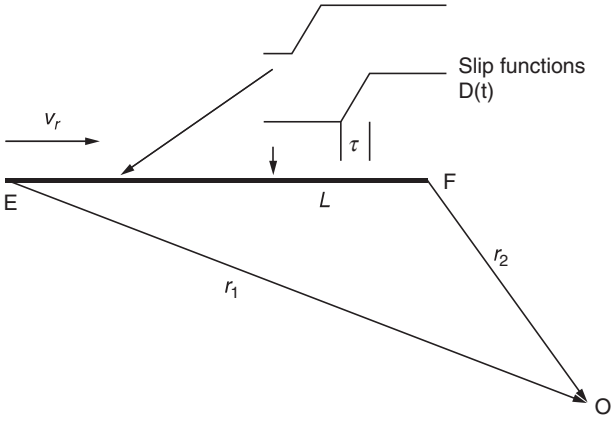

S-wave pulse duration at O:

$$\frac{L}{v_r} + \tau + \frac{r_2 - r_1}{\beta}$$

FIGURE 12 Geometry for consideration of the effect of directivity. This illustrates a vertical, strike-slip fault in map view, recorded at observation point O. The rupture is a Haskell propagating ramp with rupture velocity v_r and rise time τ. The shear velocity is β. The duration of direct arrivals at O is given by the equation in the figure. Rupture is assumed to originate below an epicenter (point E), at one end of the fault, and propagate to the far end (point F).

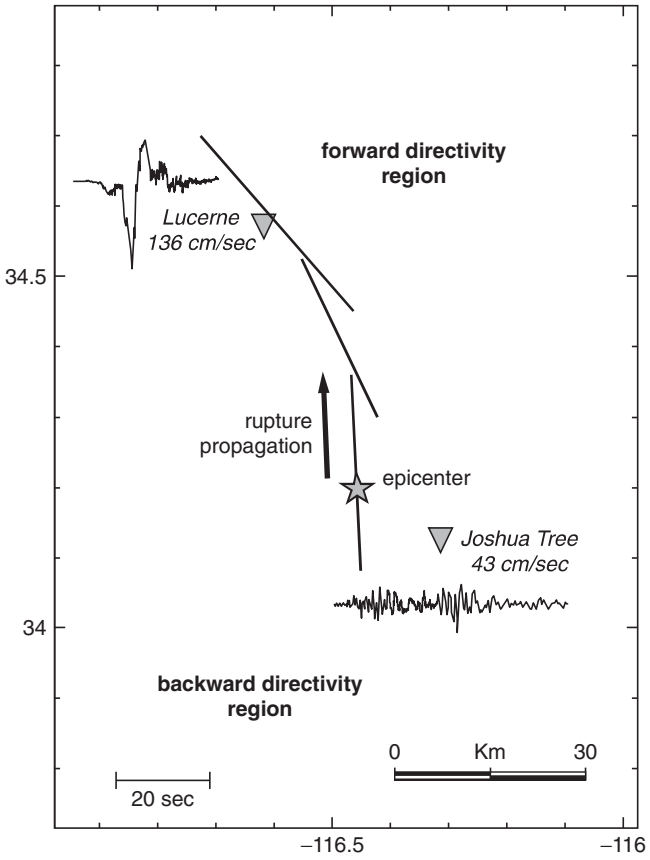

FIGURE 13 Illustration of directivity in velocity pulses recorded in the 1992 Landers, California, earthquake. Rupture propagated north from the epicenter, away from the station at Joshua Tree (with the long, low-amplitude velocity trace) and toward the Lucerne station (with the stronger, compact velocity pulse). From Somerville *et al*., 1997.

the effect, consider first Figure 12. If the observation point O is located near the origin of the rupture (E), and if τ is small and $v_r \approx 0.9\beta$, then r_1 is small and r_2 is comparable to L, so the time interval over which direct arrivals of S waves will be arriving is on the order of $2L/v_r$. On the other hand, for a station located near the far end of the rupture (F), the duration terms in L and in r_1 approximately cancel and the duration of the seismogram is short. At high frequencies, directivity shows up as a short, intense accelerogram at the far end of the fault, in contrast with a lower-amplitude, long-duration accelerogram near the origin of rupture. This is illustrated in Figure 1, where the Caleta de Campos record is near the epicenter while the La Union and Zihuatanejo stations are located in the forward directivity direction.

At low frequencies, directivity associated with propagating rupture causes constructive interference of long period waves and high-velocity pulses. Recently, seismic engineers have become very concerned about these effects. Such pulses have time–function characteristics that are correlated with their polarizations, specifically, the fault-perpendicular component of ground velocity pulses observed in the region toward which the rupture is propagating is typically a two-sided pulse (little net displacement), whereas the fault-parallel component of ground velocity observed near the fault as the rupture passes by is a one-sided pulse having significant net displacement. This was shown by Archuleta and Hartzell (1981), Luco and Anderson (1983), Anderson and Luco (1983a, b), and recently Somerville *et al*. (1997), who have developed empirical ground-motion prediction relations that include this effect. Heaton *et al*. (1995) summarized such pulses observed up to that time, which had peak velocities of up to 170 cm/sec, and they showed that such pulses could be especially dangerous to buildings 10–25 stories tall. Figure 13, from Somerville *et al*. (1997), illustrates these phenomena. A feature of the intense velocity pulse, as seen in Figure 13, is that it tends to be strongest on the component perpendicular to the fault. This result, which may initially be surprising, is predicted by dislocation modeling. It was first recognized and explained in the interpretation of accelerograms from the 1966 Parkfield, California, earthquake (Aki, 1967; Haskell, 1969).

At locations sufficiently near a rupturing fault, the ground undergoes a static offset. Digital accelerograms have succeeded in capturing this static offset in a few cases (e.g., Mexico: Figure 3; Turkey: Rathje *et al*., 2000; Safak and Erdik, 2000; Anderson *et al*., 2000b; Taiwan: Shin *et al*., 2000). The rise time of the static displacement in the Mexico earthquake is ∼10 seconds (Figure 3). The rise time of the static displacements inferred in Turkey is ∼3–6 seconds. These observations all are much shorter than the total duration of the earthquake, and are consistent

with the hypothesis that rise times are generally short (Heaton, 1990). The 1999 Chi-Chi, Taiwan, earthquake has confirmed that the hanging walls of thrust faults move much more, and have greater high-frequency ground motions (peak accelerations) than the foot walls during earthquakes (Shin *et al*., 2000). The low-frequency effect has been seen in laboratory models (Brune, 1996a), and it has been predicted in numerical models (Mikumo and Miyatake, 1993; Shi *et al*., 1998; Oglesby *et al*., 1998). The high-frequency effect has been detected in the development of some ground-motion prediction equations reviewed by Campbell in Chapter 60.

Isochrone theory is useful for understanding the relationship of ground motions in the near-source region (where the Green's function is not well approximated by a plane wave leaving the source). An isochrone is the locus of points on a fault from which the seismic waves all arrive at a selected station at the same time. The basic theory is given in Bernard and Madariaga (1984) and Spudich and Frazer (1984, 1987). In the basic theory, far-field ray theory Green's functions are used in the evaluation of the source radiation, but the assumption of plane waves is not made. The directivity of the source is manifested in a quantity, the isochrone velocity, which contains and is more general than the usual Ben-Menahem directivity function and which can be calculated as a function of position on the fault surface, showing exactly how source kinematics affect the radiation from each point of the fault. With the implicit assumption that the slip velocity at a point on the fault is discontinuous when the rupture starts and stops, Spudich and Fraser show that the high-frequency radiation reaching a station is large when the isochrone velocity for waves reaching that station is large or when the slip velocity of the dislocation on the fault is large. Archuleta and Hartzell (1981) and Spudich and Oppenheimer (1986) present several plots that show how near-source ground motions are affected by variation of radiation patterns and/or isochrone velocity over the fault surface. These effects are seen only in the near-source region. Joyner and Spudich (1994) extended the isochrone theory to include near-field terms of Green's functions, so that static offsets can be predicted using isochrone theory. Isochrone theory software will be included in the Handbook CD in the software package ISOSYN by Spudich and Xu in Chapter 85.14.

4.3 Effects of Wave Propagation

Complexities introduced into the strong ground motions by effects of wave propagation through the crust of the Earth are at least equal in importance to the complexities that are introduced at the source. These crustal complexities can be divided into four parts. The first is propagation of seismic waves through a flat-layered, attenuating Earth. The second is the effect of basins and other major systematic deviations from a flat layered model. The third is the effect of random variations in the velocity of the Earth on all scales. The fourth is the effect of nonlinearity. The success in incorporating these effects depends on how thoroughly the seismic properties of the Earth between the earthquake source and the site are known. Depending on the complexity of the Earth, success may also be limited by computer capabilities to calculate the response of the Earth. Altogether, the literature on this range of subjects is enormous. Relevant topics are covered, in part, in other chapters in this volume. This review is confined to selection of a few topics that, in the author's judgment, have particularly interesting impacts on strong ground motions.

4.3.1 Flat-Layered Attenuating Earth

The approximation of a flat- (or radially) layered Earth is widely used in all aspects of seismology, and is usually quite successful to first order for tasks such as locating earthquakes, describing arrival times of the various types of seismic waves on a global and regional scale, and modeling surface-wave dispersion at low frequencies. There are several methods to calculate the Green's functions [i.e., the response of a flat-layered, attenuating medium to seismic excitation applied at a point, including methods by Bouchon (1981), Luco and Apsel (1983), or Kennett (1983)]. Software to make this computation for a non-attenuating flat-layered structure is included in Chapter 85.14 by Spudich and Xu.

It is a little difficult to estimate the frequency band in which this model is accurate. Flat-layered models have been used to determine focal mechanisms, using moment tensor inversion, from regional records on broadband seismograms. For these inversions, records are preferably low-pass filtered to model only frequencies below 0.05 Hz (e.g., Ichinose *et al.*, 1998; Dreger and Kaverina, 2000; Ichinose, 2000). At these frequencies, with their corresponding long wavelengths, the presence of mountain ranges or basins can be argued to have a minimal effect, so the methods do not need to adjust the Green's functions for the specific source-station path, and may successfully model the complete seismogram. However, the direct *S*-wave part of the Green's function, and for smaller scales the complete Green's functions, may be reliable to much higher frequencies (e.g., 1–2 Hz) in some places.

These synthetic Green's functions have been used in inversions to find models for the slip on the causative fault, which is as consistent as possible with all observed ground motions. Observed seismic ground motions in the direct *S* waves at low frequencies (i.e., less than 1 Hz) have been reproduced with these methods, as demonstrated by several of the studies, cited in Table 1, that model the strong motion to infer a source time function. The success at low frequencies in determining the source time function may be a little misleading. Basins have a strong effect on the nature of seismic waves over a broad frequency range, starting at frequencies below 1 Hz. Inaccuracy in modeling the path can be mapped back into spurious source effects when flat-layered structure is assumed for the calculation of the

Green's function (e.g., Cormier and Su, 1994; Graves *et al.*, 1999; Graves and Wald, 2001; Wald and Graves, 2001).

4.3.2 Basin Response

Many major urban areas, particularly in regions with high seismic activity, are built in geological basins. The reasons are obvious. The tectonic activity that causes earthquakes also tends to build mountains. Flat-lying areas that develop where eroded sediments are deposited (i.e., basins) are far easier to build upon than are mountains. It is therefore of the utmost importance to understand the effects of basins on strong ground motions. The modeling of wave propagation in basins, using finite-difference or finite-element techniques, is an active field of research. The effects of basins are reviewed in Chapter 61 by Kawase, so selection of an interesting, state-of-the-art example is sufficient for this review.

The Kanto, Japan, basin (which includes Tokyo and adjacent cities) has been studied extensively (e.g., Phillips *et al*., 1993; Sato *et al*., 1998a, b, 1999; Koketsu and Kikuchi, 2000). Figures 14 and 15, from Sato *et al*. (1999), illustrate results of a finite-difference simulation of waveforms from a magnitude 5.1 earthquake. These figures illustrate several important consequences of basin response. The seismograms on rock near the basin edge (station ASK) are very simple, representing the moment rate function with probably relatively little distortion. Stations in the basin (KWS, HNG, FUT, CHB) have larger amplitudes in this frequency band, and much longer duration of strong shaking. Stations in the basin have strong arrivals much later than the *S* wave, caused by surface waves generated at the edge of the basin. In this frequency band, the surface waves dominate the seismograms in the basin. Studies in Los Angeles show all of these phenomena (e.g., Liu and Heaton, 1984; Vidale and Helmberger, 1988; Olsen *et al*., 1995; Olsen and Archuleta, 1996; Wald and Graves, 1998; and Olsen, 2000). All of these effects are probably quite general properties of basins.

The effects of basin response are not restricted to low frequencies. For example, in the Kobe earthquake, the zone with the highest damage is not directly above the causative fault, but rather it is a linear band that is offset to the southeast. An explanation for this, supported by modeling studies, is that the damage zone occurs at the location of constructive interference of waves taking two distinctly different paths: one directly from the fault through the low-velocity basin structure, and the other through higher-velocity rock on the opposite side of the fault, which is then refracted into the basin from near the top of the fault (e.g., Kawase, 1996; Kawase *et al*., 1998; Matsushima and Kawase, 1998; Pitarka *et al*., 1997, 1998). A second good example comes from the Northridge earthquake, where there was an isolated zone of high damage in Santa Monica. Davis *et al*. (2000) find, from studies of large numbers of aftershocks, that this is the result of focusing of seismic energy by a 3-dimensional lens-like high-velocity structure within the basin.

4.3.3 Scattering and Attenuation

Scattering and attenuation have an important effect on the strong-motion spectrum, particularly at high frequencies. Sato *et al.* in Chapter 13 discuss this issue in more detail. The ω–*square* spectral model predicts that the Fourier acceleration spectra should be flat at high frequencies, but in Figures 4 and 9 they fall off quite rapidly above about 5 Hz. Hanks (1982) referred to the frequency above which the acceleration spectrum falls off as $f_{\max}$ (Figure 11). He pointed out that this could be either a source or a site effect.

In favor of the site-effect model, Anderson and Hough (1984) proposed that a good asymptotic approximation to the spectral shape at these high frequencies is exponential decay [$\sim\exp(-\pi\kappa f)$] where κ is the decay parameter. In their data, κ is a function of distance and the site conditions of the station. Figure 16 shows measured values of κ at two stations, one on slightly weathered granite (Pinyon Flat in the southern California batholith) and the other on deep alluvium (Imperial Valley in the Colorado River delta of southern California, 130 km southeast of Pinyon Flat). Both stations show a systematic increase in κ with distance, but the station on alluvium shows values offset to higher κ (more rapid decay) than the station on granite. Anderson (1986) explains this behavior as an effect of attenuation. In this model, the intercept of κ (i.e., at zero distance) is controlled by attenuation near the surface, while the increase of κ with distance is an effect of lateral propagation. It should be noted that κ is at most weakly dependent on distance in Mexico (Humphrey and Anderson, 1992). Based on this model, κ has been used in some models to simulate strong motions for engineering applications (e.g., Schneider *et al*., 1993; Beresnev and Atkinson, 1998a, b). There is, however, a considerable amount of scatter in the individual measurements of κ in this figure, some of which comes from variability in the high-frequency spectrum as radiated at the source (e.g., Tsai and Chen, 2000) or highly variable attenuation in the source region (Castro *et al*., 2000).

4.3.4 Site Effects Including Nonlinearity

The term *site effects* is generally used to refer to wave propagation in the immediate vicinity of the site, as opposed to the propagation effects, which refer to the complete path from the source to receiver. The boundary between a site effect and a propagation effect is not always clear, but it is useful to discuss them separately. Site effects can include modification of seismic waves by the local sedimentary cover, particularly where this local cover is not representative of the total path from the epicenter, the effect of alluvial valleys or basins, effect of local topography, and effects of the water table. Soil–structure interaction also might be considered a site effect, but it is not considered here because it represents modification of the ground motion by artificial structures rather than by the Earth in the absence of such

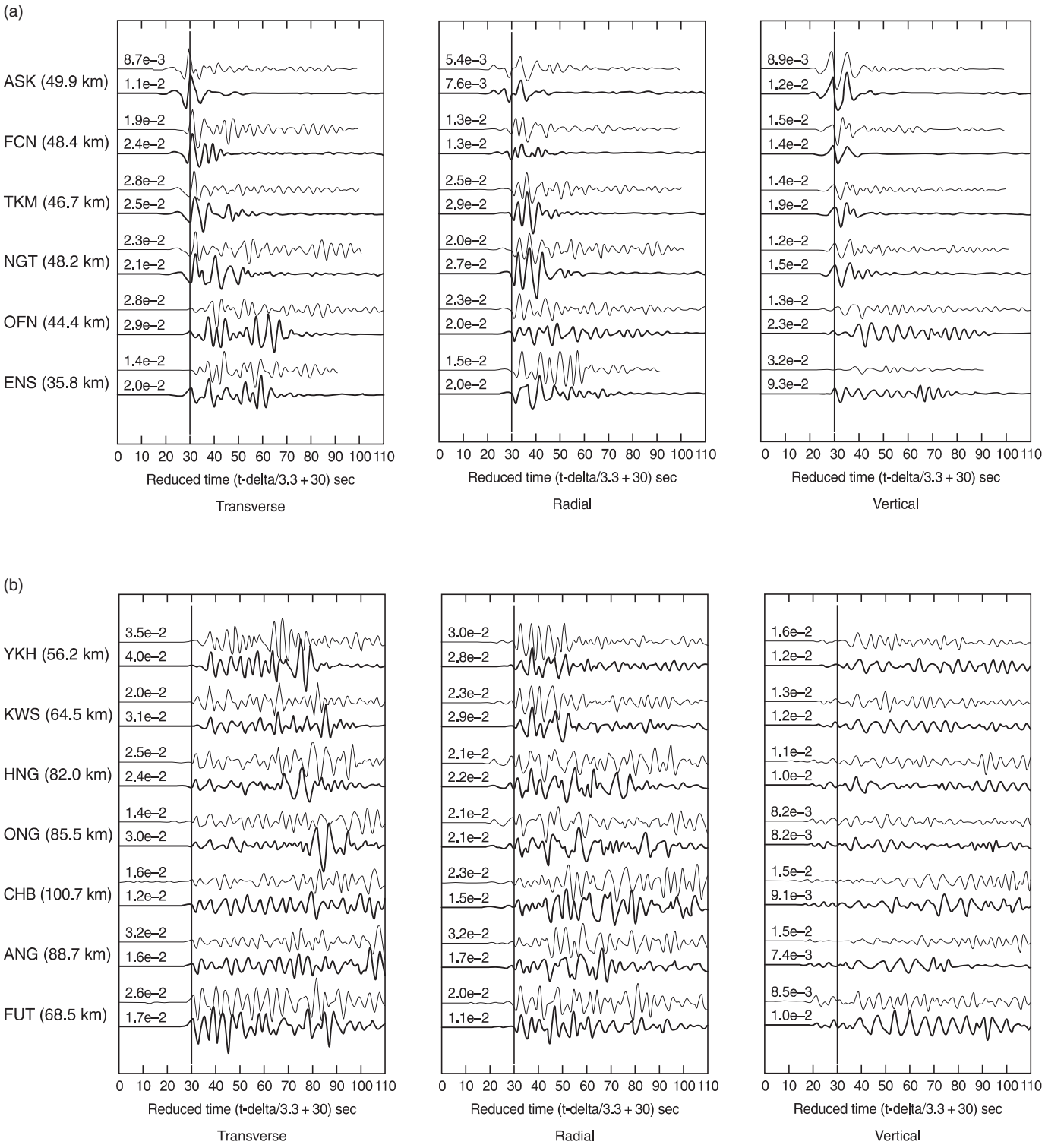

FIGURE 14 Observed (thin lines) and computed (bold lines) ground motions in the Kanto basin for various stations. Locations of the stations are shown in Figure 15 (some stations are not identified on this figure). All seismograms are aligned by the arrival time of the direct *S*-wave. From Sato *et al*., 1999.

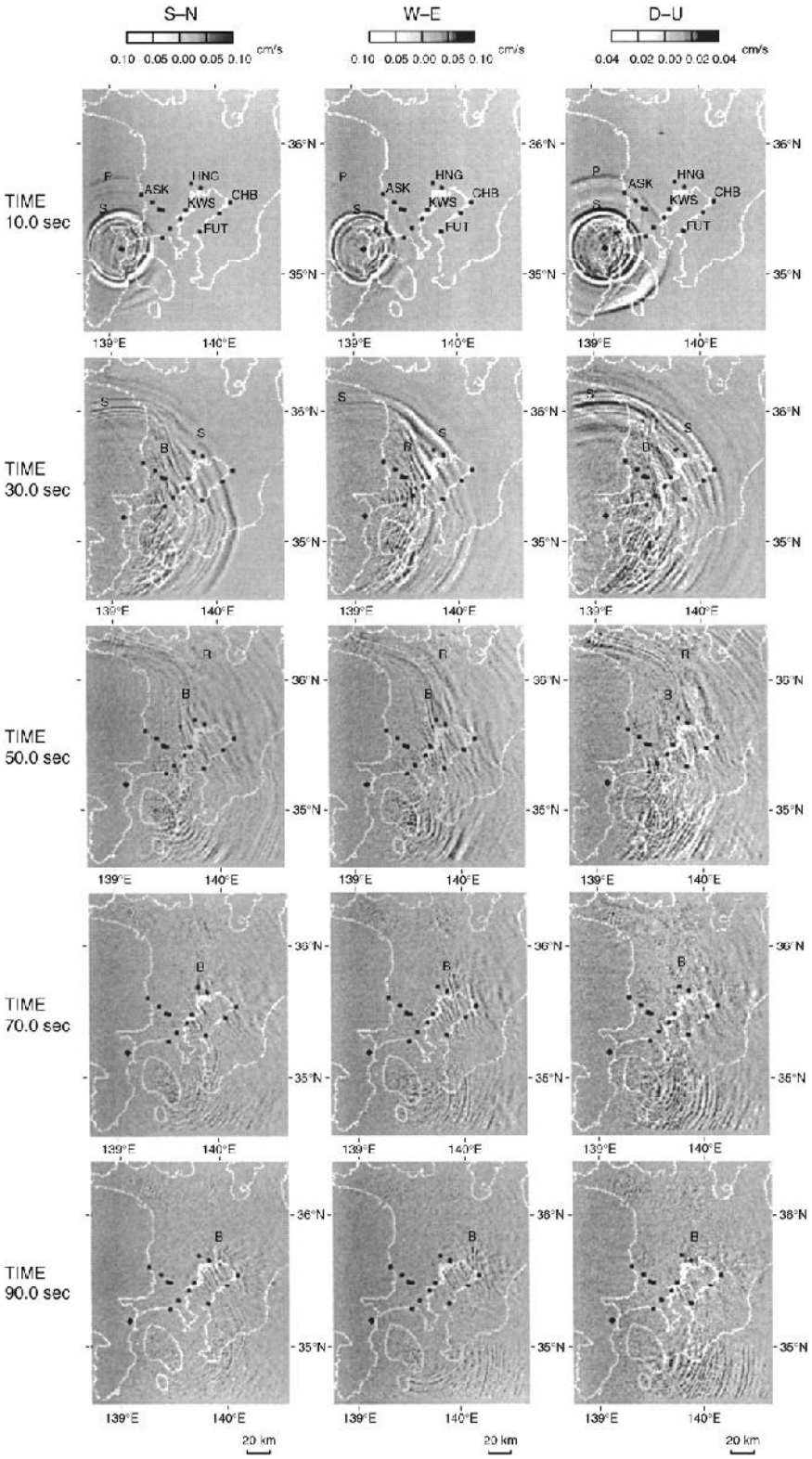

FIGURE 15 Map showing the computed surface deformation generated by a finite-difference simulation of the 1990 Odawara earthquake at five different times. From Sato *et al*. (1999). Data and calculations are bandpass filtered (0.1–0.3 Hz). On the map, P and S denote the direct *P*- and *S*-waves, and B denotes surface waves generated at the boundary of the basin.

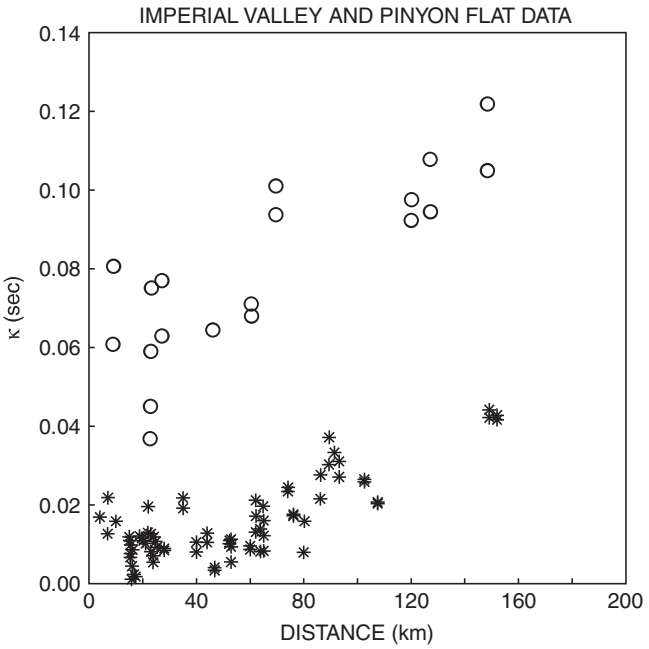

FIGURE 16 The high-frequency parameter κ as a function of distance for two stations in southern California (from Anderson, 1986). Open circles are measurements from strong-motion accelerograms recorded on deep sediments in Imperial Valley, and asterisks are from seismograms recorded on a rock station in the San Jacinto mountains west of Imperial Valley.

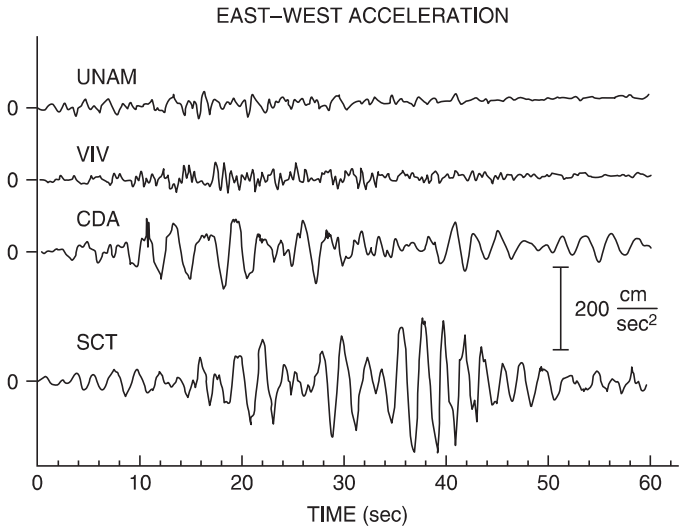

FIGURE 17 Most significant one-minute segment of strong-motion accelerograms recorded at four stations in Mexico City, in the September 19, 1985, earthquake ($M = 8.0$). Stations are 350 km from the epicenter, so differences can only be attributed to differences in geological conditions at the site. No time correlation exists among these traces (from Anderson *et al*., 1986).

structures. Site effects are discussed in more detail in Chapter 61 by Kawase.

Figure 17 shows accelerograms recorded from four locations in Mexico City in the September 19, 1985, earthquake to illustrate a classic example of site effects. The stations UNAM and VIV are least affected, while CDA and SCT have been strongly amplified at a period of two to three seconds to cause the large accelerations as shown, and cause the terrible toll of death and destruction from that event (Anderson *et al*., 1986). The main factor that causes such amplification is soft soils that form low-velocity layers near the Earth's surface. These low-velocity layers trap energy, amplify all frequencies due to the decrease in seismic impedance, and preferentially amplify resonant frequencies.

Effects of local topography, including valleys, hills, and ridges, may be grouped together and have been reviewed by Geli *et al*. (1988). The main results are that the topographic amplification is maximum at the top of the hill, and is maximum at the frequency at which one wavelength of the *S* wave equals the width of the hill base. Motions on the hill sides are not amplified much, and motions around the base of the hill are usually deamplified with respect to motions far from the hill. Geli *et al*. (1988) found that theoretical models of the topographic effects almost always underpredict the observed topographic effects. That discrepancy has not yet been resolved. For example, the Bouchon and Barker (1996) simulation of response at the Tarzana site, which recorded unexpectedly high accelerations in the 1994 Northridge, California, earthquake, underpredicts the observed amplification of Spudich *et al*. (1996).

It has been commonly assumed that the effects of wave propagation on strong and on weak ground motion are the same. However, nonlinear effects (i.e., a nonlinear stress–strain relationship) resulting in slower velocities and more rapid attenuation of large amplitude waves are predicted for soft materials. Field observational evidence has suggested this is a common phenomenon for many accelerograms (e.g., Chin and Aki, 1991; Field *et al*., 1998; Su *et al*., 1998; Irikura *et al*., 1998). Su *et al*. (1998) concluded that in the Northridge earthquake, nonlinearity is recognizable in differences between site response (defined by spectral ratios) when peak accelerations exceed about 0.3g, peak velocity exceeds 20 cm/sec, or peak strain exceeds 0.06% (Figure 18). The main effects of nonlinearity are to decrease the effective shear velocity of the sediments and to increase the damping, thus shifting resonant peaks to lower frequencies and lower amplitudes, and generally reducing amplitudes overall. Understanding of nonlinearity is an important current issue for strong-motion seismology. Chapter 61 by Kawase reviews the topic in more detail.

4.4 Theoretical Models for Estimation of Strong Shaking

All methods of generating synthetic seismograms need to be calibrated. Complete calibration includes demonstration that the method produces realistic-appearing seismograms, for which measures of ground motion match the observations. They should be able to match the spectra of "calibration events"

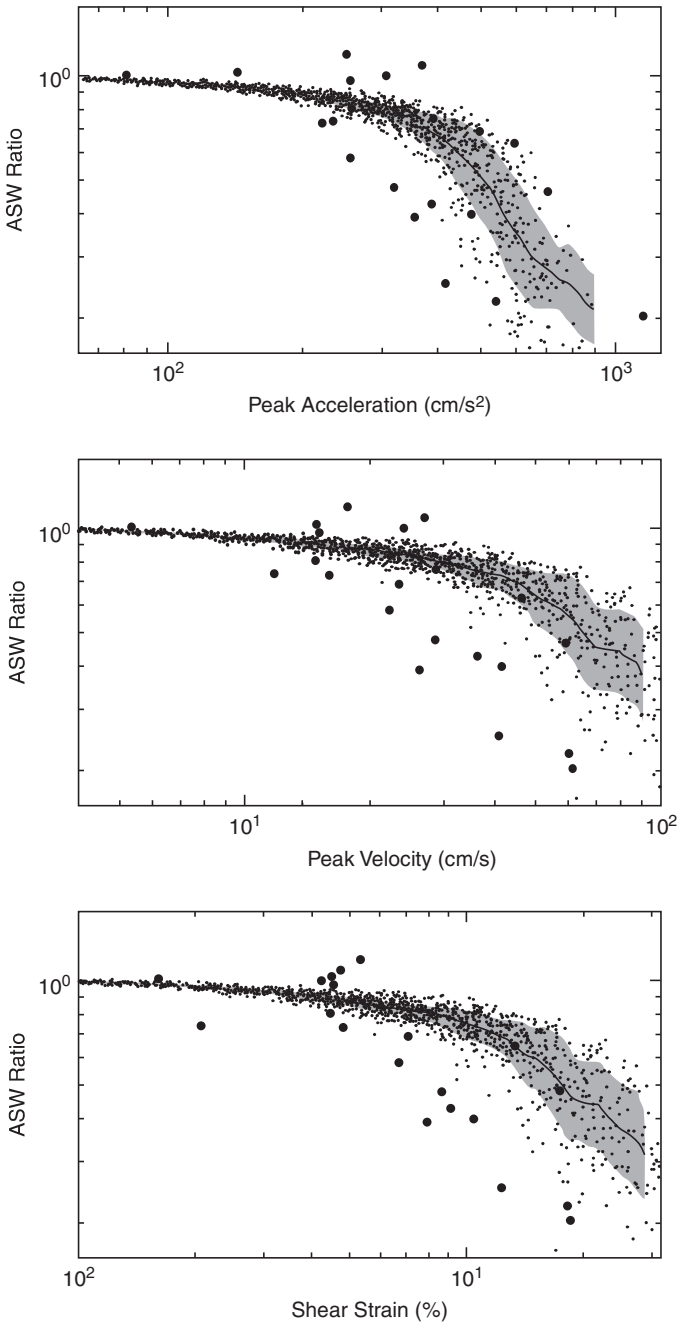

FIGURE 18 Effect of nonlinearity on the site-response contribution to the Fourier spectral amplification of strong motion. Large dots give the observed ASW ratio, from Su *et al.* (1999), defined as the average over frequency of the Fourier spectral amplification in the main shock (strong motion) to the average of the Fourier spectral amplification determined from several small aftershocks. The points are plotted as a function of the peak acceleration of the strong-motion record during the main shock (top), the peak velocity of the strong-motion record during the main shock (middle), and the peak strain related to the strong-motion record during the main shock (bottom). Peak strain is the ratio of peak velocity to average shear velocity estimated for the upper 30 meters below the station. Small points show the effect of numerical experiments based on the nonlinear model for average site conditions using the approach of Ni *et al*. (2000).

(e.g., Atkinson and Somerville, 1994; Anderson and Yu, 1996; Beresnev and Atkinson, 1998a, b) as well as the ground-motion prediction models (see Chapter 60 by Campbell) where these models are well constrained by data.

4.4.1 Stochastic Models

The broad flat portion of the Fourier spectrum motivates a model of strong motion as band-limited white noise, where the spectrum for white noise is proportional to f^0. Housner (1947) first modeled strong ground motion as a random process, and earthquake engineers employed band-limited white noise and both stationary and non-stationary Gaussian processes as models of strong-motion acceleration as early as the 1960's (see for example, Jennings *et al.*, 1969). More recent seismological models that use this approach include Hanks and McGuire (1981), Boore (1983), Boore and Atkinson (1987), Ou and Herrmann (1990), Chin and Aki (1991), Atkinson and Boore (1997), Toro *et al*. (1997), and Sokolov (1998). The process of constructing a seismogram with this approach begins with generating a white-noise time series, applying a shaping taper in the time domain to match the envelope of the expected strong motion, and then applying a bandpass filter in the frequency domain to mold the Fourier spectrum to the expected spectral shape. The frequency domain shaping can be controlled by assumptions about source spectral shape, Q, κ, and site response at high frequencies. In eastern North America, where there is little experience with large earthquakes, there is considerable uncertainty about the source spectral shape (e.g., Atkinson, 1993; Haddon, 1996b). For near-field calculations, Silva *et al*. (1990), Schneider *et al*. (1993), Beresnev and Atkinson (1998a, b) treat the total fault as a set of subfaults, which are summed to obtain seismograms with the statistical characteristics of strong motions. Software developed by D. M. Boore is given on the Handbook CD (under the directory \85\8513) and described in Chapter 85.13.

4.4.2 Synthetic Green's Function Models

A second general approach to generating synthetic strong ground motions follows the representation theorem [Eq. (1)] more closely than the stochastic methods, thus attempting to use a more complete description of the physics at every step on the process. These methods generate synthetic Green's functions based on Earth structure models of varying complexity, and combine these through Eq. (1) with a range of models of the earthquake source. Two examples of this approach are those that use a "composite source model" (Zeng *et al*., 1994; Yu *et al*., 1995; Anderson and Yu, 1996; Zeng and Anderson, 1996) and those that use an empirical source time function (e.g., Hadley and Helmberger, 1980; Somerville *et al*., 1991; Cohee *et al*., 1991; Atkinson and Somerville, 1994; Sato *et al*., 1998b). Both methods need to develop representations for both the source and the wave propagation. In the simulations by Somerville and his associates, the source is represented by an empirical source time

function. At high frequencies, ray theory in a layered medium is used to find the Green's function, and at low frequency, the Green's function has preferably been determined using a finite-element solution for ground motion in a realistic model for the regional geology, usually including a basin (e.g., Sato *et al*., 1998b). Models reported so far using the composite source model use a Green's function developed for a flat-lying layered, attenuating half space. Scattering is added to the Green's functions for more realism at high frequencies (Zeng *et al*., 1995).

The source component of the composite source model, motivated by a model by Frankel (1991), is interesting. This model describes the source as the superposition of overlapping circular cracks (subevents) with a power-law distribution of radii, $N(r) \sim r^{-p}$, where p is the fractal dimension. These subevents are distributed at random on the fault and each is triggered to radiate when a rupture front passes. Each subevent radiates a pulse of the type predicted by some model for radiation from a circular crack (e.g., Brune, 1970; Sato and Hirasawa, 1973). The source displacement spectrum of the subevents is proportional to f^{-2} at high frequencies, implying that the source acceleration spectrum is proportional to f^{0}. The source is kinematic, but this source description has the capability to generate realistic accelerograms with the proper frequency content (e.g., Zeng *et al*., 1994; Yu *et al*., 1995), and has a capability to predict ground motions (e.g., Anderson and Yu, 1996). Also, it is possible to find specific composite sources that are consistent with both the statistics and the phase of observed records (e.g., Zeng and Anderson, 1996). An example of seismograms generated by this approach is shown in Figure 19. Anderson (1997b) found a relationship between parameters of the composite source model and several physical earthquake source parameters (radiated energy, stress drop).

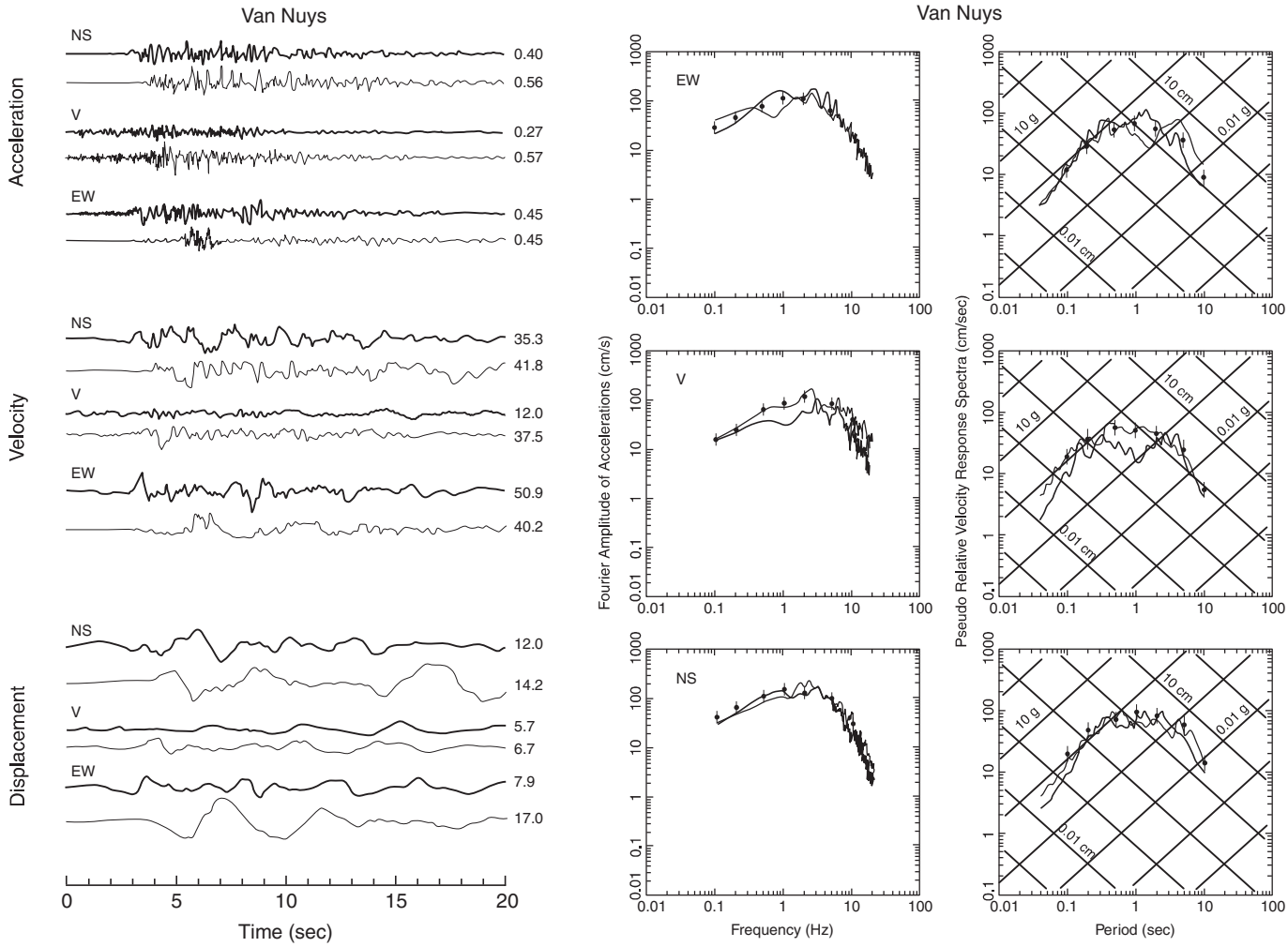

FIGURE 19 Data and synthetic broadband seismograms from the near-field of the Northridge, CA, earthquake of January 17, 1994 (from Anderson and Yu, 1996). Numbers at the end of each trace are peak acceleration (in fraction of g, the acceleration of gravity), peak velocity (in cm/s), and peak displacement (in cm). Upper trace in each pair (bold line) is data, and lower line is the synthetic. On the right, bold lines are data, and light lines are realization of one synthetic, and points with error bars are mean values of 50 realizations.

4.4.3 Empirical Green's Function Models

A third approach for simulating strong ground motions uses small earthquakes as empirical Green's functions. This method has been applied by Hartzell (1978), Wu (1978), Kanamori (1979), Irikura (1983, 1986), Joyner and Boore (1986), Takemura and Ikeura (1987), Dan *et al*., (1990), Hutchings (1991, 1994), Hutchings and Wu (1990), Wennerberg (1990), Haddon (1996a), Jarpe and Kasameyer (1996), and others. Empirical Green's functions incorporate the effects of wave propagation by the use of small earthquake seismograms recorded in the same area. With proper care in scaling the seismograms and adding them with appropriate delays to represent propagation of rupture across the fault, it is possible to generate realistic synthetic seismograms. The advantage of this approach is that the seismograms used as empirical Green's functions incorporate all the complexities of wave propagation. The limitation is that the empirical Green's functions may not have an adequate signal-to-noise ratio at all the frequencies of interest, may not be available for the desired source–station pairs, and may originate from sources with a focal mechanism different from the desired mechanism. Care must be exercised in the superposition of multiple empirical Green's functions, in order to obtain an ω–*square* spectrum in the synthetic motions (e.g., Irikura, 1986; Takemura and Ikeura, 1987; Dan *et al*., 1990; Wennerberg, 1990). Kamae *et al*. (1998) proposed a hybrid technique in which they synthesize the seismogram from a small event using 3-D finite difference at low frequencies and the stochastic method at high frequencies.

4.5 Seismic Hazard Analysis

Seismic hazard analysis transmits information on strong motions to allow for informed decisions on earthquake-resistant designs, governmental response to the hazards, and other societal impacts of earthquakes. (This topic is also reviewed by Somerville and Moriwaki in Chapter 65.) In its simplest form, a seismic hazard analysis might identify a scenario earthquake that might affect a region (see Anderson, 1997a, for a review), and estimate the ground motions expected from that earthquake, using techniques described previously. This approach does not necessarily convey information about the frequency with which this ground motion occurs. The alternative form, called a probabilistic seismic hazard analysis (PSHA), calculates a hazard curve (Fig. 20) giving the average annual probability that a ground-motion parameter, say Y, is equaled or exceeded. Thus, hazard curves predict the result of an experiment where an instrument at the site records ground motions for, say, 10^5 or 10^6 years, and the frequency of excedence of Y is tabulated. Milne and Davenport (1969) presented a method to estimate the hazard curve at relatively high occurrence rates directly from a seismic catalog and extrapolated to low probabilities using extreme value statistics, but most estimates synthesize earthquake sources and attenuation relations using an approach that can be traced to Cornell (1968).

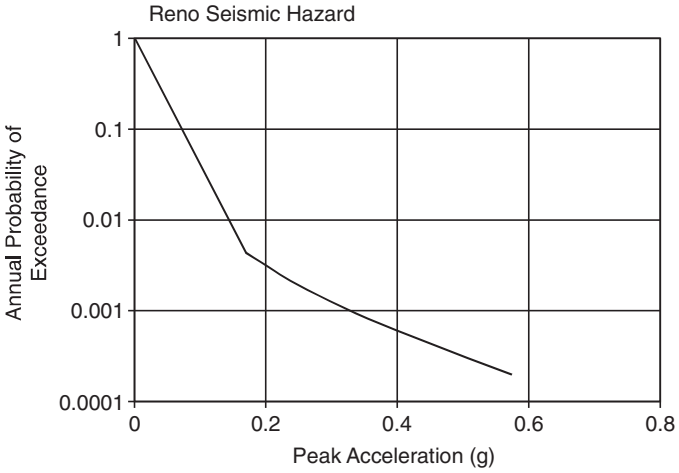

FIGURE 20 A seismic hazard curve for Reno, Nevada, based on the seismic hazard model of Frankel *et al*. (1996).

PSHA calculates the rate $r_C(Y)$ that ground motion Y is equaled or exceeded through the synthesis of the seismicity (see Chapter 41 by Engdahl and Villasenor) and ground motion prediction equations. Assuming that the earthquakes are random, uncorrelated events, then the Poisson model should hold, and we expect that the probability of exceedance in a time interval of duration T is

$$P_C(Y, T) = 1 - \exp[-r_C(Y)T]. \tag{13}$$

The curve $P_C(Y, T)$ is the *hazard curve*. The input seismicity describes the spatial distribution of earthquakes and their rates of occurrence. This is a function of both magnitude and location, $n(M, \mathbf{x})$, where M is the earthquake magnitude, $\mathbf{x}$ is the location vector of the source, and $n(M, \mathbf{x})\, dM\, d\mathbf{x}$ gives the number of earthquakes per year in a magnitude range of width dM and an area (or volume) of size $d\mathbf{x}$. Recognizing that earthquakes radiate energy from a finite fault, $n(M, \mathbf{x})$ must be consistent with fault geometry and the way the distance R from the earthquake to the site is defined.

A ground-motion prediction equation $\hat{Y}(M, R)$ estimates the mean ground motion as a function of the magnitude and distance (and sometimes additional parameters). As reviewed by Campbell in Chapter 60, $\hat{Y}(M, R)$ and its standard deviation σ_T are developed by regression using existing strong-motion data. The equation $\hat{Y}(M, R)$ can be inverted to find the cumulative probability Φ that a single realization of an earthquake with magnitude M at distance R will cause ground motion y in excess of Y, as follows:

$$\Phi(y \geq Y | \hat{Y}, \sigma_T) = \int_Y^\infty \frac{1}{\sigma_T \sqrt{2\pi}} \exp\left(-\frac{(y - \hat{Y}(M, R))^2}{2\sigma_T^2}\right) dy. \tag{14}$$

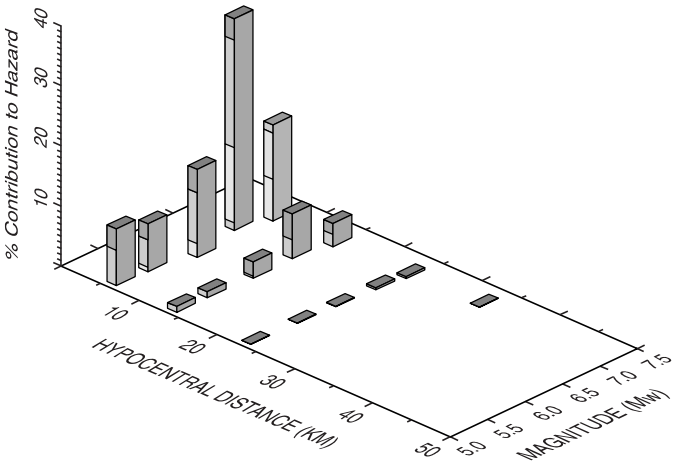

FIGURE 21 Deaggregation of the seismic hazard for Reno, Nevada (39.5°N, 119.8°W), based on the seismic hazard model developed by Frankel *et al*. (1996). This deaggregation is for a peak acceleration of 0.58 g, which is estimated to have a mean occurrence rate of 4.04×10^{-3} yr^{-1}, corresponding to a mean return time of 2475 years, or a probability of exceedance of 2% in 50 years. Differing shades of gray in each bar tell how much above (mostly in this case) or below average the ground motion must be to reach this peak acceleration from various earthquakes contributing to the hazard (modified from the USGS Web site, 2001).

The basic probabilistic seismic hazard analysis model (e.g., McGuire, 1995; SSHAC, 1997) finds

$$r_C(Y) = \iint n(M, R(\mathbf{x}))\, \Phi(y \geq Y | \hat{Y}(M, R(\mathbf{x})), \sigma_T)\, dM\, d\mathbf{x} \tag{15}$$

A more complete analysis distinguishes between aleatory and epistemic uncertainty. Aleatory uncertainty is introduced by true randomness in nature, while epistemic uncertainty is due to lack of knowledge (SSHAC, 1997). An extension of PSHA is the deaggregation or disaggregation of the seismic hazard (e.g., McGuire, 1995; Harmsen *et al*., 1999; Bazzurro and Cornell, 1999). From the integrand in Equation (15), deaggregation identifies the magnitudes and distances that contribute the most to that hazard (e.g., Fig. 21). From this, specific important earthquakes can be identified, thus providing additional information to the engineers.

In principal, every specific site has its own seismic hazard curve. Spatial variation can be presented on a probabilistic map, which might contour, for instance, estimates of peak ground accelerations that occur with a probability of 10% in 50 years (e.g., Algermissen *et al*., 1982; Frankel, 1995; Frankel *et al*., 1996; Frankel *et al*., 2000; Chapter 74 by Giardini *et al*.). Probabilistic maps thus communicate estimates of the relative hazards of different locations accounting for both severity of the potential ground motions and their frequency of occurrence (e.g., Cornell, 1995).

The difficulty in building the integrand for Eq. (15) should not be underestimated (e.g., Frankel, 1995; SSHAC, 1997; Ebel and Kafka, 1999). PSHA-generated hazard curves are thus a scientific prediction to be tested. However, it is very difficult to test because the hazard curve describes rates of events that are very rare compared to the history of rigorous strong-motion observations. At high probabilities ($\sim 10^0$–10^{-2}), the models can be tested by comparison with estimated ground motions from the historical seismicity (e.g., Ward, 1995). At somewhat lower probabilities ($\sim 10^{-2}$–10^{-3}), historical records for some old civilizations (Japan, Middle East) might be able to provide a test (Ordaz and Reyes, 1999). At even smaller probabilities, the only available recourse is to use geological indicators, in particular precarious rocks (e.g., Brune, 1996b; Brune, 1999; Anderson and Brune, 1999b). These studies find precarious rocks whose existence seems to contradict the results of PSHA. Anderson and Brune (1999a) propose that this discrepancy may be in part caused by treating spatial variability of ground motions, where site effects contribute to a large uncertainty, as a variability in time in Eq. (15). Another possibility, emphasized by the Turkey and Taiwan earthquakes (Sec. 3.2 above) is that the mean ground-motion curves are overestimating the ground motions (Brune, 1999; Anderson *et al*., 2000a). The issue remains to be resolved by future data collection and research.

5. Future Directions for Strong-Motion Seismology

This article has attempted to give an overview of the field of strong-motion seismology. Coverage of several topics has necessarily been too brief, but it is believed that the information presented here is sufficient to provide a reasonable introduction and indication of the present state of research in this exciting field of seismology. This final section identifies some future challenges.

The first is in the field of data collection. The limited number of accelerograms collected to date for major earthquakes within the zones of major damage (<20 km on rock and 100 km on soft soil) remains a severe limitation of our science. For instance, the consensus of the Monterey Strong-Motion Workshop (Stepp, 1997) is that there is a need to install on the order of 20,000 instruments in densely urbanized areas of the United States in order to ensure that the next major damaging earthquake in the US is well documented. Worldwide, a stable mechanism for funding the collection and distribution of strong-motion data has not been developed in spite of the enormous value of the data to the engineering community.

Research in strong-motion seismology is proceeding toward a capability to take any hypothetical earthquake and to generate seismograms and corresponding spectra that incorporate an understanding of all the physical phenomena as they apply in the region of interest. There is reason for confidence that this physical approach is the best way to minimize the uncertainties in anticipating ground motion for future earthquakes. Models of this type can be expected to play a role in filling in gaps in data at critical magnitudes and distances, such as predicting the characteristics of the near-field directivity pulses. It can be argued that

the modeling approach is the most reliable way of extrapolating from the present data set. However, models have sufficient flexibility in source parameters that must be extrapolated to large magnitudes that this modeling will not totally replace the important role that gathering more data must continue to play.

At low frequencies, modeling will require continued emphasis on the use of finite element/finite difference methods to predict ground motions in sedimentary basins beneath urban areas. Advances in computer codes, increasing computer speeds, and continual improvement in velocity models, will be needed to push the applicability of these methods to higher frequencies. Methods will be needed to utilize whole waveforms from multiple events to improve the urban velocity models, as exploration in these areas is most difficult.

There is little physical understanding of the role that various physical characteristics and processes play in controlling the high-frequency end of the spectrum. Factors that could contribute include the tectonic environment, fault characteristics such as total slip, time intervals between earthquakes, and lithology, issues related to the dynamics of rupture and the physics that control those dynamics, and nonlinear wave propagation along the path, especially near the source and in the near-surface geology. Collection of more data is essential, as the number of variables that are potentially involved outnumber the number of large earthquakes that have been recorded at short distances.

Because strong-motion seismology has an important application in the development of ground motions for use in engineering design, it is obvious that empirical characterization of strong-motion data will also need to continue. For the largest earthquakes, both the mean values and the uncertainty around the mean, together with the factors controlling those parameters, need to be understood much better in order to reduce uncertainties in seismic hazard analyses. Together with this, emphasis on prediction of strong motions through physical modeling is appropriate. By that approach, scientific understanding and improved prediction will go hand in hand, and the greatest progress will be made for description of seismic hazards.

Acknowledgments

The author thanks Willie Lee for the encouragement to write this article. The paper benefited enormously from several very thoughtful and extensive reviews. Five reviewers in particular, Roger Borcherdt, Kenneth Campbell, Hiroshi Kawase, Dan O'Connell, and Paul Spudich, contributed major ideas and even text and references to improve various sections of the article, and the quality of the result is enhanced enormously by their efforts. Carl Stepp made several critical recommendations. Aasha Pancha, Paul Caruso, and Jose A. Zepeda helped the process of reviewing and clarifying the manuscript. Figures 4, 5, and 6 were prepared by Matt Purvance. Figure 18 is an unpublished figure by Feng Su, compiling work from the paper by Su *et al*. (1998). The preparation of this paper was supported in part by the Southern California Earthquake Center. SCEC is funded by NSF Cooperative Agreement EAR-8920136 and USGS Cooperative Agreements 14-08-0001-A0899 and 1434-HQ-97AG01718. The SCEC contribution number for this paper is 640. The preparation of this paper was also supported in part by the National Science Foundation under Grant No. 0000050.

References

Abrahamson, N. A., and W. J. Silva (1997). Empirical response spectral attenuation relations for shallow crustal earthquakes. *Seismol. Res. Lett.* **68**, 94–127.

Aki, K. (1967). Scaling law of seismic spectrum. *J. Geophys. Res.* **72**, 1217–1231.

Aki, K. (1968). Seismic displacements near a fault. *J. Geophys. Res.* **73**, 5359–5376.

Aki, K. (1980). Possibilities of Seismology in the 1980's (Presidential Address). *Bull. Seismol. Soc. Am.* **70**, 1969–1976.

Aki, K., and P. G. Richards (1980). *Quantitative Seismology, Theory and Methods.* W. H. Freeman and Co., San Francisco.

Alcantara, L. E., Andrade, J. M. Espinosa, J. A. Flores, F. Gonzalez, C. Javier, B. Lopez, M. A. Macias, S. Medina, L. Munguia, J. A. Otero, C. Perez, R. Quaas, J. A. Roldan, H. Sandoval, R. and Vazquez (1997). Base Mexicana de datos de sismos fuertes, Disco Compacto Volumen 1, 1997, Sociedad Mexicana de Ingenieria Sismica, A.C.

Algermissen, S. T., D. M. Perkins, P. C. Thenhaus, and B. L. Bender (1982). Probabilistic estimates of maximum acceleration and velocity in rock in the contiguous United States, *US Geol. Surv. Open-File Report 82-1033*, 107 pp.

Ambraseys, N. N. (1997). Strong motion development and research in Europe. In: "Vision 2005: An Action Plan for Strong Motion Programs to Mitigate Earthquake Losses in Urbanized Areas" (J. C. Stepp, Ed.), US Committee for Advancement of Strong Motion Programs, Austin, Texas, 66–74.

Ambraseys, N., P. Smit, R. Berardi, D. Rinaldis, F. Cotton, and C. Berge-Thierry (2000). Dissemination of European Strong-Motion Data. CD-ROM collection. European Commission, Directorate General XII, Science, Research and Development, Environment and Climate Programme, Bruxelles.

Ambraseys, N., P. Smit, R. Sigbjornsson, P. Suhadolc, and B. Margaris (2001). Internet-Site for European Strong-Motion Data. *http://www.isesd.cv.ic.ac.uk*, European Commission, Research-Directorate General, Environment and Climate Programme.

Anderson, J. G. (1986). Implication of attenuation for studies of the earthquake source. In: "Earthquake Source Mechanics" (S. Das, J. Boatwright, and C. Scholz, Eds.), *Am. Geophys. Un. Geophysical Monograph* **37**, 311–318.

Anderson, J. G. (1997a). Benefits of scenario ground motion maps. *Engineering Geol.* **48**, 43–57.

Anderson, J. G. (1997b). Seismic energy and stress drop parameters for a composite source model. *Bull. Seismol. Soc. Am.* **87**, 85–96.

Anderson, J. G., and J. N. Brune (1999a). Probabilistic seismic hazard analysis without the ergodic assumption. *Seismol. Res. Lett.* **70**, 19–28.

Anderson, J. G., and J. N. Brune (1999b). Methodology for using precarious rocks in Nevada to test seismic hazard models. *Bull. Seismol. Soc. Am.* **89**, 456–467.

Anderson, J. G., and S. Hough (1984). A model for the shape of the Fourier amplitude spectrum of acceleration at high frequencies. *Bull. Seismol. Soc. Am.* **74**, 1969–1994.

Anderson, J. G., and J. E. Luco (1983a). Parametric study of near-field ground motion for a strike slip dislocation model. *Bull. Seismol. Soc. Am.* **73**, 23–43.

Anderson, J. G., and J. E. Luco (1983b). Parametric study of near-field ground motions for oblique-slip and dip-slip dislocation models. *Bull. Seismol. Soc. Am.* **73**, 45–57.

Anderson, J. G., and R. Quaas (1988). Effect of magnitude on the character of strong ground motion: an example from the Guerrero, Mexico, strong motion network. *Earthquake Spectra* **4**, 635–646.

Anderson, J. G., and G. Yu (1996). Predictability of strong motions from the Northridge, California, earthquake. *Bull. Seismol. Soc. Am.* **86**, S100–S114.

Anderson, J. G., P. Bodin, J. Brune, J. Prince, and S. K. Singh (1986). Strong ground motion and source mechanism of the Mexico earthquake of September 19, 1985. *Science* **233**, 1043–1049.

Anderson, J. G., J. N. Brune, J. Prince, R. Quaas, S. K. Singh, D. Almora, P. Bodin, M. Onate, R. Vazquez, and J. M. Velasco (1994). The Guerrero accelerograph network. *Geofisica Int.* **33**, 341–371.

Anderson, J. G., S. G. Wesnousky, and M. W. Stirling (1996). Earthquake size as a function of fault slip rate. *Bull. Seismol. Soc. Am.* **86**, 683–690.

Anderson, J. G., J. N. Brune, R. Anooshehpoor, and S.-D. Ni (2000a). New ground motion data and concepts in seismic hazard analysis. *Current Science* **79**, 1278–1290.

Anderson, J. G., H. Sucuoglu, A. Erberik, T. Yilmaz, E. Inan, E. Durukal, M. Erdik, R. Anooshehpoor, J. N. Brune, and S.-D. Ni (2000b). Implications for seismic hazard analysis. In: "Kocaeli, Turkey, earthquake of August 17, 1999 Reconnaissance Report" (T. L. Youd, J.-P. Bardet, and J. D. Bray, Eds.), *Earthquake Spectra*, Supplement A to Volume 16, 113–137.

Archuleta, R. J. (1984). A faulting model for the 1979 Imperial Valley earthquake. *J. Geophys. Res.* **89**, 4559–4585.

Archuleta, R. J., and S. H. Hartzell (1981). Effects on fault finiteness on near-source ground motion. *Bull. Seismol. Soc. Am.* **71**, 939–957.

Atkinson, G. (1993). Source spectra for earthquakes in eastern North America. *Bull. Seismol. Soc. Am.* **83**, 1778–1798.

Atkinson, G., and D. M. Boore (1997). Stochastic point-source modeling of strong motions in the Cascadia region. *Seismol. Res. Lett.* **68**, 74–85.

Atkinson, G. M., and P. G. Somerville (1994). Calibration of time-history simulation methods. *Bull. Seismol. Soc. Am.* **84**, 400–414.

Bazzurro, P., and C. A. Cornell (1999). Disaggregation of seismic hazard. *Bull. Seismol. Soc. Am.* **89**, 501–520.

Belardinelli, M. E., M. Cocco, O. Coutant, and F. Cotton (1999). Redistribution of dynamic stress during coseismic ruptures: evidence for fault interaction and earthquake triggering. *J. Geophys. Res.* **104**, 14925–14945.

Beresnev, I. A., and G. M. Atkinson (1998a). Stochastic finite-fault modeling of ground motions from the 1994 Northridge, California, earthquake, I. Validation on rock sites. *Bull. Seismol. Soc. Am.* **88**, 1392–1401.

Beresnev, I. A., and G. M. Atkinson (1998b). Stochastic finite-fault modeling of ground motions from the 1994 Northridge, California, earthquake, II. Widespread nonlinear response at soil sites. *Bull. Seismol. Soc. Am.* **88**, 1402–1410.

Bernard, P., and R. Madariaga (1984). A new asymptotic method for the modeling of near-field accelerograms. *Bull. Seismol. Soc. Am.* **74**, 539–557.

Beroza, G. C. (1991). Near-source modeling of the Loma Prieta earthquake: evidence for heterogeneous slip and implications for the earthquake hazards. *Bull. Seismol. Soc. Am.* **81**, 1603–1621.

Beroza, G. C., and P. Spudich (1988). Linearized inversion for fault rupture behavior: application to the 1984 Morgan Hill, California, earthquake. *J. Geophys. Res.* **93**, 6275–6296.

Bolt, B. (1969). Duration of strong motion. *Proc. 4th World Conf. Earthq. Engineering, Santiago, Chile*, 1304–1315.

Boore, D. M. (1983). Stochastic simulation of high-frequency ground motions based on seismological models of the radiated spectra. *Bull. Seismol. Soc. Am.* **73**, 1865–1894.

Boore, D. M., and G. M. Atkinson (1987). Stochastic prediction of ground motion and spectral response at hard-rock sites in eastern North America. *Bull. Seismol. Soc. Am.* **77**, 440–467.

Borcherdt, R. D. (1997). US National Strong Motion Program. In: "Vision 2005: An Action Plan for Strong Motion Programs to Mitigate Earthquake Losses in Urbanized Areas" (J. C. Stepp, Ed.), US Committee for Advancement of Strong Motion Programs, Austin, Texas, 81–85.

Bouchon, M. (1981). A simple method to calculate Green's functions for layered media. *Bull. Seismol. Soc. Am.* **71**, 959–971.

Bouchon, M., and J. S. Barker (1996). Seismic response of a hill: the example of Tarzana, California. *Bull. Seismol. Soc. Am.* **86**, 66–72.

Bouchon, M., M.-P. Bouin, and H. Karabulut (2000). How fast did rupture propagate during the Izmit and the Duzce earthquakes (abstract). *EOS, Trans. Am. Geophys. Un.* **81**, F836.

Brune, J. N. (1970). Tectonic stress and the spectra of seismic shear waves from earthquake. *J. Geophys. Res.* **75**, 4997–5009.

Brune, J. N. (1971). Correction. *J. Geophys. Res.* **76**, 5002.

Brune, J. N. (1996a). Particle motion in a physical model of shallow angle thrust faulting. *Proc. Indian Acad. Sci.* **105**, 197–206.

Brune, J. N. (1996b). Precariously balanced rocks and ground-motion maps for southern California. *Bull. Seismol. Soc. Am.* **86**, 43–54.

Brune, J. N. (1999). Precarious rocks along the Mojave section of the San Andreas fault, California: constraints on ground motion from great earthquakes. *Seismol. Res. Lett.* **70**, 29–33.

Campbell, K. W. (2002). Seismology, engineering. In: "Encyclopedia of Physical Science and Technology" (R. A. Meyers, Ed.), 3rd ed., Vol. 14, pp. 531–545, Academic Press, San Diego.

Campillo, M., and R. J. Archuleta (1993). A rupture model for the 28 June 1992 Landers, California, earthquake. *Geophys. Res. Lett.* **20**, 647–650.

Castro, R. R., L. Trojani, G. Monachesi, M. Mucciarelli, and M. Cattaneo (2000). The spectral decay parameter κ in the region of Umbria-Marche, Italy. *J. Geophys. Res.* **105**, 23811–23823.

Celebi, M., S. Akkar, U. Gulerce, A. Sanli, H. Bundock, and A. Salkin (2001). Main shock and aftershock records of the 1999 Izmit and Duzce, Turkey, earthquakes. *US Geol. Surv. Open File Report 01-163*.

Chin, B. H., and K Aki (1991). Simultaneous study of the source, path, and site effects on strong ground motion during the 1989 Loma Prieta earthquake: a preliminary result on pervasive nonlinear site effects. *Bull. Seismol. Soc. Am.* **81**, 1859–1884.

Cho, I., and I. Nakanishi (2000). Investigation of the three-dimensional fault geometry ruptured by the 1995 Hyogo-ken Nanbu earthquake using strong-motion and geodetic data. *Bull. Seismol. Soc. Am.* **90**, 450–467.

Cohee, B. P., and G. C. Beroza (1994). Slip distribution of the 1992 Landers earthquake and its implications for earthquake source mechanism. *Bull. Seismol. Soc. Am.* **84**, 692–712.

Cohee, B. P., P. G. Somerville, and N. A. Abrahamson (1991). Simulated ground motions for hypothesized $M_w = 8$ subduction earthquakes in Washington and Oregon. *Bull. Seismol. Soc. Am.* **81**, 28–56.

Cormier, V. F., and W.-J. Su (1994). Effects of three-dimensional crustal structure on the estimated history and ground motion of the Loma Prieta earthquake. *Bull. Seismol. Soc. Am.* **84**, 284–294.

Cornell, C. A. (1968). Engineering seismic risk analysis. *Bull. Seismol. Soc. Am.* **58**, 1583–1606.

Cornell, C. A. (1995). An advocation: map probabilistically derived quantities, ACT 35-2, National Earthquake Ground Motion Mapping Workshop, September 1995.

Cotton, F., and M. Campillo (1995). Frequency domain inversion of strong motions: application to the 1992 Landers earthquake. *J. Geophys. Res.* **100**, 3961–3975.

Cousins, W. J. (1998). New Zealand strong motion data 1965–1997. *Institute of Geological and Nuclear Sciences. Report 98/4*, Lower Hutt, New Zealand.

Dan, K., T. Watanabe, T. Tanaka, and R. Sato (1990). Stability of earthquake ground motion synthesized using different small-event records as empirical Green's functions. *Bull. Seismol. Soc. Am.* **80**, 1433–1455.

Davis, P. M., J. L. Rubenstein, K. H. Liu, S. S. Gao, and L. Knopoff (2000). Northridge earthquake damage caused by geologic focusing of seismic waves. *Science* **289**, 1746–1750.

Dreger, D. S., and A. Kaverina (2000). Seismic remote sensing for the earthquake source process and near-source shaking: a case study of the October 16, 1999, Hector Mine earthquake. *Geophys. Res. Lett.* **27**, 1941–1944.

Ebel, J. E., and A. L. Kafka (1999). A Monte Carlo approach to seismic hazard analysis. *Bull. Seismol. Soc. Am.* **89**, 854–866.

Ellsworth, W. L., and M. Celebi (1999). Near field displacement time histories of the M7.4 Kocaeli (Izmit), Turkey, earthquake of August 17, 1999 (abstract). *EOS, Trans. Am. Geophys. Un.* **80**(46), F648.

Field, E. H., S. Kramer, A. W. Elgemal, J. D. Bray, N. Matasovic, P. A. Johnson, C. Cramer, C. Roblee, D. Wald, L. F. Bonilla, P. P. Dimitriu, and J. G. Anderson (1998). Nonlinear site response: where we're at (a report from a SCEC/PEER seminar and workshop). *Seismol. Res. Lett.* **69**, 230–234.

Fletcher, J. B., and P. Spudich (1998). Rupture characteristics of the three M∼4.7 (1992–1994) Parkfield earthquakes. *J. Geophys. Res.* **103**, 835–854.

Frankel, A. (1991). High-frequency spectral falloff of earthquakes, fractal dimension of complex rupture, b-value, and the scaling of strength of faults. *J. Geophys. Res.* **96**, 6291–6302.

Frankel, A. (1995). Mapping Seismic Hazard in the Central and Eastern United States. *Seismol. Res. Lett.* **66**(4), 8–21.

Frankel, A., J. Fletcher, F. Vernon, L. Haar, J. Berger, T. Hanks, and J. Brune (1986). Rupture characteristics and tomographic source imaging of $M_L \sim 3$ earthquakes near Anza, southern California. *J. Geophys. Res.* **91**, 12633–12650.

Frankel, A., C. Mueller, T. Barnhard, D. Perkins, E. V. Leyendecker, N. Dickman, S. Hanson, and M. Hopper (1996). National Seismic Hazard Maps, June 1996, U.S. Department of the Interior, U.S. Geological Survey, MS 966, Box 25046, Denver Federal Center, Denver, CO 80255.

Frankel, A., C. Mueller, S. Harmsen, R. Wesson, E. Leyendecker, F. Klein, T. Barnhard, D. Perkins, N. Dickman, S. Hanson, and M. Hopper (2000). USGS national seismic hazard maps: methodology and analysis. *Earthquake Spectra* **16**, 1–19.

Franklin, A. G. (1997). U. S. Army Corps of Engineers strong motion instrumentation program. In: "Vision 2005: An Action Plan for Strong Motion Programs to Mitigate Earthquake Losses in Urbanized Areas" (J. C. Stepp, Ed.), U.S. Committee for Advancement of Strong Motion Programs, Austin, Texas, 91.

Freeman, J. R. (1932). *Earthquake Damage and Earthquake Insurance*. McGraw-Hill, New York.

Geli, L., P. Bard, and B. Jullien (1988). The effect of topography on earthquake ground motion: a review and new results. *Bull. Seismol. Soc. Am.* **78**, 42–63.

Graves, R. W., and D. J. Wald (2001). Resolution analysis of finite fault source inversion using one- and three-dimensional Green's functions; 1, Strong motions, *J. Geophys. Res.* **106**, 8745–8766.

Graves, R. W., D. J. Wald, H. Kawase, and T. Sato (1999). Finite fault source inversion using 3D Green's functions. *Seismol. Res. Lett.* **70**, 251.

Haddon, R. A. W. (1996a). Use of empirical Green's functions, spectral ratios, and kinematic source models for simulating strong ground motion. *Bull. Seismol. Soc. Am.* **86**, 597–615.

Haddon, R. A. W (1996b). Earthquake source spectra in eastern North America. *Bull. Seismol. Soc. Am.* **86**, 1300–1313.

Hadley, D. M., and D. V. Helmberger (1980). Simulation of strong ground motions. *Bull. Seismol. Soc. Am.* **70**, 617–630.

Hanks, T. C. (1979). b-values and $\omega^{-\gamma}$ seismic source models: implications for tectonic stress variations along active crustal fault zones and estimation of high-frequency strong ground motion. *J. Geophys. Res*. **84**, 2235–2242.

Hanks, T. C. (1982). F_{max}. *Bull. Seismol. Soc. Am.* **74**, 1867–1880.

Hanks, T., and H. Kanamori (1979). A moment magnitude scale. *J. Geophys. Res.* **84**, 2348–2350.

Hanks, T. C., and R. K. McGuire (1981). The character of high-frequency strong ground motion. *Bull. Seismol. Soc. Am.* **71**, 2071–2095.

Harmsen, S., D. Perkins, and A. Frankel (1999). Deaggregation of probabilistic ground motions in the central and eastern United States. *Bull. Seismol. Soc. Am.* **89**, 1–13.

Hartzell, S. H. (1978). Earthquake aftershocks as Green's functions. *Geophys. Res. Lett.* **5**, 1–4.

Hartzell, S. H. (1989). Comparison of seismic waveform techniques for the rupture history of a finite fault: application to the 1986 North Palm Springs, California, earthquake. *J. Geophys. Res.* **94**, 7515–7534.

Hartzell, S. H., and T. H. Heaton (1983). Inversion of strong ground motion and teleseismic waveform data for the fault rupture history of the 1979 Imperial Valley, California, earthquake. *Bull. Seismol. Soc. Am.* **73**, 1553–1583.

Hartzell, S. H., and T. H. Heaton (1986). Rupture history of the 1984 Morgan Hill, California, earthquake from the inversion of strong motion records. *Bull. Seismol. Soc. Am.* **76**, 649–674.

Hartzell, S. H., and M. Iida (1990). Source complexity of the 1987 Whittier Narrows, California, earthquake from inversion of strong motion records. *J. Geophys. Res.* **95**, 12475–12485.

Hartzell, S. H., and C. Mendoza (1991). Application of an iterative least-square waveform inversion of strong-motion and teleseismic records to the 1978 Tabas, Iran, earthquake. *Bull. Seismol. Soc. Am.* **81**, 305–331.

Hartzell, S. H., C. Langer, and C. Mendoza (1994). Rupture histories of eastern North America earthquakes. *Bull. Seismol. Soc. Am.* **84**, 1703–1724.

Hartzell, S. H., P. Liu, and C. Mendoza (1996). The 1994 Northridge, California, earthquake: investigation of rupture velocity, rise time, and high-frequency radiation. *J. Geophys. Res.* **101**, 20091–20108.

Haskell, N. A. (1964). Total energy and energy spectral density of elastic wave radiation from propagating faults. *Bull. Seismol. Soc. Am.* **54**, 1811–1841.

Haskell, N. A. (1969). Elastic displacements in the near-field of a propagating fault. *Bull. Seismol. Soc. Am.* **59**, 865–908.

Heaton, T. H. (1982). The 1971 San Fernando earthquake: a double event? *Bull. Seismol. Soc. Am.* **72**, 2037–2062.

Heaton, T. H. (1990). Evidence for and implications of self-healing pulses of slip in earthquake rupture. *Phys. Earth Planet Inter.* **64**, 1–20.

Heaton, T. H., F. Tajima, and A. W. Mori (1986). Estimating ground motions using recorded accelerograms. *Surveys in Geophys.* **8**, 25–83.

Heaton, T. H., J. F. Hall, D. J. Wald, and M. W. Halling (1995). Response of high-rise and base-isolated buildings to a hypothetical M_w 7.0 blind thrust earthquake. *Science* **267**, 206–211.

Hernandez, B., F. Cotton, and M. Campillo (1999). Contribution of radar interferometry to a two-step inversion of the kinematic process of the 1992 Landers earthquake. *J. Geophys. Res.* **104**, 13083–13099.

Horikawa, H., H. Hirahara, Y. Umeda, M. Hashimoto, and F. Kasano (1996). Simultaneous inversion of geodetic and strong-motion data for the source process of the Hyogo-ken Nanbu, Japan, earthquake. *J. Phys. Earth* **44**, 455–471.

Horton, S. (1996). A fault model with variable slip duration for the 1989 Loma Prieta, California, earthquake determined from strong-ground-motion data. *Bull. Seismol. Soc. Am.* **86**, 122–132.

Horton, S. P., J. G. Anderson, and A. Mendez (1994). Frequency domain inversion for the character of rupture during the 1989 Loma Prieta, California, earthquake using strong motion and geodetic observations. In: "The Loma Prieta, California, Earthquake of October 17, 1989—Main-Shock Characteristics" (P. Spudich, Ed.), *US Geol. Surv. Prof. Paper 1550-A*.

Housner, G. W. (1947). Characteristics of strong-motion earthquakes. *Bull. Seismol. Soc. Am.* **37**, 19–31.

Hudson, D. E. (1979). *Reading and Interpreting Strong Motion Accelerograms*. Earthquake Engineering Research Institute, Berkeley, California, 112 pp.

Humphrey, J. R., and J. G. Anderson (1992). Shear wave attenuation and site response in Guerrero, Mexico. *Bull. Seismol. Soc. Am.* **82**, 1622–1645.

Hutchings, L. (1991). "Prediction" of strong ground motion for the 1989 Loma Prieta earthquake using empirical Green's functions. *Bull. Seismol. Soc. Am.* **81**, 88–121.

Hutchings, L. (1994). Kinematic earthquake models and synthesized ground motion using empirical Green's functions. *Bull. Seismol. Soc. Am.* **84**, 1028–1050.

Hutchings, L., and F. Wu (1990). Empirical Green's functions from small earthquakes—a waveform study of locally recorded aftershocks of the San Fernando earthquake. *J. Geophys. Res.* **95**, 1187–1214.

Ichinose, G. A. (2000). Seismicity and stress transfer studies in eastern California and Nevada: implications for earthquake sources and tectonics, Ph.D. Thesis, University of Nevada, Reno, Nevada, 356 pp.

Ichinose, G. A., K. D. Smith, and J. G. Anderson (1998). Moment tensor solutions of the 1994 to 1996 Double Spring Flat, Nevada, earthquake sequence and implications for local tectonic models. *Bull. Seismol. Soc. Am.* **88**, 1363–1378.

Ide, S., M. Takeo, and Y. Yoshida (1996). Source process of the 1995 Kobe earthquake: determination of spatiotemporal slip distribution by Bayesian modeling. *Bull. Seismol. Soc. Am.* **86**, 547–566.

Inan, E., Z. Colakoglu, N. Koc, N. Bayulke, and E. Coruh (1996). *Catalog of earthquakes between 1976–1996 acceleration records, Republic of Turkey*. Ministry of Public Works and Settlements, Directorate of Disaster Affairs, Earthquake Research Department, July 1996 (in Turkish).

Irikura, K. (1983). Semi-empirical estimation of strong ground motions during large earthquakes. *Bull. Disaster Prevention Res. Inst., Kyoto Univ.* **33**, 63–104.

Irikura, K. (1986). Prediction of strong acceleration motions using empirical Green's functions. *Proc. 7th Jap. Earthq. Eng. Symp.* 151–156.

Irikura, K., K. Kudo, H. Okada, and T. Sasatani (Eds.) (1998). "The Effects of Surface Geology on Seismic Motion." (Proc. of the Second International Symposium on Effects of Surface Geology on Strong Motions, Yokohama, Japan), Bulkema, Rotterdam.

Jarpe, S. P., and P. W. Kasameyer (1996). Validation of a procedure for calculating broadband strong-motion time histories with empirical Green's functions. *Bull. Seismol. Soc. Am.* **86**, 1116–1129.

Jennings, P. C., G. W. Housner, and N. C. Tsai (1969). Stimulated earthquake motions for design purposes. *Proc. 9th World Conf. Earthq. Eng., Santiage, Chile*, 145–160.

Joyner, W. B., and D. M. Boore (1986). On simulating large earthquakes by Green's function addition of smaller earthquakes. In: "Earthquake Source Mechanics" (S. Das, J. Boatwright, and C. Scholz, Eds.), *Am. Geophys. Un. Geophys. Monograph* **37**, 269–274.

Joyner, W. B., and P. Spudich (1994). Including near-field terms in the isochrone integration method for application to finite-fault or Kirchhoff boundary integral problems. *Bull. Seismol. Soc. Am.* **84**, 1260–1265.

Kakehi, Y., and K. Irikura (1996). Estimation of high-frequency wave radiation areas on the fault plane by the envelope inversion of acceleration seismograms. *Geophys. J. Int.* **125**, 892–900.

Kakehi, Y., and K. Irikura (1997). High-frequency radiation process during earthquake faulting—envelope inversion of acceleration seismograms from the 1993 Hokkaido-Nansei-Oki, Japan, earthquake. *Bull. Seismol. Soc. Am.* **87**, 904–917.

Kakehi, Y., K. Irikura, and M. Hoshiba (1996). Estimation of high-frequency wave radiation areas on the fault plane of the 1995 Hyogo-ken Nanbu earthquake by the envelope inversion of seismograms. *J. Phys. Earth* **44**, 505–517.

Kamae, K., and K. Irikura (1998). Source model of the 1995 Hyogo-ken Nanbu earthquake and simulation of near-source ground motion. *Bull. Seismol. Soc. Am.* **88**, 400–412.

Kamae, K., K. Irikura, and A. Pitarka (1998). A technique for simulating strong ground motion using hybrid Green's functions. *Bull. Seismol. Soc. Am.* **88**, 357–367.

Kanamori, H. (1977). The energy release in great earthquakes. *J. Geophys. Res.* **82**, 2981–2987.

Kanamori, H. (1979). A semi-empirical approach to prediction of long-period ground motions from great earthquakes. *Bull. Seismol. Soc. Am.* **69**, 1645–1670.

Kanamori, H., and C. R. Allen (1986). Earthquake repeat time and average stress drop. In: "Earthquake Source Mechanics" (S. Das,

J. Boatwright, and C. Scholz, Eds.), *Am. Geophys. Un. Geophys. Monograph* **37**, 227–235.

Kanamori, H., and D. L. Anderson (1975). Theoretical basis of some empirical relations in seismology. *Bull. Seismol. Soc. Am.* **65**, 1073–1095.

Kawase, H. (1996). The cause of the damage belt in Kobe: "The basin edge effect," constructive interference of the direct S-wave with the basin-induced diffracted Rayleigh waves. *Seismol. Res. Lett.* **67**(5), 25–34.

Kawase, H., S. Matsushima, R. W. Graves, and P. G. Somerville (1998). Three-dimensional wave propagation analysis of simple two-dimensional basin structures with special reference to: "The Basin Edge Effect." *Zisin, Series-2* **50**, 431–449 (in Japanese with English abstract).

Kennett, B. L. N. (1983). *Seismic Wave Propagation in Stratified Media*. Cambridge University Press, Cambridge, 342 pp.

Kramer, S. L. (1996). *Geotechnical Earthquake Engineering*. Prentice Hall, Upper Saddle River, New Jersey, 653 pp.

Koketsu, K., and M. Kikuchi (2000). Propagation of seismic ground motion in the Kanto basin, Japan. *Science* **288**, 1237–1239.

Kostrov, B. V. (1970). The theory of the focus for tectonic earthquakes. *Izv. Acad. Sci. USSR Phys. Solid Earth, Engl. Transl.*, No. 4, 84–101.

Lee, W. H. K. (Coordinator) (2001). CD-ROM Supplement of Seismic Data, Special Issue on the 1999 Chi-Chi, Taiwan, Earthquake. *Bull. Seismol. Soc. Am.* **91**, CD-ROM Supplement.

Liu, H.-L., and T. Heaton (1984). Array analysis of the ground velocities and accelerations from the 1971 San Fernando, California, earthquake. *Bull. Seismol. Soc. Am.* **74**, 1951–1968.

Liu, H. L., and D. V. Helmberger (1983). The near-source ground motion of the 6 August 1979 Coyote Lake, California, earthquake. *Bull. Seismol. Soc. Am.* **73**, 201–218.

Luco, J. E., and J. G. Anderson (1983). Steady state response of an elastic half-space to a moving dislocation of finite width. *Bull. Seismol. Soc. Am.* **73**, 1–22.

Luco, J. E., and R. J. Apsel (1983). On the Green's functions for a layered half space; Part I., *Bull. Seismol. Soc. Am.* **73**, 909–929.

Ma, K.-F., J. Mori, S.-J. Lee, and S. B. Yu (2001). Spatial and temporal distribution of slip for the 1999 Chi-Chi, Taiwan, earthquake. *Bull. Seismol. Soc. Am.* **91**, 1069–1087.

Madariaga, R. (1983). Earthquake source theory: a review. In: "Earthquakes: Observation, Theory and Interpretation" (H. Kanamori and E. Boschi, Eds.), North Holland Publishing Company, Amsterdam, 1–44.

Matsushima, S., and H. Kawase (1998). 3-D wave propagation analysis in Kobe referring to "The basin-edge effect." In: "The Effects of Surface Geology on Seismic Motions" (K. Irikura, K. Kudo, H. Okada, and T. Sasatani, Eds.), Bulkema, Rotterdam, 1377–1384.

McGuire, R. K. (1995). Probabilistic seismic hazard analysis and design earthquakes: closing the loop. *Bull. Seismol. Soc. Am.* **85**, 1275–1284.

Mendez, A. J., and J. G. Anderson (1991). The temporal and spatial evolution of the 19 September 1985 Michoacan earthquake as inferred from near-source ground-motion records. *Bull. Seismol. Soc. Am.* **81**, 844–861.

Mendoza, C., and S. H. Hartzell (1988). Inversion for slip distribution using GDSN P waves: North Palm Springs, Borah Peak, and Michoacan earthquakes. *Bull. Seismol. Soc. Am.* **78**, 1092–1111.

Mendoza, C., and S. H. Hartzell (1989). Slip distribution of the 19 September 1985 Michoacan Mexico earthquake: near source and teleseismic constraints. *Bull. Seismol. Soc. Am.* **79**, 655–669.

Mikumo, T., and T. Miyatake (1993). Dynamic rupture process on a dipping fault, and estimates of stress drop and strength excess from the results of waveform inversion. *Geophys. J. Int.* **112**, 481–496.

Mikumo, T., and T. Miyatake (1995). Heterogeneous distribution of dynamic stress drop and relative fault strength recovered from the results of waveform inversion: the 1984 Morgan Hill, California, earthquake. *Bull. Seismol. Soc. Am.* **85**, 178–193.

Milne, W. G., and A. G. Davenport (1969). Distribution of earthquake risk in Canada. *Bull. Seismol. Soc. Am.* **59**, 729–754.

Nakahara, H. (1998). Seismogram envelope inversion for the spatial distribution of high-frequency energy radiation from the earthquake fault; application to the 1994 far east off Sanriku earthquake, Japan. *J. Geophys. Res.* **103**, 855–867.

Nakahara, H., H. Sato, M. Ohtake, and T. Nishimura (1999). Spatial distribution of high-frequency energy radiation on the fault of the 1995 Hyogo-Ken Nanbu, Japan, earthquake (M_w 6.9) on the basis of the seismogram envelope Inversion. *Bull. Seismol. Soc. Am.* **89**, 22–35.

Newmark, N. M., and W. J. Hall (1982). *Earthquake Spectra and Design*. Earthquake Engineering Research Institute Monograph, Berkeley, Calif., 103 pp.

Ni, S.-D., J. G. Anderson, Y. Zeng, and R. V. Siddharthan (2000). Expected signature of nonlinearity on regression for strong ground motion parameters. *Bull. Seismol. Soc. Am.* **90**(6B), S53–S64.

Oglesby, D. D., and S. M. Day (2001). Fault geometry and the dynamics of the 1999 Chi-Chi (Taiwan) earthquake. *Bull. Seismol. Soc. Am.* **91**, 1099–1111.

Oglesby, D. D., R. J. Archuleta, and S. B. Nielsen (1998). Earthquakes on dipping faults: the effects of broken symmetry. *Science* **280**, 1055–1059.

Olsen, K. B. (2000). Site amplification in the Los Angeles basin from 3D modeling of ground motion. *Bull. Seismol. Soc. Am.* **90**(6B), S77–S94.

Olsen, K. B., and R. J. Archuleta (1996). Three-dimensional simulation of earthquakes on the Los Angeles fault system. *Bull. Seismol. Soc. Am.* **86**, 575–596.

Olsen, K. B., R. Madariaga, and R. J. Archuleta (1997). Three-dimensional dynamic simulation of the 1992 Landers earthquake. *Science* **278**, 834–838.

Olsen, K. B., R. J. Archuleta, and J. R. Matarese (1995). Three-dimensional simulation of a magnitude 7.75 earthquake on the San Andreas fault. *Science* **270**, 1628–1632.

Olsen, K. B., R. Madariaga, and R. J. Archuleta (1997). Three-dimensional dynamic simulation of the 1992 Landers earthquake. *Science* **278**, 834–838.

Olson, A. H., and R. J. Apsel (1982). Finite fault and inverse theory with applications to the 1979 Imperial Valley earthquake. *Bull. Seismol. Soc. Am.* **72**, 1969–2001.

Ordaz, M., and C. Reyes (1999). Earthquake hazard in Mexico City; observations versus computations. *Bull. Seismol. Soc. Am.* **89**, 1379–1383.

Ou, G. B., and R. B. Herrmann (1990). A statistical model for ground motion produced by earthquakes at local and regional distances. *Bull. Seismol. Soc. Am.* **80**, 1397–1417.

Phillips, W. S., S. Kinoshita, and H. Fujiwara (1993). Basin-induced Love waves observed using the strong-motion array at Fuchu, Japan. *Bull. Seismol. Soc. Am.* **83**, 65–84.

Pitarka, A., K. Irikura, and T. Iwata (1997). Modeling of ground motion in the Higashinada (Kobe) area for an aftershock of the 1995

January 17 Hyogo-ken Nanbu, Japan earthquake. *Geophys. J. Int.* **131**, 231–239.

Pitarka, A., K. Irikura, T. Iwata, and H. Sekiguchi (1998). Local geological structure effects on ground motion from earthquakes on basin-edge faults. In: "The Effects of Surface Geology on Seismic Motions" (K. Irikura, K. Kudo, H. Okada, and T. Sasatani, Eds.), Bulkema, Rotterdam, 901–906.

Quaas, R. (1997). Mexican strong motion program. In: "Vision 2005: An Action Plan for Strong Motion Programs to Mitigate Earthquake Losses in Urbanized Areas" (J. C. Stepp, Ed.), US Committee for Advancement of Strong Motion Programs, Austin, Texas, 53–65.

Rathje, E. (Coordinator) (2000). Strong ground motions and site effects. In *Earthquake Spectra*, Supplement A to Volume 16, 65–96.

Richter, C. F. (1958). *Elementary Seismolgy*. W. H. Freeman, San Francisco, 768 pp.

Ruff, L. J. (1984). Tomographic imaging of the earthquake rupture process. *Geophys. Res. Lett.* **11**, 629–632.

Safak, E., and M. Erdik (Coordinators) (2000). Recorded main shock and aftershock motions. *Earthquake Spectra*, Supplement A to Volume 16, 97–112.

Sato, T., and T. Hirasawa (1973). Body wave spectra from propagating shear cracks. *J. Phys. Earth* **21**, 415–431.

Sato, T., D. V. Helmberger, P. G. Somerville, R. W. Graves, and C. K. Saikia (1998a). Estimates of regional and local strong motions during the Great 1923 Kanto, Japan, earthquake (M_S 8.2). Part 1: source estimation of a calibration event and modeling of wave propagation paths. *Bull. Seismol. Soc. Am.* **88**, 183–205.

Sato, T., R. W. Graves, P. G. Somerville, and S. Kataoka (1998b). Estimates of regional and local strong motions during the Great 1923 Kanto, Japan, earthquake (M_S 8.2). Part 2: forward simulation of seismograms using variable-slip rupture models and estimation of near-fault long-period ground motions. *Bull. Seismol. Soc. Am.* **88**, 206–227.

Sato, T., R. W. Graves, and P. G. Somerville (1999). Three-dimensional finite-difference simulations of long-period strong motions in the Tokyo metropolitan area during the 1990 Odawara earthquake (M_J 5.1) and the Great 1923 Kanto earthquake (M_S 8.2) in Japan. *Bull. Seismol. Soc. Am.* **89**, 579–607.

Scholz, C. H., C. A. Aviles, and S. G. Wesnousky (1986). Scaling differences between large intraplate and interplate earthquakes. *Bull. Seismol. Soc. Am.* **76**, 65–70.

Schneider, J. F., W. J. Silva, and C. Stark (1993). Ground motion model for the 1989 M 6.9 Loma Prieta earthquake including effects of source, path, and site. *Earthquake Spectra* **9**, 251–287.

Seekins, L. C., A. G. Brady, C. Carpenter, and N. Brown (1992). Digitized strong-motion accelerograms of North and Central American earthquakes 1933–1986. *US Geol. Surv. Digital Data Series DDS-7.*

Sekiguchi, H., and T. Iwata (2002). Rupture process of the 1999 Kocaeli, Turkey, earthquake estimated from strong motion waveforms. *Bull. Seismol. Soc. Am.* **92**, 300–311.

Sekiguchi, H., K. Irikura, T. Iwata, Y. Kakehi, and M. Hoshiba (1996). Minute locating of faulting beneath Kobe and the waveform inversion of the source process during the 1995 Hyogo-ken Nanbu, Japan, earthquake using strong ground motion records. *J. Phys. Earth* **44**, 473–487.

Shakal, A. F. (1997). California strong motion instrumentation program. In: "Vision 2005: An Action Plan for Strong Motion Programs to Mitigate Earthquake Losses in Urbanized Areas" (J. C. Stepp, Ed.), US Committee for Advancement of Strong Motion Programs, Austin, Texas, 75–80.

Shi, B., A. Anooshehpoor, J. N. Brune, and Y. Zeng (1998). Dynamics of thrust faulting: 2D lattice model. *Bull. Seismol. Soc. Am.* **88**, 1484–1494.

Shin, T. C., K. W. Kuo, W. H. K. Lee, T. L. Teng, and Y. B. Tsai (2000). A preliminary report on the 1999 Chi-Chi (Taiwan) earthquake. *Seismol. Res. Lett.* **71**, 24–30.

Silva, W. J., R. B. Darragh, C. Stark, I. Wong, J. C. Stepp, J. Schneider, and S. J. Chiou (1990). A methodology to estimate design response spectra in the near-source region of large earthquakes using the band-limited-white-noise ground motion model. *Proc. 4th Int. Conf. Earthq. Engineering, Palm Springs, CA*. Earthquake Engineering Research Institute, Berkeley, 487–494.

Sokolov, V. Y. (1998). Spectral parameters of the ground motions in Caucasian seismogenic zones. *Bull. Seismol. Soc. Am.* **88**, 1438–1444.

Somerville, P. (2000). Magnitude scaling of near fault ground motions (abstract). *EOS, Trans. Am. Geophys. Un.* **81**, F822.

Somerville, P., M. Sen, and B. Cohee (1991). Simulation of strong ground motions recorded during the 1985 Michoacan, Mexico, and Valparaiso, Chile earthquakes. *Bull. Seismol. Soc. Am.* **81**, 1–27.

Somerville, P. G., N. F. Smith, R. W. Graves, and N. A. Abrahamson (1997). Modification of empirical strong ground motion attenuation relations to include the amplitude and duration effects of rupture directivity. *Seismol. Res. Lett.* **68**, 199–222.

Somerville, P., K. Irikura, R. W. Graves, S. Sawada, D. Wald, N. Abrahamson, Y. Iwasaki, T. Kagawa, N. Smith, and A. Kowada (1999). Characterizing crustal earthquake slip models for the prediction of strong ground motion. *Seismol. Res. Lett.* **70**, 59–80.

Spudich, P., and R. J. Archuleta (1987). Techniques for earthquake ground-motion calculations with applications to source parameterization of finite faults. In: "Seismic Strong Motion Synthetics" (B. A. Bolt, Ed.), Academic Press, Orlando, Florida, 205–265.

Spudich, P., and E. Cranswick (1984). Direct observation of rupture propagation during the 1979 Imperial Valley earthquake using a short baseline accelerometer array. *Bull. Seismol. Soc. Am.* **74**, 2083–2114.

Spudich, P., and L. N. Frazer (1984). Use of ray theory to calculate high-frequency radiation from earthquake sources having spatially variable rupture velocity and stress drop. *Bull. Seismol. Soc. Am.* **74**, 2061–2082.

Spudich, P., and L. N. Frazer (1987). Erratum. *Bull. Seismol. Soc. Am.* **77**, 2245.

Spudich, P., and D. Oppenheimer (1986). Dense seismograph array observations of earthquake rupture dynamics. In: "Earthquake Source Mechanics" (S. Das, J. Boatwright, and C. Scholz, Eds.), Am. Geophys. Un. *Geophys. Monograph,* **37**, 285–296.

Spudich, P., M. Hellweg, and W. H. K. Lee (1996). Directional topographic site response observed in aftershocks of the 1994 Northridge, California, earthquake: implications for main shock motions. *Bull. Seismol. Soc. Am.* **86**, S193–S208.

Spudich, P., W. B. Joyner, A. G. Lindh, D. M. Boore, B. M. Bargaris, and J. B. Fletcher (1999). SEA99: a revised ground motion prediction relation for use in extensional tectonic regimes. *Bull. Seismol. Soc. Am.* **89**, 1156–1170.

SSHAC (Senior Seismic Hazard Analysis Committee) (1997). Recommendations for Probabilistic Seismic Hazard Analysis: Guidance on Uncertainty and Use of Experts, NUREG/CR-6372, U.S. Nuclear Regulatory Commission.

Steidl, J. H., R. J. Archuleta, and S. H. Hartzell (1991). Rupture history of the 1989 Loma Prieta, California, earthquake. *Bull. Seismol. Soc. Am.* **81**, 1573–1602.

Stepp, J. C. (Ed.) (1997). *Vision 2005: An Action Plan for Strong Motion Programs to Mitigate Earthquake Losses in Urbanized Areas*, US Committee for Advancement of Strong Motion Programs, Austin, Texas. [This report is reproduced on the attached Handbook CD #2, under the directory of \57Anderson.]

Su, F., J. G. Anderson, and Y. Zeng (1998). Study of weak and strong ground motion including Nonlinearity from the Northridge, California, earthquake sequence. *Bull. Seismol. Soc. Am.* **88**, 1411–1425.

Takemura, M., and I. Ikeura (1987). Semi-empirical synthesis of strong ground motions for the description of inhomogeneous faulting. *J. Seismol. Soc. Japan* **40**, 77–88.

Trifunac, M. D., and A. G. Brady (1975). A study of the duration of strong earthquake ground motion. *Bull. Seismol. Soc. Am.* **65**, 581–626.

Trifunac, M. D., and F. E. Udwadia (1974). Parkfield, California, earthquake of June 27, 1966: a three-dimensional moving dislocation. *Bull. Seismol. Soc. Am.* **64**, 511–533.

Tsai, C.-C. P., and K.-C. Chen (2000). A model for the high-cut process of strong-motion accelerations in terms of distance, magnitude, and site condition: an example from the SMART 1 Array, Lotung, Taiwan. *Bull. Seismol. Soc. Am.* **90**, 1535–1542.

Tsai, Y.-B., and M.-W. Huang (2000). Strong ground motion characteristics of the Chi-Chi, Taiwan earthquake of September 21, 1999. *Earthq. Engin. and Engin. Seismol.* **2**, 1–21.

Toro, G. R., N. A. Abrahamson, and J. F. Schneider (1997). Model of strong ground motions from earthquakes in central and eastern North America: best estimates and uncertainties. *Seismol. Res. Lett.* **68**, 41–57.

Tucker, B. E., and Brune, J. N. (1973). Seismograms, S-wave spectra, and source parameters for aftershocks of San Fernando earthquake. In: "San Fernando, California, Earthquake of February 9, 1971" (N. A. Benfer, J. L. Coffman, and J. R. Bernick, Eds.), Volume III, US Dept. Commer., Natl. Oceanic Atmos. Adm., Environ. Res. Lab., Washington, D.C., 69–121.

Udwadia, F. E., and M. D. Trifunac (1973). Damped Fourier spectrum and response spectra. *Bull. Seismol. Soc. Am.* **63**, 1775–1783.

U.S. Geological Survey (1999). An Assessment of Seismic Monitoring in the United States. Requirement for an Advanced National Seismic System. *US Geol. Surv. Circular 1188*, US Department of Interior, Denver, Colorado.

USGS Web site (2001). *http://geohazards.cr.usgs.gov/eq/index.html*, accessed January 2001, National Seismic Hazard Mapping Project, United States Geological Survey, Golden, Colorado.

Vidale, J. E., and D. V. Helmberger (1988). Elastic finite-difference modeling of the 1971 San Fernando, California, earthquake. *Bull. Seismol. Soc. Am.* **78**, 122–141.

Viksne, A., C. Wood, and D. Copeland (1997). Bureau of Reclamation seismic monitoring/strong motion program and notification system. In: "Vision 2005: An Action Plan for Strong Motion Programs to Mitigate Earthquake Losses in Urbanized Areas" (J. C. Stepp, Ed.), US Committee for Advancement of Strong Motion Programs, Austin, Texas, 86–90.

Wald, D. J. (1996). Slip history of the 1995 Kobe, Japan, earthquake determined from strong-motion, teleseismic, and geodetic data. *J. Phys. Earth* **44**, 489–503.

Wald, D. J., and R. W. Graves (1998). The seismic response of the Los Angeles basin, California. *Bull. Seismol. Soc. Am.* **88**, 337–356.

Wald, D. J., and R. W. Graves (2001). Resolution analysis of finite fault source inversion using one- and three-dimensional Green's functions; 2, Combining seismic and geodetic data. *J. Geophys. Res.* **106**, 8767–8788.

Wald, D. J., and T. H. Heaton (1994). Spatial and temporal distribution of slip for the 1992 Landers, California, earthquake. *Bull. Seismol. Soc. Am.* **84**, 668–691.

Wald, D. J., D. V. Helmberger, and S. H. Hartzell (1990). Rupture process of the 1987 Superstition Hills earthquake from the inversion of strong motion data. *Bull. Seismol. Soc. Am.* **80**, 1079–1098.

Wald, D. J., D. V. Helmberger, and T. H. Heaton (1991). Rupture model of the 1989 Loma Prieta earthquake from the inversion of strong-motion and broadband teleseismic data. *Bull. Seismol. Soc. Am.* **81**, 1540–1572.

Wald, D. J., T. H. Heaton, and K. W. Hudnut (1996). The slip history of the 1994 Northridge, California, earthquake determined from strong-motion, teleseismic, GPS, and leveling data. *Bull. Seismol. Soc. Am.* **86**, S49–S70.

Ward, S. N. (1995). A multidisciplinary approach to seismic hazards in southern California. *Bull. Seismol. Soc. Am.* **85**, 1293–1309.

Wells, D. L., and K. J. Coppersmith (1994). New empirical relationships among magnitude, rupture length, rupture width, rupture area, and surface displacement. *Bull. Seismol. Soc. Am.* **84**, 974–1002.

Wennerberg, L. (1990). Stochastic summation of empirical Green's functions. *Bull. Seismol. Soc. Am.* **80**, 1418–1432.

Wu, F. T. (1978). Prediction of strong ground motion using small earthquakes. *Proc. 2nd Int. Microzonation Conf., San Francisco*, 701–704.

Yagi, Y., and M. Kikuchi (2000). Source rupture process of the Kocaeli, Turkey, earthquake of August 17, 1999, obtained by joint inversion of near-field data and teleseismic data. *Geophys. Res. Lett.* **27**, 1969–1972.

Yoshida, S., K. Koketsu, T. Sagiya, and T. Kato (1996). Joint inversion of near- and far-field waveforms and geodetic data for the rupture process of the 1995 Kobe earthquake. *J. Phys. Earth* **44**, 437–454.

Yu, G., K. N. Khattri, J. G. Anderson, J. N. Brune, and Y. Zeng (1995). Strong ground motion from the Uttarkashi, Himalaya, India earthquake: comparison of observations with synthetics using the composite source model. *Bull. Seismol. Soc. Am.* **85**, 31–50.

Zeng, Y., and J. G. Anderson (1996). A composite source model of the 1994 Northridge earthquake using genetic algorithms. *Bull. Seismol. Soc. Am.* **86**, S71–S83.

Zeng, Y., and C.-H. Chen (2001). Fault rupture process of the 20 September 1999 Chi-Chi, Taiwan, earthquake. *Bull. Seismol. Soc. Am.* **91**, 1088–1098.

Zeng, Y., K. Aki, and T. L. Teng (1993a). Source inversion of the 1987 Whittier Narrows earthquake, California, using the isochron method. *Bull. Seismol. Soc. Am.* **83**, 358–377.

Zeng, Y., K. Aki, and T. L. Teng (1993b). Mapping of the high-frequency source radiation for the Loma Prieta earthquake, California. *J. Geophys. Res.* **98**, 11981–11993.

Zeng, Y., J. G. Anderson, and G. Yu (1994). A composite source model for computing realistic synthetic strong ground motions. *Geophys. Res. Lett.* **21**, 725–728.

Zeng, Y., J. G. Anderson, and F. Su (1995). Subevent rake and random scattering effects in realistic strong ground motion simulation. *Geophys. Res. Lett.* **22**, 17–20.

This Page Intentionally Left Blank

58

Strong-Motion Data Processing

A. F. Shakal, M. J. Huang, and V. M. Graizer
California Geological Survey, Sacramento, CA, USA

1. Introduction

Initially very challenging, the digitizing and processing of recorded strong motion has seen great advances in the last 30 years. The evolution from the first digitization attempts, which defined problems still being dealt with today, through subsequent developments in computer digitizing and modern instrumentation has allowed significant progress in understanding near-source strong motion.

Although traditional seismological instruments were developed in the 1800s and perfected in the 1900s, instruments that could measure strong motion were not developed until the 1930s. The U.S. Coast and Geodetic Survey began the development of an accelerograph (Wenner, 1932) in response to a need expressed by earthquake engineers following an earthquake conference in Tokyo. Background aspects of the early development are reviewed by Housner (Scott, 1997; see also Chapter 2 by Housner). The first instruments were deployed in the Los Angeles area during the March 10, 1933, Long Beach earthquake, and very important records were obtained. Once earthquake recordings were obtained, processing of the records to extract crucial strong-motion information became important, and that forms the topic of this chapter.

2. Early Digitizing and Processing

2.1 Early Mechanical Analysis

The record from the Los Angeles Subway site from the 1933 Long Beach earthquake was one of the first strong-motion records. It was not exceeded in amplitude until the 1940 Imperial Valley earthquake, and it received extensive digitization and processing efforts.

Early analysis and digitization was difficult, partly because of the equipment limitations of the time, and partly because much was being learned about pitfalls in digitization and processing. The initial efforts involved cooperative work by the U.S. Coast and Geodetic Survey (USCGS), the National Bureau of Standards, and the Massachusetts Institute of Technology. The earliest analysis of a record was performed using a mechanical analyzer system at the USCGS (Neumann, 1943) by means of which operators could manually generate an approximate displacement record from an acceleration recording. A second approach utilized a mechanical differential analyzer already in use at MIT for studying other problems. These approaches using analyzing machines were paralleled by a manual numerical integration approach. The early work led to a symposium focused on "Determination of True Ground Motion by Integration of Strong Motion Records." Part of the Bulletin of the Seismological Society of America for January 1943 is devoted to the symposium, and it includes analysis of the differential analyzer and the importance of accuracy results from an engineering standpoint (Ruge, 1943a, b) and an appraisal of the numerical integration efforts (Neumann, 1943). The most important element from a historical perspective was the numerical methods approach, which became the basis of the progress that occurred in the succeeding decades.

2.2 Early Numerical Processing

The early procedures and difficulties in numerical integration of accelerograms are described in Neumann (1943), and many carry over in some form to the present. Digitization consisted of manually measuring and recording the position of the acceleration trace at fixed intervals along the length of the accelerogram. The accelerograms were photographically enlarged to make the measurement process more accurate and less difficult.

The ground motion could be calculated from these measurements using the fundamental equation of motion of a damped pendulum when subjected to an external acceleration,

$$-\mathrm{d}^2x(t)/\mathrm{d}t^2 = \mathrm{d}^2y(t)/\mathrm{d}t^2 + 2\mathrm{h}(2\pi/\mathrm{T_o})\mathrm{d}y(t)/\mathrm{d}t + (2\pi/\mathrm{T_o})^2y(t), \quad (1)$$

INTERNATIONAL HANDBOOK OF EARTHQUAKE AND ENGINEERING SEISMOLOGY, VOLUME 81B ISBN: 0-12-440658-0

where $x(t)$ is the instantaneous displacement of the instrument housing (i.e., normally the ground), $y(t)$ is the instantaneous displacement of the pendulum relative to the instantaneous position of the housing (measured from the record), h is a damping constant, and T_o is the instrument period. With integration twice, the housing or ground displacement is obtained as,

$$-x(t) = y(t) + 2h(2\pi/T_o)\int_o^t y(t)\,dt + (2\pi/T_o)^2 \int_o^t \int_o^t y(t)\,dt\,dt + c_1 + c_2 t. \quad (2)$$

where c_1 and c_2 are the integration constants. Once the amplitude values have been scaled from the record, the housing (or ground) displacement can be approximated using the numerical equation (with C_1 and C_2 being the re-defined integration constants):

$$-x_i = y_i + 2h(2\pi/T_o)\left(\sum_0^t y_i \Delta t + C_1\right) + (2\pi/T_o)^2\left[\sum_0^t \left(\sum_0^t y_i \Delta t + C_1\right)\Delta t + C_2\right]. \quad (3)$$

The practical steps involve measuring, or scaling, the y_i ordinate values of the recorded accelerogram at constant time steps t_i. The effort and time required to accurately scale peak values on analog records even today underscores the extensive efforts required by the USCGS to obtain reasonable accuracy during this period. Once the measured values from the record were available, the process of numerical integration could begin, performed using an adding machine with which an operator tediously obtained the necessary partial sums to calculate the displacement.

The constants of integration, C_1 and C_2, had to be estimated once initial sums had been obtained. Note that regardless of advances in technology, the initial conditions remain an issue. However, most modern digital accelerographs have adequate pre-event memory so that the pre-event zero-acceleration values can be estimated.

If the ground is at rest during the time interval immediately prior to the event, then C_1 is the zero-acceleration value (or pre-event y mean value), and C_2 is zero. However, many analog or optical recorders are still deployed; in these units, recording is initiated by the shaking itself, and so some of the motion is necessarily lost. In general, if the threshold level necessary to initiate recording is set low enough, the effect will not be severe, especially for recordings with high-amplitude acceleration. However, if the shaking at the site is of low amplitude, an important part of the total motion will be missed. For example, a distant earthquake with only long-period motion at a site illustrates the problem. In the Mexico City earthquake of 1957, only $0.04g$ was recorded. Because the motion was at long period, near the period of many structures, significant damage occurred (Duke and Leeds, 1959), though many film recorders in that situation would trigger late in the motion (or not trigger). For late-triggered records, accurate determination of displacements is still problematic.

The determination of displacement by manual numeric integration was performed as an interactive process, each time obtaining better estimates of C_1 and C_2. Of course, the accuracy problems associated with summing many numbers in a machine with finite register size are now well known. The early work was groundbreaking, grappling with many of the problems that strong-motion processing continued to address for the rest of the century.

In a parallel instrumentation effort during this period, the USCGS deployed instruments designed to have a long-period response, called displacement meters. These units typically had a 10-second pendulum period so that the recording would more closely correspond to the displacement motion of the ground. Although not many of these instruments were installed because of difficulty and cost, some records were obtained. It was an important step to compare displacement records calculated by numeric integration of the accelerometer records with these displacement meter records, to help understand the source and amplitude of the various errors. These comparisons have been made for several records, generating confidence in the processing procedures (e.g., Trifunac and Lee, 1974).

2.3 Standardized Digitizing and Processing—The Caltech Bluebook Project

Until 1970, the USCGS continued to obtain strong-motion recordings, but a need developed for standardized processing of the records obtained so that investigators would be analyzing the same time histories and spectral inputs for engineering design and structural dynamics studies. Some studies highlighted the uncertainty associated with calculating long-period displacements (Hershberger, 1955; Berg and Housner, 1961). The records from El Centro in 1940, Kern County in 1952, and Parkfield in 1966 underscored the need for uniform processing, particularly because of the unexpected amplitudes and periods recorded.

A project initiated in 1968 at Caltech focused on the computer processing of all records available at the time in a standardized approach. The San Fernando earthquake that occurred in 1971 caused a large increase in the number of records while the project was underway. The San Fernando records included the largest motions recorded up to that time, which increased the importance of standard processing.

The Caltech project moved forward from the USCGS numerical integration effort in several aspects. The most important was the use of large, fast digital computers, which had become available at major universities and research centers. The project was very productive, and the series of reports produced, all in blue cover, gave the project its unofficial name. By releasing the complete results by means of printed reports and files on digital computer tapes, the project allowed major progress by many

investigators in analytical studies of the data, and the records processed became the foundation of many research advances in subsequent years.

The second major difference between this project and earlier work was the use of a mechanical–electrical digitizing table incorporating a hand cursor with crosshairs. The cursor would be positioned over the center of the trace, and the (x, y) coordinate pair was output onto punched cards or magnetic tape when a button was pushed.

In one manual-digitizing approach, points on the waveform were digitized at equal time intervals on the record. In the second, the peaks, troughs, and points of inflection in the waveform were digitized, and the waveform was assumed to be comprised of straight-line segments between these points. The goal of this approach was to efficiently preserve most of the full-frequency content of the record while digitizing a reduced number of points. However, the effects of a varying sample rate are not well documented in signal theory. Current digitizing technology has made this approach unnecessary, and equal-interval sampling is now standard.

The use of a digital computer in the processing steps allowed much more complicated procedures to replace the adding machine in order to improve speed, accuracy, and precision. The resulting process became quite complicated, as reflected in Figure 1 (EERL, 1971), which illustrates that while there was a significant advance upon the Neumann USCGS effort, it was still a highly complex, iterative process. The technical documentation and computer program listings for the Caltech project are included in Trifunac and Lee (1973).

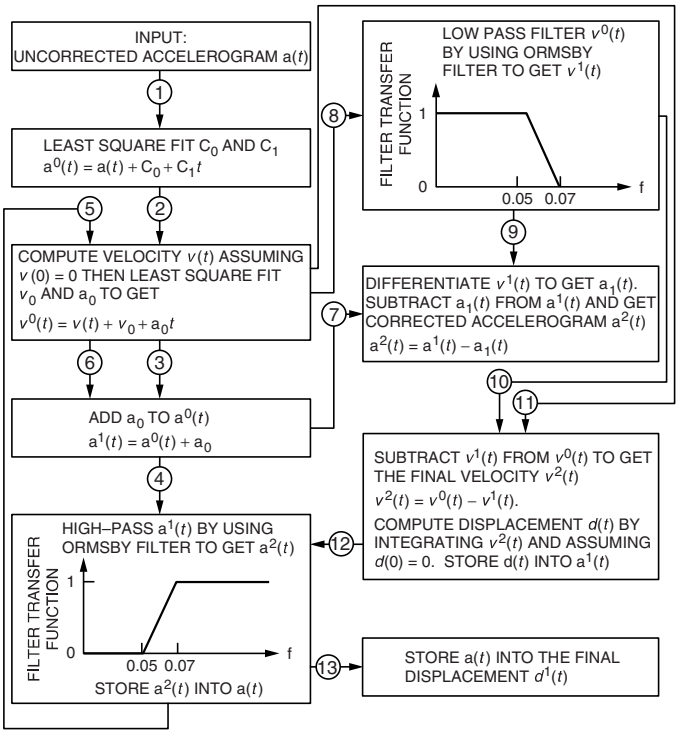

FIGURE 1 Flow chart summarizing the steps originally used in processing strong-motion accelerograms in the Caltech Bluebook Project (from EERL, 1971). Though simplified from the previous approaches, the process was still highly complex and iterative.

2.3.1 Standard Data Products

Results were released at several stages in the Caltech processing, and the names for these have become traditional: (1) Volume 1: Raw acceleration, as digitized, usually given as acceleration–time pairs, and expressed in units of acceleration; no instrument correction or filtering applied. (2) Volume 2: "Corrected" acceleration, velocity, and displacement; basically the final time-history product, with constant time steps. The raw acceleration has been bandpass filtered, and various other processing steps, including correcting for the instrument response, applied to obtain the best estimate of the acceleration. This acceleration has been numerically integrated, with follow-up filtering as necessary, once to obtain velocity, and once again to obtain displacement. (It was unfortunate that the word "corrected" became attached to this product, because it implied to some engineers that the data needed to be corrected because of errors. However, this misunderstanding has become less common over the years.) (3) Volume 3: Response spectrum values, for five damping values (0 through 20%) and 91 periods (from 0.04 through 15 seconds), including spectral acceleration and the pseudovelocity and displacement spectra.

The preceding three products are sometimes denoted as Phase 1, 2, etc., rather than Volume 1, 2 (e.g., Brady *et al.*, 1980), and this usage avoids the confusion often associated with the word volume. Several additional numbered products were generated during the Caltech project, but these are not commonly used today. Nearly all strong-motion networks and projects, worldwide, generate these three primary data products.

3. Modern Digitization

3.1 Semi-automated Accelerogram Scanning and Digitization

Advances in computer hardware resulted in the commercial availability of computer-controlled scanning systems in the mid-1970s. Early scanning machines were expensive and required careful handling. The first semi-automatic, computer-controlled digitization system was introduced by Trifunac and Lee (1979) at the University of Southern California. This system replaced the cursor-and-crosshairs of the Caltech project with an optical-density sensor that moved across the film image under the control of a computer, yielding an x–y grid of optical density values. Curve-following software was applied to the grid of optical densities, ultimately yielding acceleration–time pairs like that obtained in manual digitization.

This system yielded a major increase in digitizing speed, though extensive work was still sometimes required at graphic

workstations to construct accurate acceleration–time functions. The difficulty depended on the quality of the film accelerogram and the amplitude of the records. High-amplitude records with acceleration traces that repeatedly crossed traces from adjacent channels were particularly difficult.

A system like that of Trifunac and Lee has been used for many years at the California Strong Motion Instrumentation Program of the California Geological Survey (formerly the Div. of Mines and Geology) to digitize and process many records. As part of that effort, the system was further studied in terms of noise and long period response and certain improvements made to lower noise levels (Shakal and Ragsdale, 1984).

Another computer digitization system used during this time was a specialized commercial laser scanning and curve-following system that had some of the same difficulties and benefits (IOM/Towill; described in Converse, 1984). Many records were digitized by the U.S. Geological Survey through this company. Scanning systems were also developed in Japan (Iai *et al*., 1978) and Italy (Berardi *et al*., 1991) during this period.

3.2 PC-Based Desktop Digitization

As personal computers became more widespread and more powerful, it became practical to use them in strong-motion processing. In addition, development of scanning devices continued and economical desktop units became available that had marginally adequate resolution for use in accelerogram digitization. The first system of this type was developed by Lee and Trifunac (1990), for which they converted their earlier operator-intensive mainframe system (Trifunac and Lee, 1979) to use a desktop scanner and PC.

Another strategy was to take a fresh approach using the full capacity of a PC and the higher resolution desktop scanners that become available around 1990. Cao *et al*. (1994) describe a high-resolution desktop system that is almost fully automated except for the most difficult records. Many records have now been digitized using this system, including over 200 Northridge records from privately owned code-required instruments, which produced film records of lower optical quality than regular network records.

Other PC-based digitization systems have also been developed, but some have higher noise levels either because of inadequate step size or because the trace is approximated as a black-and-white image. The subtleties that gray-scale imaging allows yield results that more smoothly match the accelerogram. Of course quality must be carefully monitored, and some of these systems have encountered problems, as noted by Trifunac *et al*. (1998).

3.3 Digital Accelerographs

A transition in the 1980s significantly changed the strong-motion digitization and processing problem. As technology progressed, economical and reliable digitally recording accelerographs became available. For these units the onerous laboratory task of digitizing the recording is performed in the field by an internal analog-to-digital converter. The earliest digital accelerographs recorded data on magnetic tape but these did not approach the reliability of analog units (due to the effects of temperature cycling and aging, the magnetic tapes were often difficult, if not impossible, to decode). With the introduction of solid-state memory, the potential of digital accelerographs was fully realized. These units have now begun to be the source of new strong-motion records, and are supplanting analog accelerographs, worldwide.

Most accelerograms recorded by modern digital accelerographs are of high quality, so that processing of records is much less difficult. Certain serious problems can occur, however, and these are discussed subsequently. Excepting these cases, the traditional issues of base-line correction and high-frequency problems are often not as serious today. Recovering the maximum amount of information at long periods is still a challenge, as discussed further shortly. For most cases, however, the period band of most importance in earthquake engineering, up to 3 or 4 seconds, can be provided with confidence from digital accelerographs.

3.3.1 Accelerograph Dynamic Range and Noise Levels

The range of ground-motion amplitudes that can be recorded by an accelerograph is very important in controlling final processed signal quality and long-period noise levels. The largest acceleration that common analog accelerographs can record is nominally $1g$, and the smallest value that can be read from a film record is about $0.005g$. The ratio of the largest to smallest accelerations, the dynamic range, is about 200, or in the logarithmic decibel scale, about 50 dB. Recordings have shown that accelerographs need to be able to record accelerations as high as $2g$. Until about 1995, common digital accelerographs had a 12-bit analog-to-digital converter (A/D), so the smallest value they could record was the range of $\pm 2g$ divided into $2^{12} = 4096$ parts, or about $0.001g$. The dynamic range of these units, 72 dB, is significantly better than the analog film recorders. A few digital accelerographs currently use a 10-bit A/D. The dynamic range of these units is not much better than the analog units; although they have value in simple monitoring and alarm systems, noise levels make it very difficult to obtain processed data with quality similar to that of 12-bit accelerographs.

Most contemporary digital accelerographs have 18-bit or better resolution. For 18 bits, the least acceleration readable from a $2g$ sensor is about $\pm 2g/2^{18} = 0.015$ mg (108 dB dynamic range). The noise level at many urban sites where strong-motion instruments are installed is higher than 0.015 mg, so this resolution may be more than needed at these sites. The Northridge earthquake showed again that accelerations during earthquake shaking could exceed $2g$, at least in the near-field zone and in structures. Sensors with the next higher range, $4g$, are generally not more costly and the impact of raising the maximum

(increasing the minimum recordable motion to 0.03 mg) has little negative effect at urban sites because of the noise level. This range yields a record unlikely to be clipped and with resolution low enough for performing accurate processing of the recorded accelerogram. It is noted that some accelerographs now have 24-bit A/D capability. These units, with a minimum recordable motion of 0.24 μg with a 2g sensor, have their most effective application in low-noise, non-urban environments.

Digital accelerographs have advanced so much in the last decade that the importance of the recorder itself has receded for strong-motion processing, and other noise sources have become the major concerns. The primary noise sources that may compromise processed strong-motion data include sensor noise and electronic/communication noise, discussed further following.

4. Strong-Motion Processing Procedures

Whether a digital record has been recorded digitally or obtained through laboratory digitization of an analog record, procedures for processing the digital record are similar, and are described next.

4.1 Uniform Processing—Long-Period Filtering Dependent on Noise Spectra

A major lesson of the Caltech project was that the calculation of displacements for long periods was problematic. This problem was noted by Neumann (1943), but it became particularly important as more records were processed. Certain specific long-period problems were identified, for example, a problem at a spectral period near 14 seconds due to the practical aspect of digitizing table length (e.g., Hanks, 1973). More experience with the long-period problem was gained in the Caltech project, and during this period the method of choosing the most appropriate long-period filter was not yet standardized.

A realization developed that displacements computed for the longest periods were heavily influenced by noise intrinsic to the digitization and processing steps, and that this noise was largely understandable and could be handled in a uniform way (e.g., Trifunac, 1977). In general, the velocity response spectrum for records from intermediate-magnitude events increases from a low value at short periods until it reaches a maximum at intermediate periods, beyond which it decreases once again at longer periods. In contrast, the noise spectrum obtained by digitizing and processing a straight-line record increases in the long-period range, where the data spectrum is decreasing. As a result, the spectrum of a digitized accelerogram plotted against period, before filtering, often has a characteristic shape, which is shown schematically in Figure 2. The noise spectrum is present for both analog and digital records, though it is generally higher for optically digitized analog records than for records from digital recorders.

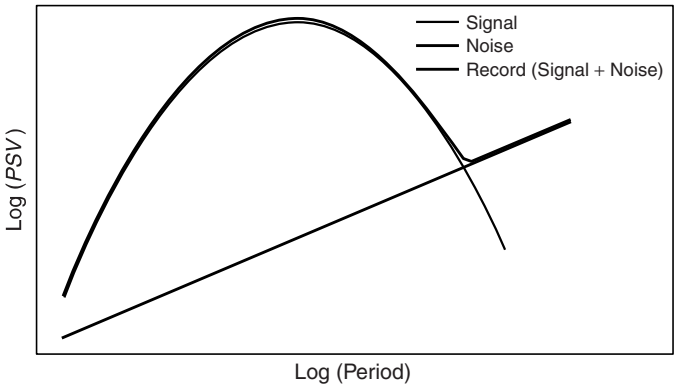

FIGURE 2 Schematic shape of the response spectrum of a typical digitized earthquake record (solid line). It is a combination of the actual earthquake spectrum (thin dash) and the noise from digitization and other sources (wide dash). The objective in data processing is to determine the maximum period band for which the final result preserves as much signal as possible but retains as little noise as possible.

The principle of uniform processing is the utilization of this characteristic form as the basis for selecting the filter period. This approach was introduced in the reprocessing of the Caltech records by Trifunac and Lee (1978). They selected the long-period filter location uniformly based on where the accelerogram spectrum intersected the average spectrum obtained for a set of straight-line accelerograms (e.g., Figure 2). This was an important step in handling long-period noise in a coherent manner.

This approach coincides with signal-to-noise ratio approaches used in signal processing and is used by several strong-motion networks. A signal-to-noise ratio (SNR) of 2 to 3 may be used to obtain an initial estimate of the filter period. Specifically, a period is chosen to the left (toward shorter periods) of the minimum that occurs where the signal and noise spectra intersect. A period is then selected at which the spectrum has increased to 2–3 times the minimum.

A practical aspect remaining, even in uniform processing, is the choice of a single filter corner for all components of a given record. This means that some components (e.g., horizontal) are filtered more severely because the filter is set to control noise in the components with the lowest amplitudes (e.g., vertical). This practice continues at many networks, though the practice is arguable.

4.2 Procedural Steps in Strong-Motion Processing

The post-digitization processing procedures and steps described next have their origin in the procedures developed in the Caltech project (EERL, 1969, 1971, 1972) and modified by Trifunac and Lee (1978) and others. There are variations in the steps, and Converse and Brady (1992) use a procedure that is somewhat

simpler, but the basic principles are shared in common. The seven steps are:

Step 1. Baseline Correction

The raw data are interpolated to obtain equal-interval sampling, if necessary (e.g., 200 points/sec, for a 100 Hz folding frequency), and converted to acceleration units using the sensitivity constant of the accelerometer. At least a first-order baseline operation is performed, to make the data zero-mean. More involved baseline correction may also be performed on certain records, though this is less common in the past, because there is normally no physical basis for removing a parabola or other high-level function from an accelerogram. In contrast, when baseline correction is performed via long-period filtering (Step 4) it has well-defined properties in the frequency domain; these are largely independent of the record length (e.g., Trifunac, 1971). Simple baseline correction using a constant or linear trend, where appropriate, is most effective in projects handling a large number of records. The results of this step are usually denoted as Volume (or Phase) 1, and released as the raw-data product.

Step 2. Instrument Correction

The baseline corrected data are corrected for instrument response using a simple finite-difference operator to obtain $\mathrm{d}y(t)/\mathrm{d}t$ and $\mathrm{d}^2y(t)/\mathrm{d}t^2$ in Equation (1). Note that the sensitivity constant has already been applied in Step 1. In frequency domain processing, discussed further following, the finite-difference process is replaced by simply dividing the spectrum by the instrument response spectrum.

Step 3. High-Frequency Filtering

After instrument correction, a filter is generally applied to remove high-frequency noise. In the Caltech and USC processing, an Ormsby filter (Ormsby, 1961) with a corner frequency at 23 Hz and a termination frequency at 25 Hz was applied. Current approaches typically use a more common filter (such as a Butterworth filter) with a corner frequency near 40% of the final sampling frequency (i.e., 80% of the Nyquist frequency) and a 3rd or 4th order decay. After filtering, the data are decimated to the final sample rate at which the acceleration data will be distributed to the user community (50 points/sec in the Caltech/USC data; 100 points/sec is common today for data recorded digitally). Note that if time-domain processing is used, the instrument correction should be performed prior to decimation, rather than after, in order to improve the high-frequency accuracy (Sunder and Connor, 1982; Shakal and Ragsdale, 1984). Some networks currently release processed data with the same sample rate as the original data; in this case, decimation is not performed.

Step 4. Initial Integration and Long-Period Filtering

An initial long-period filter is applied to the instrument-corrected acceleration data with a cutoff corner near 15 seconds period (longer periods are filtered out), which is the maximum period used in Caltech/USC processing. Recent data has shown that a longer period cutoff may be appropriate for digital records from large earthquakes. Velocity and displacement are obtained by numerically integrating the acceleration and filtered using the same low-frequency filter. In time-domain processing, if decimation is performed prior to the long-period filtering, prevention of spurious long-period energy requires use of an Ormsby or similar filter, rather than a running mean filter, because of its side-lobe leakage (Shakal and Ragsdale, 1984).

Step 5. Computation of Maximum-Bandwidth Response Spectra

The pseudovelocity (*PSV*) response spectra are calculated in the time domain for the full set of 91 periods defined in the Caltech project, ranging from 0.04 seconds to 15 seconds, using the method of Nigam and Jennings (1969) or an equivalent. The spectra are computed for damping values of 0, 2, 5, 10, and 20% of critical, using the acceleration obtained in Step 4, and plotted for 0.04 to 15 seconds (the full bandwidth) for use in comparative analyses to select the best filter.

Step 6. Long-Period Filter Selection

A suite of long-period filters is applied to the data obtained in Step 3 using corner periods near the long-period minimum of the spectrum obtained in Step 5. The long-period intersection of the maximum-bandwidth spectrum and the average noise spectrum determined for the system (e.g., Trifunac, 1977; Shakal and Ragsdale, 1984) is used to indicate the long-period limit of useful information in the record, as discussed previously. The final value of the filter corner is selected after studying the resulting suite of displacement plots, comparing them to one another, to displacement plots computed from noise records, and to records obtained for nearby stations, if available (e.g., Huang *et al*., 1989). Choosing a filter period at which the signal-to-noise ratio (SNR) is 2 to 3 or greater usually gives a result with low noise, though this may be more conservative than some desire.

Selection of the optimal long-period filter remains the most difficult part of strong-motion processing. The effect of earthquake magnitude is to raise the response spectrum at long periods, such that the crossing with the noise spectrum may not occur in the usual strong-motion processing band. An approach has been suggested in which the long-period filter is selected based on a theoretical model of the spectrum radiated by a simplified source (e.g., Basili and Brady, 1978). However, as more data have become available, especially from larger events, it appears best to choose the long-period filter based on the signal

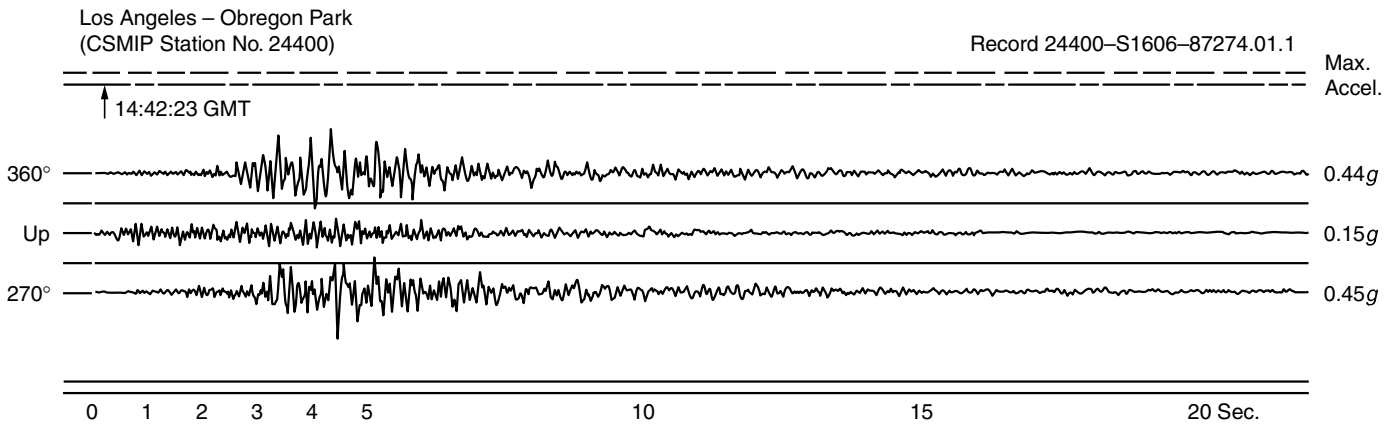

FIGURE 3 Copy of the analog (film) record obtained from the Obregon Park station in Los Angeles during the 1987 Whittier earthquake.

as recorded, regardless of theoretical models, especially since theoretical models will be revised as more data from large earthquakes becomes available.

Step 7. Final Output Preparations

The acceleration, velocity, and displacement time histories obtained using the final filter are plotted for presentation in reports and saved as files for distribution. The response spectra may be plotted with tripartite logarithmic scaling or the linear scaling most commonly used in building codes.

4.3 Illustrative Example

To illustrate the process just described, a copy of a raw accelerogram is shown in Figure 3. This analog record contains three acceleration traces corresponding to the three component directions, two fixed reference traces, a half-second time mark pattern at the bottom, and a time mark trace containing the IRIG-encoded time at the top. This record was digitized (not necessary for a digital record) and scaled to produce the Vol. 1 (Phase 1) data plotted in Figure 4. Steps 2 through 4 were then performed, and the full-bandwidth spectrum of Step 5 was computed. For the first component, the velocity spectrum of the full-bandwidth output is compared with the noise spectrum of the digitization system in Figure 5. As part of Step 6, a suite of displacement time histories, computed using a range of long-period filter corners, are compared in Figure 6 to guide the selection of the optimal filter. The final "corrected" acceleration, velocity, and displacement (Phase 2 data), and response spectra (Phase 3 data) of Step 7 are shown in Figures 7 and 8, respectively. Note that the final filter bandwidth is indicated in both plots.

4.4 Usable Data Bandwidth

Processed data has a bandwidth, extending from the period of the high-frequency (short-period) filter of Step 3 to the long-period filter of Step 6, within which the final spectrum corresponds to the original record. Outside of this band, filters have removed as much as possible of the information because of noise contamination, and this band may be called the Usable Data Bandwidth (Figure 9). The UDB defines the range within which the results can be used in modeling structure response, etc. Comparisons of model results to data outside this period band are not valid, of course, and may be misleading. Note that the spectra of the final result in Step 7 should only be plotted to the period of the long-period filter—beyond that the spectra are smoothly decreasing, but this is because of the asymptotic nature of the response spectrum at long periods (e.g., Hudson, 1979), and does not reflect the shape of the data spectrum.

4.5 Time Domain vs. Frequency Domain

Some operations in strong-motion processing may be most effectively performed in the frequency domain. The early Caltech processing was all performed in the time domain because it occurred before the Fast Fourier Transform (Cooley and Tukey, 1965) was widely available. The Ormsby filter was used because it is a relatively stable recursive filter. Today the FFT is very common, and filters such as the Butterworth are easily applied in the frequency domain, and integration to obtain velocity and displacement is as simple as dividing the spectrum by $-i\omega$. With fast computers and cheap memory, even the large transforms that may be needed are within the capacity of most personal computers.

Care must be taken in frequency-domain processing regarding certain aspects. Tapering the ends of the acceleration time series with a raised cosine bell, or Tukey interim window (e.g., Bergland, 1969), once the mean has been removed, prevents spurious side-lobe leakage in the spectrum. If there is an adequate pre-event data segment, this does not affect the data at the beginning of the data. In general, the time-history length to be transformed to the frequency domain must have a power-of-two

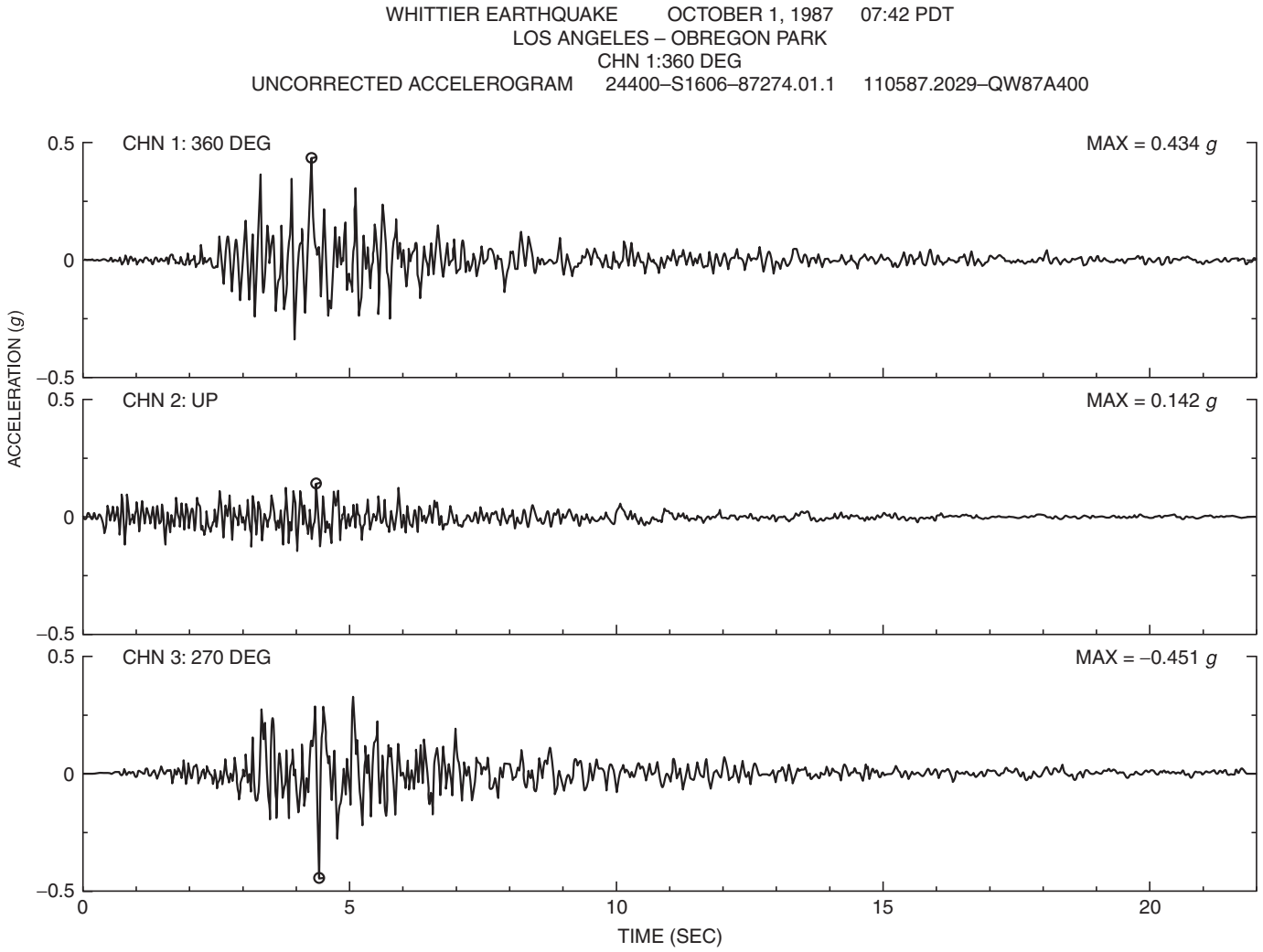

FIGURE 4 Acceleration records (Phase 1 data) after the data traces in the film record of Figure 3 have been digitized and converted to acceleration using the sensitivity constants of the accelerometers, and the means have been removed (Step 1).

number of points, and a zero-filled section should be included at the end of adequate length (perhaps 20% of the record length or more) to prevent problems with periodicity.

Some operations, such as complex baseline corrections, may be most effectively done in the time domain. For example, if there is an a priori reason that certain time functions should be used to compensate for a baseline shift that occurs at a certain time in an accelerogram (e.g., Iwan *et al*., 1985), a time domain application is most effective.

In general, frequency domain methods are fast, understandable, stable, and give replicatable results in situations where many records are to be processed. They are also well understood in signal analysis and processing theory (e.g., Rabiner and Gold, 1975; Kanasewich, 1973). Response spectra calculations need to be at least evaluated in the time domain because they involve obtaining the time-domain maximum for each spectral period.

4.6 Processing by Other Networks in the World

Several networks in countries of Europe and the Pacific also process and release strong-motion data. For example, the Port and Harbor Research Institute in Japan has been processing and releasing data for many years using a system described by Iai *et al*. (1978) that shares many features of the approach developed in the Caltech project. They also use a semi-automated analog record digitization system for analog records. Of course, the recently instrumented Kyoshin network in Japan is a forward evolution with no analog instruments, like the TriNet network in the United States, both described elsewhere in this volume.

The New Zealand and Italian strong-motion networks have also digitized and released records from important events in the area, and key parts of their processing are also similar to, and grew out of, the Caltech system (e.g., Hodder, 1983; Berardi *et al*., 1991).

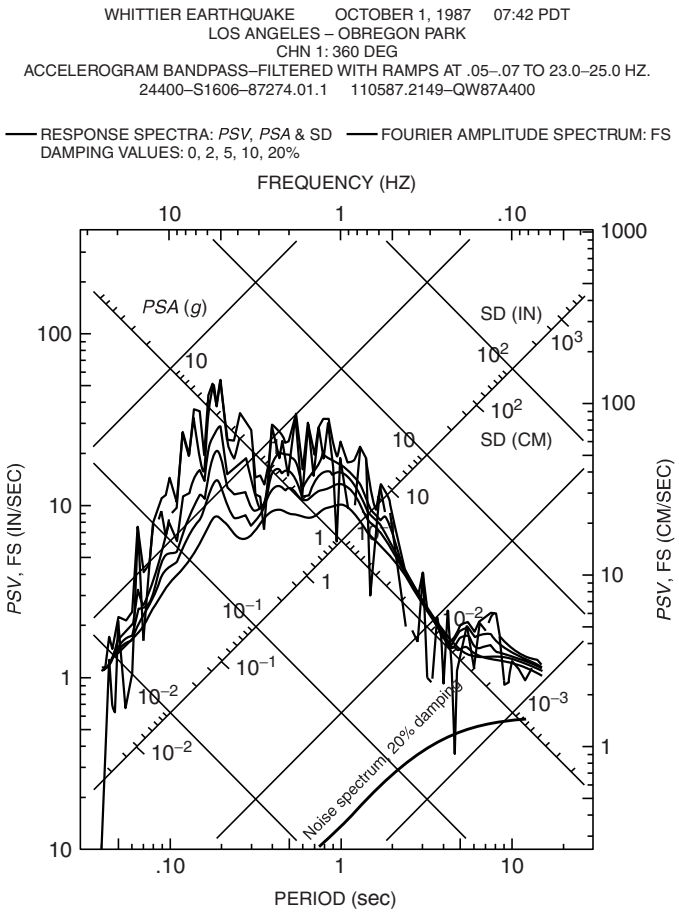

FIGURE 5 Spectrum computed (with a wide-bandwidth filter) for the first component of the record in Figure 4 is compared with the noise-level spectrum (*PSV*, 20% damping) of the digitization system to guide the selection of the long-period filter.

5. Specific Issues in Processing

Several issues are of particular importance in strong-motion processing. Some, such as natural frequency, have seen beneficial developments. Others, including DC offsets, can be as problematic today as they were years ago.

5.1 Instrument Response—Accelerometer Natural Frequency

Changes in accelerometer natural frequency over the last decades have had significant positive impacts on strong-motion processing. The earliest USCGS accelerometers of 1933 had a natural frequency of about 10 Hz (0.1 sec period); this increased to around 20 Hz with the commercial film recorders (e.g., SMA-1). The natural frequency increased again to 50 Hz for accelerometers used with the digital recorders. Some of the latest sensors have a natural frequency near 80 Hz.

The result of this increase in natural frequency is to make correction for the response of the sensor much less critical in the frequency range below 20 Hz, which is of most importance in strong motion. As the sensor natural frequency increases, the last term in the response equation (Eq. 1) dominates. The principal effect of instrument correction then becomes multiplication of the observed record by the static sensitivity. As a result, instrument correction has become much less critical than in the earlier years of strong-motion processing, when the natural frequency was 10 to 20 Hz, and errors in natural frequency or damping could significantly affect the results.

5.2 Accelerometer Offsets and Tilts

Calculated long-period displacements are very sensitive to the stability of the DC or zero level of the accelerometer. Small errors in the zero level can lead to significant errors in displacements and long-period spectrum levels. This problem is more important for modern digital recorders, largely because more information is being extracted from records due to their greater dynamic range. An illustrative example occurred in the Northridge earthquake records from a six-story office building in Los Angeles (Station 24652; Shakal *et al*., 1994a, p. 153). The recording indicates that a shift of several percent *g* occurred around the time of the strongest shaking, implying a significant permanent tilt or adjustment at the 3rd-floor level of the building. However, the building was subsequently inspected and no structural changes were observed. Routine processing of a record like this would indicate significant results for velocity and especially displacement level, as well as spectral levels at long periods. In this case, the source of the implied structural change was actually a change in the zero of the sensor.

The ability of sensors to move to a new zero value during or after strong, or even weak, motion is an important caution to bear in mind in strong-motion processing. This phenomenon had been observed before, though never with such implications. For example, Iwan *et al*. (1985) described this in laboratory tests and proposed a numerical approach to correct for this effect. This behavior was also observed in early small-amplitude field recordings, especially in the early digital accelerographs that recorded on magnetic tape. It has also been observed in the records from other arrays and instrument types, such as those from the SMART array in Taiwan, and most recently the 1999 Taiwan earthquake (W. H. K. Lee, personal communication, 1999).

Correction for a changing zero level remains problematic, because it requires an assumption of the nature and timing of any changes. If the change can be approximated by a simple step, it is easy to introduce a correction in the processing. If a change can be approximated as a constant during an interval of unknown duration, followed by a new constant value, an approach suggested by Iwan *et al*. (1985) can be used. However, if the change occurs over a period of time as a ramp, curve, oscillatory function, or a series of steps (as slippage in the sensor might cause), the appropriate correction function is uncertain. Boore (2001) applied the Iwan approach in working with certain Taiwan earthquake data and found varying results.

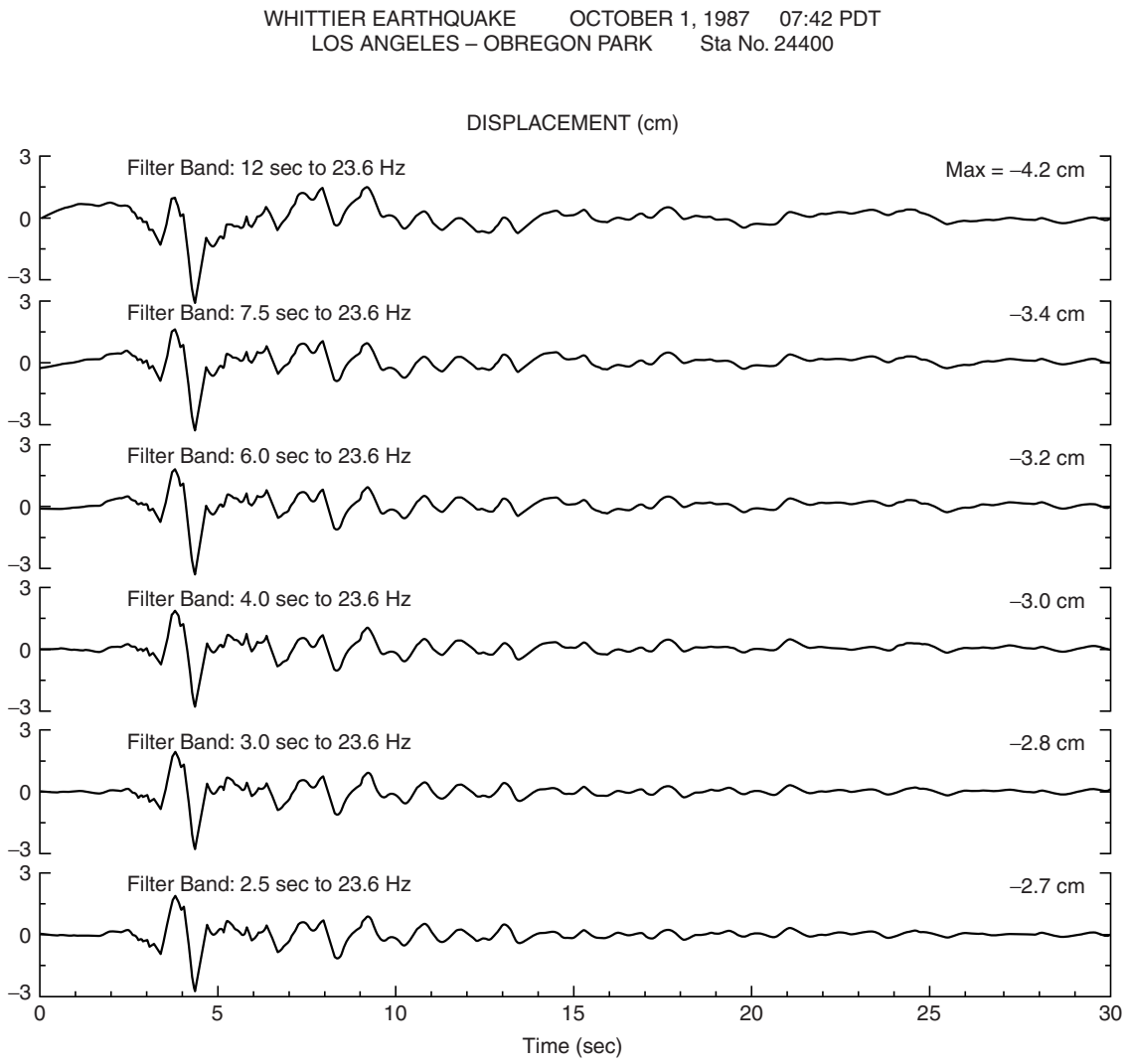

FIGURE 6 Displacement plots for the first component in Figure 4 processed with a suite of long-period filters. These plots are compared with each other, and the corresponding spectra are compared with the noise spectra in Figure 5, to select the long-period filter. The wandering of the uppermost trace is clearly due to noise, corresponding to the long-period noise in Figure 5. In contrast, very little noise is apparent in the bottom trace, also reflected in Figure 5 near 2 seconds, where the signal is well above the noise. In this case, the filter with a 3-second corner period (corresponding to a 0.2 to 0.4 Hz ramp) was selected (Huang *et al.*, 1989).

Of course, a zero-level change due to an actual tilt of the instrument is indistinguishable in a record from a sensor zero-offset problem. For example, the Pacoima Dam upper left abutment record in the Northridge earthquake showed offsets found in processing that were able to be substantiated in the field as actual tilts (Shakal *et al.*, 1994b).

In summary, zero-level offsets or tilts remain an important difficulty in strong-motion processing, especially in the recovery of the longest period motions. However, in the period band of most importance in engineering, this effect is not as important as it is in seismological source model research. For example, Shakal *et al.* (1994b) found little effects at periods less than 10 seconds, and Boore (2001) found no important effects below 20 seconds in the examples he studied.

5.3 Determination of Permanent Displacement

Permanent displacement is generally not important in earthquake engineering unless a structure straddles a fault. However, it is of scientific interest, and can help constrain the longest-period part of the source spectrum. The determination of permanent displacement has been attempted from the earliest tests (Neumann, 1943), and it has been fraught with controversy. In some cases it is possible to make estimates of the

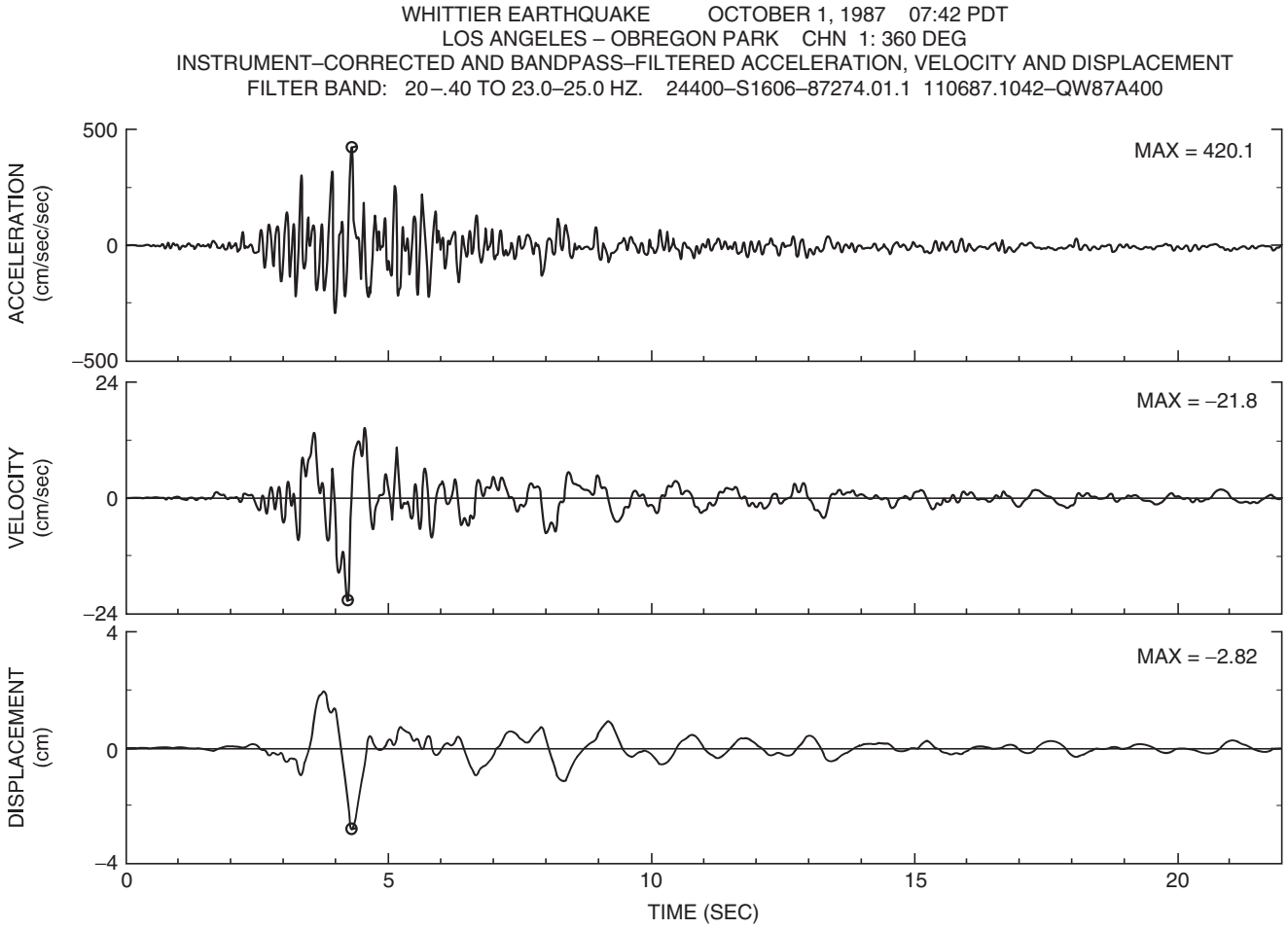

FIGURE 7 Instrument and baseline-corrected acceleration, velocity, and displacement (Phase 2 data) for the first component of the record in Figure 4. The filter bandwidth selected during the processing and analysis is indicated on the plot.

permanent displacement, but in general independent knowledge of the actual ground displacement is important to guide the calculations. One example is the record from the Lucerne station in the 1992 Landers earthquake (Hawkins *et al*., 1993), from which Iwan and Chen (1994) estimated permanent displacements, and several possibilities occur in the data from the Taiwan earthquake of September 21, 1999, and the Hector Mine, California, earthquake of October 16, 1999. The potential presence of baseline offsets in the accelerogram challenge the determination of permanent displacements, though several analytic means have been suggested (e.g., Graizer, 1979; Iwan *et al*., 1985).

In summary, except for records from sites at which the permanent displacement during an earthquake was relatively large, the determination of permanent displacements from acceleration records may not generally be practical, largely because of sensor limitations. Though this is an important scientific issue, it is not critical for most earthquake engineering applications.

5.4 Cross-Axis Sensitivity and Channel Cross Talk

A concern of long standing in strong motion is the sensitivity of an accelerometer to motion perpendicular to its sensing direction (e.g., Skinner and Stephenson, 1973; Wong and Trifunac, 1977). Mechanical limits in manufacturing and mechanical coupling effects limit how small this effect can be; common technical specifications list 3% or less. If a cross-axis signal is as large as this, it can be a significant noise (i.e., false signal) source. In general, it should be held to significantly less than this, and this and other aspects should be verified by static tilt tests (e.g., Lee, 1993) or other means.

In structural or geotechnical array configurations, where sensors may be located remotely from recorders, channel-to-channel electronic signal leaking, or cross talk, can be as important as, and indistinguishable from, cross-axis sensitivity of sensors. Cross talk must be prevented, before an earthquake, through signal tests and static tilt tests of individual sensors. Data analysis

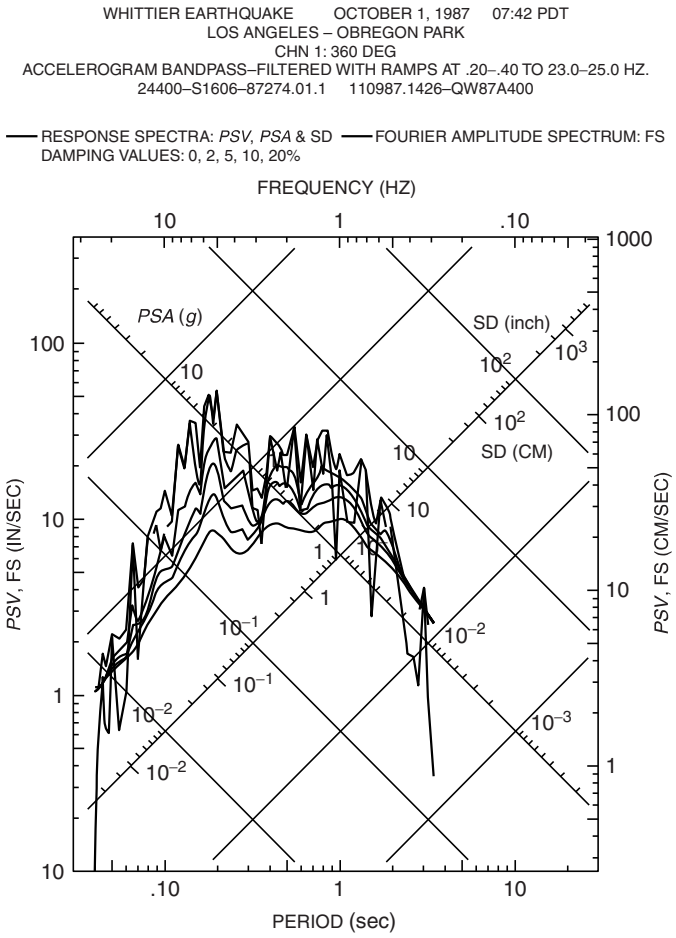

FIGURE 8 Response spectra (Phase 3 data) for the first component of the record in Figure 4. The spectra are plotted for periods within the filter bandwidth determined in the Phase 2 processing.

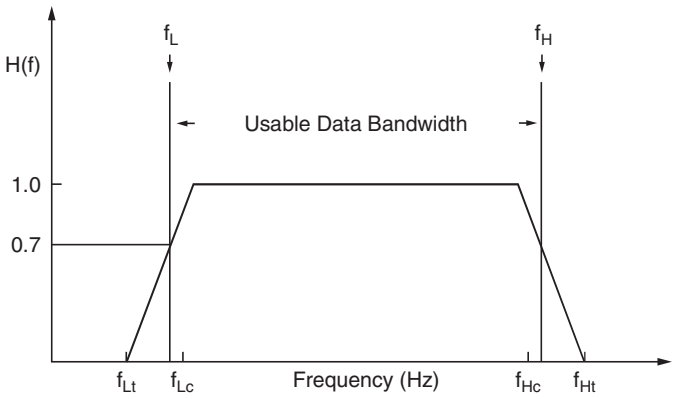

FIGURE 9 The "Usable Data Bandwidth" for a processed strong-motion record is the band between frequencies f_H and f_L, the high and low −3 dB corner frequencies. The data contains little useful information for analyses or modeling outside this band. The amplitude of the filter transfer function H(f) is reduced to approximately 0.7 at −3 dB and the transmitted power is reduced to 0.5. [The 3 dB corners are well defined for filters like the Butterworth. For Ormsby filters, they can be determined from the ramp corner (f_{Hc}, f_{Lc}) and termination frequencies (f_{Ht}, f_{Lt}) using $f_H = f_{Hc} + 0.3(f_{Ht} - f_{Hc})$ and $f_L = f_{Lc} - 0.3(f_{Lc} - f_{Lt})$. For example, the UDB for data filtered with Ormsby ramps from 0.3 to 0.6 Hz and 23 to 25 Hz is 0.51 Hz to 23.6 Hz, or 0.042 to 2.0 seconds period.]

methods such as cross correlation and coherency are commonly used to study and characterize earthquake motion. Even low cross-axis sensitivity or channel cross talk will significantly contaminate these estimates.

5.5 Processing High-Amplitude Records

One continuing lesson of strong-motion recording in the last half of the century is that the largest recorded accelerations have continued to exceed expectations. These range from about 1.25*g* in the San Fernando earthquake of 1971 to nearly 2*g* in the 1994 Northridge earthquake. Some of these peak acceleration values are not of engineering significance because they are of short duration.

For strong-motion processing purposes the key issue is that the motion occurring be recorded and processed correctly. Recent data show that instruments need to be capable of recording more than 1*g* on the ground and 2*g* in certain structures. (Nearly all of the analog film recorders, and even some of the digital recorders, are not capable of that.) Assumptions are necessary to process any record that exceeds the instrument maximum, even for a short time. These assumptions, which can be challenged, can taint the perception of users regarding the quality of processing for the many other high-quality, lower amplitude records. The most effective way to manage this problem is to field instruments with adequate recording range at the outset.

5.6 Electronic Noise Issues

As technological equipment becomes more widespread in the environment it can present a challenge for strong-motion accelerograph stations, especially in urban situations. It has been observed that some strong-motion sensors are susceptible to the effects of radio frequency (RF) electromagnetic radiation. This can cause false or phantom events, or distortion during the recording of actual events. In most cases, the nature of RF-caused records has allowed them to be recognizable, and the occurrence of the events can be decreased with good field practices. Recent years have seen an increasing amount of RF transmission, and it may be expected that this problem will increase as communication channels continue to expand.

6. Automatic Preliminary Processing

> "Civilization advances by extending the number of operations which we can perform without thinking about them. . . ."
>
> A. N. Whitehead

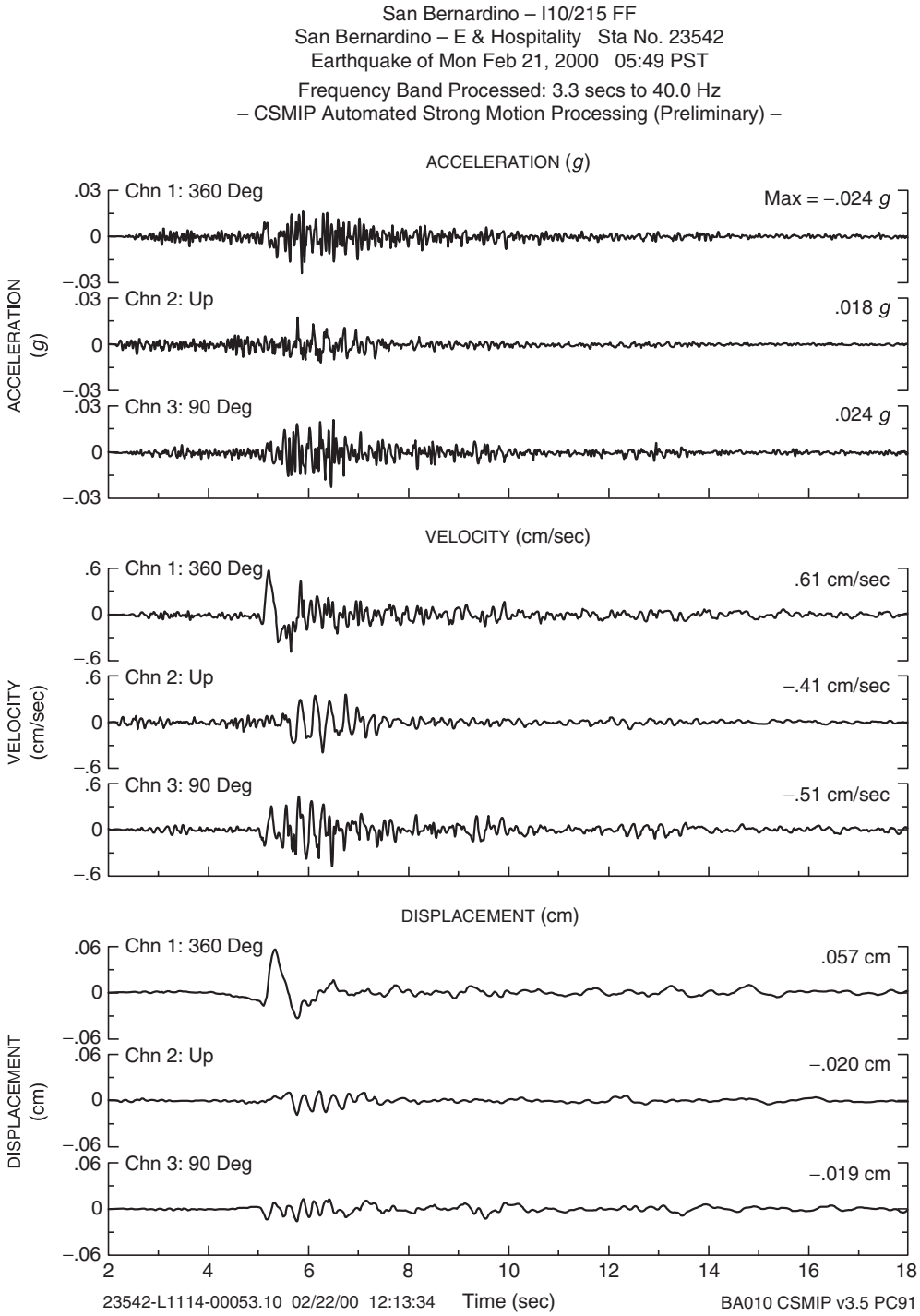

FIGURE 10 Automatic preliminary processing results—three components of acceleration, velocity, and displacement at San Bernardino from a M4.4 earthquake that occurred on February 21, 2000.

Advances in recording technology have opened the possibility of automated preliminary processing, and initial steps in this direction show promise for the future (e.g., Figure 10). Automated processing will never approach the quality level that human analysis can yield, but the rapid results obtained are useful if treated as preliminary. To get the best possible results, the preliminary processing must be followed up by professional analysis of noise levels and possible filter settings, just as has been performed for years in strong-motion processing.

A recent development that has opened new possibilities in rapid use of strong-motion recordings is communication with recorders at remote sites via telephone lines and modems.

With additional control at the field sites, it is possible to go to the next step of having field instruments initiate communication with a central site upon recording an event, and transmitting the recorded data. This has been done successfully for several years in the California Strong Motion Instrumentation Program (Shakal *et al*., 1995) and the U.S. Bureau of Reclamation (Viksne *et al*., 1995) and recently in the U.S. Geological Survey and other networks. This approach has shown such promise that accelerograph manufacturers have begun to include the necessary auxiliary field components within the accelerograph itself.

For automated, preliminary processing, a process similar to that described above may be used. For all but large-earthquake records, a long-period filter near 3 or 4 seconds can be used as a reasonable first estimate. Because sensors have a high natural frequency, as noted, an approximate instrument correction as simple as multiplication by a sensitivity factor can often be used with little penalty. Of course, this preliminary processing must be augmented by careful processing and filter selection by analysts at a later time to obtain optimal quality results.

7. Summary

The processing of strong-motion recordings has undergone great progress from the first recording in 1933 through the modern instruments available at the end of the century. Processing went from tedious, manual calculations to almost completely computerized processing. Some problems and issues associated with sensors, offsets and tilts, and electronics remain, despite the great progress. However, these problems are relatively small. The evolution of automated strong-motion processing in the 1990s will make strong-motion data increasingly useful for emergency response and rapid post-earthquake investigation of damage as well as for long-term research.

References

Basili, M., and A. G. Brady (1978). Low frequency filtering and the selection of limits for accelerogram corrections. *Proc. Sixth European Conf. on Earthq. Engineering*, Yugoslavia.

Berardi, R., G. Longhi, and D. Rinaldis (1991). Qualification of the European strong-motion databank: influence of the accelerometric station response and pre-processing techniques. *J. European Earthquake Engineering* **2**, 38–53.

Berg, G. V., and G. W. Housner (1961). Integrated velocity and displacement of strong earthquake ground motion. *Bull. Seism. Soc. Amer*. **51**, 175–189.

Bergland, G. D. (1969). A guided tour of the fast Fourier transform. *IEEE Spectrum* **6**, 51–52. In: "Digital Signal Processing" (L. R. Rabiner and C. M. Rader, Eds.), IEE Press, New York.

Boore, D. M. (2001). Effect of baseline corrections on response spectra for several recordings of the 1999 Chi-Chi, Taiwan, earthquake. *Bull. Seismol. Soc. Am.* **91**, 1199–1211.

Brady, A., V. Perez, and P. Mork (1980). The Imperial Valley earthquake, October 15, 1979, Digitization and processing of accelerograph records. *US Geol. Surv. Open-File Report 80-703*, Menlo Park.

Cao, T. Q., R. Darragh, and A. Shakal (1994). Digitization of strong motion accelerograms using a personal computer and flatbed scanner (abstract). *Seismol. Res. Lett.* **65**(1), 42.

Converse, A. (1984). AGRAM: a series of computer programs for processing digitized strong-motion accelerograms. *Open-File Report 84-525, U.S. Geological Survey*, Menlo Park.

Converse, A., and A. G. Brady (1992). BAP: basic strong motion accelerogram processing software. *Open-File Report, 92-296A, U.S. Geological Survey*, Menlo Park.

Cooley, J. W., and J. W. Tukey (1965). An algorithm for the machine calculation of complex Fourier series. *Math. Computation* **19**, 297–301.

Duke, C. M., and D. J. Leeds (1959). Soil conditions and damage in the Mexico earthquake of July 28, 1957. *Bull. Seismol. Soc. Amer*. **49**, 179–191.

Earthquake Engineering Research Laboratory (1969). Strong motion earthquake accelerograms, digitized and plotted data, Vol. I – Uncorrected accelerograms; Part A, *EERL Report 70-20*, California Institute of Technology, Pasadena.

Earthquake Engineering Research Laboratory (1971). Strong motion earthquake accelerograms, digitized and plotted data, Vol. II – Corrected accelerograms and integrated ground velocity and displacement curves; Part A, *EERL Report 71-50*, California Institute of Technology, Pasadena.

Earthquake Engineering Research Laboratory (1972). Analysis of strong motion earthquake accelerograms, Vol. III – Response spectra; Part A, *EERL Report 72-80*, California Institute of Technology, Pasadena.

Graizer, V. M. (1979). Determination of true ground displacement by using strong motion records. *Izv. Acad. Sci. USSR* (translated by Amer. Geophys. Un.) **15**, 875–884.

Hanks, T. (1973). Current assessment of long-period errors. In: "Strong-motion Earthquake Accelerograms, Digitized and Plotted Data." *Vol. II, Earthquake Engineering Research Laboratory, EERL 73-52*, California Institute of Technology, Pasadena.

Hawkins, H. G., D. K. Ostrom, and T. A. Kelley (1993). Comparison of strong motion records, Landers earthquake 28 June 1992, near Lucerne Valley, California. *Unpublished manuscript.*

Hershberger, J. (1955). Recent developments in strong motion analysis. *Bull. Seismol. Soc. Amer*. **45**, 11–22.

Hodder, S. B. (1983). Computer processing of New Zealand strong-motion accelerograms. *Bull. New Zealand Nat. Soc. Earthq. Eng.* **16**(3), 234–245.

Huang, M. J., T. Q. Cao, D. L. Parke, and A. F. Shakal (1989). Processed strong-motion data from the Whittier, California earthquake of 1 October 1987. *Report OSMS 89-03*, Calif. *Strong Motion Instrumentation Program, Calif. Div. Mines and Geology, Sacramento.*

Hudson, D. E. (1979). *Reading and Interpreting Strong Motion Accelerograms*. Earthquake Engineering Research Institute, Berkeley.

Iai, S., E. Kurata, and H. Tsuchida (1978). Digitization and correction of strong-motion accelerograms. *Technical Note 286, Port and Harbor Research Institute*, Yokosuka, Japan, 286 pp.

Iwan, W. D., and X. D. Chen (1994). Important near-field ground motion data from the Landers earthquake. *Proc. 10th European Conf. Earthq. Eng.*, Vienna, Austria.

Iwan, W. D., M. A. Moser, and C.-Y. Peng (1985). Some observations on strong-motion earthquake measurement using a digital accelerograph. *Bull. Seismol. Soc. Am.* **75**, 1225–1246.

Kanasewich, E. R. (1973). *Time Sequence Analysis in Geophysics*. Univ. Alberta Press, Canada, 352 pp.

Lee, V. W., and M. D. Trifunac (1979). Automatic digitization and processing of strong motion accelerograms, Part II: Computer processing of accelerograms. *Report CE 79-15 II*, Dept. Civil Engineering, Univ. Southern California, Los Angeles.

Lee, V. W., and M. D. Trifunac (1990). Automatic digitization and processing of accelerograms using PC. *Report CE 90-03*, Dept. Civil Engineering, Univ. Southern Calif. Los Angeles, 150 pp.

Lee, W. H. K. (1993). 1993 tilt test results. *Appendix 2 of the Central Weather Bureau Research Report No. 446*, Seismology Center, Central Weather Bureau, Taipei, Taiwan.

Neumann, F. (1943). An appraisal of numerical integration methods as applied to strong-motion data. *Bull. Seismol. Soc. Am.* **33**, 13–20.

Nigam, N. C., and P. C. Jennings (1969). Calculation of response spectra from strong-motion earthquake records. *Bull. Seismol. Soc. Am.* **59**, 909–922.

Ormsby, J. F. A. (1961). Design of numerical filters with application to missile data processing. *J. Assoc. Comput. Machinery* **8**, 440–466.

Rabiner, L. R., and B. Gold (1975). *Theory and Application of Digital Signal Processing*. Prentice Hall, New Jersey, 762 pp.

Ruge, A. C. (1943a). Analysis of accelerograms by means of the M.I.T. differential analyzer. *Bull. Seismol. Soc. Am.* **33**, 61–63.

Ruge, A. C. (1943b). Discussion of principal results from the engineering standpoint. *Bull. Seismol. Soc. Am.* **33**, 13–20.

Scott, S. (1997). "George W. Housner," *Connections, EERI Oral History Series No. 4*, Earthquake Engineering Research Institute, Oakland, CA, 275 pp.

Shakal, A. F., and J. T. Ragsdale (1984). Acceleration, velocity and displacement noise analysis for the CSMIP accelerogram digitization system. *Proc. 8th World Conf. Earthquake Engineering* **2**, 111–118.

Shakal, A., M. Huang, R. Darragh, T. Cao, R. Sherburne, P. Malhotra, C. Cramer, R. Sydnor, V. Graizer, G. Maldonado, C. Petersen, and J. Wampole (1994a). CSMIP strong-motion records from the Northridge, California earthquake of 17 January, 1994. *Calif. Strong Motion Instrumentation Program, Report 94-07*, Calif. Div. Mines and Geology, Sacramento, 308 pp.

Shakal, A., T. Cao, and R. Darragh (1994b). Processing of the upper left abutment record from Pacoima Dam for the Northridge earthquake. *Calif. Strong Motion Instrumentation Program, Report OSMS 94-13*, Calif. Div. Mines and Geology, Sacramento.

Shakal, A. F., C. D. Petersen, A. B. Cramlet, and R. B. Darragh (1995). CSMIP near-real-time strong motion monitoring system: Rapid data recovery and processing for event response. In: "Proceedings SMIP95 Seminar on Seismological and Engineering Implications of Recent Strong-Motion Data" (M. J. Huang, Ed.), pp. 1–10, Calif. Div. Mines and Geol., Sacramento.

Skinner, R. I., and W. R. Stephenson (1973). Accelerograph calibration and accelerogram correction. *Earthq. Eng. Struct. Dynamics* **2**, 71–86.

Sunder, S. S., and J. J. Connor (1982). A new procedure for processing strong-motion earthquake signals. *Bull. Seismol. Soc. Amer.* **72**, 643–661.

Trifunac, M. D. (1971). Zero baseline correction of strong-motion accelerograms. *Bull. Seismol. Soc. Amer.* **61**, 1201–1211.

Trifunac, M. D. (1977). Uniformly processed strong earthquake ground accelerations in the western United States of America for the period from 1933 to 1971: pseudo relative velocity spectra and processing noise. *Report CE 77-04*, Univ. Southern Calif., Los Angeles.

Trifunac, M. D., and V. Lee (1973). Routine computer processing of strong-motion accelerograms. *Earthquake Engineering Research Laboratory, Report EERL 73-03*, Pasadena.

Trifunac, M. D., and V. W. Lee (1974). A note on the accuracy of computed ground displacements from strong-motion accelerographs. *Bull. Seismol. Soc. Am.* **64**, 1209–1219.

Trifunac, M. D., and V. W. Lee (1978). Uniformly processed strong earthquake ground accelerations in the Western United States of America for the period from 1933 to 1971: corrected acceleration, velocity and displacement curves. *Report CE 78-01*, Dept. Civil Engineering, Univ. Southern California, Los Angeles.

Trifunac, M. D., and V. W. Lee (1979). Automatic digitization and processing of strong motion accelerograms, Part I: automatic Digitization. *Report CE 79-15 I, Dept. Civil Engineering*, Univ. Southern California, Los Angeles.

Trifunac, M. D., M. I. Todorovska, and V. W. Lee (1998). The Rinaldi strong motion accelerogram of the Northridge, California earthquake of 17 January 1994. *Earthquake Spectra* **14**, 225–240.

Viksne, A., C. Wood, and D. Copeland (1995). Seismic monitoring/ strong motion program and notification system. In: "Water Operation and Maintenance Bulletin," No. 171, pp. 161–168, Bureau of Reclamation, Denver.

Wenner, F. (1932). Development of seismological instruments at the Bureau of Standards. *Bull. Seismol. Soc. Am.* **22**, 60–67.

Wong, H. L., and M. D. Trifunac (1977). Effects of cross-axis sensitivity and misalignment on the response of mechanical-optical accelerographs. *Bull. Seismol. Soc. Am.* **67**, 929–956.

This Page Intentionally Left Blank

59

Estimation of Strong Seismic Ground Motions

Bruce A. Bolt
University of California, Berkeley, CA, USA
Norman A. Abrahamson
Pacific Gas and Electric Co., San Francisco, CA, USA

1. Special Problems of Strong-Motion Seismology

At the beginning of instrumental seismology, seismologists such as John Milne and his colleagues in Japan endeavored to design seismographs that could record both weak and strong wave motion from earthquakes (see Chapter 1 by Agnew; Bolt, 1996). As instrumental technology evolved, the paths of seismologists recording teleseisms and of those who were concerned with measuring large amplitude seismic waves near to an earthquake source diverged. By the 1960s, strong-motion seismometers for the latter purpose were largely the domain of earthquake engineers, while seismographic stations operated sensitive seismographs that could record waves of order micrometer amplitude from small local or distant earthquakes. (A 1 μm displacement of a 1 Hz frequency seismic wave from a teleseism corresponds to a ground acceleration of only about $4 \times 10^{-6} g$.) In more recent decades, the problem of wide dynamic seismograph range in both amplitude (about 180 dB) and frequency (about 6 decades) was solved with the advent of digital recording with 18 bits or greater (Bullen and Bolt, 1985; see also Chapter 18 by Wielandt). Consequently, modern seismographic stations in earthquake country are now able to record both weak and strong motions over a very large frequency band. As a rough guide we define strong ground motion as seismic waves with accelerations in excess of about $0.05 g$ to over $1 g$. Similar ranges are of order 10 to 200 centimeters per second in velocity, and 1 to 100 centimeters in displacement. Examples of large strong ground motions from crustal earthquakes are given in Table 1.

Seismologists working on strong ground motion have a number of goals that are not shared by those interpreting records from highly sensitive seismographs (e.g., Heaton *et al*., 1995; Vidale and Helmberger, 1987). They are concerned with accurate measurement of high-amplitude (even nonlinear) waves but are not concerned with microseisms. Strong-motion seismographs are often deliberately sited not only on hard rock (normal for sensitive instruments) but on soil of various types. Of particular interest is the progression of elastic wave motion from linear to nonlinear behavior (e.g., Darragh and Shakal, 1991); for example, in extreme cases as soil layers "liquefy." Finally, in order to understand the effect of soil variability, strong-motion instrumentation is needed throughout urban areas, both close to, and some distance from, engineered structures and across geological boundaries and topographic relief.

The preceding description makes clear that strong-motion seismology presents a number of specific scientific problems, many of which remain unsolved. For example, seismograms from teleseisms usually show a progression of different seismic phases, such as P, PP, SSS, ScS, PKP, surface-wave modes, etc. (e.g., see Bullen and Bolt, 1985). In contrast, strong-motion records near to an extended rupturing fault source often have much less easily identified wave patterns; in many cases, it is not possible to separate clearly the elastic wave types. Typically, the strong motions arrive at a recording site as a mix of source and path and site responses (e.g., Mikumo and Miyatake, 1987). The result is wave incoherency of various degrees. In estimation attempts, there is also the problem of differences of strong ground motion near to faults of different types (e.g., thrust-type sources versus strike-slip sources; see Archuleta, 1984; Spudich *et al*., 1996) and the geological complexities that produce marked contrasts between horizontal and vertical components of ground motion (Amirbekian and Bolt, 1998).

INTERNATIONAL HANDBOOK OF EARTHQUAKE AND ENGINEERING SEISMOLOGY, VOLUME 81B *ISBN: 0-12-440658-0*

TABLE 1 Examples of Near-Fault Strong-Motion Recordings from Crustal Earthquakes with Large Peak Horizontal Ground Motions

Earthquake	Magnitude M_w	Source Mechanism	Distance km*	Acceleration (g)	Velocity (cm/sec)	Displacement (cm)
1940 Imperial Valley (El Centro, 270)	7.0	Strike-Slip	8	0.22	30	24
1971 San Fernando (Pacoima, 164)	6.7	Thrust	3	1.23	113	36
1979 Imperial Valley (EC #8, 140)	6.5	Strike-Slip	8	0.60	54	32
Erizican (Erizican, 000)	6.9	Strike-Slip	2	0.52	84	27
1989 Loma Prieta (Los Gatos, 000)	6.9	Oblique	5	0.56	95	41
1992 Landers (Lucerne, 260)	7.2	Strike-Slip	1	0.73	147	63
1992 Cape Mendocino (Cape Mendocino, 000)	7.1	Thrust	9	1.50	127	41
1994 Northridge (Rinaldi, 228)	6.7	Thrust	3	0.84	166	29
1995 Kobe (Takatori, 000)	6.9	Strike-Slip	1	0.61	127	36
1999 Kocaeli (SKR, 090)	7.4	Strike-Slip	3	0.41	80	205
1999 Chi-Chi (TCU068, 000)	7.6	Thrust	1	0.38	306	940

* rupture distance (see Figure 1).

In this chapter, we discuss recording, interpretations, and prediction of strong motions in large earthquakes. The approach is largely historical and concentrates on the direct use of recordings of strong ground motion for estimation of seismic ground shaking for engineering purposes. We address the modern success in acquiring and analyzing strong ground motion by seismologists, particularly those working on seismic hazard maps and geological site response. Our emphasis is on the presently available strong-motion recordings and a description of ground-motion estimation methods. We do not attempt to describe in detail the major allied seismological field of theoretical modeling of seismic wave motion.

2. Growth of Significant Recordings of Intense Ground Motion

Until the 1970s, only a small sample of ground-motion recordings near to sources generating large magnitude earthquakes was available for either seismological research or engineering use. The situation, while not yet completely satisfactory, has recently improved. Recording programs in several countries have produced many important records; a helpful summary has been given by Ambraseys (1988). A further major augmentation occurred in the 1990s: We note here the ground-motion recordings from the 1989 Loma Prieta, California, earthquake (M6.9); the 1994 Northridge, California, earthquake (M6.7); the 1992 Landers, California, earthquake (M7.2), and the 1995 Kobe, Japan, earthquake (M6.8). Particularly valuable recordings in the near field were obtained in the August 1999 Kocaeli, Turkey, earthquake (M7.4), the November 1999 Duzce, Turkey, earthquake (M7.2), and (an unprecedented number, over 400 digital recordings) in the September 1999 Chi-Chi, Taiwan, earthquake (M7.6).

As this chapter was being written it became clear that studies of the major 1999 Taiwan earthquake and its aftershocks are likely to throw light on many seminal seismological and engineering questions (see the Dedicated Issue on the Chi-Chi, Taiwan Earthquake of 20 September, 1999, edited by Teng *et al.*, 2001). The Central Weather Bureau (CWB) was operating at the time the densest network of digital strong-motion instruments in the world as described by Shin *et al.* in Chapter 64. For comparison, station spacing of the free-field accelerographs in Taiwan was about 3 km in the metropolitan areas versus a 25-km uniform spacing of a comparable digital system (the Kyoshin Net) in Japan. For a description of the Kyoshin Net, please see Chapter 63 by Kinoshita.

3. Strong Ground-Motion Characteristics

The ground-motion characteristics depend on the seismic source, wave propagation (attenuation), and site response. The most commonly used method for characterizing the ground motion is through attenuation relations, but more complex numerical simulations are also used. As mentioned earlier, in this chapter we do not address the large topic of numerical simulation procedures. In attenuation relations, the earthquake source, wave propagation, and site response are typically parameterized by the magnitude, fault-type, source-to-site distance, and site condition. Recently, additional parameters describing the rupture direction have also been used to parameterize the source (discussed next).

3.1 Ground-Motion Parameters

Beginning about the 1960s, the most used ground-motion parameter for quantification of ground motion was the peak ground acceleration. The peak acceleration was picked from accelerograms irrespective of seismic phase, wave type, or frequency band. In practice, the peak horizontal acceleration occurs in most recordings in the *S*-wave portion of the seismogram with predominant frequencies typically between 3 and 8 Hz.

The peak vertical acceleration occurs sometimes in the *P* wave and sometimes in the *S* waves, with predominant frequencies typically between 5 and 20 Hz. More recently in engineering risk assessment, more emphasis is given to values of maximum velocity and displacement (see Bolt, 1996; Gregor and Bolt, 1997). A sample of some of the largest ground motions (in terms of peak acceleration, velocity, or displacement) is given in Table 1.

In addition to peak acceleration, velocity, and displacement, a descriptive construct special to the field of strong-motion seismology is that of seismic response spectrum, first proposed by Benioff (1934) and developed by Housner (1959). This spectrum is defined as the maximum response of a damped harmonic system to input motions. While the ground motion may be represented fully by Fourier spectra, the response of the structure is better represented by a response spectrum. It is common for modern attenuation relations to include relations for response spectral accelerations as well as peak acceleration.

Another commonly used ground-motion parameter is the duration of shaking. While it is generally agreed that duration can impact the response of soils, foundations, and structures, particularly when strength or stiffness degradation is encountered, there is not general agreement as to how the duration of shaking should be parameterized. This is evidenced by the 30 different definitions of strong-motion duration reviewed by Bommer and Martinez-Pereira (1998). A thorough description of the ground motion for engineering applications should include an estimation of the duration of strong motion, but given the wide range of duration measures currently being used, it is important to be clear as to how the specified duration is defined.

3.2 Independent Parameters Used in Attenuation Relations

The most common source, ray path, and site parameters are magnitude, distance, style-of-fault, and site classification. In some studies, additional parameters are used: hanging wall flag, rupture directivity parameters, focal depth, and soil depth. These independent parameters are discussed subsequently.

Different measures of earthquake magnitude are used in different regions of the world. At the International Workshop on Strong Motion Data held in 1993 in Menlo Park, California, various researchers working on ground-motion attenuation problems agreed to the recommendation that moment magnitude (M_w) should be universally adopted as the measure of earthquake size. Moment magnitude has been adopted in most recent attenuation relations developed in the United States and New Zealand, but this is not the case worldwide. In many regions, region-specific attenuation relations are still developed for magnitudes other than M_w, making it difficult to compare relations from different regions.

Whereas agreement was reached on the preferred magnitude, no such consensus was developed for the definition of distance used in attenuation relations, but there was a recommendation from the 1993 workshop that some form of "closest" distance to the rupture be used rather than epicentral or hypocentral distance. A variety of measures of the closest distance from the rupture to the site are used in various attenuation relations. Some examples of closest distance measures used in attenuation relations are listed in Table 2. These different distance measures are shown graphically in Figure 1 for a vertical fault and for

TABLE 2 Alternative Definitions of Distance That Are Used in Attenuation Relations

Distance Definition	Distance Measure	Examples of Attenuation Relations Using the Distance Measure
Shortest horizontal distance to the vertical projection of the rupture	"Joyner-Boore" distance	Joyner and Boore (1981), Boore *et al.* (1997), Spudich *et al.* (1996)
Closest distance to the rupture surface	Rupture distance	Sadigh *et al.* (1997), Abrahamson and Silva (1997), Idriss (1995)
Closest distance to the seismogenic part of the rupture	Seismogenic distance	Campbell (1997)
Closest distance to the hypocenter	Hypocentral distance	Atkinson and Boore (1995)
Closest distance to the centroid	Centroid distance	Crouse (1991)

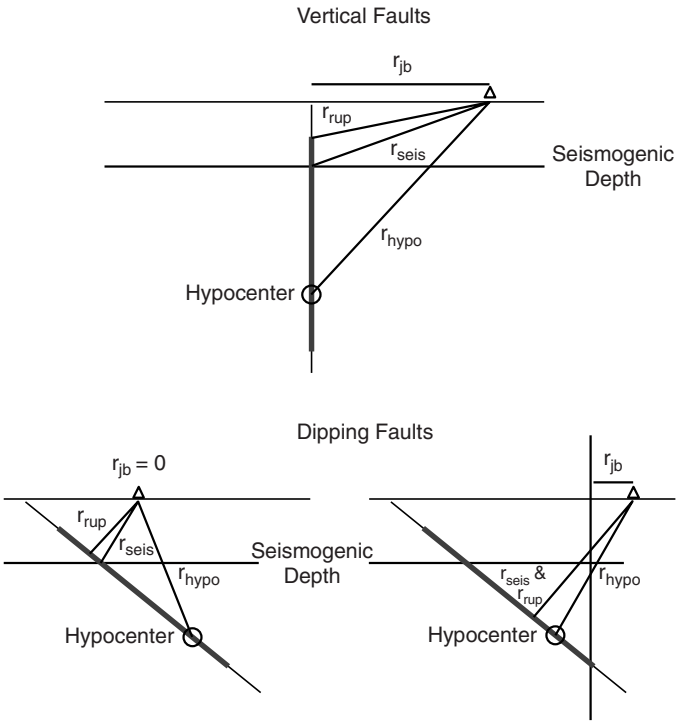

FIGURE 1 Source-to-site distance measures for ground-motion attenuation models (after Abrahamson and Shedlock, 1997).

a dipping fault. It is important to use the appropriate distance measure for a given attenuation relation.

Differences in site classification schemes in different regions also make comparison of ground motions and attenuation relations difficult. Most attenuation relations use broad site categories such as "rock," "stiff-soil," and "soft-soil." Recently, there has been a move toward using quantitative site classifications based on the shear-wave velocity measured at the strong-motion site, which would provide a standard site classification. The most commonly used parameter is the average shear-wave velocity over the top 30 m (e.g., Boore *et al*., 1997). The difficulty with using quantitative site descriptions is that the information is not available for the majority of strong-motion sites that have recorded strong motions. This situation is improving as studies are now being conducted to systematically collect and compile shear-wave velocities at strong-motion sites.

The style-of-faulting parameter is used to distinguish between different source types. For crustal earthquakes, ground motions systematically differ when generated by strike-slip, thrust, or normal mechanisms (e.g., Somerville and Abrahamson, 1995; Spudich *et al*., 1996). Given the same earthquake magnitude, distance to the site, and site condition, the ground motions from thrust earthquakes tend to be larger than the ground motions from strike-slip earthquakes (about 20–30% larger), and the ground motions from normal faulting earthquakes tend to be smaller than the ground motions from strike-slip earthquakes (about 20% smaller). For subduction earthquakes, the ground motions systematically differ when generated by interface or intraslab earthquakes (e.g., Youngs *et al*., 1997). Again, for the same magnitude, distance, and site condition, the ground motions from intraslab earthquakes tend to be larger than the ground motions from interface earthquakes (about 40% larger).

Other independent parameters used in some attenuation relations include hanging wall, rupture directivity, and soil depth. Rupture directivity is discussed in detail in Section 4 and is not discussed here.

For thrust faults, high-frequency ground motions on the upthrown block (hanging wall side of a thrust fault) tend to be larger than on the downdropped block (footwall) (e.g., Somerville and Abrahamson, 1995). This increase in ground motions on the hanging wall side is in part an artifact of using a rupture distance measure. If a site on the hanging wall and footwall are at the same rupture distance (see Figure 1), the site on the hanging wall side is closer to more of the fault than the site on the footwall side. Using the Joyner-Boore distance measure implicitly accounts for this geometric difference because all sites over the hanging wall of the rupture are at a Joyner-Boore distance of zero. This distance definition effect does not account for all of the differences between the ground motions on the hanging wall and footwall.

Most attenuation relations simply use a site category such as "deep soil"; however, this broad category covers a wide range of soil depths from less than 100 m to several km of sediments. Some attenuation relations (e.g., Campbell, 1997) use an additional site parameter to describe the depth of the soil. This additional parameter improves the model predictions of long-period ($T > 1$ sec) ground motions.

3.3 Development of Attenuation Relations

For a selected ground-motion parameter and set of independent parameters (magnitude, distance, etc.), attenuation relations are typically developed using regression analyses. The first issue is the selection of the assumed functional form of the attenuation. There are in general two types of magnitude scaling that are used in attenuation relations (Figure 2). In the first case, the shape of the attenuation with distance is independent of magnitude. A typical form of this type of model for rock site conditions is given in Eq. (1).

$$\text{Ln } Y(M, R, F) = c_1 + c_2 M + c_3 M^2 + c_4 \ln(R + c_5) + c_6 F \quad (1)$$

where Y is the ground-motion parameter (peak acceleration or response spectral value), M is the magnitude, R is the distance measure, and F is a flag for the style-of-faulting (reverse, strike-slip, normal). This is one of the simplest forms used for attenuation relations. An example of an attenuation model that uses this form is Boore *et al.* (1997).

An alternative form allows the shape of the attenuation relation to depend on magnitude with the curves pinching together at short distances (Figure 2). This saturation of the ground motion implies that at short distances, moderate magnitude earthquakes produce similar levels of shaking as large magnitude earthquakes. Some attenuation relations use a combination of

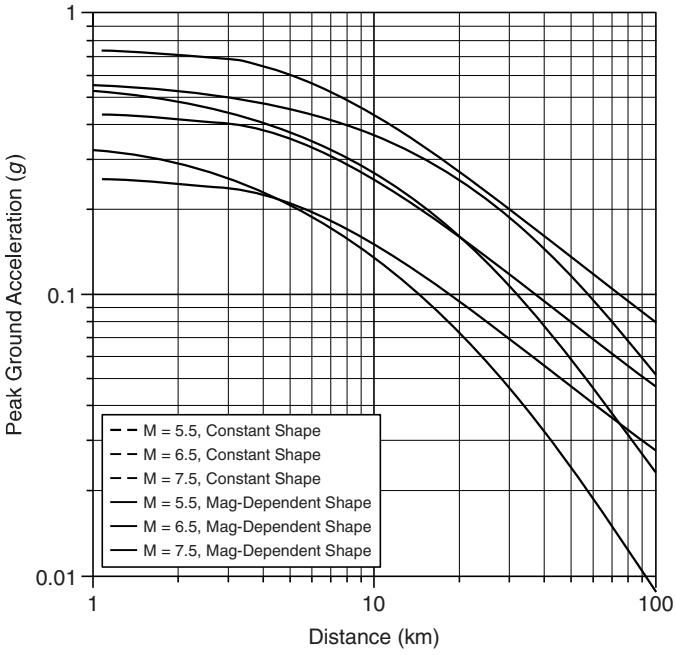

FIGURE 2 Comparison of constant and magnitude-dependent shapes of attenuation relations.

these two models with constant attenuation shapes for moderate magnitudes (e.g., $M < 6.5$) and saturation for large magnitudes (e.g., $M \geq 6.5$).

This type of saturation of the ground motion at short distances has been parameterized in two ways as shown in Eq. (2) and Eq. (3): replacing c_5 in Eq. (1) with a magnitude-dependent term, $f_1(M)$; or replacing the distance slope, c_4, in Eq. (1) with a magnitude-dependent slope, $f_2(M)$. For rock ground site conditions, two commonly used forms of the attenuation relation are

$$\text{Ln } Y(M, R, F) = c_1 + c_2M + c_3M^2 + c_4 \ln[R + f_1(M)] + c_6F \quad (2)$$

and

$$\text{Ln } Y(M, R, F) = c_1 + c_2M + c_3M^2 + (c_4 + f_2(M)) \ln(R + c_5) + c_6F \quad (3)$$

An example of an attenuation relation based on the model in Eq. (2) is Sadigh *et al*. (1997). A common form of the function $f_1(M)$ is

$$f_1(M) = c_7 \exp(c_8M) \quad (4)$$

If $c_3 = 0$ (which is common for high frequencies) and $c_8 = -c_2/c_4$, then the ground motion at zero distance is independent of magnitude and the model is said to have 100% magnitude saturation. If $c_8 > -c_2/c_4$, then the model is said to be oversaturated. In that case, at short distances, the median ground motion is reduced as the magnitude increases. An example of an attenuation relation based on the model in Eq. (3) is Abrahamson and Silva (1997). A common form of the function $f_2(M)$ is $f_2(M) = c_9M$. In this case, the model has 100% saturation if $c_8 = -c_2/\ln(c_5)$. If $c_8 < -c_2/\ln(c_5)$, then the model is oversaturated.

At distances less than about 50 km, these two different functional forms of the attenuation relation lead to similar curves, but at large distances, they become different (Figure 3). As most of the focus of attenuation relations for shallow crustal earthquakes in active tectonic regions has been on distances less than 50 km, these differences in slopes at large distances have not been subject to detailed studies. Part of the reason for this is that distant stations from moderate magnitude earthquakes were not available because the instruments did not trigger or the ground motions were too small to digitize. With the new digital recorders with wide dynamic range, we should be able to distinguish between these two alternatives.

In the eastern United States, it is common to incorporate a variation in the distance slope of the attenuation relation, which accommodates the increase in ground motions due to supercritical reflections from the base of the crust (e.g., Atkinson and Boore, 1995; Saikia and Somerville, 1997). This is usually done by incorporating a multi-linear form of the attenuation relation with different c_4 terms for different distance ranges. This typically leads to a flattening of the attenuation curve at distances of about 100 km (Figure 4). This is most significant for regions in which the high-activity sources are at a large distance from the site.

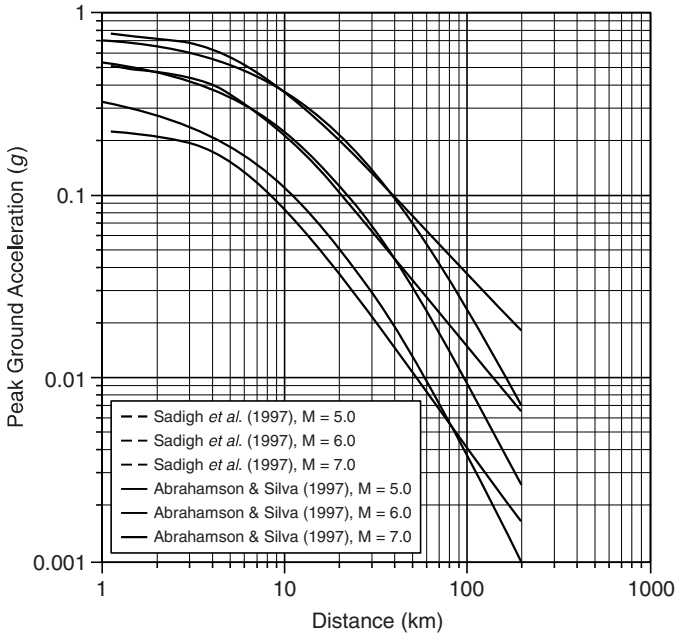

FIGURE 3 Comparison of predicted ground motions using alternative functional forms for saturation at short distances.

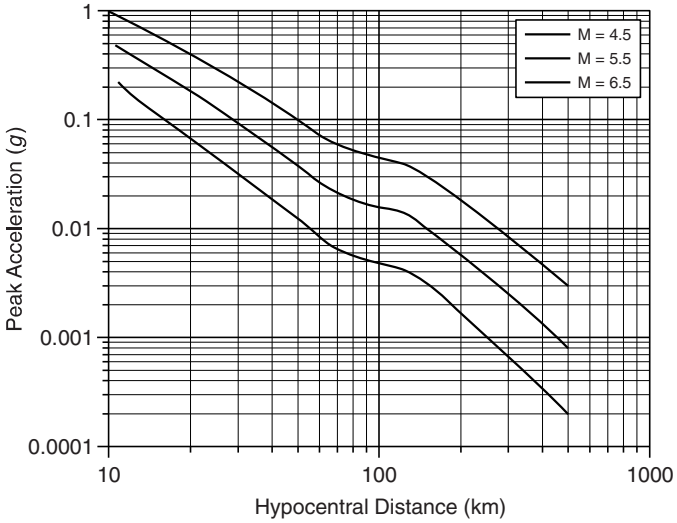

FIGURE 4 Form of attenuation relations in the eastern United States showing flattening of the attenuation relation due to crustal structure.

An important statistical issue in developing attenuation relations is the uneven sampling of the data from different earthquakes. For example, in some cases, an earthquake may have only one or two recordings (e.g., 1940 El Centro), whereas some recent earthquakes have hundreds of recordings (e.g., 1999 Chi-Chi earthquake). Should the well-recorded earthquakes overwhelm the poorly recorded earthquakes? Should the poorly

recorded earthquakes be given equal weight to the well-recorded earthquakes? Weighting schemes are typically used as a way to account for this uneven sampling problem. There are two extremes: Give equal weight to each data point or give equal weight to each earthquake. We do not attempt to cover all of the various weighting procedures here, but two commonly used methods are the two-step procedure and the random effects method. The two-step regression procedure first used by Joyner and Boore (1981) gives equal weight to each earthquake. The random effect model (Brillinger and Preisler, 1984) uses a weighting scheme that is between equal weight to each earthquake and equal weight to each data point depending on the distribution of the data. As the number of data points from each earthquake becomes large, these two methods give the same result.

In addition to the median ground motion, the standard deviation of the ground motion is also important for either deterministic or probabilistic hazard analyses. Worldwide, it is most common to use a constant standard deviation, but recently, several attenuation relations have incorporated magnitude or amplitude dependence to the standard deviation. For example, Abrahamson and Silva (1997) allow the standard deviation to vary as a function of the magnitude of the earthquake. The result is that the standard deviation is smaller for large magnitude earthquakes (Youngs *et al*., 1995). Campell (1997) allows the standard deviation to vary as a function of the amplitude of the ground motion. The result is that the standard deviation is smaller for larger amplitudes of ground motion. Both of these models can significantly affect the development of design ground motions.

3.4 Regional Differences in Attenuation

Many published studies have found significant differences in attenuation between various tectonic regions and also for various geologic conditions and seismic sources (e.g., Ambraseys and Bommer, 1991, 1995; Raoof *et al*., 1999). Results for North America were recently summarized (Abrahamson and Shedlock, 1997). In the latter summary paper it was found useful to group the attenuation relations into three main tectonic categories: shallow crustal earthquakes in active tectonic regions (e.g., California), shallow crustal earthquakes in stable continental regions (e.g., eastern U.S.), and subduction zone earthquakes.

In some regions of the world, there are recordings from both crustal earthquakes and subduction earthquakes (e.g., Japan, New Zealand, Taiwan). It has been common to lump these data together in developing attenuation relations. Because peak ground motions from subduction zone earthquakes generally attenuate more slowly than those from shallow crustal earthquakes in tectonically active regions, ground motions from these different types of sources should be modeled separately.

As the number of recordings of strong ground motion increase, there has been a trend toward developing region-specific attenuation relations rather than just using the global average models developed for the broad tectonic categories. Often, there is a tendency to overemphasize region-specific data in developing region-specific attenuation. Typically, there is not enough data in a specific region to completely determine the attenuation relation. In particular, there is often not enough data close to the fault to constrain the behavior of the attenuation relation at short distances, or not enough earthquakes to constrain the magnitude scaling.

One way to address regionalization of attenuation relations is to only update parts of the global attenuation relations. For example, the simplest update is to estimate a constant scale factor to use to adjust a global attenuation model to a specific region. (This can reflect differences in the earthquake source or differences in the site categories.) If there is enough data over a range of distances, the slope of the attenuation could be updated while maintaining the magnitude scaling of the global model. As more strong-motion data become available, additional parameters can be made region specific. An example of this approach to regionalizing attenuation relations is McVerry and Zhao (1999).

3.5 Types of Uncertainties

In developing ground motions for design, random variability and scientific uncertainty in ground motions are treated differently (Toro *et al*., 1997). Variability is the randomness in the ground motions that a model predicts will occur in future earthquakes. For example, variability in ground motion is often quantified by the standard deviation of an attenuation relation. In contrast, uncertainty represents the scientific uncertainty in the ground-motion model due to limited data. For example, the uncertainty in attenuation relations is often characterized by alternative attenuation relations. That is, uncertainty is captured by considering alternative models. In seismic hazard analyses, the terms "aleatory" and "epistemic" are used for variability and uncertainty, respectively. To keep the notation clear, in this chapter we will use the terms aleatory variability and epistemic uncertainty.

The distinction between aleatory variability and epistemic uncertainty is useful for seismic hazard analysis; however, a further subdivision is needed for the practical estimation of these two factors, which is shown in Table 3. There are two ways that the variability of ground-motion models is evaluated. First the models can be evaluated against recordings from past earthquakes. This is called the modeling term. The second way that a model is evaluated is by varying the free parameters of the model. This is called the parametric term.

The modeling component is a measure of the inability of the model to predict ground motions from past earthquakes. In general, the cause of the modeling variability is not understood. It is assumed to be random. If the cause of the modeling variability were understood, then the model could be improved to fit the observations. The parametric component is a measure of the variability of the ground motion from causes that are understood. That is, there is randomness in the earthquake source process that is understood and its effect on ground motion is part of the model.

In general, both the modeling and parametric terms need to be considered in a ground-motion model. As our understanding and

TABLE 3 Decomposition of Variability and Uncertainty

	Aleatory Variability	Epistemic Uncertainty
Modeling	Variability between model predictions of ground motions and observations of ground-motion data.	*Select (and weight) alternative ground-motion models.* Results in differences in both the median ground motion and the variability of the ground motion.
Parameteric	Variability of ground motions due to variability of *additional* earthquake source parameters. Additional source parameters are those that are not included in the specification of the design earthquake.	*Select (and weight) alternative models for the distributions of the additional parameters.* Results in differences in both the median ground motion and the variability of the ground motion.

modeling of earthquakes improves, there will be a trend of reducing the modeling variability (unexplainable variability), but this will likely be offset by an increase in the parametric variability (explainable variability). While the total variability (combination of the modeling variability and the parametric variability) may not be reduced significantly with improved models, there is an advantage to understanding the causes of the variability, particularly if the model is being extrapolated beyond the empirical data on which it was evaluated.

In empirical attenuation models, the standard deviation given for the model is modeling variability. In most attenuation models, there is no parametric variability component to the aleatory variability, but this is not necessarily the case. As new attenuation models are developed, they may begin to include a parametric variability component. For example, if an attenuation relation used the static stress-drop as an additional source parameter, then the variability of static stress-drop would be treated as parametric variability. Typically, for empirical attenuation relations, epistemic uncertainty is addressed by considering alternative attenuation relations.

4. The Special Case of Near-Fault Ground Motions

Near-fault ground motions often contain large long-period pulses in the ground motion. There are two causes of long-period pulses in near-fault ground motions. One is constructive interference of the dynamic shaking due to rupture directivity effects. The other is due to the movement of the ground associated with the permanent offset of the ground. This is the velocity of the ground due to the elastic rebound proposed by H. F. Reid after the 1906 earthquake. These two causes of long-period pulses attenuate very differently from one another. To keep these two effects separate, the terms "directivity pulse" and "fling-step" are used for the rupture directivity and elastic rebound effects, respectively.

Rupture directivity effects occur when the rupture is toward the site and the slip direction (on the fault plane) is aligned with the rupture direction (Somerville *et al*., 1997). As described in the next section, it is strongest on the component of motion perpendicular to the strike of the fault (fault-normal component). Fling-step effects occur when the site is located close to a fault with significant surface rupture. It is polarized onto the component parallel to the slip direction. For strike-slip earthquakes, rupture directivity is observed on the fault-normal component and static displacement effects are observed on the fault-parallel component. Thus, for strike-slip earthquakes, the rupture directivity pulse and the fling-step pulse will naturally separate themselves on the two horizontal components. For dip-slip earthquakes, it is more complicated. The rupture directivity effect will be strongest on the fault-normal component at a location direct updip from the hypocenter. The fling-step will also be observed on the horizontal component perpendicular to the strike of the fault. Thus for dip-slip faults, directivity-pulse effects and fling-step effects occur on the same component.

The horizontal recordings of stations in the 1966 Parkfield, California, earthquake and the Pacoima station in the 1971 San Fernando, California (Bolt, 1971) earthquake were the first to be discussed in the literature as showing near-fault velocity pulses. These cases, with maximum amplitudes of 78 and 113 cm/sec, respectively, consisted predominantly of horizontally polarized SH wave motion and were relatively long period (about 2–3 sec). These velocity pulses were due to rupture directivity.

Additional recordings in the near field of large sources have confirmed the presence of energetic pulses of this type, and they are now included routinely in synthetic ground motions for seismic design purposes. Most recently, the availability of instrumented measured ground motion close to the sources of the 1994 Northridge earthquake (Heaton *et al*., 1995), the 1995 Kobe earthquake (Nakamura, 1995), and the 1999 Chi-Chi earthquake (Lee *et al*., 2001) provided important recordings of the velocity pulse.

4.1 Directivity

In the case of a fault rupture toward a site at a more or less constant velocity (almost as large as the shear-wave velocity), most of the seismic energy from the extended fault rupture arrives in a short time interval, resulting in a single large long-period pulse of motion, which occurs near the beginning of the record. This wave pulse represents the cumulative effect of almost all of the seismic radiation from the moving dislocation. In addition, the radiation pattern of the shear dislocation causes this large pulse of motion to be oriented mostly in the direction perpendicular to the fault. Coincidence of the radiation pattern maximum for tangential motion and the wave focusing due to the rupture propagation direction toward the site produces a large displacement pulse normal to the fault strike (see Bullen and Bolt, 1985, p. 443).

The directivity of the fault source rupture causes spatial variations in ground-motion amplitude and duration around faults and produces systematic differences between the strike-normal and strike-parallel components of horizontal ground-motion amplitudes (Somerville *et al.*, 1997). These variations become significant at a period of 0.6 seconds and generally grow in size with increasing period. Modifications to empirical strong ground-motion attenuation relations have been developed (Somerville *et al.*, 1997) to account for the effects of rupture directivity on strong-motion amplitudes and durations based on an empirical analysis of near-fault recordings. The ground-motion parameters that are modified include the average horizontal response spectral acceleration, the duration of the acceleration time history, and the ratio of strike-normal to strike-parallel spectral acceleration.

The results are that when rupture propagates toward a site, the spectral acceleration is larger for periods longer than 0.6 seconds, and the duration is smaller. That is, the duration and long-period amplitude are inversely correlated. For sites located close to faults, the strike-normal spectral acceleration is larger than the strike-parallel spectral acceleration at periods longer than 0.6 seconds in a manner that depends on magnitude, distance, and azimuth.

As in acoustics, the amplitude and frequency of the directivity pulse have a geometrical focusing factor, which depends on the angle between the direction of wave propagation from the source and the direction of the source velocity. Instrumental measurements show that such directivity focusing can modify the amplitude velocity pulses by a factor of up to 10, while reducing the duration by a factor of 2. The pulse may be single or multiple, with variations in the *impetus* nature of its onset and in its half-width period. A widely accepted illustration is the recorded ground velocity of the October 15, 1979, Imperial Valley, California, earthquake generated by a strike-slip fault source (see Figure 5). The main rupture front moved toward El Centro and away from Bonds Corner.

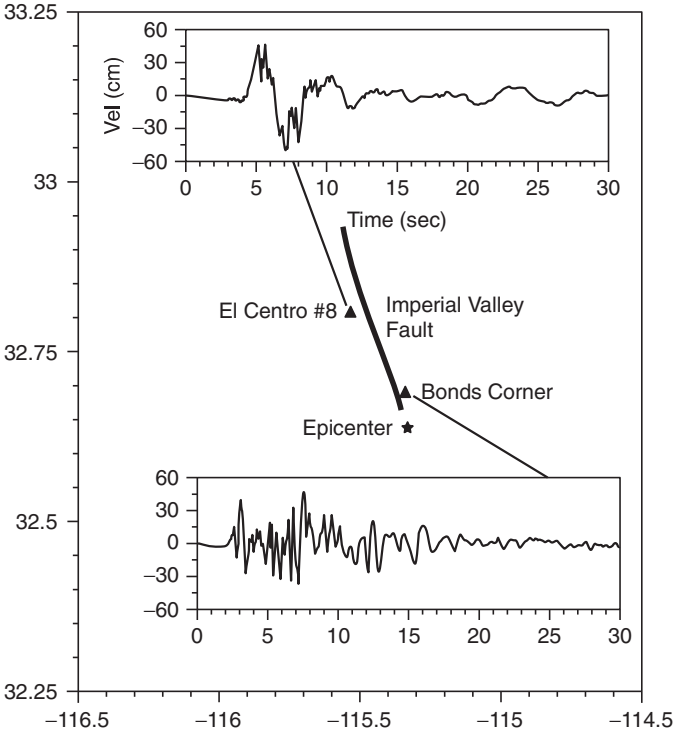

FIGURE 5 Velocity–time histories (230 Comp) from the 1979 Imperial Valley, California, earthquake at the Bonds Corner and El Centro Differential Array strong ground-motion recording sites.

4.2 Fling-Step

Prior to the 1999 Turkey and Taiwan earthquakes, nearly all of the observed large long-period pulses in near-fault ground motions were caused by rupture directivity effects. The Lucerne recording from the 1992 Landers earthquake contained a directivity pulse on the fault-normal component and a very long-period fling-step pulse on the fault-parallel component. The ground-motion data from the 1999 Turkey and Taiwan earthquakes contain large long-period velocity pulses due to the fling-step. As an example, the east–west components of velocity from selected recordings of the Chi-Chi earthquake are shown in Figure 6. The ground motions at station TCU068, located on the hanging wall near the northern end of the rupture, had the largest peak velocities ever recorded (300 cm/sec). The velocity pulse from the fling-step effect is one-sided. Most of the very large velocity at TCU068 is associated with the fling-step. If the fling-step is separated from the dynamic shaking, the peak

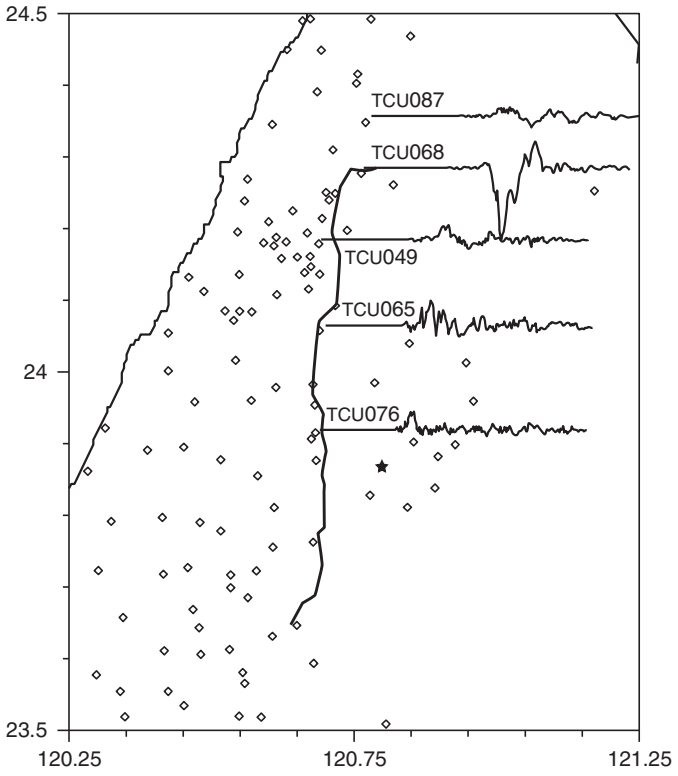

FIGURE 6 Selected velocity–time histories (east–west component) from the 1999 Chi-Chi earthquake.

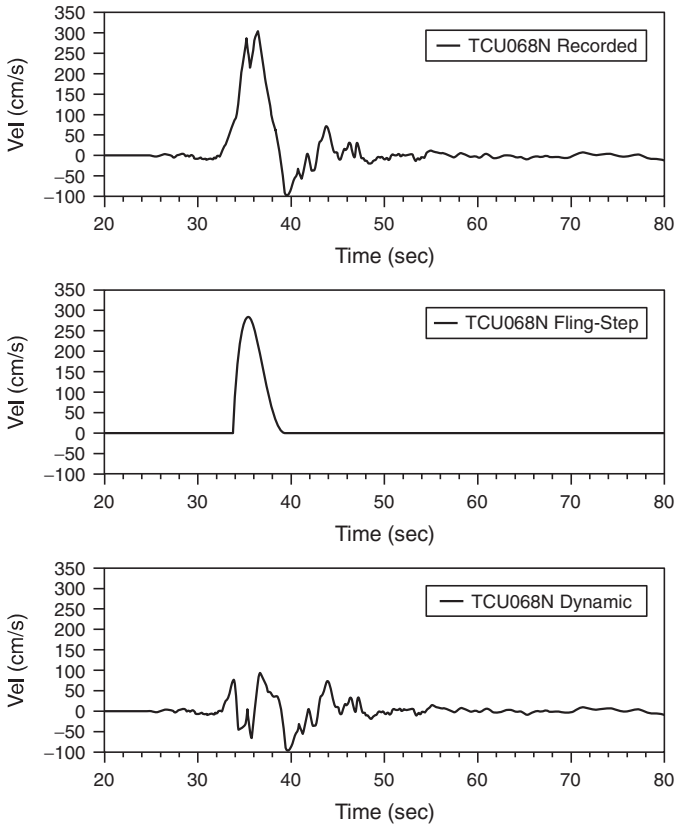

FIGURE 7 Velocity–time histories for the north–south component of station TCU068 (see Figure 6) separated into dynamic shaking and fling-step components.

velocity of the dynamic component of shaking is reduced to about 100 cm/sec (Figure 7). The very large fling-step velocity pulses do not attenuate at the same rate as the directivity pulses such as seen in Northridge and Kobe. Fling-step ground motion should not be simply thrown into the strong motion data set consisting of dynamic shaking. Separate attenuation relations will be needed for the fling-step and dynamic parts of the ground motion.

Models for the peak velocity from the fling-step have not been developed at this time. This represents an area of strong ground motion that can benefit from theoretical seismology. In displacement, the fling-step can be parameterized simply by the amplitude of the tectonic deformation and the rise time (time it takes for the fault to slip at a point).

5. Numerical Computation of Strong Ground Motion

Because of the lack of a complete library of strong ground motions and spectra from appropriate earthquakes, extrapolation from the available records is needed for estimation of large and unrepresented seismic motions. Confidence in such numerical predictions relies on the theoretical side of strong ground-motion seismology and from calibrating numerical techniques against empirical data. Important developments have occurred in this area in the last decades. In this section we briefly summarize some aspects of numerical computations of ground motions. This field is a major topic unto itself, which we only briefly cover here.

Numerous methods and examples of synthesizing seismograms numerically from source and wave theory in the near field of a large seismic source have been published (see, for example, Bolt, 1987; Irikura, 1983). Because the computation of site-dependent and phased-time histories is not unique, a number of alternative methods are available (see, e.g., Joyner and Boore, 1988; Vidale and Helmberger, 1987; Gusev, 1983; Mikumo and Miyatake, 1987; Panza and Suhadolc, 1987).

A more empirical approach is often adopted for engineering design practice (e.g., Bolt, 1994). The first step is to define, from geological and seismological information, the appropriate earthquake sources for the site of interest. The source selection may be deterministic or probabilistic and may be decided on the grounds of acceptable risk (Bolt, 1999a). Next, specification of the propagation path distance is needed, as well as the *P*-, *S*-, and surface-wave velocities in the zone. These speeds allow calculation of the appropriate wave propagation attenuation and angles of approach of the incident waves.

The construction of realistic motions consists of a series of iterations from the most appropriate observed strong-motion record already available to a set of more specific time histories that incorporate the seismologically defined wave patterns. Where feasible, strong-motion accelerograms are chosen that satisfy the seismic source (dip-slip, etc.) and path specifications for the seismic zone in question.

The iterative synthesis process is controlled by applying seismological (e.g., Kanamori, 1971; Anderson, 1997; Zeng *et al.*, 1994) and engineering constraints. For example, the response amplitude spectra might be required to fall within one standard error of a specified target spectrum obtained, say, from previous data analysis or an earthquake building code. Similarly, each seismogram is restricted to prespecified statistical bounds of peak-ground accelerations, velocities, and displacements. The durations of each wave section (mainly, *P*-, *S*-, and surface-wave portions) of each time history should also satisfy prescribed source, path, and site conditions. At the conclusion, experience with observed seismograms and knowledge of seismic wave theory are needed as a check on the results.

Arguably, currently, the most reliable estimation is based on a stochastic model of earthquake ground motions. This model uses simplified, yet physically based, representations of seismic energy release and wave propagation to obtain predictions of ground-motion amplitude for given values of earthquake size and depth, distance to the site, and model parameters. Tests are needed to confirm that any adopted stochastic model is consistent with recorded ground motions for the frequency, distance, and magnitude range of interest (i.e., the bias in the model predictions should be essentially zero for most frequencies, considering statistical uncertainty). The key parameters for representative stochastic models are stress-drop, crustal velocity

structure, crustal anelastic attenuation (Q), near-site anelastic attenuation (κ or kappa), and focal depth. Adopted values for these parameters have considerable uncertainties in most cases.

Finally, we would like to stress that much of the modeling in the seismological literature depends on assumptions on a range of key model parameters (see Boore *et al.*, 1997; Brune and Anooshehpoor, 1999) and has until recently been restricted to two-dimensional structures (see cases in Bolt, 1987; Boore and Joyner, 1997; Takei and Kanamori, 1997). Significant surface topography has been shown to affect ground motions (e.g., Spudich *et al*., 1995; Bard, 1982). Now, recent work has begun to produce synthetic ground motions based on realistic three-dimensional geological and source mechanics models (e.g., Olsen and Archuleta, 1996; Olsen *et al.*, 1995; Stidham *et al.*, 1999). There is clear observational evidence of the importance of three-dimensional structural variation in the surface motions, as observed, for example, in the isoseismal maps of the 1906 San Francisco earthquake (see Bolt, 1999b) and in the irregular patterns of seismic intensity in alluvial basins. O'Connell (1999) has addressed the key tradeoffs between nonlinear wave amplifications and linear scattering from crustal and basin velocity variations. A case has been published (Lomax and Bolt, 1992) that illustrates a significant lateral diffraction effect from the varied geology of the San Francisco Bay Area. We reproduce in Figure 8 the recordings of strong-motion displacements (transverse wave component) along three profiles that demonstrate the basin effect; the comparison is with synthetic motions calculated using the regional geological structures. In a follow-up study, Stidham *et al*. (1999) used full seismic-wave theory and three-dimensional modeling also to simulate the 1989 Loma Prieta earthquake. Their results demonstrated the significant variability in the radiated wave pattern due to different rock types across the San Andreas fault, the directivity focusing effect, and the azimuthally dependent amplification due to the Tertiary basin. Such physical predictions are likely to be a vigorous part of strong-motion research in seismology's future.

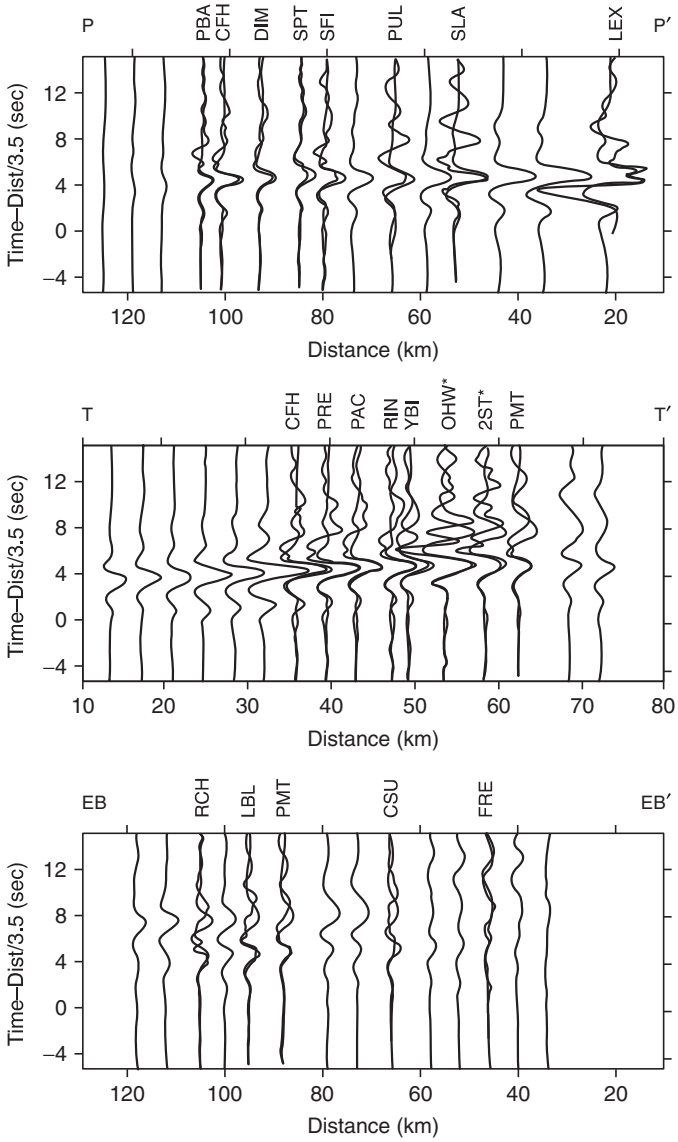

FIGURE 8 Observed strong-motion transverse displacement recordings of the 1989 Loma Prieta, California, earthquake (solid) and synthetics (dotted) shown along three lines: San Francisco peninsula (P–P′), Bay transverse (T–T′), and East Bay (EB–EB′). Traces are plotted as a function of distance along section; travel time is reduced with respect to epicentral distance. Trace distance on section P–P′ only is identical to epicentral distance. All amplitudes on each section are plotted to the same scale; the observed traces are bandpass filtered from 1 to 8 sec and shifted in time to align the interpreted direction SH arrival on the synthetics. (* indicates soft-soil sites.)

6. Seismic Strong-Motion Hazard and Design Ground Motions

It is now usual to use the word *hazard* to describe the actual danger itself (that is, in this discussion, the earthquake), and *risk* for the result of this hazard applied to vulnerable structures. The most commonly mapped ground-motion parameters are horizontal and vertical peak ground accelerations (PGA), peak ground velocity (PGV), and 5% damped spectral acceleration (SA) for a given site classification. The 1996 U.S. National Hazard maps include PGA and 0.2, 0.3, and 1.0 sec period SA with a 10%, 5%, and 2% chance of exceedance in 50 years (Frankel *et al*., 2000), assuming a "firm rock" site (see *http://geohazards.cr.usgs.gov/eq/*).

There are two basic approaches to developing design spectra: deterministic and probabilistic. The deterministic approach uses selected individual earthquake scenarios (magnitude, distance, directivity, etc). The ground motion is then computed using appropriate attenuation relations with a specified probability of not being exceeded given that the specified scenario earthquake occurs. Typically, a probability of nonexceedance of either 0.5 (median) or 0.84 (median plus one standard deviation) is used.

The engineering seismic risk analysis (Cornell, 1968) differs from the probabilistic approach in that it considers the rate of

occurrence of each scenario and variability of the ground motion (number of standard deviations above or below the median) and its associated probability distribution. The hazard curve gives the probability that any of the scenarios will produce a ground motion exceeding the ground-motion test value (ground motion on the x-axis). For probabilistic analyses, the design ground motion is typically given by an equal hazard spectrum. A description of probabilistic hazard analysis is given by Reiter (1990).

An equal hazard spectrum gives at each spectral period the response spectral value that has the specified return period. Equal hazard spectra are constructed by first computing the hazard at each spectral period independently (using response spectral attenuation relations, see Section 3). Because the hazard analysis is done independently at each period, an equal hazard spectrum may not correspond to the same earthquakes at both short and long periods. The equal hazard spectrum may not be physically realizable in a single event, but is meant to represent reasonable design criteria.

7. Design Time Histories

The construction of strong-motion seismograms is now an essential part of the definition of hazard for the design and testing of critical structures. There are two main approaches used to develop design ground motions: (a) scaling ground motions and (b) adjusting ground motions to match a design spectrum.

Scaling refers to multiplying a recorded or simulated time history by a constant factor at all time points. This approach has the advantage that the time histories maintain the natural phasing of the recorded motion and realistic peaks and troughs in the spectral shape; the disadvantage is that a large number of time histories need to be used to get a reliable estimate of the average response of the structure (e.g., 10 sets of time histories may be needed). The suite of time histories should be scaled such that their ensemble average is close to the design spectra over the critical period range of the structure.

Spectrum-compatible time histories refers to time histories that are modified in terms of their frequency content to match the entire design spectrum. Various methods have been developed to modify a reference time history so that its response spectrum is compatible with a specified target spectrum. A review of spectral-matching methods is given by Preumont (1984). A commonly used method adjusts the Fourier amplitude spectrum based on the ratio of the target response spectrum to the time history response spectrum while keeping the Fourier phase of the reference time history fixed. While this approach is straightforward, it has two drawbacks. First, it generally does not have good convergence properties, particularly for multiple damping spectra. Second, it can alter the nonstationary character of the time history if the shape of the Fourier amplitude spectrum is changed significantly.

There are two alternative approaches for spectral matching. The first is a frequency domain approach in which the Fourier amplitude spectrum of the initial motion is replaced by a Fourier amplitude spectrum that is consistent with the target spectrum based on random vibration theory. The second alternative approach for spectral matching adjusts the time history in the time domain by adding wavelets to the reference time history. A formal optimization procedure for this type of time-domain spectral matching was first proposed by Kaul (1978) and was extended to simultaneously match spectra at multiple damping values by Lilhanand and Tseng (1988). While this procedure is more complicated than the frequency-domain approach, it has good convergence properties and in most cases preserves the nonstationary character of the reference time history.

If spectrum-compatible motions are used, then a small number of sets of time histories can be used and still provide a reliable estimate of the average response of the structure (e.g., 3 sets may be adequate).

7.1 Selection of Initial Time Histories

The selection of the starting time histories for use in either scaling or spectral matching is important due to nonlinear response of the soil and structure. Potential motions should be based on their duration, site characteristics, event magnitude and recording distance, and general character of the displacement history. In particular, for near-fault time histories, the character of the displacement pulse as either one-sided, two-sided, or multi-sided should be considered so that the selected motions will have distinctly different time-signatures to thoroughly test the structural design. If the scaling approach is used, then selecting records with a similar site condition to the project site is also an important factor. However, if the spectral matching approach is used, then the site condition of the initial time history is not critical because the spectral matching process will adjust the frequency content to match the project site conditions to the extent that they are captured by the design spectrum.

8. Special Case for Extended Structures

For most engineering applications, the ground motion is defined at a single point. In reality, for viaducts, large bridges, and dams, out-of-phase wave motions over inter-support distances cause differential ground accelerations and differential rotations along the base of the structure.

The spatial variation of seismic ground motion results from several effects: non-vertical wave propagation (wave passage effect), scattering and complex 3–D wave propagation (spatial coherency effect), variable distance to the fault rupture (attenuation effect), and variable site conditions (local site effect). The variable site condition can be considered in the site response calculations, which are not discussed in this chapter. Studies of the spatial variation of strong ground motions from array observations have been published (see Abrahamson *et al.*, 1987), and the results have been incorporated into structural response analyses for some large critical structures.

8.1 Wave-Passage Effect

The wave-passage effect is due to non-vertical wave propagation that produces systematic time shifts in the arrival of the seismic waves at the support locations. The wave-passage effect depends on the apparent velocity of the waves along the axis of the bridge. This requires information on both the apparent velocity of the waves in the direction of the wave propagation and the orientation of the structure with respect to the earthquake. Studies of strong- and weak-motion array data have shown that the apparent velocity of *S* waves is typically in the 2.0 to 3.5 km/sec range (Abrahamson, 1992b). In other studies, numerical simulations have been used to estimate the horizontal wave speed. These numerical simulations typically lead to higher horizontal wave speeds than measured from array data. The discrepancy may be due to the use of simplified crustal models in the simulations. The array measurements of the wave speeds are considered to be more reliable than the numerical simulations.

The wave-passage effect is included by applying systematic time shifts to the time histories. Although the *P*, *S*, and surface wave will have different phase velocities, the *S*-wave phase velocity is applied to the entire time history. The rationale for this approach is that the *S* waves generally contain the strongest shaking. Therefore, for an engineering analysis, it is adequate to simply model the *S*-wave wave-passage effect. More complex wave propagation methods can be used if the differential motion caused by the *P* wave and surface waves are considered to be important for the structural response.

8.2 Spatial Coherency Effect

The scattering and complex wave propagation result in variations in both Fourier amplitude and Fourier phase of the ground motions (Hao *et al*., 1989). The phase variations can be included through a spatial coherency function. The coherency is a complex number. The absolute value of the complex coherency is called the "lagged coherency" because it is equivalent to lining up (lagging) the ground motion at the two locations so that the wave passage effect is removed. The lagged coherency does not restrict the alignment of the ground motions to be consistent from frequency to frequency; that is, the apparent wave speeds can be different at each frequency. At high frequencies, the wave speed implied by the complex coherency becomes more random. However, in the application of the wave-passage effect, a constant wave speed is typically used for all frequencies. To be consistent with such an application, the coherency function needs to correspond to the coherency that would be computed by aligning the ground motion to a single wave speed. This coherency is called the "plane-wave coherency." Generic empirical models for the plane-wave coherency were developed from worldwide dense array recordings. An example of the coherency model for the horizontal component is given in Figure 9. Additional details of the coherency model are given in Fugro *Earth Mechanics* (1998).

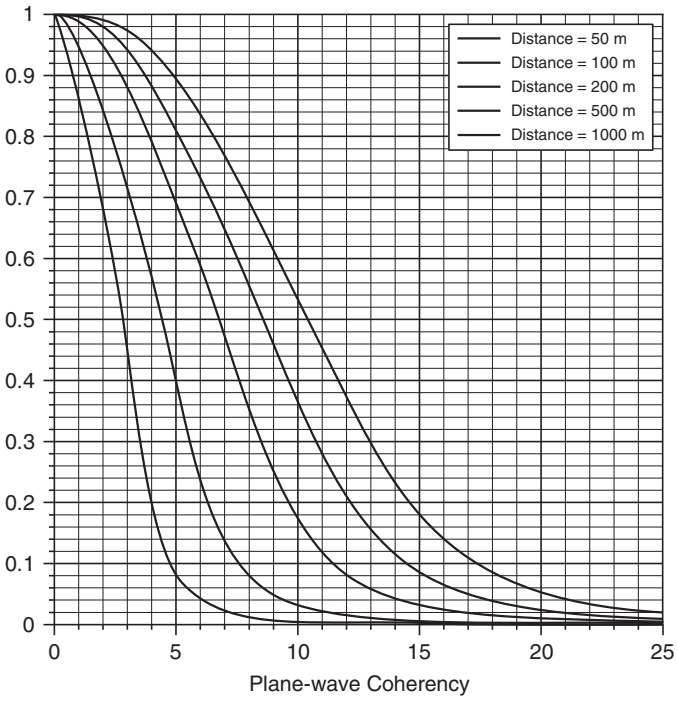

FIGURE 9 Plane-wave coherency model for the horizontal component.

8.3 Attenuation

For sources near to the structure, the different distances to the various support locations can result in different ground motions due to attenuation of the ground motion. The attenuation effect can be estimated simply using the attenuation relations with different distances to the controlling source for different parts of the structure.

8.4 Site Response

The effect of variable site conditions along extended structures is accommodated by conducting site-specific estimates of the site response using the appropriate rock motion for each location along the structure.

9. Example Application of Strong Ground-Motion Estimation to Critical Engineered Structural Design

In this concluding section, we briefly describe a recent application of the preceding methods to the estimation of the strong-motion parameters for a major bridge over San Francisco Bay, California. The details of the application are given in a report to the California Department of Transportation (Caltrans, Office

of Structure Foundations) (Fugro Earth Mechanics, 1998). The San Francisco–Oakland Bay Bridge consists of two bridges: an East Crossing and a West Crossing. This example is for the East Crossing. The bridge lies between two major active faults: the Hayward fault 8 km to the east and the San Andreas fault 15 km to the west.

9.1 Design Spectrum

A design spectrum was derived based on a probabilistic seismic hazard. A response spectrum with a return period of 1500 years was selected as a "Safety Evaluation Earthquake." The dynamics of near-source effects, discussed in Section 4, are crucial in this application. Therefore, the hazard analysis must include the effects of rupture directivity. This was done by modifying the attenuation relations to include directivity focusing and modifying the hazard computation to include variability of rupture direction. The equal hazard spectrum for fault normal motion is given in Figure 10.

The hazard for the 1500-year return period was deaggregated to determine the controlling earthquakes (Bazzurro and Cornell, 1999). In this case, the deaggregation indicated that the seismic hazard at the bridge is dominated by a M7.8 earthquake at about 20 km distance on the San Andreas fault and a M7.0 earthquake at about 10 km distance on the Hayward fault. The deaggregation also showed that at a spectral period of 3 seconds (a critical period for the bridge foundations), the 1500-year return period ground motion is dominated by forward rupture directivity.

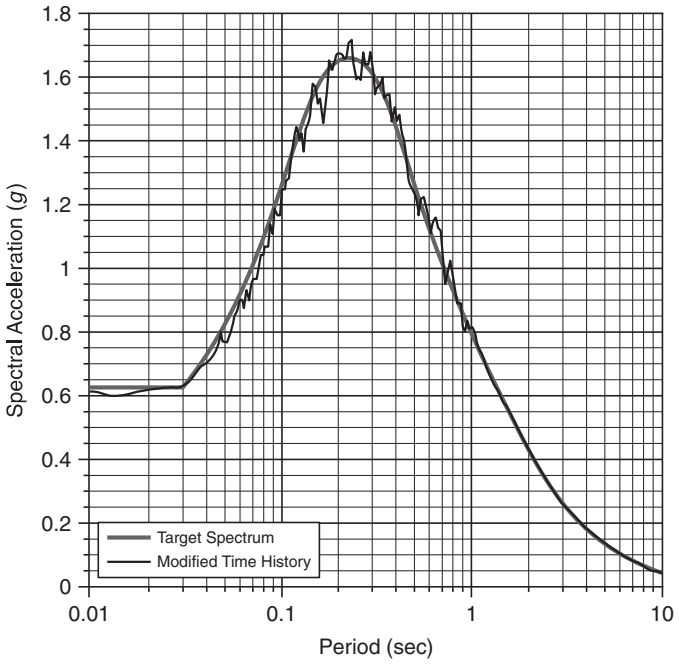

FIGURE 10 Comparison of the design spectrum and the spectrum of the modified time history (5% damping).

9.2 Design Time Histories for Rock Site Conditions

In order to allow for aleatory variability in the time histories associated with the design spectrum (see Section 3.5), three sets of three-component seismograms (time histories) were computed for each of the dominant sources (three sets for San Andreas fault sources and three sets for Hayward fault sources). Because forward directivity dominated the long-period hazard for the design return period, forward rupture direction was assumed for all six sets of ground-motion time histories.

Next, available recorded accelerograms from earthquakes with magnitudes greater than 6.5 and recorded at distances less than 15 km were evaluated (Tables 4a, 4b, 4c). Both rock and soil time histories were considered for selection because the response spectral matching adjusts to a large extent for the wave frequency differences at soil and rock sites (Aki, 1988). These candidate time histories were rotated to their principle directions (in displacement) and then classified in terms of the character of the displacement waveform: one-sided pulse, two-sided pulse, multiple pulses. Because the bridge will undergo significant nonlinear response under the design ground motions, it is important to get a range of nonstationary characteristics of the near-fault ground motions to represent a range of possible ground motions from future earthquakes in order to adequately test the performance of the bridge.

For the Hayward fault sources, suitable empirical time histories could be found and used directly as initial time histories; however, for the San Andreas source scenarios, there are as yet no recorded time histories that are directly applicable to the required magnitude and distance range. As an alternative, two procedures were used to develop the initial ground motions: splicing together empirical time histories and numerical simulations. As an example, the initial displacement time history for the fault-normal component derived by splicing the El Centro #6 recording from the 1979 earthquake onto the end of the 1940 El Centro recording (to increase the duration) is shown in Figure 11.

The selected initial time histories were modified to match the design response spectra using a time domain spectral-matching procedure (e.g., Lihanand and Tseng, 1988). The spectrum-compatible time histories are shown in Figure 12 and the fit to the spectrum is shown in Figure 10. Comparing the time histories in Figures 11 and 12 shows that this spectral matching procedure preserves the gross nonstationary characteristics of the acceleration, velocity, and displacement time histories.

9.3 Coherency and Multiple Support Time Histories

After development of the reference rock motions that are spectrum compatible, multiple-support rock ground motions were generated at all support points for the bridge structure to characterize the spatial variation of the rock ground motion

TABLE 4a Candidate Time Histories Considered for the Bay Bridge: One-Sided Displacement Pulses

Earthquake	Station	Rupture Distance (km)	Site	Major Axis (degrees)
1940 Imperial Valley, CA	El Centro #9	8.3	Soil	255
1985 Nahanni, Canada	Site 1	6.0	Rock	310
1989 Loma Prieta, CA	Corralitos	5.1	Rock	055
1989 Loma Prieta, CA	Gilroy–Historic Bldg	12.7	Soil	260
1989 Loma Prieta, CA	Gilroy Array #3	14.4	Soil	105
1992 Cape Mendocino, CA	Cape Mendocino	8.5	Rock	005
1992 Landers, CA	Lucerne	1.1	Rock	275
1994 Northridge, CA	Arleta	9.2	Soil	055
1994 Northridge, CA	W. Lost Canyon	13.0	Soil	075
1994 Northridge, CA	W. Pico Canyon	7.1	Soil	051
1994 Northridge, CA	Sylmar Converter Stn (east)	6.2	Soil	092
1994 Northridge, CA	Sylmar Converter Stn	6.1	Soil	333

TABLE 4b Candidate Time Histories Considered for the Bay Bridge: Two-Sided Displacement Pulses

Earthquake	Station	Rupture Distance (km)	Site	Major Axis (degrees)
1978 Tabas, Iran	Tabas	3.0	Soil	045
1989 Loma Prieta, CA	Gilroy–Gavilan College	11.6	Rock	097
1989 Loma Prieta, CA	Gilroy #1	11.2	Rock	045
1989 Loma Prieta, CA	Saratoga, Aloha Ave.	13.0	Soil	070
1992 Erzinkan,	Erzinkan	2.0	Soil	045
1992 Cape Mendocino, CA	Petrolia	9.5	Soil	100
1994 Northridge, CA	Jensen Filter Plant	6.2	Soil	012
1994 Northridge, CA	Newhall	7.1	Soil	160
1994 Northridge, CA	Pacoima Dam, Upper Left	8.0	Rock	199

TABLE 4c Candidate Time Histories Considered for the Bay Bridge: Multiple Displacement Pulses

Earthquake	Station	Rupture Distance (km)	Site	Major Axis (degrees)
1996 Gazli, USSR	Gazli	3.0	Rock	035
1986 Superstition Hills, CA	El Centro, ICC	13.9	Soil	045
1986 Superstition Hills, CA	Westmoreland Fire Station	13.3	Soil	240
1989 Loma Prieta, CA	Bran	10.3	Rock	085
1989 Loma Prieta, CA	Capitola	14.5	Soil	070
1989 Loma Prieta, CA	Gilroy #2	12.7	Soil	145
1989 Loma Prieta, CA	Los Gatos Pres. Center	6.1	Rock	100
1992 Landers, CA	Joshua Tree	11.6	Soil	005
1994 Northridge, CA	Montebello, Bluff Rd	12.3	Soil	211
1994 Northridge, CA	Cold Water Canyon	14.6	Soil	195
1994 Northridge, CA	Pacoima Dam Downstream	8.0	Rock	305
1994 Northridge, CA	Kagel Canyon	8.2	Rock	360
1994 Northridge, CA	Rinaldi Receiving Station	7.1	Soil	298
1994 Northridge, CA	Sepulveda VA	8.9	Soil	290
1994 Northridge, CA	Simi Valley, Katherine Rd.	14.6	Soil	115
1994 Northridge, CA	Sun Valley, Roscoe Blvd	12.3	Soil	045
1994 Northridge, CA	Sylmar, Olive View Med.	6.4	Soil	055
1995 Kobe, Japan	KJMA	0.6	Rock	050
1995 Kobe, Japan	Kobe Univ.	0.2	Rock	075
1995 Kobe, Japan	Amagasaki	10.2	Soil	030

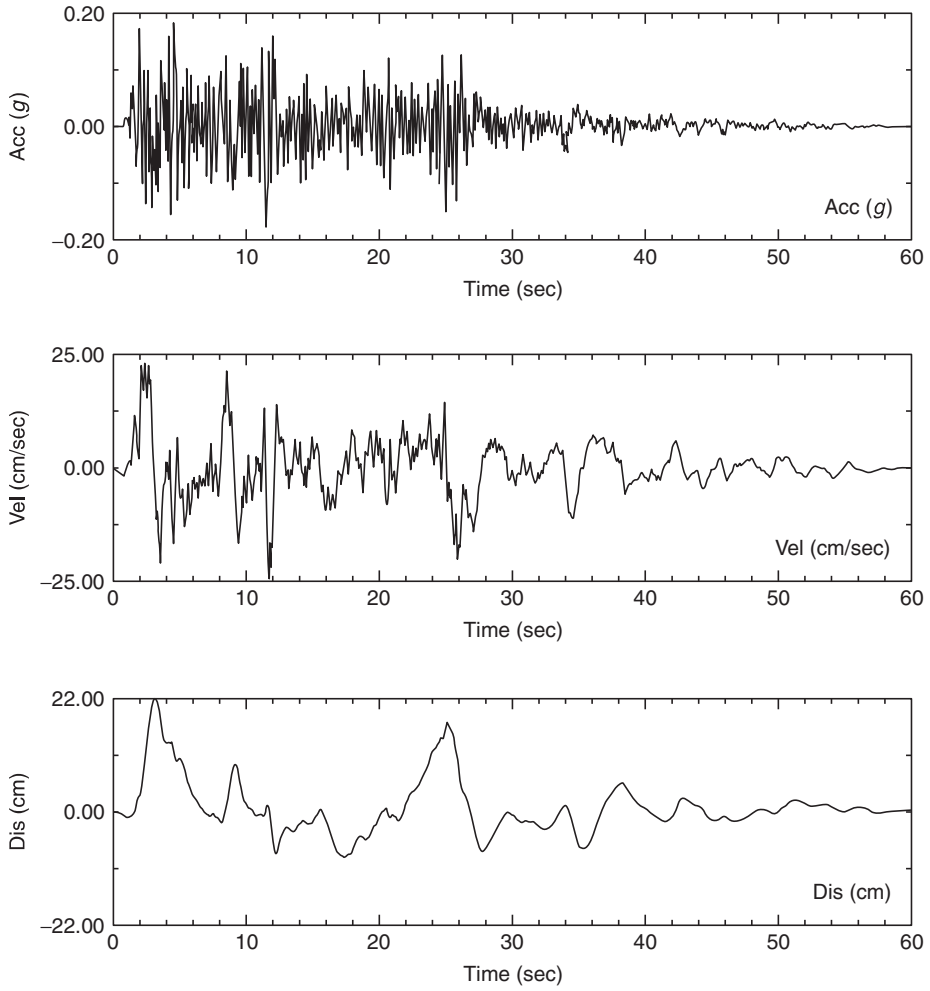

FIGURE 11 Initial fault-normal time history for the San Andreas event based on splicing together empirical recordings.

(see Section 8). The spatial variation of the rock motion resulted from several effects: non-vertical wave propagation (wave-passage effect) scattering and complex 3–D wave propagation (spatial coherency effect), and variable distance to the fault rupture (attenuation effect). Because most of the Bay Bridge supports are founded on piles driven into deep mud, the actual input motions also include spatial variability due to variability of the soil profile along the bridge. (Such site response variability in this project was incorporated using 1D site response calculations. In this chapter we only discuss the rock ground motions.) The steps in developing the incoherent rock ground motions were fourfold:

Step 1: Generate coherency compatible time histories at each support location.
Step 2: Modify the incoherent time histories to be compatible with the target spectrum using a frequency-domain approach.
Step 3: Apply a baseline correction to the incoherent time histories.
Step. 4: Apply the wave passage and attenuation effect.

9.3.1 Generation of Multiple Support Ground Motions

Multiple support time histories were generated at a total of 30 pier locations along the bridge using the procedure by Abrahamson (1992a). This procedure modifies the Fourier phase angles at each support location, using a relation between the spatial coherency and the degree of randomness in the phase angle.

9.3.2 Wave-Passage Effect

Based on the array data measurements, an apparent wave-speed of 2.5 km/sec for *S* waves was used. This velocity was selected because it is toward the lower end of the range of measured speeds and leads to somewhat conservative estimates of the differential motions. The wave propagation was projected along the axis of the bridge with apparent velocity along the bridge, V_{bridge}, given by

$$V_{bridge} = V_a / \sin(\theta) \tag{5}$$

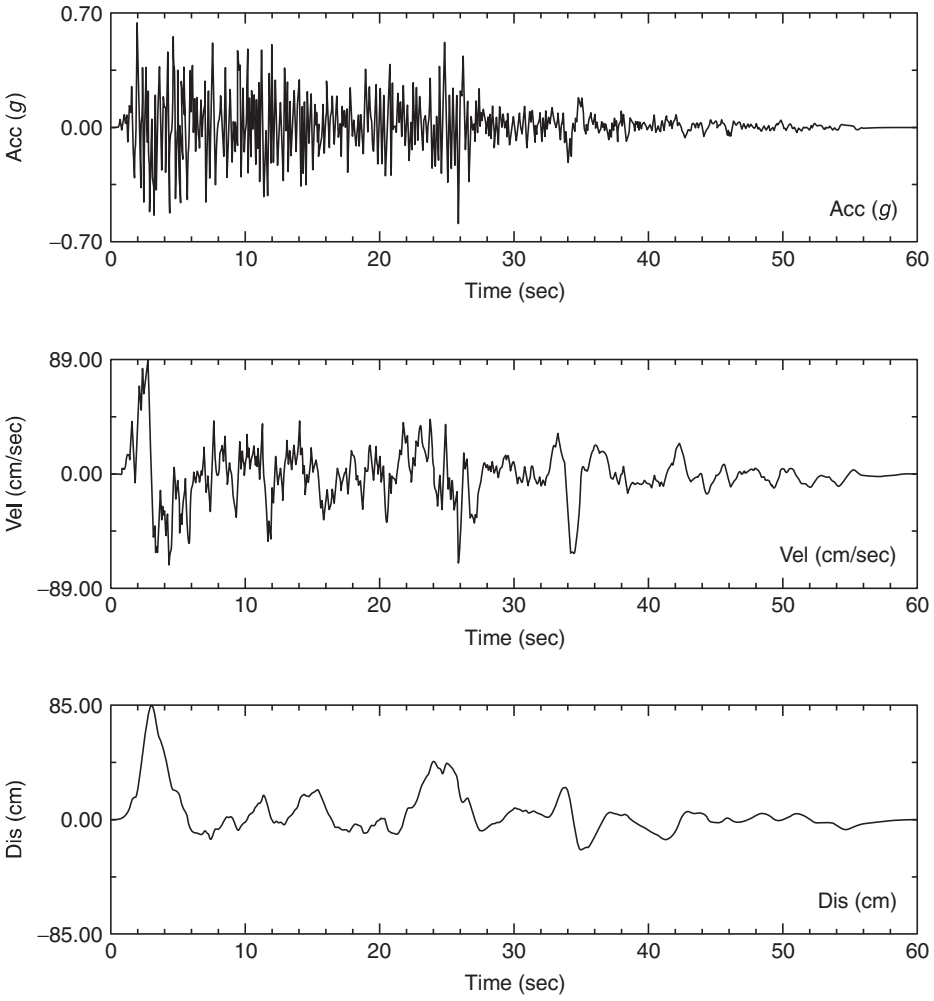

FIGURE 12 Spectrum compatible fault-normal time history.

where V_a is the apparent wave velocity and θ is the angle between the line perpendicular to the bridge axis and the line connecting the closest point of the fault and the center of the bridge. (Of course, waves arrive from all fault rupture segments in addition to waves arriving from the closest point on the fault, but here it is approximated by a single wave direction.)

9.3.3 Attenuation across the Structure

For fault sources near to long structures, such as the San Francisco Bay Bridge, the different distances to the various support locations result in different ground motions due to attenuation of the ground motion. To account for this attenuation, the ground motion at each bridge pier was scaled by the ratio of the predicted T = 1 second spectral acceleration to the target T = 1 second spectral acceleration using the empirical attenuation relations. While the attenuation could have been computed separately for each frequency, the T = 1 second spectral value was used for all periods to allow simple scaling of the ground motions. Because the structure is a long-period structure, this was considered reasonable.

9.3.4 Results

An example of the resulting incoherent rock ground motions for the two ends of the bridge is shown in Figure 13. The differential displacements are shown in Figure 14 as a function of the separation distance. These multiple supports are then propagated through site-specific soil profiles to incorporate the local site response.

10. Overview

An important point in summarizing the present status of assessment of seismic strong ground motions is that in a number of countries digital strong-motion systems linked to computer

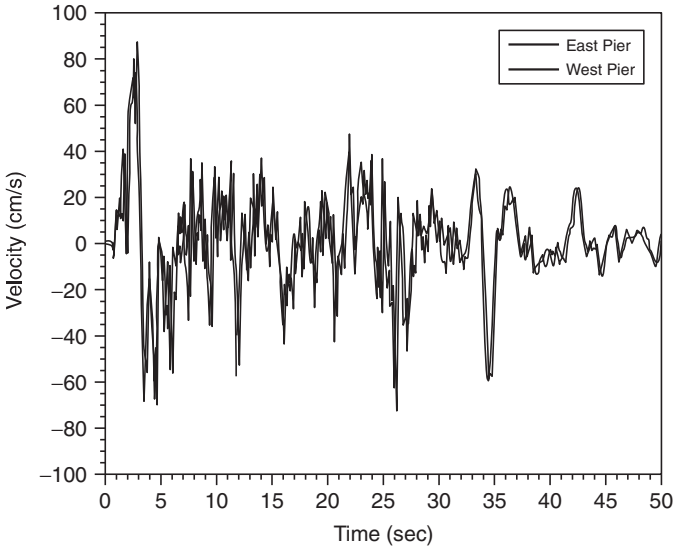

FIGURE 13 Incoherent rock time histories at the two ends of the Bay Bridge.

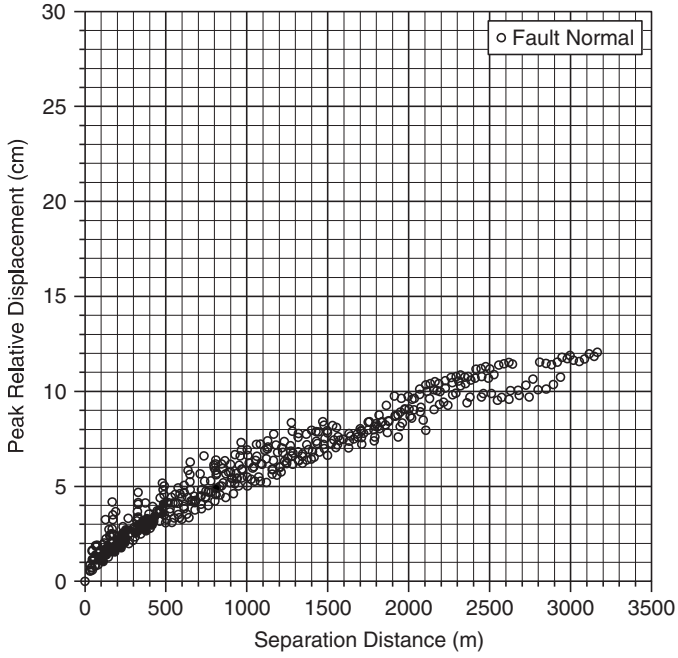

FIGURE 14 Peak differential displacement for the fault-normal component of motion from a set of incoherent spectrum-compatible time histories for the Oakland crossing of the San Francisco–Oakland Bay Bridge.

centers have now been installed. They provide processed observational data within a few minutes after shaking occurs. These near real-time data can be a basis for postearthquake response and evaluation of damage to structures, and for urgent risk decisions. By the end of 1999, computer-generated maps of intensity were being generated in California from the network of digital stations installed in the Los Angeles region. These displays, called "shake maps", available on the Internet for public use (*http://www.trinet.org*). One format of the maps contours peak ground velocity and spectral acceleration at 0.3, 1.0, and 3.0 seconds and displays in color a ground-motion strength-parameter called "instrumental intensity." Similar maps were provided immediately after the 1999 Chi-Chi earthquake in Taiwan. The maps have a variety of applications in postearthquake valuation of structures, damage and loss estimation, and in guiding emergency response but lack estimation detail.

The seismological problems dealt with in this chapter will no doubt be much extended in subsequent years. First, greater sampling of strong ground motions at all distances from fault sources of various mechanisms and magnitudes will inevitably become available. An excellent example is the wide recording of the 1999 Chi-Chi, Taiwan, earthquake (see Shin *et al*., 2000; Lee *et al*., 2001). Second, more realistic 3–D numerical models will solve the problem of the sequential development of the wave mixtures as the waves pass through different geological structures. Two difficulties may persist: the lack of knowledge of the roughness distribution along the dislocated fault and, in many places, quantitative knowledge of the soil, alluvium, and crustal rock variations in the region.

A new significant ingredient in general motion measurement is correlation with precisely mapped coseismic ground deformations. Networks of GPS instruments will help greatly in understanding of the source problem and the correct adjustment to strong-motion displacement records. A broad collection of standardized strong-motion time histories represented by both amplitude spectra and phase spectra is now being accumulated in virtual libraries for easy access on the Internet. Such records will provide greater confidence in seismologically sound selection of ground-motion estimates.

Additional instrumentation to record strong ground motion remains a crucial need in earthquake countries around the world (see e.g., Bolt, 1999b; Frankel, 1999). Such basic systems should measure not only free-field surface motions, but downhole motions to record the wave changes as they emerge at the Earth's surface.

Many contemporary attenuation estimates will no doubt be updated as more recorded measurements are included, rendering earlier models obsolete. To keep abreast of changes, ground-motion attenuation model information may be found at *http://www.geohazards.cr.usgs.gov/earthquake.html*. Click on Engineering Seismology, then on Ground Motion Information.

Acknowledgments

We thank the three referees for their comments on the manuscript draft.

References

Abrahamson, N. A. (1992a). Generation of spatially incoherent strong motion time histories. *Proc. 10th World Conf. Earthq. Eng.*, Madrid, Spain, 845–850.

Abrahamson, N. A. (1992b). Spatial variation of earthquake ground motion for application to soil–structure interaction. *Electric Power Research Institute, report TR-100463*.

Abrahamson, N. A., and B. A. Bolt (1987). Array analysis and synthesis mapping of strong ground motion. In: "Strong Motion Synthetics" (B. A. Bolt, Ed.), Academic Press, Orlando, Florida, 55–90.

Abrahamson, N. A., and K. M. Shedlock (1997). Overview. *Seism. Res. Lett.* **68**, 9–23.

Abrahamson, N. A., and W. Silva (1997). Empirical response spectral attenuation relations for shallow crustal earthquakes. *Seismol. Res. Lett.* **68**, 94–127.

Abrahamson, N. A., B. A. Bolt, R. D. Darragh, J. Penzien, and Y. B. Tsai (1987). The SMART1 accelerograph array (1980–1987): a review. *Earthq. Spectra* **3**, 263–288.

Aki, K. (1988). Local site effects on strong ground motion. In: *Proc. Earthq. Eng. and Soil Dyn. II,* Park City, Utah, 103–155.

Ambraseys, N. N. (1988). Engineering seismology, First Mallet Milne Lecture. *Earthq. Eng. Struc. Dyn.* **17**, 1–105.

Ambraseys, N. N., and J. J. Bommer (1995). Attenuation relations for use in Europe: An overview. *Proc. Fifth Society for Earthq. and Civil Eng. Dyn. Conf. on European Seismic Design Practice,* Chester, England, 67–74.

Ambraseys, N. N., and J. J. Bommer (1991). The attenuation of ground accelerations in Europe. *Earthq. Eng. Struc. Dyn.* **20**, 1179–1202.

Amirbekian, R. W., and B. A. Bolt (1998). Spectral comparison of vertical and horizontal seismic strong ground motions in alluvial basins. *Earthq. Spectra* **14**, 573–595.

Anderson, J. G. (1997). Seismic energy and stress-drop parameters for a composite source model. *Bull. Seismol. Soc. Am.* **87**, 85–96.

Archuleta, R. (1984). A faulting model for the 1969 Imperial Valley earthquake. *J. Geophys. Res*. **89**, 4559–4585.

Atkinson, G. M., and D. M. Boore (1995). New ground motion relations for eastern North America. *Bull. Seismol. Soc. Am.* **85**, 17–30.

Bard, P. Y. (1982). Diffracted waves and displacement field over two-dimensional elevated topographics. *Geophys. J. Roy. Astr. Soc.* **71**, 731–760.

Bazzurro, P., and C. A. Cornell (1999). Disaggregation of seismic hazard. *Bull. Seismol. Soc. Am.* **89**, 335–341.

Benioff, H. (1934). The physical evaluation of seismic destructiveness. *Bull. Seismol. Soc. Am.* **24**, 9–48.

Bolt, B. A. (1971). The San Fernando Valley, California, earthquake of February 9, 1971: data on seismic hazards. *Bull. Seismol. Soc. Am.* **61**, 501–510.

Bolt, B. A. (Ed.) (1987). *Seismic Strong Motion Synthetics*. Academic Press, Orlando, Florida, 328 pp.

Bolt, B. A. (1996). From earthquake acceleration to seismic displacement, Fifth Mallet-Milne Lecture. *Society for Earthq. and Civil Eng. Dyn.*, London, 50 pp.

Bolt, B. A. (1999a). Modern recording of seismic strong motion for hazard reduction. In: "Vrancea Earthquakes: Tectonic and Risk Mitigation" (F. Wenzel, Ed.), Kluwer, Netherlands, 1–14.

Bolt, B. A. (1999b). *Earthquakes*, 4th ed. W. H. Freeman, New York.

Bommer, J. J., and A. Martinez-Pereira (1998). The effective duration of earthquake strong motion. *J. Earthq. Eng.* **3**(2), 127–172.

Boore, D. M., and W. B. Joyner (1997). Site amplifications for generic rock sites. *Bull. Seismol. Soc. Am*. **87**, 327–341.

Boore, D. M., W. B. Joyner, and T. Fumal (1997). Equations for estimating horizontal response spectra and peak acceleration from western North American earthquakes: a summary of recent work. *Seismol. Res. Lett.* **68**, 128–153.

Brillinger, D. R., and H. K. Preisler (1984). Further analysis of the Joyner-Boore attenuation data. *Bull. Seismol. Soc. Am.* **75**, 611–614.

Brune, J., and A. Anooshehpoor (1999). Dynamic geometrical effects on strong ground motion in normal fault model. *J. Geophy. Res.* **104**, 809–815.

Bullen, K. E., and B. A. Bolt (1985). *An Introduction to the Theory of Seismology*. Cambridge University Press, Cambridge, 499 pp.

Campbell, K. W. (1997). Empirical near-source attenuation relationships for horizontal and vertical components of peak ground acceleration, peak ground velocity, and pseudo absolute acceleration response spectra. *Seismol. Res. Lett.* **68**, 154–179.

Cornell, C. A. (1968). Engineering seismic risk analysis. *Bull. Seismol. Soc. Am.* **58**, 1583–1606.

Crouse, C. B. (1991). Ground-motion attenuation equations for earthquakes on the Cascadia subduction zone. *Earthquake Spectra* **7**, 201–235; and 506.

Darragh, R. B., and A. F. Shakal (1991). The site response of two rock and soil station pairs to strong and weak ground motion. *Bull. Seismol. Soc. Am*. **81**, 1884–1899.

Frankel, A. D. (1999). How does the ground shake? *Science* **283**, 2032–2033.

Frankel, A. D., C. Mueller, T. Barnhard, D. Perkins, E. Leyendecker, N. Dickman, S. Hanson, and M. Hopper (2000). USGS national seismic hazard maps. *Earthquake Spectra* **16**, 1–19.

Fugro/Earth Mechanics (1998). Seismic ground motion report for San Francisco–Oakland Bay Bridge, East Span Seismc Safety Project, Report to Caltrans, Contract No. 59A0053. [A copy of this report may be accessed at both the Earthquake Engineering Research Center Library at the University of California, Berkeley, and at the Earthquake Engineering Research Library at Caltech, Pasadena.]

Gregor, N. J., and B. A. Bolt (1997). Peak strong motion attenuation relations for horizontal and vertical ground displacements. *J. Earthq. Eng*. **1**(2), 275–292.

Gusev, A. (1983). Descriptive statistical model of earthquake source radiation and its application to an estimate of short-period strong motion. *Geophys. J. R. Astr. Soc.* **74**, 787–808.

Hao, H., C. S. Oliveira, and J. Penzien (1989). Multiple-station ground motion processing and simulation based on SMART-1 array data. *Nuclear Eng. and Design* **11**, 293–310.

Heaton, T. H., J. F. Hall, D. J. Wald, and M. W. Halling (1995). Response of high-rise and base-isolated buildings to a hypothetical M_W 7.0 blind thrust earthquake. *Science* **267**, 206–211.

Housner, G. W. (1959). Behavior of structures during earthquakes. *Proc. ASCE EM4* **85**, 109–129.

Idriss, I. M. (1995). An overview of earthquake ground motions pertinent to seismic zonation. In: *Proc. 5th International Conference On Seismic Zonation*, Oct. 17–19, 1995, Nice, Vol. III, 2111–2126. Ouest Editions - Presses Academiques, Nantes Cedex, France.

Irikura, K. (1983). Semi-empirical estimation of strong ground motions during large earthquakes. *Bull. Disaster Prevention Res. Inst. (Kyoto Univ.)* **33**, 63–104.

Joyner, W. B., and D. M. Boore (1981). Peak horizontal acceleration and velocity from strong-motion records including records from the 1979 Imperial Valley, California, earthquake. *Bull. Seismol. Soc. Am.* **71**, 2021–2038.

Joyner, W. B., and D. M. Boore (1988). Measurement, characteristics and prediction of strong ground motion. *Proc. Specialty Conf. on Earthq. Eng. and Soil Dyn. II*, ASCE Park City, Utah, 43–102.

Kanamori, H. (1971). Faulting of the great Kanto earthquake of 1923 as revealed by seismological data. *Bull. Earthq. Res. Inst. Univ. Tokyo* **49**, 13–18.

Kaul, M. K. (1978). Spectrum-consistent time-history generation. *ASCE J. Eng. Mech., EM4*, 781–788.

Lee, W. H. K., T. C. Shin, K. W. Kuo, K. C. Chen, and C. F. Wu (2001). CWB free-field strong-motion data from the 21 September Chi-Chi, Taiwan, earthquake, *Bull. Seismol. Soc. Am.* **91**, 1370–1376.

Lilhanand, K., and W. S. Tseng (1988). Development and application of realistic earthquake time histories compatible with multiple damping response spectra. *Ninth World Conf. Earth. Eng.*, Tokyo, Japan, Vol II, 819–824.

Lomax, A., and B. A. Bolt (1992). Broadband waveform modelling of anomalous strong ground motion in the 1989 Loma Prieta earthquake using three-dimensional geological structures. *Geophys. Res. Lett.* **19**, 1963–1966.

McVerry, G. H., and J. X. Zhao (1999). A response spectrum model for New Zealand including high attenuation in the volcanic zone. *Institute of Geological and Nuclear Science, Ltd.*

Mikumo, T., and T, Miyatake (1987). Numerical modeling of realistic fault rupture processes. In: "Seismic Strong Motion Synthetics" (B. A. Bolt, Ed.), Academic Press, New York, 91–151.

O'Connell, D. R. (1999). Replication of apparent nonlinear seismic response with linear wave propagation model. *Science* **283**, 2045–2050.

Olsen, K. B., R. J. Archuleta, and J. R. Matarese (1995). Three-dimensional simulation of a magnitude 7.75 earthquake on the San Andreas fault. *Science* **270**, 1628–1632.

Olsen, K. B., and R. J. Archuleta (1996). Three-dimensional simulation of earthquakes on the Los Angeles fault system. *Bull. Seismol. Soc. Am.* **86**, 575–596.

Panza, G. F., and P. Suhadolc (1987). Complete strong motion synthetics. In: "Seismic strong motion synthetics" (B. A. Bolt, Ed.), Academic Press, New York, 153–204.

Preumont, A. (1984). The generation of spectrum compatible accelerograms for the design of nuclear power plants. *Earthq. Eng. Struct. Dyn.* **12**, 481–497.

Raoof, M., R. B. Herrmann, and L. Malagnini (1999). Attenuation and excitation of three-component ground motion in Southern California. *Bull. Seismol. Soc. Am.* **89**, 888–902.

Reiter, L. (1990). *Earthquake Hazard Analysis: Issues and Insights*. Columbia University Press, New York, 254 pp.

Sadigh, K., C.-Y. Chang, J. A. Egan, F. Makdisi, and R. R. Youngs (1997). Attenuation relationships for shallow crustal earthquakes based on California strong motion data. *Seismol. Res. Lett.* **68**, 180–189.

Saikia, C. K., and P. G. Somerville (1997). Simulated hard-rock motions in Saint Louis, Missouri, from large New Madrid earthquakes. *Bull. Seismol. Soc. Am.* **87**, 123–139.

Shin, T. C., K. W. Kuo, W. H. K. Lee, T. L. Teng, and Y. B. Tsai (2000). A preliminary report on the 1999 Chi-Chi (Taiwan) earthquake. *Seismol. Res. Lett.* **71**, 23–29.

Somerville, P. G., and N. A. Abrahamson (1995). Ground motion prediction for thrust earthquakes. *Proc. SMIP95 Seminar*, Cal. Div. of Mines and Geology, San Francisco, Calif., 11–23.

Somerville, P. G., N. F. Smith, R. W. Graves, and N. A. Abrahamson (1997). Modification of empirical strong ground motion attenuation relations to include the amplitude and duration effects of rupture directivity. *Seismol. Res. Lett.* **68**, 199–222.

Spudich, P., J. Fletcher, M. Hellweg, J. Boatwright, C. Sullivan, W. Joyner, T. Hanks, D. Boore, A. McGarr, L. Baker, and A. Lindh (1996). Earthquake ground motions in extensional tectonic regimes. *Open-File Report 96-292*, *U.S. Geological Survey,* 351 pp.

Spudich, P., M. Hellweg, and W. H. K. Lee (1995). Directional topographic site response at Tarzana observed in aftershocks of the 1994 Northridge, California, earthquake: implications for main shock motions. *Bull. Seismol. Soc. Am.* **85**, S193–S208.

Stidham, C., M. Antolik, D. Dreger, S. Larsen, and B. Romanowicz (1999). Three-dimensional structure influences on the strong-motion wavefield of the 1989 Loma Prieta earthquake. *Bull. Seismol. Soc. Am.* **89**, 1184–1202.

Takei, M., and H. Kanamori (1997). Simulation of long-period ground motions near a large earthquake. *Bull. Seismol. Soc. Am.* **87**, 140–156.

Teng, T. L., Y. B. Tsai, and W. H. K. Lee, Eds. (2001). Dedicated Issue on the Chi-Chi, Taiwan Earthquake of 20 September, 1999. *Bull. Seismol. Soc. Am.* **91**, 893–1395, with attached CD-ROM.

Toro, G. R., N. A. Abrahamson, and J. F. Schneider (1997). Model of strong ground motions from earthquakes in central and eastern North America: best estimates and uncertainties. *Seismol. Res. Lett.* **68**, 41–57.

Vidale, J., and D. V. Helmberger (1987). Path effects in strong ground motion seismology. In: "Seismic Strong Motion Synthetics" (B. A. Bolt, Ed.), Academic Press, New York, 267–319.

Youngs, R. R., N. A. Abrahamson, and K. Sadigh (1995). Magnitude-dependent variance of peak ground acceleration. *Bull. Seismol. Soc. Am.* **85**, 1161–1176.

Zeng, Y., J. G. Anderson, and G. Yu (1994). A composite source model for computing realistic synthetic strong ground motions. *Geophys. Res. Lett.* **21**, 725–728.

Editor's Note

Please see also Chapter 57, Strong-Motion Seismology, by Anderson; Chapter 58, Strong-Motion Data Processing, by Shakal *et al.*; Chapter 60, Strong-Motion Attenuation Relations, by Campbell; and Chapter 61, Site Effects of Strong Ground Motions, by Kawase.

This Page Intentionally Left Blank

60

Strong-Motion Attenuation Relations

Kenneth W. Campbell
ABS Consulting and EQECAT Inc., Beaverton, Oregon, USA

1. Introduction

An evaluation of seismic hazards, whether deterministic (scenario based) or probabilistic, requires an estimate of the expected ground motion at the site of interest. The most common means of estimating this ground motion in engineering practice, including probabilistic seismic hazard analysis (PSHA), is the use of an attenuation relation. An attenuation relation, or ground-motion model as seismologists prefer to call it, is a mathematical-based expression that relates a specific strong-motion parameter of ground shaking to one or more seismological parameters of an earthquake. These seismological parameters quantitatively characterize the earthquake source, the wave propagation path between the source and the site, and the soil and geological profile beneath the site.

In its most fundamental form, an attenuation relation can be described by an expression of the form

$$Y = c_1 e^{c_2 M} R^{-c_3} e^{-c_4 r} e^{c_5 F} e^{c_6 S} e^{\varepsilon} \tag{1}$$

or by its more common logarithmic form

$$\ln Y = c_1 + c_2 M - c_3 \ln R - c_4 r + c_5 F + c_6 S + \varepsilon \tag{2}$$

where "ln" represents the natural logarithm (log to the base e), Y is the strong-motion parameter of interest, M is earthquake magnitude, r is a measure of source-to-site distance, F is a parameter characterizing the type of faulting, S is a parameter characterizing the type of local site conditions, ε is a random error term with zero mean and standard deviation equal to the standard error of estimate of $\ln Y$ ($\sigma_{\ln Y}$), and R is a distance term often given by one of the alternative forms

$$R = \begin{cases} r + c_7 \exp(c_8 M) & \text{or} \\ \sqrt{r^2 + [c_7 + \exp(c_8 M)]^2} \end{cases} \tag{3}$$

Alternatively, the regression coefficients c_3, c_6, and c_7 can be defined as functions of M and R.

The mathematical relationships in Eqs. (1) to (3) have their roots in earthquake seismology (e.g., see Lay and Wallace, 1995, and contributions in this volume). The relationships $Y \propto e^{c_2 M}$ and $\ln Y \propto c_2 M$ are consistent with the definition of earthquake magnitude, which Richter (1935) originally defined as the logarithm of the amplitude of ground motion. The relationships $Y \propto R^{-c_3}$ and $\ln Y \propto -c_3 \ln R$ are consistent with the geometric attenuation of the seismic wave front as it propagates away from the earthquake source. Some attenuation relations set $c_3 = 1$, which is the theoretical value for the diminution of amplitude with distance from a point source in a half space, referred to as spherical spreading. If not constrained in the regression analysis, c_3 will be typically larger than unity. Sometimes c_3 is varied as a function of distance to accommodate differences in the attenuation rate of different wave types (e.g., direct waves versus surface waves) and critical reflections off the base of the crust (e.g., the Moho). The relationships $Y \propto e^{-c_4 r}$ and $\ln Y \propto -c_4 r$ are consistent with the anelastic attenuation caused by material damping and scattering as the seismic waves propagate through the crust. The relationship between Y and the remaining parameters has been established over the years from ground-motion observations and theoretical ground-motion studies.

The mathematical relationships defined in Eq. (3) are used to incorporate the widely held belief that short-period ground motion should become less dependent on magnitude close to the causative fault. Schnabel and Seed (1973) were the first to model this behavior theoretically using simple geometrical considerations. Since then similar results have been obtained using theoretical finite-source models (e.g., see Anderson, 2000). Campbell (1981) was one of the first investigators to identify and model this behavior empirically. Since then many other investigators have adopted similar models.

The remainder of this chapter defines the strong-motion and seismological parameters commonly found in an attenuation relation and provides a brief discussion of the various factors that can affect these parameters. The discussion specifically

INTERNATIONAL HANDBOOK OF EARTHQUAKE AND ENGINEERING SEISMOLOGY, VOLUME 81B *ISBN: 0-12-440658-0*

addresses issues regarding the use of attenuation relations to estimate strong ground motion in engineering practice, including PSHA. Particular emphasis is placed on the estimation of peak time-domain and peak frequency-domain parameters. A more general discussion of strong-motion seismology is given in Chapter 57 by Anderson. The development of earthquake time histories and other related engineering estimates of ground motion is the topic of Chapter 59 by Bolt and Abrahamson. The estimation of seismic hazards, including PSHA, is the topic of Chapter 65 by Somerville and Moriwaki. Due to length limitations, this chapter can only provide a brief introduction to the attenuation relation and its constitutive strong-motion and seismological parameters. A contemporary guide to some recent attenuation relations and their use in engineering practice is included on the attached Handbook CD (hereafter referred to as the *Contemporary Guide*). This *Contemporary Guide* includes a comprehensive list of references to previous discussions on the empirical and theoretical prediction of strong ground motion as well as a selected compilation of recently published attenuation relations and guidance on their use in engineering practice. Most notable amongst these, because of their recency and comprehensiveness, are those of Douglas (2002), which cover relations developed from empirical methods, and Boore (2002), which cover relations developed from seismological models. Also included on the attached Handbook CD is an interactive electronic workbook that allows the user to evaluate the attenuation relations presented in the *Contemporary Guide* for a variety of seismological parameters.

Although this chapter is not intended to give a complete history of the attenuation relation, it would be remiss not to mention some of the pioneers whose early and continued development of attenuation relations first led to their widespread acceptance in engineering, particularly in the then-fledgling field of PSHA. These pioneers include (listed alphabetically) Neville Donovan, Luis Esteva, George Housner, Ed Idriss, Bill Joyner, Kiyoshi Kanai, Robin McGuire, H. Bolton Seed, and Mihailo Trifunac. Many others have followed in their footsteps, many whose contributions are significant and noted in the remainder of this chapter.

2. Strong-Motion Parameters

Strong-motion parameters represent in simple terms a specific characteristic of an earthquake time history (peak time-domain parameters) or its frequency-domain equivalent (peak frequency-domain parameters). A brief description of these two types of strong-motion parameters is given next.

2.1 Peak Time-Domain Parameters

Historically, peak ground acceleration (PGA) and to a lesser extent peak ground velocity (PGV) and peak ground displacement (PGD) have been the most common peak time-domain parameters used to describe strong ground motion in engineering practice. They represent the maximum absolute amplitude of ground motion scaled from a recorded or synthetic acceleration, velocity, or displacement time series. They serve as a simple representation of the short-, mid-, and long-period components of ground motion, respectively.

2.2 Peak Frequency-Domain Parameters

As seismic design procedures have become more sophisticated, engineers have begun to incorporate the natural period of a structure into its design through the use of a response spectrum (Chapter 68 by Borcherdt *et al.*). A response spectrum is a plot versus undamped natural period of the maximum response of a viscously damped, single-degree-of-freedom (SDOF) system subjected to ground-motion input at its base. (For a more complete description see Chapter 67 by Jennings.) The most common response-spectral parameters are pseudoacceleration (known variously as PSSA, PSA, or SA) and pseudovelocity (known variously as PSRV, PSV, or SV). The terms PSA and PSV are used throughout this chapter to represent pseudoacceleration and pseudovelocity in order to avoid confusion, noting that Gupta (1993) prefers the terms SA and SV. However, the latter notation has been used in the past to define absolute acceleration and relative velocity, which are similar, but not identical, to PSA and PSV (see Chapter 67 by Jennings or any text on earthquake engineering for a description of these parameters). PSA and PSV are related to one another and to relative displacement (SD) by the expression

$$\mathrm{PSA} = \frac{2\pi}{T_n}\,\mathrm{PSV} = \left(\frac{2\pi}{T_n}\right)^2 \mathrm{SD} \tag{4}$$

where T_n is the undamped natural period of a SDOF system. Relative displacement is the maximum absolute displacement of a SDOF system relative to its base.

Response spectra can be developed from PGA alone or from PGA, PGV, and PGD (Newmark and Hall, 1982; Campbell, 2002; see also Chapter 67 by Jennings), or they can be developed from one or two key response-spectral ordinates, such as PSA at $T_n = 0.2$ and $T_n = 1$ sec (Leyendecker *et al.*, 2000; see also Chapter 68 by Borcherdt *et al.*). Such procedures are typically used in building codes and other seismic regulations where a simple prescribed method for estimating a seismic design spectrum is required. However, it has become more common in engineering practice to develop a design response spectrum directly from attenuation relations representing individual spectral ordinates of PSA or PSV.

3. Earthquake Source Parameters

Earthquake source parameters describe a characteristic of an earthquake's source, such as its size, mechanism (type of faulting), stress drop, source directivity, or radiation pattern. Some common source parameters are discussed next.

3.1 Magnitude

Magnitude is used to define the "size" of an earthquake. There are many different scales that can be used to define magnitude. Some of the more common magnitude scales used in attenuation relations are moment magnitude (**M** or M_W), surface-wave magnitude (M_S), short-period body-wave magnitude (m_b), local magnitude (M_L), Lg-wave magnitude (m_{Lg} or m_N), and JMA magnitude (M_J). The symbol M_W used by engineers and engineering seismologists is used to denote moment magnitude throughout this chapter, noting that many seismologists prefer the symbol **M**. Network operators in different parts of the world will use one of the just-mentioned magnitude scales as a standard for quantifying magnitude in their region. However, it should be noted that even the use of the same magnitude scale can lead to different regional estimates of magnitude due to the way magnitude is locally defined and calculated. The mathematical definition of all peak time-domain magnitude scales can be given by the expression (e.g., Lay and Wallace, 1995)

$$M = \log(A/T) + f(R, h_{\text{hypo}}) + C_s + C_r \tag{5}$$

where "log" represents the common logarithm (log to the base 10), A is the recorded ground displacement of the seismic phase on which the amplitude scale is based, T is the period of the signal, $f(R, h_{\text{hypo}})$ is a correction for the distance from the earthquake source to the instrument (R) and the focal depth (h_{hypo}), C_s is a correction for the siting of the instrument, and C_r is a correction for the source region. Figure 1 gives a comparison of the different magnitude scales. A more thorough discussion of magnitude scales is given in Chapter 44 by Utsu.

There is an increasing tendency to adopt M_W as the worldwide standard for quantifying magnitude because of its strong physical and seismological basis (Bolt, 1993). By definition, M_W is related to seismic moment M_0, which is a measure of the energy radiated by an earthquake (Kanamori, 1978; Hanks and Kanamori, 1979). Seismic moment can be defined as

$$M_0 = \mu A_f \bar{D} = 2\mu E_S/\Delta\sigma \tag{6}$$

where μ is the shear modulus of the crust, A_f is the rupture area of the fault, $\bar{D}$ is the coseismic displacement averaged over the rupture area, $\Delta\sigma$ is the static stress drop averaged over the rupture area, and E_S is the radiated seismic energy. The definition based on $A_f \bar{D}$ allows M_0 to be derived from geological faulting parameters that can be measured in the field. The definition based on $E_S/\Delta\sigma$ allows M_0 to be derived from seismological data.

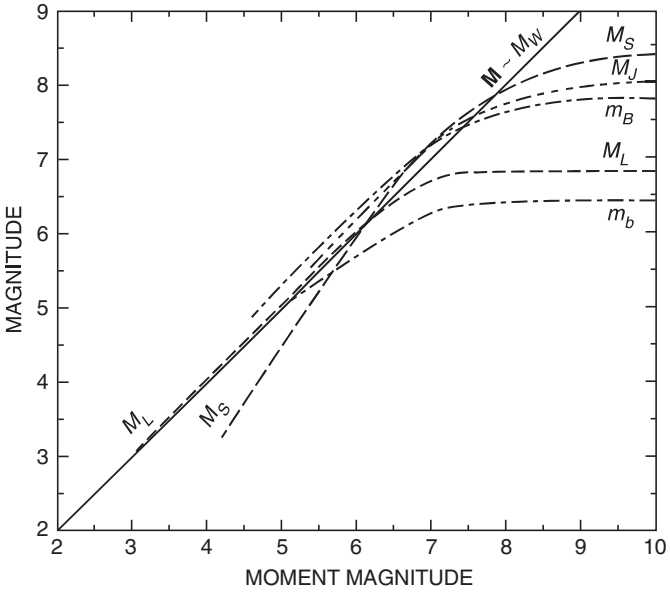

FIGURE 1 Comparison of magnitude scales (after Heaton *et al.*, 1986).

3.2 Type of Faulting and Focal Mechanism

The type of faulting, or focal mechanism, characterizes the orientation of slip on the fault plane, known as the rake, and the dip of the fault plane. Although rake is a continuous variable representing the angle between the direction of slip and the strike of the fault (the orientation of the fault on the Earth's surface), the type of faulting is typically classified into two or more categories for convenience. These categories will typically include strike slip (horizontal slip), reverse (dip slip with hanging-wall side up), thrust (same as reverse but with shallow dip) and normal (dip slip with hanging-wall side down). The values of rake corresponding to the pure form of these mechanisms are 0° (left-lateral slip) and 180° (right-lateral slip) for strike-slip faulting, 90° for reverse faulting, and 270° for normal faulting (Lay and Wallace, 1995).

Campbell (1981) was the first to empirically demonstrate that reverse and thrust-faulting earthquakes have relatively higher ground motions than strike-slip or normal-faulting earthquakes. All subsequent empirical and theoretical studies have found similar results (e.g., see the *Contemporary Guide* and Chapter 57 by Anderson). It has been common practice in the past to lump strike-slip events and normal-faulting events in the same category. However, a recent empirical study by Spudich *et al.* (1999) suggests that normal-faulting events, or for that matter strike-slip events in an extensional stress regime, might have lower ground motion than other types of shallow crustal events, an attribute first suggested by McGarr (1984). A preliminary interpretation of precarious rock observations by Brune (2000) suggests the presence of relatively low near-fault ground shaking on the footwall of normal faults, possibly due to a combination of faulting mechanism and footwall effects (see Section 4) that is not currently incorporated in any known attenuation relation (see the *Contemporary Guide*).

There has been a great deal of interest in blind-thrust faults after unusually large ground motions were observed during the 1987 Whittier Narrows, California, earthquake, the 1988 Saguenay, Canada, earthquake, and 1994 Northridge, California, earthquake. Whether similarly high ground motions can be expected from all future blind-thrust earthquakes is speculative. However, considering the current limited observational

database, it cannot be ruled out. The higher ground motions observed during these earthquakes have been found to correspond to higher-than-average dynamic stress drops (see Section 3.3), which have been speculatively attributed to a lack of surface rupture (Somerville, 2000) or a relatively low total slip on the causative faults (see Chapter 57 by Anderson). More theoretical and empirical studies will be needed before there is a clear understanding of why these earthquakes produced high stress drops and how such events might be identified in the future.

3.3 Stress Drop

Stress drop, or more correctly dynamic stress drop, is the amount of stress that is relieved at the rupture front during an earthquake. Theoretical studies have shown that higher stress drops correspond to higher ground motion. It has been shown theoretically (e.g., Boore and Atkinson, 1987) and implied empirically (Campbell and Bozorgnia, 2000) that stress drop has a larger effect on short-period ground motion, including PGA, than on long-period ground motion. The author is not aware of any current attenuation relation that explicitly includes stress drop as a parameter (see the *Contemporary Guide*). However, stress drop is one of the parameters that must be included either explicitly or implicitly in the theoretical calculation of ground motion. A more thorough discussion of this parameter is given in the *Contemporary Guide*.

As mentioned in Section 3.2, high stress drops are the likely cause of the relatively high ground motions observed during some recent blind-thrust earthquakes. On the other hand, low stress drops might be the cause of the relatively low short-period ground motions observed during the 1999 Chi-Chi (M_W 7.6), Taiwan, earthquake (Tsai and Huang, 2000; Boore, 2001) and the 1999 Kocaeli (M_W 7.4), Turkey, earthquake (Anderson, 2000). The observation of relatively low ground motions during the Chi-Chi earthquake is particularly significant, because it is a large thrust earthquake, which had been expected from previous empirical and theoretical studies to have relatively large ground motions. The relatively low stress drops implied for the Taiwan and Turkey earthquakes could be caused by the large total slip on the causative faults (see Chapter 57 by Anderson) or because they ruptured the Earth's surface (Somerville, 2000). More study will be needed to better understand the phenomena that might have contributed to these low ground motions. If these earthquakes are found to be typical of similar large earthquakes worldwide, then the implication is that the current attenuation relations overpredict short-period ground motions from large earthquakes, an attribute suggested from observations of precarious rocks near great earthquakes on the San Andreas fault (Brune, 1999).

3.4 Source Directivity and Radiation Pattern

Radiation pattern is the geographic asymmetry of the ground motion caused by the faulting process. It is closely related to the focal mechanism of the earthquake. The radiation pattern can be perturbed by source directivity, which is an increase or decrease in the ground motion caused by the propagation of the rupture along the fault. Ground-motion amplitudes in the forward direction of rupture propagation will be increased while those in the backward direction will be decreased due to source directivity. This effect is particularly important during unilateral faulting for sites located close to the fault (Somerville *et al*., 1997). Source directivity has its largest effect at long periods (periods greater than about 1 sec) on the horizontal component oriented perpendicular or normal to the fault plane.

Rupture directivity is a well-known seismological principle (Lay and Wallace, 1995). It has been observed or proposed as a factor in controlling the azimuthal dependence of ground motion during the 1979 Imperial Valley earthquake (Singh, 1985), the 1980 Livermore earthquakes (Boatwright and Boore, 1982), the 1989 Loma Prieta earthquake (Campbell, 1998), and the 1992 Landers earthquake (Campbell and Bozorgnia, 1994). Somerville *et al.* (1997) and Abrahamson (2000) present general empirical models for estimating the effects of source directivity and radiation pattern on the prediction of the fault-normal and fault-parallel components of the response spectrum. Somerville *et al.* also provide a list of near-source time histories that they believe to incorporate these effects. These models, along with a graphical description of the concept of radiation pattern and source directivity, are given in the *Contemporary Guide*.

Somerville (2000) suggests that the empirical models proposed by Abrahamson and Somerville *et al.* might be too simplistic. He has found that the near-fault directivity effects observed in several subsequent large earthquakes appear to manifest themselves as narrow-band pulses whose period markedly increases with increasing magnitude. This increase in period can actually lead to lower response-spectral ordinates at mid periods ($T_n \approx 1$ sec) as earthquakes exceed a magnitude threshold of around $7\frac{1}{4}$. This observation is inconsistent with the assumptions made in the Abrahamson and Somerville *et al*. directivity models that imply that directivity effects increase monotonically with magnitude at all periods. However, the directivity pulse model needs more development before it is ready to be used in engineering practice. Until then, the empirical models of Somerville *et al.* (1997) and Abrahamson (2000) remain the state of the art in the engineering characterization of source directivity effects.

4. Hanging-Wall and Footwall Effects

Generally speaking, the hanging wall is that portion of the crust that lies above the rupture plane of a dipping fault and the footwall is that portion of the crust that lies below this plane. The exact definitions of these two crustal regimes differ depending on the particular application. The definitions used to characterize hanging-wall and footwall effects on strong ground motion are given in the *Contemporary Guide*. Somerville and Abrahamson (1995, 2000), Abrahamson and Somerville (1996), and Abrahamson and Silva (1997) found empirical evidence to

indicate that sites located on the hanging wall of a reverse or thrust fault generally exhibit higher-than-average ground motion. Furthermore, Somerville and Abrahamson (1995) found that sites located on the footwall generally have lower-than-average ground motion. Although based on limited data, both hanging-wall and footwall effects were clearly demonstrated in the 1999 Chi-Chi, Taiwan, thrust earthquake (Shin and Teng, 2001). The hanging-wall effect is probably caused by a combination of radiation pattern, source directivity, and the entrapment of seismic waves within the hanging-wall wedge of the fault. The authors present a generalized empirical model for estimating the effects of the hanging wall and footwall on the estimation of strong ground motion. These models, together with a graphical description of the concept of hanging-wall and footwall effects, are given in the *Contemporary Guide*.

5. Source-to-Site Distance

Source-to-site distance, or simply distance, is used to characterize the decrease in ground motion as it propagates away from the earthquake source. Distance measures can be grouped into two broad categories depending on whether they treat the source of an earthquake as a single point (point-source measures) or as a finite rupture (finite-source measures). A brief description of the distance measures commonly used in attenuation relations is given next.

5.1 Point-Source Distance Measures

Point-source distance measures include epicentral distance (r_{epi}) and hypocentral distance (r_{hypo}). Hypocentral distance is the distance from the site to the point within the Earth where the earthquake rupture initiated (the hypocenter). Epicentral distance is the distance from the site to the point on the Earth's surface directly above the hypocenter (the epicenter). Generally speaking, r_{epi} and r_{hypo} are poor measures of distance for large earthquakes with extended ruptures. They are primarily used for characterizing small earthquakes that can be reasonably represented by a point source or for characterizing large earthquakes when the fault-rupture plane cannot be identified for past or future (design) earthquakes. Experience shows that attenuation relations that use point-source measures should not be used to estimate ground motion from large earthquakes unless there is absolutely no other means available.

5.2 Finite-Source Distance Measures

There are three finite-source distance measures that are commonly used in attenuation relations: r_{jb}, the closest horizontal distance to the vertical projection of the rupture plane, introduced by Joyner and Boore (1981); r_{rup}, the closest distance to the rupture plane, introduced by Schnabel and Seed (1973); and r_{seis}, the closest distance to the seismogenic part of the rupture plane, introduced by Campbell (1987, 2000a). The distance measure r_{seis} assumes that fault rupture within the near-surface sediments or the shallow portions of fault gouge is non-seismogenic, as suggested by Marone and Scholz (1988). These different distance measures are compared in Figure 1 of Chapter 59 by Bolt and Abrahamson.

The distance measure r_{jb} is reasonably easy to estimate for a future (design) earthquake. On the other hand, r_{rup} and r_{seis} are not as easily determined, particularly when the earthquake is not expected to rupture the entire seismogenic width of the crust. In such cases, the average depth to the top of the inferred rupture plane (d_{rup}) or to the seismogenic part of this rupture plane (d_{seis}) for an earthquake of moment magnitude M_W can be calculated from the equation (generalized from Campbell, 1997, 2000b)

$$d_i = \begin{cases} \frac{1}{2}[H_{\text{top}} + H_{\text{bot}} - W \sin(\gamma)] & \text{for } d_i \geq H_i \\ H_i & \text{otherwise} \end{cases} \tag{7}$$

where i = rup or seis, H_{bot} is the depth to the bottom of the seismogenic part of the crust, H_{top} is the depth to the top of the fault, H_{seis} is the depth to the top of the seismogenic part of the fault (to be used with the distance measure r_{seis}), γ is the fault dip; and W is the down-dip width of the fault-rupture surface. The down-dip width of the rupture plane can be calculated from the expression (Wells and Coppersmith, 1994)

$$\log W = -1.01 + 0.32 M_W \tag{8}$$

where W is in km and the standard deviation of $\log W$ is 0.15.

Campbell (1997) recommends $d_{\text{seis}} \geq 3$ km, even when the fault ruptures the Earth's surface. This recommendation is based on the following factors: (1) observations of aftershock distributions and background seismicity, (2) slip distributions from earthquake modeling studies, and (3) an independent assessment of seismogenic rupture by Marone and Scholz (1988). Representative values of d_{rup} and d_{seis} are given in the *Contemporary Guide*.

6. Local Site Conditions

Local site conditions describe the materials that lie directly beneath the site. They are usually defined in terms of surface and near-surface geology, shear-wave velocity, and sediment depth. The latter two descriptions are preferred because they represent parameters that can be related directly to the dynamic response of the site profile from vertically propagating body waves or horizontally propagating surface waves. Different classifications of local site conditions used in recently published attenuation relations are defined in the *Contemporary Guide*. A general description of these classifications is presented next. A more complete description of site effects is given in Chapter 61 by Kawase.

6.1 Surface and Near-Surface Geology

Traditionally, local site conditions have been classified as either soil or rock. Many attenuation relations still use this simple classification. Campbell (1981) proposed that soil should be further

subdivided into shallow soil, soft soil, Holocene or firm soil, and Pleistocene or very firm soil, and that rock should be further subdivided into soft or primarily sedimentary rock and hard or primarily crystalline rock. Although this more refined geological classification has generally not been used, Campbell and Bozorgnia (2000) empirically demonstrate the importance of this more refined classification scheme in the estimation of near-source ground motion. Park and Elrick (1998) and Wills and Silva (1998) have also shown that a more refined geological classification might be warranted based on measurements of shear-wave velocity for different geologic units in California.

6.2 Shear-Wave Velocity

There are typically two methods for classifying a site in terms of shear-wave velocity (V_S). The first is the average value of V_S in the top 30 m (100 ft) of a site profile, known as 30-meter velocity. The second is the average value of V_S over a depth equal to a quarter-wavelength of the ground-motion frequency or period of interest, known as effective velocity. A brief description of these two velocity-based site parameters is given next.

6.2.1 30-Meter Velocity

The 1997 *Uniform Building Code* (UBC), the 1997 *NEHRP* (National Earthquake Hazard Reduction Program) *Recommended Provisions for Seismic Regulations for New Buildings and Other Structures*, and the 2000 *International Building Code* (IBC) have all adopted the 30-meter velocity ($\bar{v}_s$) as the primary basis for classifying a site for purposes of incorporating local site conditions in the estimation of strong ground motion (see Chapter 68 by Borcherdt *et al.*). Seven site classes, designated S_A or A (Hard Rock) through S_F or F (Soft Soil Profile), are defined in terms of $\bar{v}_s$ (Table 1). The value of $\bar{v}_s$ is determined from the formula

$$\bar{v}_s = \frac{\sum_{i=1}^{n} d_i}{\sum_{i=1}^{n} d_i / v_{si}} \tag{9}$$

where d_i is the thickness and v_{si} is the shear-wave velocity of site layer i. The summation in the numerator must equal 100 ft (30 m).

Boore *et al.* (1993) were the first to use site categories based on $\bar{v}_s$ in the development of an attenuation relation. In 1994, these same authors were the first to use $\bar{v}_s$ directly as a parameter in an attenuation relation (this same attenuation relation was later published in Boore *et al.*, 1997). Because of its adoption by the building codes, $\bar{v}_s$ has become the preferred site parameter to use in engineering practice. According to Boore and Joyner (1997), $\bar{v}_s = 310$ m/sec and $\bar{v}_s = 620$ m/sec are reasonable estimates of 30-meter velocity for generic soil and generic rock sites in western North America. An approximate correspondence among values of $\bar{v}_s$, their related site classes, and the site parameters used in recently published attenuation relations are given in the *Contemporary Guide*.

TABLE 1 Site Classes Defined in the U.S. Building Codes

Site Class	Soil Profile Name	30-Meter Velocity, $\bar{v}_s$ m/sec (ft/sec)
S_A or A	Hard Rock	>1500 (>5000)
S_B or B	Rock	760–1500 (2500–5000)
S_C or C	Very Dense Soil and Soft Rock	360–760 (1200–2500)
S_D or D	Stiff Soil Profile	180–360 (600–1200)
S_E or E	Soft Soil Profile	<180 (<600)
S_F or F	Soil Requiring Site-Specific Evaluation	

6.2.2 Effective Velocity

Joyner *et al.* (1981) proposed a V_S-based site parameter that is related to the nonresonant amplification produced as a result of the energy conservation of seismic waves propagating vertically upward through a site profile of gradually changing velocity. This parameter, which was later referred to as effective velocity by Boore and Joyner (1991), is defined as the average velocity from the surface to a depth corresponding to a quarter-wavelength of the ground-motion period or frequency of interest. Effective velocity can be calculated from Eq. (9) by summing to a depth corresponding to a quarter-wavelength rather than to 30 m. This depth is given by the expression

$$D_{1/4}(f) = \frac{\sum_{i=1}^{n} d_i}{4f \sum_{i=1}^{n} d_i / v_{si}} \tag{10}$$

where $T = 1/f$ is the period of interest. Progressively deeper soil layers are included in the summations until the equality $\sum_{i=1}^{n} 1/v_{si} = 1/(4f)$ is met.

Effective velocity is expected to represent site response better than 30-meter velocity because of its direct relationship to the period of the ground motion. Joyner and Fumal (1984) are the only investigators to include it as a parameter in an empirical attenuation relation (this same attenuation relation was later published in Joyner and Boore, 1988). Effective velocity has found widespread use in the calculation of site response in the stochastic simulation of ground motion (see the *Contemporary Guide*).

6.3 Sediment Depth

Sediment depth, also referred to as basin depth, is the depth to basement rock beneath the site. Basement rock is a geological term that is used to describe the more resistant, generally crystalline rock beneath layers or irregular deposits of younger, relatively deformed sedimentary rock. It was introduced as a site parameter by Trifunac and Lee (1979) and later used by Campbell (1987, 2000a) to quantify the response of long-period response-spectral ordinates. All of these investigators have continued to use this parameter in their more recent studies (e.g., Trifunac and Lee, 1989, 1992; Campbell, 1997). Recently, its importance has been recognized by several seismologists (e.g., Field, 2000; Lee and Anderson, 2000). Based on empirical and theoretical considerations, Joyner (2000) found that sediment

depth appeared to be a reasonable proxy for the effects of traveling surface waves generated at the edge of a sedimentary basin. Field and the SCEC Phase III Working Group (2000) found that sediment depth could be used as a proxy for the three-dimensional response of the Los Angeles basin.

7. Site Location

Attenuation relations are intended to provide estimates of strong ground motion on level ground in the free field. This means that the strong-motion recordings used to develop these relations should not be located on or near a large structure, in an area of strong topographic relief, or below the ground surface. All of these situations have been shown to significantly modify free-field ground motion in some situations (e.g., Campbell, 1986, 1987, 2000a; Stewart, 2000). To avoid these effects, most investigators exclude certain recordings from their database. However, not all of these investigators agree on which types of recordings should be excluded. Also, because the majority of the available strong-motion recordings were obtained in or near a structure, it is impossible to restrict the database to truly free-field recordings without decimating it to the point where there are an insufficient number of recordings for a robust statistical analysis.

It has been shown both empirically and theoretically that recordings obtained in a large building, especially when located on soil, or on an embedded instrument, reduce the amplitude of ground motion at high frequencies. Therefore, it is clear that such recordings should be excluded. The effects of other site locations are not so easily quantified. Stewart (2000) has proposed some quantitative criteria that will help to identify which recordings should be excluded in the future. Different data selection criteria used to develop some recently published attenuation relations are described in the references to the attenuation relations provided in the *Contemporary Guide*.

8. Tectonic Environment

The tectonic environment has a significant impact on the amplitude and attenuation of strong ground motion. Tectonic environment can be classified into four basic types as follows: (1) shallow-crustal earthquakes in active tectonic regions, (2) shallow-crustal earthquakes in stable tectonic regions, (3) intermediate-depth earthquakes (also known as Wadati-Benioff or intraslab earthquakes) within a subducting plate, and (4) earthquakes on the interface of two subducting plates. The shallow-crustal environment can be further divided into compressional and extensional stress regimes. Subduction interface earthquakes occur on the seismogenic interface between two tectonic plates, where one plate (usually oceanic crust) thrusts, or is subducted, beneath another (usually continental crust). Depending on the age of the subducting plate, this interface can occur at depths ranging anywhere from 20 to 50 km. Wadati-Benioff earthquakes occur within the subducting plate as it descends within the Earth's mantle below the subduction interface zone. Recently published attenuation relations representing these different tectonic environments are given in the *Contemporary Guide*. Moores and Twiss (1995) provide a general discussion of the different tectonic environments that are found throughout the world. Johnston (1996) gives a map that shows the location of stable continental regions throughout the world. Zoback (1992) and Chapter 34 by Zoback and Zoback provide a map that shows the distribution of compressional and extensional stress regimes throughout the world.

9. Random Error

Random error is the scatter of the observed values of ground motion about their predicted values. It is derived from Eq. (2) by performing a regression analysis and calculating the standard error of estimate of $\ln Y$ from the resulting residuals. The basic assumption in this process, which is rarely tested statistically, is that $\ln Y$ can be represented by a normal, or Gaussian, distribution (i.e., Y is lognormally distributed).

9.1 Regression Analysis

Whether developed from empirical observations or theoretical "data," all attenuation relations are derived from a statistical fitting procedure known as regression analysis. This analysis is used to determine the best estimate of the coefficients c_1 through c_8 in Eqs. (2) and (3) using a fitting procedure such as least squares or maximum likelihood. Traditionally, there have been three different methods used to perform this analysis: (1) weighted nonlinear least-squares regression, introduced by Campbell (1981); (2) two-step regression, introduced by Joyner and Boore (1981) and later refined by Joyner and Boore (1994); and (3) random-effects regression, introduced by Brillinger and Preisler (1984). Each of these methods has its strengths and weaknesses, but they all have the same goal of reducing the bias introduced by the uneven distribution of recordings with respect to magnitude, distance, and other seismological parameters. The advantage of the latter two methods is that they provide a direct estimate of the intra-earthquake and inter-earthquake components of randomness (see Section 9.2).

9.2 Standard Deviation

The difference between a ground-motion observation and its predicted value is known as a residual. The standard deviation of the residuals is called the standard error of estimate of regression and represents a measure of aleatory variability (randomness) in the estimate of the ground motion. The standard deviation of $\ln Y$ is calculated from the expression

$$\sigma_{\ln Y} = \sqrt{\frac{1}{n-p}\sum_{i=1}^{n}(\ln Y_i - \overline{\ln Y_i})^2} \qquad (11)$$

where n is the number of observations, p is the number of regression coefficients, $\ln Y_i$ is the ith observation, and $\overline{\ln Y_i}$ is the predicted value of the ith observation. A plot of the residuals versus a seismological parameter can be used to identify a trend or bias in the regression model. A bias that is observed either visually or statistically using a hypothesis test can indicate a problem with the functional form of the regression model or the need to include another parameter in the model.

It is often convenient to segregate $\sigma_{\ln Y}$ into its intra-earthquake and inter-earthquake components, traditionally designated σ and τ. Abrahamson and Youngs (1992) and Joyner and Boore (1993, 1994) give specific algorithms that can be used to estimate intra-earthquake and inter-earthquake standard deviations from random-effects and two-step regression analyses, respectively. Furthermore, if the regression analysis is performed on the geometric mean of the two horizontal components of a ground-motion parameter, equivalent to the average of the logarithms of these two components, and the variability between these components is desired, an additional component-to-component random error term is needed. Referring to the three random error terms as σ_{intra}, σ_{inter} and σ_{comp}, the total standard deviation of $\ln Y$ can be given by the expression

$$\sigma_{\ln Y} = \sqrt{\sigma_{\text{inter}}^2 + \sigma_{\text{intra}}^2 + \sigma_{\text{comp}}^2} \tag{12}$$

The standard deviation of $\ln Y$ has been found to be a function of magnitude (e.g., Youngs *et al.*, 1995) and the amplitude of ground motion (introduced by Donovan and Bornstein, 1978, and later statistically defined by Campbell, 1997). However, not all attenuation relations take these dependencies into account in defining the value of $\sigma_{\ln Y}$. These dependencies can be significant and will always result in relatively lower estimates of $\sigma_{\ln Y}$ at larger magnitudes or higher ground-motion amplitudes. Lower estimates of standard deviation can lead to a significant reduction in deterministic estimates of ground motion at the upper percentiles of the ground-motion distribution and in probabilistic estimates of ground motion at the longer return periods of the seismic hazard curve.

9.3 Predicted Value

Because the predicted value of ground motion from Eq. (2) is the logarithm of Y, it represents the mean of $\ln Y$ or equivalently the 50^{th}-percentile (median value) of Y. The median is the value of Y that is exceeded by 50% of the observations and is, therefore, the value of Y that is expected to have a 50–50 chance of being exceeded by a future recording. The $100(1-\alpha)$-percentile estimate of the mean of n_0 future observations of $\ln Y$ is statistically defined by the expression (Draper and Smith, 1981)

$$\ln Y_{1-\alpha} = \ln Y + t_\nu(\alpha)\sqrt{\frac{\sigma_{\ln Y}^2}{n_0} + \sigma_{\overline{\ln Y}}^2} \tag{13}$$

where $t_\nu(\alpha)$ is the Student's t-statistic for an exceedance probability of α and for $\nu = n - p$ degrees of freedom (this statistic can be found in any statistics book) and $\sigma_{\overline{\ln Y}}$ is the standard error of the mean value of $\ln Y$ excluding random error (Draper and Smith, 1981). The $100\,(1-\alpha)$-percentile estimate of a single future observation of $\ln Y$, the most common application of Eq. (13), is calculated by setting $n_0 = 1$.

Equation (13) is most commonly used to calculate the $100(1-\alpha)$-percentile estimate of a single future value of $\ln Y$ by setting $\sigma_{\overline{\ln Y}} = 0$ and replacing the t-statistic with the standard normal variable, giving

$$\ln Y_{1-\alpha} = \ln Y + z_\alpha \sigma_{\ln Y} \tag{14}$$

where z_α is the standard normal variable for an exceedance probability of α (this variable can be found in any statistics book). Although statistically incorrect, the use of Eq. (14) does not result in significantly different results, except when the regression model is based on very few recordings, in which case the t-statistic should be used, or when the predicted value is based on an extrapolation of the regression equation, in which case the value of $\sigma_{\overline{\ln Y}}$ cannot be neglected.

The most common application of Eq. (14) is to estimate the median or 50th-percentile value of $Y(\alpha = 0.5)$ by setting $z_\alpha = 0$, or to estimate the 84th-percentile value of $Y(\alpha = 0.16)$ by setting $z_\alpha = 1$. The 84th-percentile is often used as a conservative estimate of Y to use for the design of important facilities. Epistemic uncertainty in these estimates is usually incorporated by using more than one attenuation relation to estimate Y.

References

Abrahamson, N. A. (2000). Effects of rupture directivity on probabilistic seismic hazard analysis. In: "Proc., 6th International Conference on Seismic Zonation," Nov. 12–15, 2000, Palm Springs, CA, Proc. CD-ROM, 6 pp. Earthquake Engineering Research Institute, Oakland, CA.

Abrahamson, N. A., and K. M. Shedlock (1997). Overview. *Seismol. Res. Lett.* **68**, 9–23.

Abrahamson, N. A., and W. J. Silva (1997). Empirical response spectral attenuation relations for shallow crustal earthquakes. *Seismol. Res. Lett.* **68**, 94–127.

Abrahamson, N. A., and P. C. Somerville (1996). Effects of the hanging wall and footwall on ground motions recorded during the Northridge earthquake. *Bull. Seismol. Soc. Am.* **86**, S93–S99.

Abrahamson, N. A., and R. R. Youngs (1992). A stable algorithm for regression analyses using the random effects model. *Bull. Seismol. Soc. Am.* **82**, 505–510.

Anderson, J. G. (2000). Expected shape of regressions for ground motion parameters on rock. *Bull. Seismol. Soc. Am.* **90**, S43–S52.

Boatwright, J. A., and D. M. Boore (1982). Analysis of the ground accelerations radiated by the 1980 Livermore Valley earthquakes for directivity and dynamic source characteristics. *Bull. Seismol. Soc. Am.* **72**, 1843–1865.

Bolt, B. A. (1993). *Earthquakes and Geological Discovery*. Scientific American Library, New York.

Boore, D. M. (2001). Comparisons of ground motions from the 1999 Chi-Chi earthquake with empirical predictions largely based

on data from California. *Bull. Seismol. Soc. Am.* **91**, 1212–1217.

Boore, D. M. (2002). Prediction of ground motion using the stochastic method. *Pure Appl. Geophys.* (in press).

Boore, D. M., and G. M. Atkinson (1987). Stochastic prediction of ground motion and spectral response parameters at hard-rock sites in eastern North America. *Bull. Seismol. Soc. Am.* **77**, 440–467.

Boore, D. M., and W. B. Joyner (1991). Estimation of ground motion at deep-soil sites in eastern North America. *Bull. Seismol. Soc. Am.* **81**, 2167–2185.

Boore, D. M., and W. B. Joyner (1997). Site amplification for generic rock sites. *Bull. Seismol. Soc. Am.* **87**, 327–341.

Boore, D. M., W. B. Joyner, and T. E. Fumal (1993). Estimation of response spectra and peak accelerations from western North American earthquakes: An interim report. *Open-File Report 93-509, U.S. Geol. Surv.*, Menlo Park, California.

Boore, D. M., W. B. Joyner, and T. E. Fumal (1994). Estimation of response spectra and peak accelerations from western North American earthquakes: An interim report, part 2. *Open-File Report 94-127, U.S. Geol. Surv.*, Menlo Park, California.

Boore, D. M., W. B. Joyner, and T. E. Fumal (1997). Equations for estimating horizontal response spectra and peak acceleration from western North American earthquakes: a summary of recent work. *Seismol. Res. Lett.* **68**, 128–153.

Brillinger, D. R., and H. K. Preisler (1984). An exploratory analysis of the Joyner-Boore attenuation data. *Bull. Seismol. Soc. Am.* **74**, 1441–1450.

Brune, J. N. (1999). Precarious rocks along the Mojave section of the San Andreas fault, California: constraints on ground motion from great earthquakes. *Seismol. Res. Lett.* **70**, 29–33.

Brune, J. N. (2000). Precarious rock evidence for low ground shaking on the footwall of major normal faults. *Bull. Seismol. Soc. Am.* **90**, 1107–1112.

Campbell, K. W. (1981). Near-source attenuation of peak horizontal acceleration. *Bull. Seismol. Soc. Am.* **71**, 2039–2070.

Campbell, K. W. (1986). Empirical prediction of free-field ground motion using statistical regression models. In: "Proc., Soil Structure Interaction Workshop," NUREG/CR-0054, pp. 72–115. U.S. Nuclear Regulatory Commission, Washington, D.C.

Campbell, K. W. (1987). Predicting strong ground motion in Utah. In: "Assessment of Regional Earthquake Hazards and Risk Along the Wasatch Front, Utah" (P. L. Gori and W. W. Hays, Eds.), *U.S. Geol. Surv. Open-File Report 87-585*, Vol. II, pp. L1–L90, Reston, Virginia.

Campbell, K. W. (1997). Empirical near-source attenuation relationships for horizontal and vertical components of peak ground acceleration, peak ground velocity, and pseudo-absolute acceleration response spectra. *Seismol. Res. Lett.* **68**, 154–179.

Campbell, K. W. (1998). Empirical analysis of peak horizontal acceleration, peak horizontal velocity, and modified Mercalli intensity. In: "The Loma Prieta, California, Earthquake of October 17, 1989—Earth Structures and Engineering Characterization of Ground Motion" (T. L. Holzer, Ed.), *U.S. Geol. Surv., Profess. Paper 1552-D*, pp. D47–D68.

Campbell, K. W. (2000a). Predicting strong ground motion in Utah. In: "Assessment of Regional Earthquake Hazards and Risk Along the Wasatch Front, Utah" (P. L. Gori and W. W. Hays, Eds.), *U.S. Geol. Surv., Profess. Paper 1500-L*, pp. L1–L31.

Campbell, K. W. (2000b). Erratum: empirical near-source attenuation relationships for horizontal and vertical components of peak ground acceleration, peak ground velocity, and pseudo-absolute acceleration response spectra. *Seismol. Res. Lett.* **71**, 353–355.

Campbell, K. W. (2002). Engineering seismology. In: "Encyclopedia of Physical Science and Technology," 3rd ed., Academic Press, San Diego, Vol. 14, pp. 531–545.

Campbell, K. W., and Y. Bozorgnia (1994). Empirical analysis of strong ground motion from the 1992 Landers, California, earthquake. *Bull. Seismol. Soc. Am.* **84**, 573–588.

Campbell, K. W., and Y. Bozorgnia (2000). New empirical models for predicting near-source horizontal, vertical, and V/H response spectra: Implications for design. In: "Proc., 6th International Conference on Seismic Zonation," Nov. 12–15, 2000, Palm Springs, CA, Proc. CD-ROM, 6 pp. Earthquake Engineering Research Institute, Oakland, CA.

Donovan, N. C., and A. E. Bornstein (1978). Uncertainties in seismic risk procedures. *J. Geotech. Eng. Div.*, ASCE **104**, 869–887.

Douglas, J. (2002). Earthquake ground motion estimation using strong-motion records: a review of equations for the estimation of peak ground acceleration and response spectral ordinates. *Earth-Science Reviews* (submitted).

Draper, N. R., and H. Smith (1981). *Applied Regression Analysis*, 2nd ed. John Wiley and Sons, New York.

Field, E. H. (2000). A modified ground-motion attenuation relationship for southern California that accounts for detailed site classification and a basin-depth effect. *Bull. Seismol. Soc. Am.* **90**, S209–S221.

Field, E. H. and the SCEC Phase III Working Group (2000). Accounting for site-effects in probabilistic seismic hazard analyses of Southern California: Overview of the SCEC Phase III Report. *Bull. Seismo. Soc. Am.* **90**, S1–S31.

Gupta, A. K. (1993). *Response Spectrum Method in Seismic Analysis and Design.* CRC Press, Boca Raton, FL.

Hanks, T. C., and H. Kanamori (1979). A moment-magnitude scale. *J. Geophys. Res.* **84**, 2348–2350.

Heaton, T. H., F. Tajima, and A. W. Mori (1986). Estimating ground motions using recorded accelerograms. *Surv. in Geophys.* **8**, 25–83.

Johnston, A. C. (1996). Seismic moment assessment of earthquakes in stable continental regions, I. Instrumental seismicity. *Geophys. J. Int.* **124**, 381–414.

Joyner, W. B. (2000). Strong motion from surface waves in deep sedimentary basins. *Bull. Seismol. Soc. Am.* **90**, S95–S112.

Joyner, W. B., and D. M. Boore (1981). Peak horizontal acceleration and velocity from strong-motion records including records from the 1979 Imperial Valley, California, earthquake. *Bull. Seismol. Soc. Am.* **71**, 2011–2038.

Joyner, W. B., and D. M. Boore (1988). Measurement, characterization, and prediction of strong ground motion. In: "Proc., Conference on Earthquake Engineering and Soil Dynamics II—Recent Advances in Ground-Motion Evaluation" (J. L. Von Thun, Ed.), June 27–30, 1988, Park City, UT, Geot. Spec. Pub. No. 20, pp. 43–102. American Society of Civil Engineers, New York.

Joyner, W. B., and D. M. Boore (1993). Methods for regression analysis of strong-motion data. *Bull. Seismol. Soc. Am.* **83**, 469–487.

Joyner, W. B., and D. M. Boore (1994). Errata: methods for regression analysis of strong-motion data. *Bull. Seismol. Soc. Am.* **84**, 955–956.

Joyner, W. B., and T. E. Fumal (1984). Use of measured shear-wave velocity for predicting geologic site effects on strong ground motion. In: "Proc., 8th World Conference on Earthquake Engineering," Vol. 2, pp. 777–783.

Joyner, W. B., R. E. Warrick, and T. E. Fumal (1981). The effect of Quaternary alluvium on strong ground motion in the Coyote Lake, California, earthquake of 1979. *Bull. Seismol. Soc. Am.* **71**, 1333–1349.

Kanamori, H. (1978). Quantification of earthquakes. *Nature* **271**, 411–414.

Lay, T., and T. C. Wallace (1995). *Modern Global Seismology*. Academic Press, San Diego, CA.

Lee, Y., and J. G. Anderson (2000). Potential for improving ground-motion relations in Southern California by incorporating various site parameters. *Bull. Seismol. Soc. Am.* **90**, S170–S186.

Leyendecker, E. V., J. R. Hunt, A. D. Frankel, and, K. S. Rukstales (2000). Development of maximum considered earthquake ground motion maps. *Earthquake Spectra* **16**, 21–40.

Marone, C., and C. H. Scholz (1988). The depth of seismic faulting and the upper transition from stable to unstable slip regimes. *Geophys. Res. Lett.* **15**, 621–624.

McGarr, A. (1984). Scaling of ground motion parameters, state of stress, and focal depth. *J. Geophys. Res.* **89**, 6969–6979.

Moores, E. M., and R. J. Twiss (1995). *Tectonics*. W.H. Freeman and Company, New York.

Newmark, N. M., and W. J. Hall (1982). *Earthquake Spectra and Design*. Earthquake Engineering Research Institute, Berkeley, CA.

Park, S., and S. Elrick (1988). Predictions of shear-wave velocities in southern California using surface geology. *Bull. Seismol. Soc. Am.* **88**, 677–685.

Richter, C. F. (1935). An instrumental earthquake magnitude scale. *Bull. Seismol. Soc. Am.* **25**, 1–32.

Schnabel, P. B., and H. B. Seed (1973). Accelerations in rock for earthquakes in the western United States. *Bull. Seismol. Soc. Am.* **63**, 501–516.

Shin, T. C., and T. L. Teng (2001). An overview of the 1999 Chi-Chi, Taiwan, earthquake. *Bull. Seismol. Soc. Am.* **91**, 895–913.

Singh, J. P. (1985). Earthquake ground motions: implications for designing structures and reconciling structural damage. *Earthquake Spectra* **1**, 239–270.

Somerville, P. (2000). New developments in seismic hazard estimation. In: "Proc., 6th International Conference on Seismic Zonation," Nov. 12–15, 2000, Palm Springs, CA, Proc. CD-ROM, 25 pp. Earthquake Engineering Research Institute, Oakland, CA.

Somerville, P., and N. Abrahamson (1995). Ground motion prediction for thrust earthquakes. In: "Proc., SMIP95 Seminar on Seismological and Engineering Implications of Recent Strong-Motion Data," May 16, 1995, San Francisco, pp. 11–23. California Strong Motion Instrumentation Program, Sacramento, CA.

Somerville, P., and N. Abrahamson (2000). Prediction of ground motions for thrust earthquakes. *Data Utilization Rept. No. CSMIP/00-01* (*OSMS 00-03*), California Strong Motion Instrumentation Program, Sacramento, CA.

Somerville, P. G., N. F. Smith, R. W. Graves, and N. A. Abrahamson (1997). Modification of empirical strong ground motion attenuation relations to include the amplitude and duration effects of rupture directivity. *Seismol. Res. Lett.* **68**, 199–222.

Spudich, P., W. B. Joyner, A. G. Lindh, D. M. Boore, B. M. Margaris, and J. B. Fletcher (1999). SEA99: a revised ground motion prediction relation for use in extensional tectonic regimes. *Bull. Seismol. Soc. Am.* **89**, 1156–1170.

Stewart, J. P. (2000). Variations between foundation-level and free-field earthquake ground motions. *Earthquake Spectra* **16**, 511–532.

Trifunac, M. D., and V. W. Lee (1979). Dependence of pseudo-relative velocity spectra of strong motion acceleration on the depth of sedimentary deposits. *Report No. CE79-02*, Dept. of Civil Engineering, University of Southern California, Los Angeles.

Trifunac, M. D., and V. W. Lee (1989). Empirical models for scaling pseudo relative velocity spectra of strong earthquake accelerations in terms of magnitude, distance, site intensity and recording site conditions. *Soil Dyn. and Earthq. Eng.* **8**, 126–144.

Trifunac, M. D., and V. W. Lee (1992). A note on scaling peak acceleration, velocity and displacement of strong earthquake shaking by Modified Mercalli Intensity (MMI) and site soil and geologic conditions. *Soil Dyn. and Earthq. Eng.* **11**, 101–110.

Tsai, Y. B., and M. W. Huang (2000). Strong ground motion characteristics of the Chi-Chi, Taiwan earthquake of September 21, 1999. *Earthq. Eng. and Eng. Seismol.* **2**, 1–21.

Wells, D. L., and K. J. Coppersmith (1994). New empirical relationships among magnitude, rupture length, rupture width, rupture area, and surface displacement. *Bull. Seismol. Soc. Am.* **84**, 974–1002.

Wills, C. J., and W. Silva (1998). Shear-wave velocity characteristics of geologic units in California. *Earthquake Spectra* **14**, 533–556.

Youngs, R. R., N. A. Abrahamson, F. Makdisi, and K. Sadigh (1995). Magnitude dependent dispersion in peak ground acceleration. *Bull. Seismol. Soc. Am.* **85**, 1161–1176.

Zoback, M. L. (1992). First- and second-order patterns of stress in the lithosphere: the world stress map project. *J. Geophys. Res.* **97**, 11703–11728.

Editor's Note:

Due to space limitations, a supplemental contemporary guide to strong-motion attenuation relations is included as a computer-readable file on the attached Handbook CD under the directory \60Campbell. Also included in this directory is a supplemental electronic workbook that can be used to evaluate the attenuation relations and other engineering models that are presented in this *Contemporary Guide*.

61

Site Effects on Strong Ground Motions

Hiroshi Kawase
Graduate School of Human Environment Studies, Kyushu University, Fukuoka, Japan

1. Introduction

Site effects play a very important role in characterizing seismic ground motions because they may strongly amplify (or deamplify) seismic motions at the last moment just before reaching the surface of the ground or the basement of man-made structures. Because of the high level of amplification caused by site effects, which can be almost two orders of magnitude, we cannot neglect them in engineering practice. The purpose of this chapter is to review the essential aspects of site effects on strong ground motions.

For much of the history of seismological research, site effects or the effects of surface geology have received much less attention than they should, with the exception of Japan, where they have been well recognized through pioneering works by Sezawa and Ishimoto as early as the 1930s (Kawase and Aki, 1989). A typical example can be found in a paper by Hudson (1972), who found no strong correlation between the strength of observed ground motion and the surface geology of the stations for the San Fernando earthquake dataset. The situation was drastically changed by the catastrophic disaster in Mexico City during the Michoacan, Mexico earthquake of 1985, in which strong amplification due to extremely soft clay layers caused many high-rise buildings to collapse despite their long distance from the source. The real cause of the observed long duration of shaking during the earthquake is not well resolved yet even though considerable research has been conducted since then (e.g., Bard *et al*., 1988; Kawase and Aki, 1989; Singh and Ordaz, 1993; Chavez-Garcia and Bard, 1994; Furumura and Kennett, 1998). However, there is no room for doubt that the primary cause of the large amplitude of strong motions in the soft soil (lakebed) zone relative to those in the hill zone is a simple one-dimensional (1-D) site effect of these soft layers.

The time was right when the joint working group of IASPEI and IAEE on the effects of surface geology (ESG) on strong motions was formed in 1985 as an international task force for promoting and coordinating research in this field (Kudo *et al*., 1992). As a result of their activity, international symposia have been held twice, both in Japan, in 1992 and 1998, where many ongoing activities have been reported. Interested readers should refer to the proceedings of these symposia (JWG-ESG, 1992; Irikura *et al*, 1998).

There are plenty of ways to estimate site effects. The simplest way is to characterize them in terms of soil-type classification. Such soil-type specific amplification factors were implemented in the first version of the Japanese building code as early as the 1950s. Problems associated with such an idea are discussed in detail by Aki (1988), who concluded that the conventional broad classification of soil types is not effective for characterizing site effects. Because site amplification factors are strongly frequency and site dependent, any averaged values for different sites with the same site category yield relatively small and flat frequency characteristics, which is far from the reality at any sites in that category. Unfortunately, the soil-type approach continues to be a favored way to characterize site effects. Because our space is limited and further encouragement of the soil-type approach is not appropriate, we skip a review of studies for that approach.

Another empirical approach is to obtain site amplification factors in the frequency domain directly from the observed records. The observed ground motion itself is the final product of source, path, and site effects, so we need a way to extract only the site effects from the data. A basic but effective approach is to take spectral ratios of two adjacent records with different soil conditions. An ideal case is a free-field site on an intact hard rock outcrop next to a site on soft sedimentary layers. In reality, it is hard to find a site-effect-free reference site either because

INTERNATIONAL HANDBOOK OF EARTHQUAKE AND ENGINEERING SEISMOLOGY, VOLUME 81B *ISBN: 0-12-440658-0*

topographic irregularities around the site or weathered layers below the site yield strong site effects or because such a reference site is situated far away from the target site.

If we install borehole stations just beneath the surface station, i.e., conduct downhole measurements, then we can directly observe wave propagation phenomena between these stations. We should note, however, that a borehole seismogram inside the bedrock is not the same as an outcrop rock motion. In the borehole station we observe both incident waves coming up from below and reflected waves going back from the surface. Spectral ratios of surface records with respect to borehole records have predominant peaks either due to the amplification of surface soils or due to the interference (i.e., cancellation) of incident and reflected waves. Another drawback of borehole measurements is their high cost compared to a surface implementation.

Another recent innovation for finding site characteristics is to take ratios of horizontal to vertical components (H/V). We only need one three-component station on the surface. However, the physical meaning of the ratio is not so easy to interpret. And neither borehole ratios nor H/V ratios directly represent the real soil amplification relative to the unit input, so we also need to simulate these observed spectral ratios through physical modeling.

Physical modeling of the ground as a medium of seismic wave propagation from the source to the receiver or from the reference position to the receiver is the most rigorous approach to characterizing site effects. By modeling the ground theoretically, we can simulate ground motions for any arbitrary source of vibration. If the incident wave is so intense that soft-soil sediments go to the nonlinear regime, then we can introduce a nonlinear constitutive relationship in the physical model. If the layered structure is very complicated and has lens-like structures here and there, then we can construct irregular interfaces between layers to reproduce wave propagation and scattering through these interfaces. Once we establish an appropriate physical model around a target site, any kind of strong-motion prediction becomes possible.

The down side of this approach is that we must invest time and effort to characterize and model the ground, to develop theoretical or numerical methodologies, and to collect observed data. Once we have an initial model of the ground, an initial technique to solve the problem, and an initial database of observed data, we can calibrate our model and method to the observed data. If the initial matching with data is not satisfactory, then we will upgrade either our model or our method, or both. We may need additional data to constrain the model more strongly. The importance of such ongoing activity in the model-oriented approach is emphasized by Kawase (1993), who characterized the ground modeling, numerical technique development, and strong-motion observation as a triadic structure of the site-effect studies. We would like to emphasize here the importance of the calibration phase in the physical modeling approach because any results from modeling are just hypothesized ones if not calibrated. In this chapter we devote ourselves mainly to this modeling approach because this is the most efficient way to quantitatively characterize site effects in the long run.

2. Physical Modeling of Site Effects

When we model physical behavior of the actual ground by a seismic disturbance, we must introduce some kind of simplification because the actual ground is extremely complex in a three-dimensional manner. The simplest model of the ground is a homogeneous full-space, in which there is no site effect because there are no boundaries and no interfaces. The second simplest model is a homogeneous half-space, in which interaction with reflected waves may give very conspicuous amplification in a critical incidence (Aki, 1988) and Rayleigh waves may transport a significant part of wave energy for a shallow source. Although theoretically interesting, these models are too simple to be meaningful models for site-effect studies. We must at least take into account the impedance contrast due to younger sediments overlying older bedrock. When we assume a horizontally homogeneous but *vertically* varying medium, we can call it a one-dimensional (1-D) medium. Literally speaking, we could also consider a 1-D medium varying only in one *horizontal* axis, as is the case of a fault gouge deep inside the Earth. However, for most of the cases in site-effect studies a 1-D medium means a vertically varying structure.

If we introduce another variation in one horizontal axis, then it will be a two-dimensional (2-D) medium. Naturally, if we have variations in both horizontal directions then it will be a three-dimensional (3-D) medium. As the number of varying dimensions increases, the degree of complexity in wave propagation increases and so does the difficulty of modeling and calculation. We will start from 1-D modeling of site effects, including theoretical and observational aspects and a brief look at nonlinear problems. Then we review 2-D/3-D modeling in which we see several interesting phenomena due to constructive (and destructive) interference by different types of waves.

If the spatial variation is only on the surface of a homogeneous medium, the effects of such a surface irregularity, often called a topographic irregularity, should be much simpler than the variation inside the medium. In the last section we briefly describe topographic effects.

2.1 One-D Model

2.1.1 Amplification Factor

A very simple yet quite meaningful physical model of the ground for characterizing site effects is a single layer over a half-space extending infinitely in the horizontal direction. The frequency characteristics of the amplification factor for this 1-D two-layered model can be obtained by solving a simple wave equation of sinusoidal ($e^{i\omega t}$) input. In the case of vertical incidence of body waves, either *S* waves or *P* waves with propagation

speeds of β_0 in the half-space and β_1 in the layer, to the layer with the thickness of h, we have the well-known amplification factor as

$$|U_1(\omega)| = 2.0\{\cos^2(\kappa_1 h) + \gamma^2 \sin^2(\kappa_1 h)\}^{-1/2} \quad (1)$$

where $\kappa_1 = \omega/\beta_1$ is the wavenumber in the surface layer and $\gamma = \rho_1\beta_1/\rho_0\beta_0$ is the impedance contrast of two media in which ρ_0 and ρ_1 are the densities of half-space and the surface layer. If the angular frequency $\omega = 2\pi f$ becomes zero, then Eq. (1) yields a numerical value of 2.0, the amplification due to the free surface of a half-space. When we compare the observed spectral ratios with respect to the outcrop motion, then we need to normalize $|U_1(w)|$ by 2.0. We should note that at the resonant frequencies where $\kappa_1 h = \pi(2n + 1)/2\,(n = 0, 1, 2, \ldots)$ the maximum amplification factor is equal to twice the inverse of the impedance contrast, $2\gamma^{-1}$.

If we calculate the amplification factor of the surface with respect to the ground motion at the bottom of the surface layer, i.e., borehole at the depth of h, then

$$|U_1(\omega)/U_0(\omega)| = \{\cos(\kappa_1 h)\}^{-1} \quad (2)$$

The amplification factor is independent of the impedance contrast and becomes infinite at the same resonant frequencies, i.e., $\kappa_1 h = \pi(2n + 1)/2\,(n = 0, 1, 2, \ldots)$. This is due to perfect cancellation of incident and reflected waves at the borehole level. Because it does not depend on the impedance contrast of the surface layer, even a half-space gives exactly the same amplification factor as any two-layered structure. We should also note that if the impedance contrast is zero, Eq. (1) becomes Eq. (2) except for the factor of 2.0. This means that the amplification factor relative to the borehole motion corresponds to the amplification factor of a structure with a rigid basement. In reality, we have intrinsic as well as scattering attenuation in the media so that the amplification factor always remains finite. Also, layering within surface sediments makes the amplification factor a function of impedance and thickness of each layer even for the surface/borehole spectral ratios. A complete calculation for any multiple-layered structures for arbitrary incidence of body wave is quite easy using the Thomson-Haskell matrix (e.g., Haskell, 1960) or the Propagator matrix (e.g., Aki and Richards, 1980).

In the case of a borehole measurement, we usually have an advantage for modeling as a by-product. That is, we usually conduct geotechnical as well as geophysical exploration when we excavate a hole before installing the instrument. This information is invaluable because it is an in-situ measurement independent from seismic observation. In particular, an *S*-wave velocity profile obtained by either *P*-*S* logging or suspension logging is important because the *S* wave usually has larger amplitude as input, stronger contrast between layers, and therefore, greater effect on the amplification factor. Once we obtain a 1-D structure by such an exploration, we can calculate site amplification factors using it as an initial model. Usually a 1-D model can give quite satisfactory results on average, but it is difficult to have exact matching on all the peak frequencies observed. Before introducing more complicated 2-D/3-D modeling, we should refine and improve our 1-D model as much as possible. Damping factors, or Q values as an inverse of damping, of surface layers are especially difficult to measure independently so that the calibration procedure is almost the only way to get their realistic values. Here we would like to show an example of such a procedure to get realistic 1-D models for several borehole stations.

2.1.2 Simulation

In the paper by Satoh *et al*. (1995a), the primary goal of the analysis is to obtain the so-called "engineering bedrock waves" from observed ground motions recorded in the borehole with various types of soil conditions. The definition of the engineering bedrock can depend on the purpose of the study, but usually it is Tertiary rock or hard Pleistocene commonly found in the studied region with some constraints on its geotechnical and geophysical properties. Satoh *et al*. (1995a) defined their engineering bedrock as the layer of sedimentary rock of Pliocene or earlier age with an *S*-wave velocity of 500 m/sec or larger and a SPT (Standard Penetration Test) blow count of 50 or more. From an engineering point of view, it is desirable to predict ground motions directly on the engineering bedrock on which foundation systems of important buildings and civil engineering structures will be constructed. Satoh *et al*.'s procedure for obtaining the engineering bedrock waves is as follows. First they identified a 1-D soil structure for each site using spectral ratios between surface and borehole records observed at each site among eighteen small- to moderate-sized ($3.4 \leq$ Mjma ≤ 7.1) earthquakes. Then they calculated the theoretical 1-D transfer function of the ground motion at the borehole level to the input motion at the engineering bedrock level and deconvolved it from the observed borehole record.

Data used were recorded by twelve borehole stations deployed in Sendai City, a cultural center of the Tohoku district, Japan, as shown in Figure 1. Among the twelve stations, two are situated on outcrops of the engineering bedrock so that the remaining ten stations are the targets of deconvolution. The initial *S*-wave velocity model for each site was developed from the *P*-*S* logging profile. The initial damping factors are determined to be $0.1f^{-0.5}$ for softer sites or $0.3f^{-0.5}$ for harder sites through several preliminary tests. Depths of the ten boreholes range from 27 to 81 meters.

The scheme of inversion for an optimal *S*-wave velocity and damping structure is a modified quasi-Newton method for the residual between a theoretical spectral amplification factor and an observed one. Layer properties between surface and borehole are identified and the remaining structure is assumed to be the same as the *P*-*S* logging. In their paper, the authors performed the inversion analyses for each horizontal component for each earthquake independently. This yields the best structure for each observed ratio and, hence, the most site-effect-free engineering bedrock wave. In most of the previous studies based

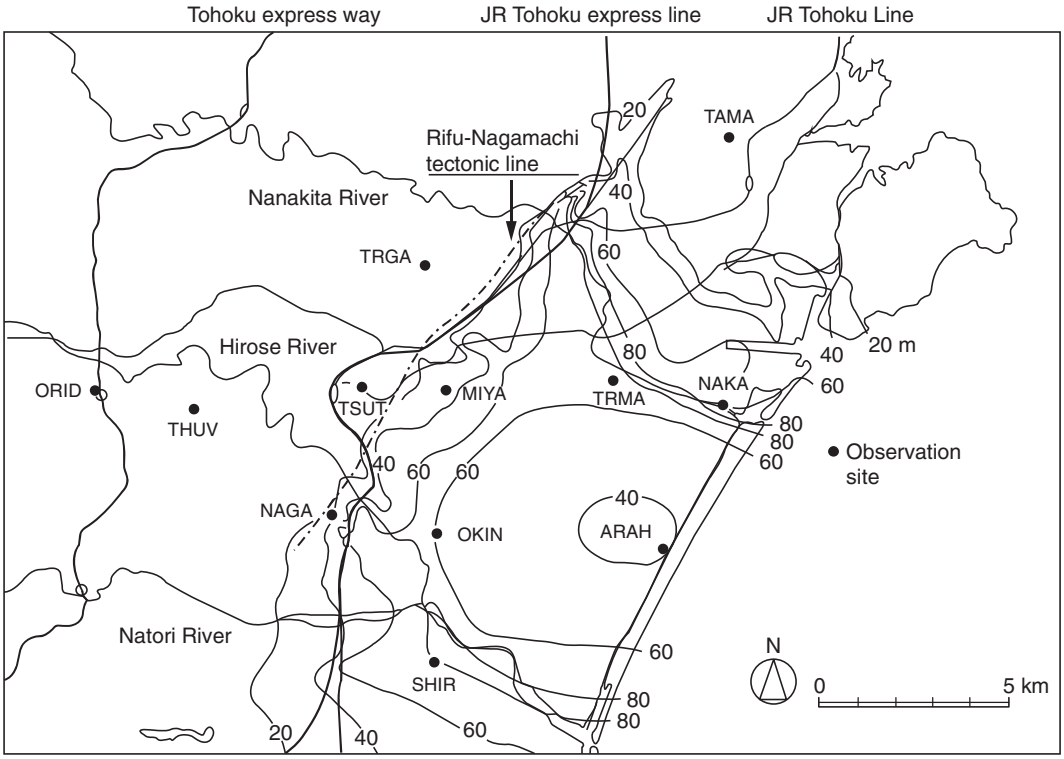

FIGURE 1 Twelve borehole stations deployed in Sendai City, a cultural center of the Tohoku district, Japan, used in Satoh *et al*. (1995a).

on the borehole data, the average of the observed ratios was determined first and then used as a target of inversion. If we use an averaged amplification ratio, the inverted structure may be not an averaged structure of the real ground but a smoothed one because of the stochastic nature of observed spectral ratios. This is especially true for the damping factor, which is very sensitive to peak values. Once we average observed ratios for different components for different earthquakes, the peak values are then smeared out so that the damping tends to be overestimated. If spectral ratios at a site are not stable and need to be averaged, then it means that the site effect there is not simple enough to be characterized by a 1-D model.

Figure 2 shows examples of the spectral ratios of all ten stations by one earthquake, EQ9101, for the EW component. A vertical line in each figure is the upper frequency limit for which the optimization is enforced. The matching between data and theory is quite good up to this high-frequency limit, especially at softer sites such as NAKA, OKIN, SHIR, and ARAH. Note that the peak amplification factors reach more than 10 primarily because these factors are of surface/borehole factors as in Eq. (2). In Figure 3, the authors compare the observed spectral ratios at NAKA and SHIR with two theoretical ones, namely, the optimal structures determined as previously mentioned and the predefined ones using the P-S logging velocities and a frequency-independent (2%) damping factor. At SHIR peak frequency shift between the observed ratio and that of the predefined model is apparent. Although the difference is small, this prompts us to refine the S-wave velocity structure to get the best matching. The differences of S-wave velocities between the initial models ($=P$-S logging values) and the optimal ones are about 10% in softer ($\leq$200 m/sec) layers and less than that in harder layers. It is interesting to note that for most of the layers, the optimal values are smaller than the P-S logging values. Figure 3 also shows the importance of the frequency dependency in damping factors to explain spectral ratios in a wider frequency range. The obtained frequency dependency in damping factors (as power of frequency) range from 0.46 to 1.15, mostly centering around 0.8. The frequency dependency is not negligible because the spectral ratio between surface and borehole is controlled by the damping factor of soil layers between them.

Figure 4 shows the final spectral ratios at twelve stations with respect to the engineering bedrock waves at one station, ORID, averaged for all the data analyzed. Thick solid lines represent ratios of engineering bedrock waves, while thin solid lines represent those of surface records, and thin dotted lines represent the borehole records. The engineering bedrock waves are running between these observed data and are close to unity. We should note that the borehole records show quite deep troughs, which is exactly as expected from Eq. (2). Amplification higher than the lowest frequency of such troughs, shown by solid triangles, should be real amplification due to shallow soil layers, while amplification or deamplification lower than that, such as those shown by small arrows, should be due to a deep basin structure below the engineering bedrock.

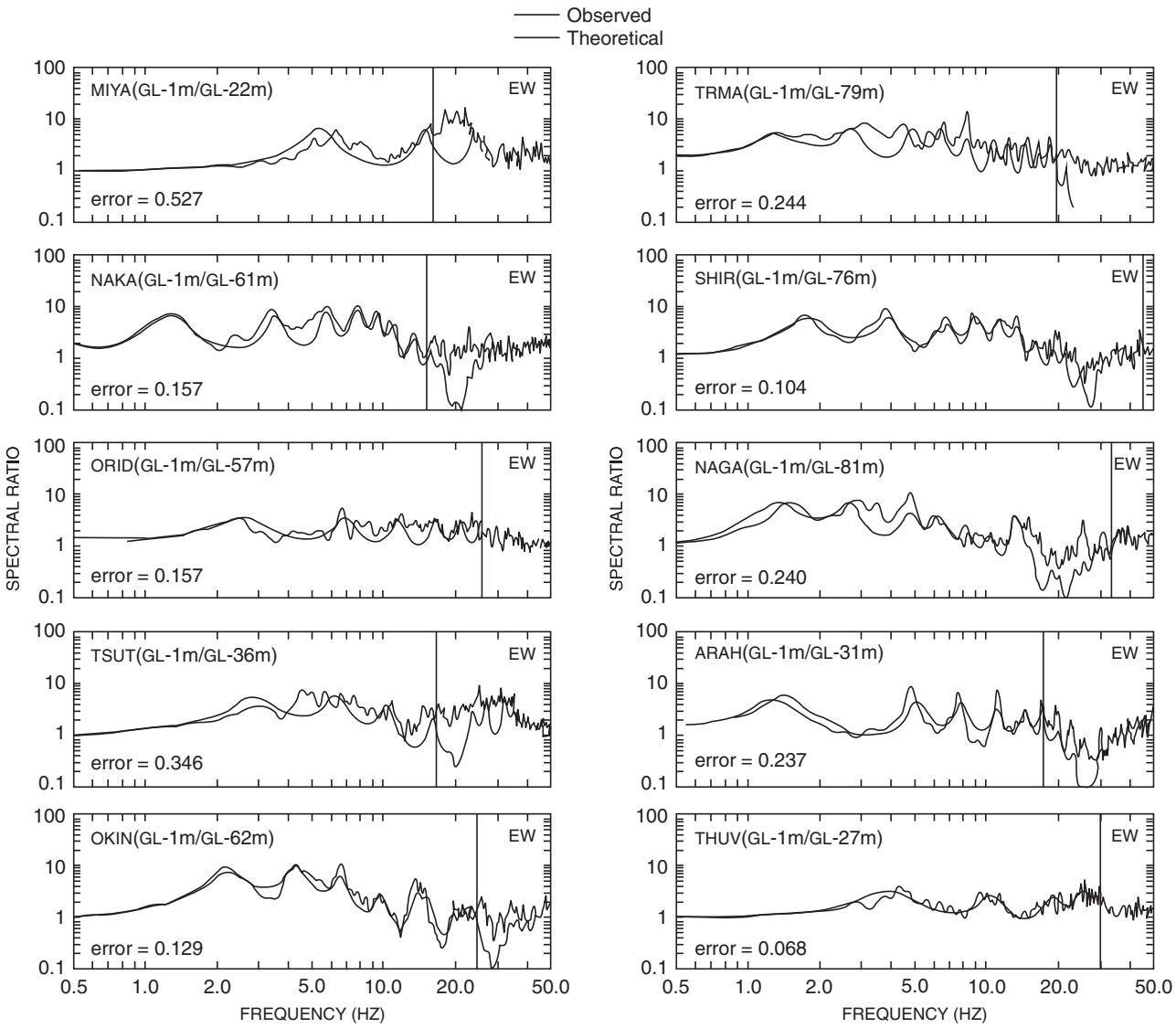

FIGURE 2 Examples of the spectral ratios of EW component between surface and borehole stations observed at all the ten stations during an earthquake of M_{JMA}4.7, EQ9101 (Satoh *et al*., 1995a).

In conclusion, Satoh *et al*. (1995a) show that 1-D structures are capable of representing the basic characteristics of the site amplification due to shallow sedimentary layers if *S*-wave velocities and damping factors are properly assigned. We should note, however, that the assumed physical models in this study are considered to be equivalent ones, which are determined to reproduce the observed spectral ratios. For example, damping factors obtained here range from 10% to 50% at 1 Hz, which is quite large as a value of intrinsic attenuation of normal soft soil. These values should be the result of many plausible factors not considered in the simple 1-D model used, such as, 2-D/3-D basin effects, stochastic nature of incident waves, incidence angle rotation, different types of incident waves, and so on.

The effectiveness of such 1-D modeling in reproducing spectral ratios between observed surface and borehole records has also been reported by others such as Takahashi *et al*. (1988), Seale and Archuleta (1989), Kinoshita (1992), Kobayashi *et al*. (1992), Satoh *et al*. (1995b), and numbers of papers collected in the proceedings of the second International Symposium on the Effects of Surface Geology (Irikura *et al*., 1998). In these proceedings, a good review by Archuleta (1998) on the recent borehole studies in the United States can be found.

2.1.3 Nonlinearity

If an input motion to soft-surface layers becomes so intense that the shear stain built up inside the layer reaches a certain threshold, then soil behaves nonlinearly. Soil nonlinearity is characterized by reduction of shear rigidity and, hence, reduction of shear wave velocity, and increase of damping factor. In terms of

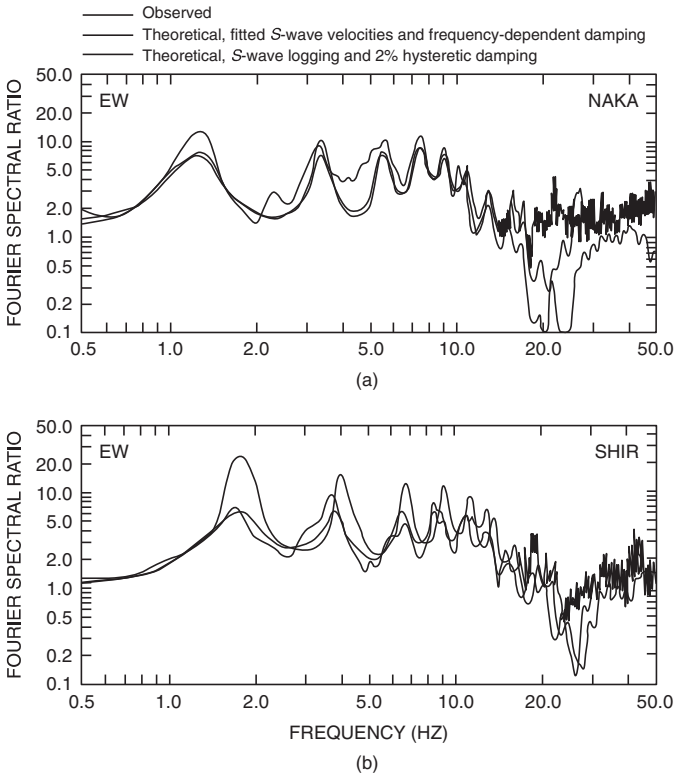

FIGURE 3 Comparisons of the observed spectral ratios at NAKA and SHIR (thick solid lines) with two theoretical ones, namely, the optimal structures determined by the inversion (thick broken lines) and the predefined ones using the *P*-*S* logging velocities and a frequency-independent damping factor of 2% (thin solid lines). Reproduced from Satoh *et al*. (1995a).

site effects, this results in prolongation of the predominant periods and reduction of amplification factors. In the geotechnical engineering field, nonlinearity in the soil as a microscopic (on the order of centimeters) level has been real and obvious based on laboratory experiments. Using a shear rigidity reduction factor and a damping increasing function in relation to the shear strain established by such laboratory experiments, Schnabel *et al*. (1972) proposed and distributed the famous SHAKE computer program. SHAKE combines a multiple 1-D wave propagation theory with these relationships as an equivalent linear method. In the equivalent linear method, iterative calculations are performed until convergence of the material properties used in the former calculation and the material properties in relation to the calculated strain is achieved. In essence, the equivalent linear method works if we focus our attention to only the major part of the seismogram with maximum strain.

On the other hand, the seismological community had been reluctant to accept the concept that nonlinearity was happening in a pervasive manner until Chin and Aki (1992) proposed a seismological method for finding evidence of nonlinearity in the observed strong-motion data. In similar work, Field *et al*. (1998) compared relative site responses for the mainshock and aftershocks of the Northridge earthquake sequence and reported a large difference between them. Although the data in these studies are extensive, they are indirect evidence of nonlinearity.

In Japan, borehole measurements are quite common and much strong-motion data has been observed in boreholes embedded in soft sediments. One example is a paper by Satoh *et al*. (1995b) in which the authors inverted soil properties between borehole and surface sensors and found quite good matching between the relationships of the calculated shear rigidity and damping factors to the shear strain and those of laboratory testing. Shear rigidities obtained by the equivalent linear method and those obtained by the inversion also coincide with each other, and both methods explain observed surface seismograms much better than the linear model determined by the inversion for a low strain input. Even for quite a strong level of input, such a scheme seems to work as Satoh *et al*. (1998) recently showed for borehole data of the Hyogo-ken Nanbu earthquake.

In the case of loose sand saturated by water, soil under strong shaking becomes liquefied because pore water pressure built up by shear strain destroys the grain structure. After much effort by the engineering community, we can now simulate ground motions on the surface of liquefied soil more or less quantitatively. A good example can be found in Kawase *et al*. (1996), who succeeded in reproducing Port Island borehole records during the Hyogo-ken Nanbu earthquake based on the 1-D effective stress analysis code developed by Fukutake *et al*. (1990). Many interesting papers, including one review paper on nonlinearity, are found in the proceedings of Irikura *et al*. (1998).

2.2 Two-D/three-D Models

2.2.1 Basin-induced Surface Wave

In 1-D modeling of soil layers, we assume that the soil layers are flat and extend infinitely in the horizontal directions. In reality, soil and sedimentary rock layers are confined by the surrounding intact rock to form sediment-filled basins. At the edge of the basin, strong diffraction takes place due to a large velocity contrast. In case of vertically or near vertically incident body waves, such diffraction at the edge creates basin-induced diffracted waves, which are transformed into surface waves very quickly. The basin-induced surface waves will propagate in the horizontal direction inside the basin, back and forth. Under normal circumstances these basin-induced waves will arrive later than the direct body waves on the surface of the basin simply because aspect ratios (horizontal extent/vertical extent) of normal basins are quite large and so surface waves have a longer distance to travel. A site close to the edge of the basin is an exception to this condition and if the shape of the basin edge is sharp (i.e., if the slope is steep), the edge-induced waves arrive at the same time as body waves, so that a strong constructive interference takes place. Kawase (1996) called such a phenomenon "the Edge Effect" and attributed the damage concentration formed during the Hyogo-ken Nanbu (Kobe) earthquake to it. Some details on the edge effect will follow later.

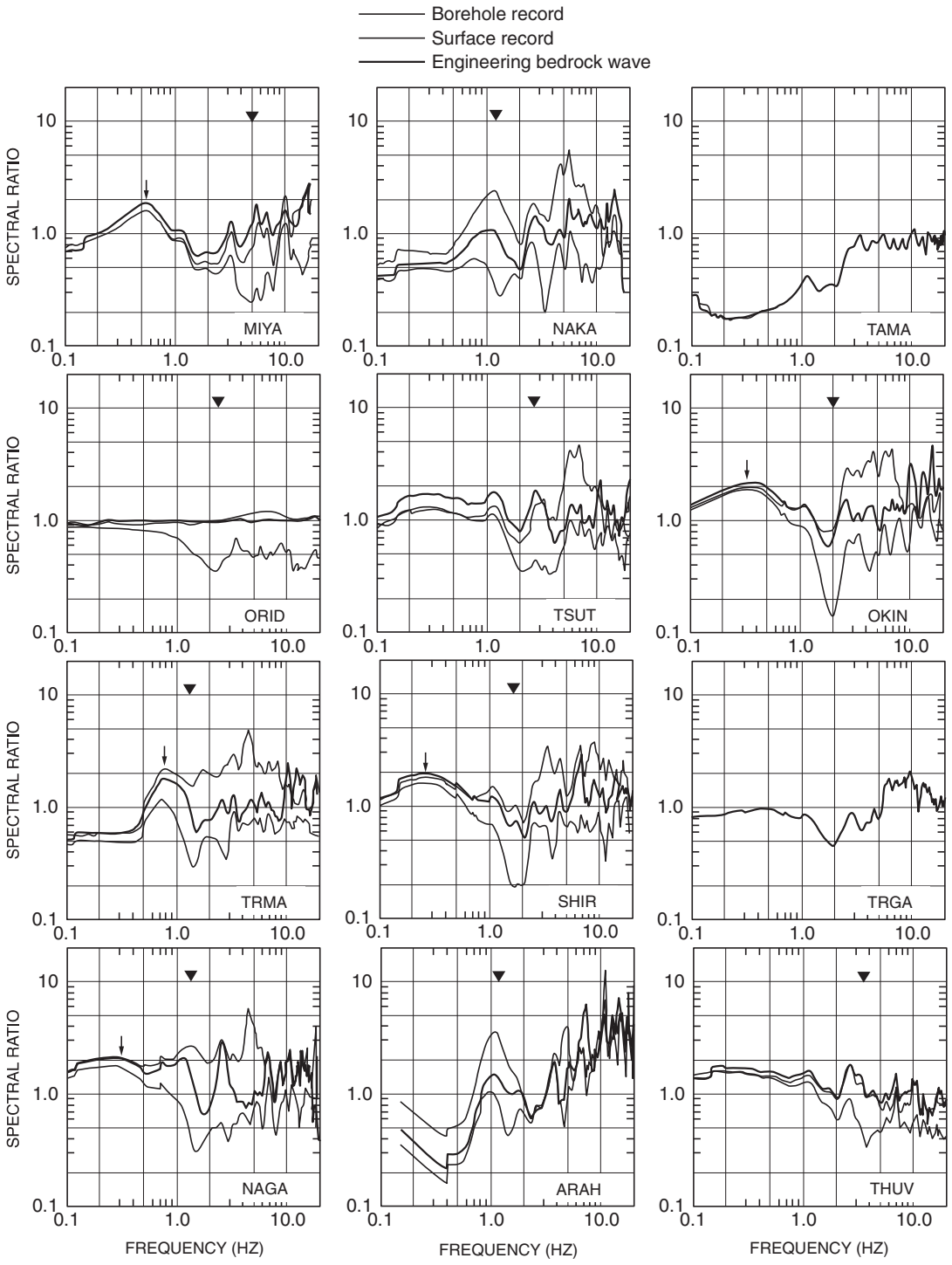

FIGURE 4 Final spectral ratios at twelve stations with respect to the engineering bedrock waves at one station, ORID, averaged for all the data analyzed. Thick solid lines represent ratios of engineering bedrock waves. Thin solid lines represent ratios of surface records. Thin dotted lines represent those of borehole records. Solid triangles correspond to the first resonant frequency of each surface–borehole pair, while arrows indicate low-frequency peak, probably due to the deeper basin amplification (Satoh *et al*., 1995a).

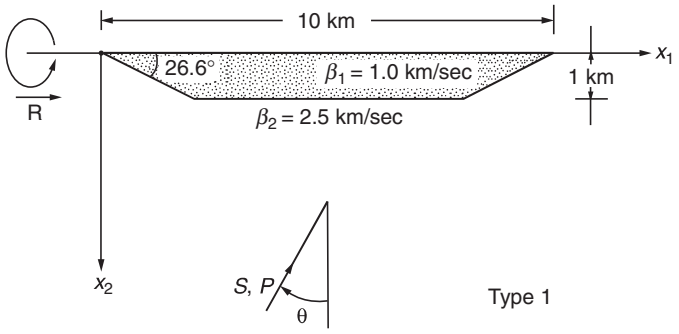

FIGURE 5 A simple hypothetical model of a trapezoidal 2-D basin used in Kawase and Aki (1989).

Let us go back to the basin-induced surface waves. Observational evidence of the basin-induced surface waves was reported for the first time by Toriumi (1975), who found distinctive later arrivals in the ground motions observed in the Osaka basin. At that time, no clear interpretation of the physical entity of the wave was given, but later it was confirmed to be basin-induced surface waves (Toriumi, 1984; Kagawa *et al*., 1992). Comprehensive theoretical demonstration of this type of wave was made by Bard and Bouchon (1980) using many synthetic seismograms along the surface of a basin, calculated by the Aki-Larner method (Aki and Larner, 1970). Synthetic waveforms at several points for the same basin had been presented before (e.g., Boore 1972; Hong and Helmberger, 1978), but we cannot see clear wave propagation phenomenon without dense spatial sampling. Basic wave generation and propagation phenomena for a basin subject to incident body and surface waves can be better understood in the follow-up work by Kawase and Aki (1989), who used the so-called discrete wavenumber boundary element method (DWBEM) to obtain responses of a trapezoidal 2-D basin as shown in Figure 5. The responses of the basin for vertically incident SH waves with the time-domain shapes of Ricker wavelets with two different characteristic frequencies, namely, 0.25Hz and 0.5Hz, are plotted in Figure 6. We can clearly see that surface waves, Love waves in this case, are generated at the edges and propagate toward the opposite side. At the other side of the edge, a part of the surface wave energy is reflected back to the basin and the rest passes through to the surrounding rock. This symmetric generation and propagation of surface waves forms x-shaped wave patterns on the basin surface, their amplitude gradually decreasing as time goes by. As for the direct S-wave part, the amplitudes are the same on the surface of surrounding rock and in the flat part of the basin, but they are largest near the edges because of the constructive interference of the direct S-wave and the basin-induced surface waves—the edge effect.

Development of the theoretical techniques for irregular underground structures, including the Aki-Larner method and DWBEM, has been reviewed by Sanchez-Sesma (1987), Aki (1988), Kawase (1993), and Takenaka *et al*. (1998), among others. Through the development of such techniques and rapid increase of computational power, we have made it possible to simulate observed ground motions using 2-D/3-D models of realistic underground structures. Two examples of such simulation studies that try to reproduce observed strong motions by physical modeling of the ground are described following.

Kawase and Sato (1992) used strong-motion data and geological data distributed for a blind prediction experiment conducted by the Japanese Working Group on Effects of Surface Geology (Kudo *et al*., 1992). First they analyzed observed ground motions at two stations on the soft soil inside the Ashigara basin. Figure 7 shows observed accelerograms and their nonstationary spectra at the station S8 during the East off Chiba earthquake. We can see a very isolated later phase at about 40 seconds in the N30°W component whose predominant period ranges from 1.0 to 1.5 second. Based on the polarization and an apparent group velocity between two stations, it is interpreted to be the basin-induced Love wave. We cannot see any similar later phases either in the N60°E component or in the horizontal components of the record on the surrounding rock. Kawase and Sato (1992) constructed a 2-D model, shown in Figure 8, and obtained its response by using their own finite element code similar to those used by Lysmer and Waas (1972). The convolution with a nearby rock record yielded the Fourier spectra indicated by a dashed line in Figure 9. For comparison, synthetic spectra using a 1-D model (dotted lines) as well as the observed spectra (solid lines) are shown. It is clear that the 2-D model gives additional amplification in the N30°W component at around 1.5 Hz, which is a little higher than the observed spectral peak at around 1 Hz; the amount of additional amplification is enough to fill the gap between the 1-D model and the observed Fourier spectra. Note, however, that spectral shapes of both 1-D and 2-D models coincide with the observed shapes in the frequency range higher than 2 Hz (for 2-D up to 5 Hz, maximum frequency for the finite element mesh). We should also note that there is no need to introduce a 2-D model for the N60°E component. The discrepancy of the 2-D amplification frequency between the model and reality is attributable to inappropriate modeling of soil layers between the edge of the basin and the site. Because the major part of the spectra is well reproduced by the 1-D model, we need to assign much softer properties for the layers in the traveling path of the surface wave. Unfortunately, the authors did not have any information on the properties of layers other than the P-S logging data at two borehole sites, so the simulation remained a qualitative one. However, the important lesson here is that a soil column just below the site controls the 1-D response, while the whole path from the edge to the site controls the 2-D response. Thus, we need much wider structural information for 2-D models than for 1-D models. This study also suggests that 1-D response should work for most of the cases and we should introduce 2-D/3-D models only if data show such a necessity.

Another simulation was provided by Hatayama *et al*. (1995) for an array measurement in the eastern part of the Osaka basin.

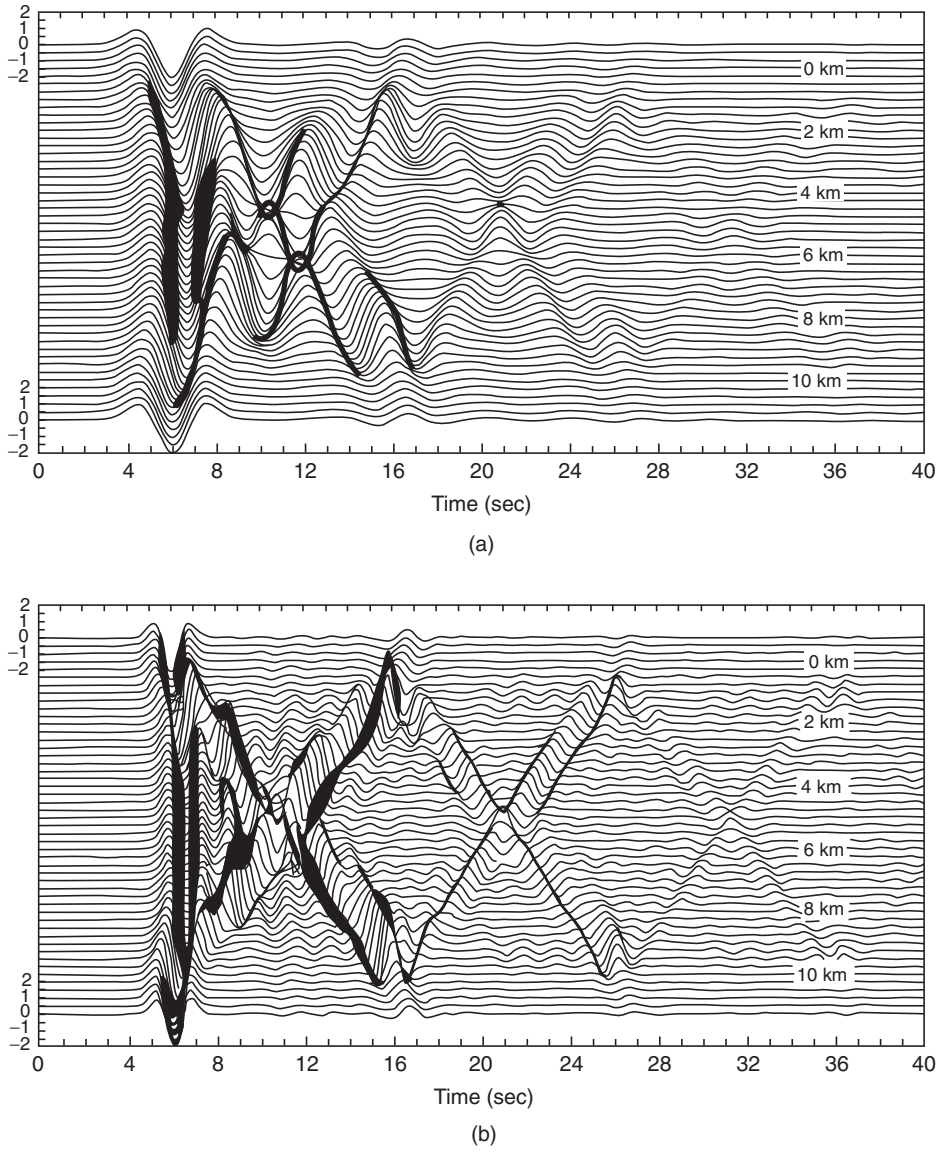

FIGURE 6 Responses of a trapezoidal basin for vertically incident SH waves with the time-domain shapes of Ricker wavelets with two different characteristic frequencies, namely, (a) 0.25Hz and (b) 0.5Hz.

In Figure 10, they compared the synthetic responses at four stations inside the basin calculated by their own 2-D boundary element code with the observed records. The topmost traces are for the rock motion used as a reference. The observed records inside the basin show clear propagation of the basin-induced surface waves, which is labeled as SL1 at the trace of OSA. They confirmed that this later phase was Love wave propagating from east to west based on a small array measurement near the OSA station. They succeeded in reproducing the basin-induced Love wave at OSA, but its peak amplitude was only half of the observed. They used relatively high Q, 100 for sediments, so it may be difficult to increase the amplitude by adjusting Q values. Similar amplitude deficiency for basin-induced surface waves in 2-D/3-D models has been commonly reported in the literature (e.g., Yamanaka *et al*., 1989; Graves, 1998). This suggests that further study is necessary for the soil properties between the basin edge and the site to better simulate the basin-induced surface waves.

2.2.2 Edge Effect

Near the edge of a basin, generation and propagation of basin-induced diffracted and surface waves and incidence of body waves from the bottom of the basin are taking place simultaneously. If they meet in phase at some point, then constructive interference happens and amplitude of ground motion there becomes

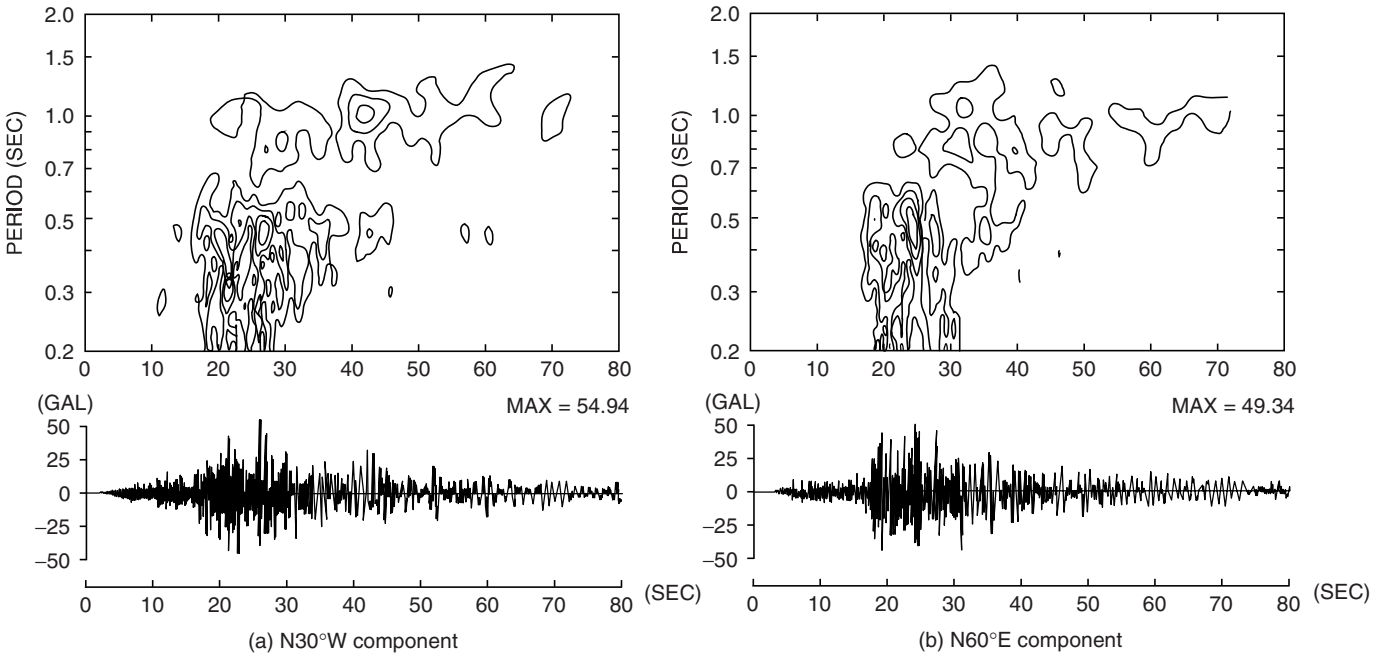

FIGURE 7 Observed accelerograms and their nonstationary spectra at a sediment site, S8, in the Ashigara basin in Kanto area, Japan, during the East off Chiba earthquake (Kawase and Sato, 1992).

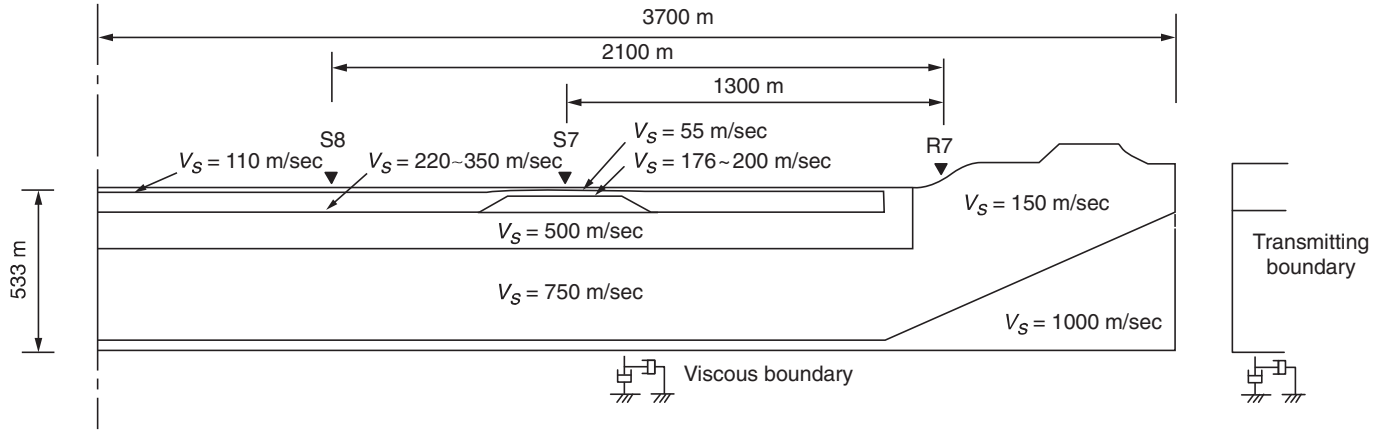

FIGURE 8 A two-dimensional model used by Kawase and Sato (1992) for the simulation.

much larger than a simple 1-D response. This amplification effect near the edge of the basin was named "the (Basin) Edge Effect" by Kawase (1996). The damage concentration found in Kobe during the Hyogo-ken Nanbu (Kobe) earthquake, often called the damage belt because of its large length (~20 km) compared to its small width (~1 km), was created as a consequence of both source extension along the strike of the damage belt and the edge effect along the northwestern edge of the Osaka basin. Kawase (1996) used a 2-D rectangular basin to simulate the observed strong motions in Sannomiya, downtown Kobe, where a heavy damage concentration was formed near the JR Sannomiya station. He showed snapshots for 1 Hz Ricker wavelet input in the vertical cross section to delineate the mechanisms of constructive interference happening near the edge of the basin. After his paper, Inoue and Miyatake (1997) showed snapshots of surface velocity response for a moving dislocation (strike-slip) source. They attributed the cause of the damage belt primarily to the source effect, rather than the edge effect, because it looks as if a high-amplitude zone is moving as rupture propagates. However, in defending Kawase's hypothesis, Kawase *et al*. (1998a) showed that the edge effect is present whatever the source of incident wave, and a 1-D response of the basin without the constructive interference with the edge-induced waves is not sufficient to cause the damage concentration seen in Kobe.

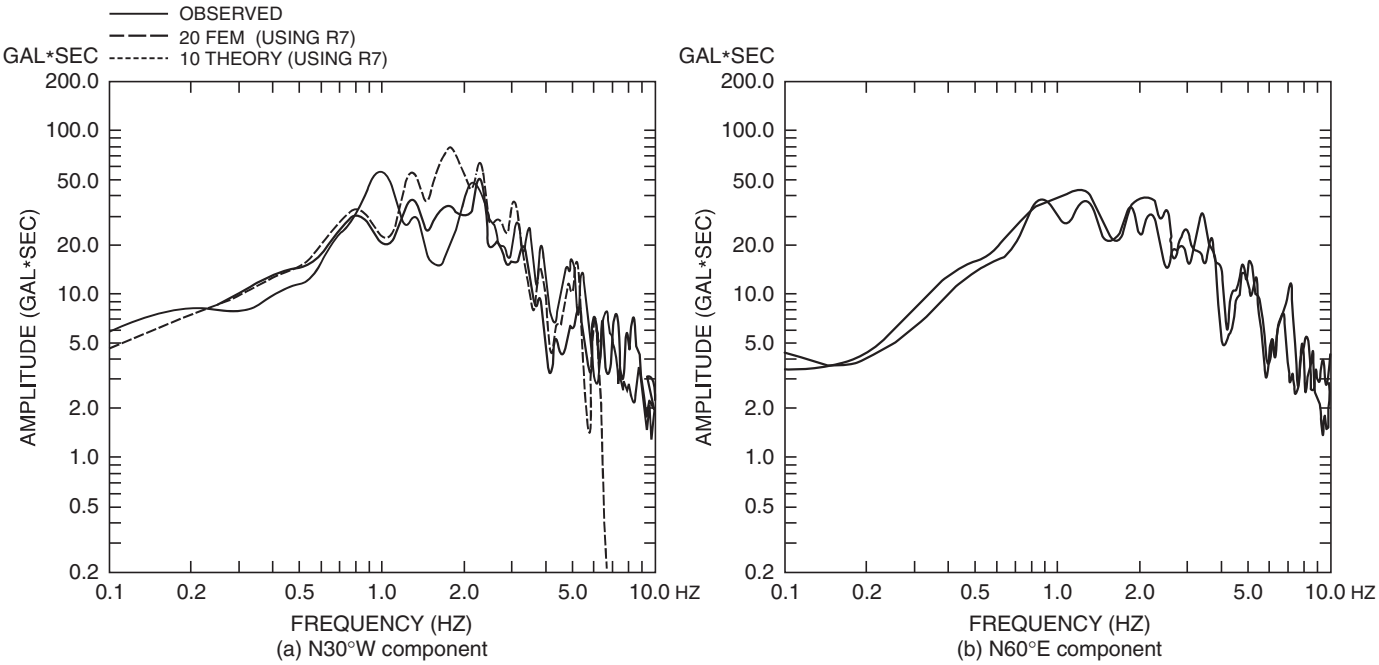

FIGURE 9 Fourier spectra of the observed surface motions (solid lines), the synthetic motions using the 1-D model (dotted lines) just below the site, and the synthetic motions using the 2-D model in Figure 8 (a broken line, only in the N30°W component).

More quantitative simulation for Kobe can be found in Matsushima and Kawase (1998), where a complex rupture process and a 3-D basin model were used in their finite difference calculation. Pitarka *et al*. (1997, 1998) support the idea of the basin-edge effect in Kobe. An introduction of the essential part of the edge effect study of Kawase *et al*. (1998a) is presented following.

Figure 11 shows a simple 2-D rectangular basin model used in the analysis. Kawase *et al*. considered three different models: 1) a simple 2-D model, 2) a 2-D model with a reflection layer in the rock side, and 3) a 2-D model with a reflection layer in the basin side. The reason for embedding a reflection layer in only one side of the model space is to separate incident and reverberated *S* waves in the basin (=1-D response) and the basin-induced diffracted/surface waves (=2-D additional amplification). An assumed incident wave was a vertically incident *S* wave with a bell-shaped function of about 1 second of the predominant period. The left panel of Color Plate 25 shows the whole response of a simple 2-D model, while the center panel and the right panel show responses of a 2-D model with rock-side reflection (called Rock-S-cut model), and a 2-D model with basin-side reflection (called Basin-S-cut model), respectively. In the center panel of Color Plate 25, clear vertical propagation and reflection of the *S* wave can be seen only in the basin side. This is a normal 1-D response of the basin. In the right panel of Color Plate 25, when an incident *S* wave in the rock side hits the surface, strong energy concentration appears at the edge and it radiates energy to the basin quite efficiently. The edge-induced waves, which are transforming themselves into surface waves quite rapidly as they propagate, have two distinctive phases that are indicated by open and solid triangles in the right panel of Color Plate 25. The faster phase consists primarily of diffracted *P* wave and a higher mode of Rayleigh wave, while the slower phase consists primarily of diffracted *S* wave and the fundamental mode of Rayleigh wave. The constructive interference mentioned in Kawase (1996) was only with the faster phase. Although the lobe of the faster phase is larger, the conspicuous amplification near the edge found for the realistic input (Figure 6 in Kawase, 1996) is mainly caused by the constructive interference with the slower phase. Note that these two phases of the edge-induced waves have opposite signs, the faster one sharing the same sign as the input. Thus for quantitative evaluation of the interference with the slower one, the waveform of the incident *S* wave is very important.

The basin-edge effect is not an extraordinary phenomenon found only in Kobe. Any kind of a basin edge would have the edge effect, although the degree of interference depends on the edge shape as well as the input waveform. An example for the northern edge of the great Los Angeles Basin near Santa Monica was reported by Graves *et al*. (1998), who succeeded in explaining velocity waveforms of the observed ground motion record at Santa Monica City Hall during the Northridge, California, earthquake of 1994.

2.2.3 Basin-transduced Surface Wave

If a source is distant and shallow, then the incident wave to a basin will consist mainly of surface waves. When they reach the basin, a part of the incident wave energy is reflected back

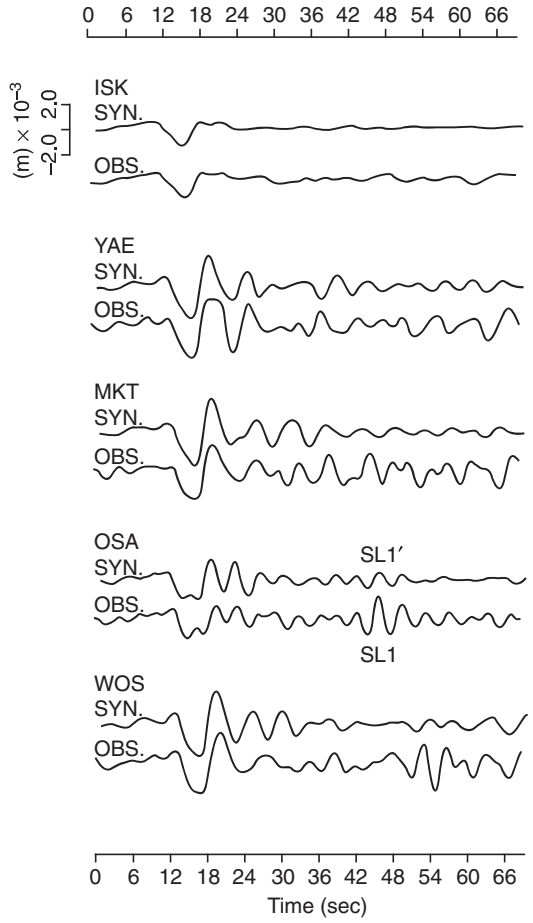

FIGURE 10 Comparisons of synthetic responses at five stations calculated by a 2-D model of the eastern part of the Osaka basin with the observed records (Hatayama *et al*., 1995). The topmost traces are for the rock motion used as a reference.

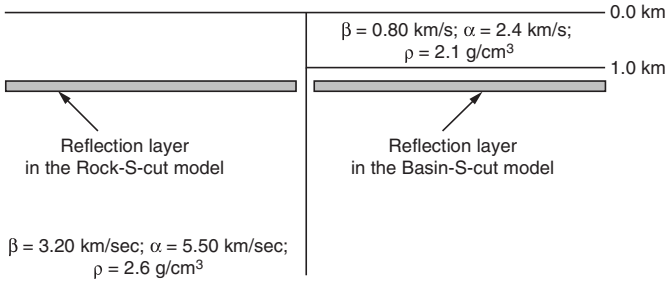

FIGURE 11 A simple 2-D rectangular basin model used in the analysis of the basin-edge effect (Kawase *et al*., 1998a). In addition to the normal basin, two variations are considered. One has a reflection layer only below the rock surface (Rock-S-cut model) and the other has the same reflection layer only below the basin (Basin-S-cut model).

but the rest is impinging into the basin. At the edge, complex transformation from one mode of surface waves for the surrounding rock to different modes for the basin sediments, i.e., mode conversion between two different media, is taking place. Kawase (1993) called these types of surface waves inside the basin basin-transduced surface waves. In this case, we do not see two distinctive phases as seen in the case of the basin-induced surface wave. Instead, we see continuous arrivals of long-period waves from the beginning because mainly basin-transduced surface waves exist.

The existence of basin-transduced surface wave is reported by Hanks (1975), who showed a series of displacement seismograms recorded during the San Fernando, California, earthquake of 1971. For the rock sites near the source, the duration of displacement records is short and the waveform is simple, while those inside the Los Angeles basin are quite long and dispersed. Hanks (1975) noted that despite the relatively short distance from the fault, the observed waveforms inside the basin have the characteristics of surface waves. Continuous arrivals of relatively short period (∼3 seconds) waves are a clear indication of basin-transduced surface waves. Later, Vidale and Helmberger (1988) succeeded in simulating these observed velocity seismograms in the San Fernando and Los Angeles basins. Figure 12 shows the comparison of filtered transverse

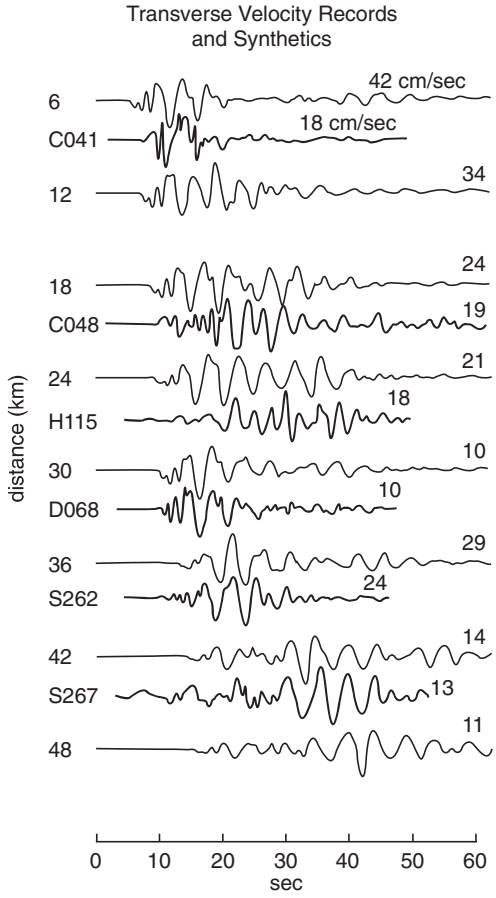

FIGURE 12 Comparison of filtered transverse components of the observed velocity records in the San Fernando and Los Angeles basins during the San Fernando earthquake of 1971 with those of the synthetics by Vidale and Helmberger (1988).

components of the observed velocity records with those of the synthetics. The matching of the synthetics with the data is generally very good. But we should note that source properties are controlled so as to match the synthetics with the observed at D068 and therefore the synthetics are not fully theoretical but similar to the convoluted ones with a reference record. Complete physical modeling of source, path, and site could be possible for simulation with basin-transduced surface waves because their predominant period tends to be longer than a few seconds. One pioneering work of this kind was done by Sato (1990, reproduced in Kawase, 1993), who succeeded in simulating long-period basin response of the Osaka basin during Kita-Mino, Japan, earthquake of 1961 by using the so-called thin-layer element method (TLEM) combined with reciprocity. Recently, Sato *et al*. (1999) show remarkably well-reproduced results of the displacement records observed at Tokyo during the Kanto earthquake of 1923, which is shown in Figure 13. They used a small recent earthquake that occurred near the hypocenter of the Kanto earthquake as a calibration event to refine the basin structure used in their 3-D finite difference calculation. 3-D basin effects can be clearly seen in Figure 14, in which they compare the observed records with 1-D and 3-D calculations. Note that before using the 3-D basin structure, they calibrated source, path, and site effects very carefully using 1-D models (Sato *et al*., 1998a, 1998b), without which the good matching seen in Figures 13 and 14 could not be achieved.

2.2.4 Focusing Effects

In case of a basin with an irregular bottom shape subject to a body wave incidence below, we will see focusing effects in which seismic rays propagating in different paths meet together at certain points on the surface. At these points, there will be amplification or deamplification depending on their phases. Because such a ray concept is a high-frequency approximation, the focusing effects should emerge in the high-frequency amplification characteristics. Hartzell *et al*. (1996) attributed conspicuous amplification and large damage difference along the southern edge of the San Fernando Valley to such focusing effects created by irregular layer boundaries supposedly underlying the observation sites. We should note, however, that under normal circumstances the frequency range of our interest remains relatively low, a few Hz for most of the cases, and so the diffraction plays a major role in wave propagation and a simple ray concept would not always work.

2.3 Topographic Effects

Topographic effects have been reviewed in some detail by Geli *et al*. (1988), Aki (1988), and Kawase (1993). Because there are so many different observations on the strength of the topographic effect, we cannot draw clear conclusions. However, many studies in the past suggest that even a rock site has strong

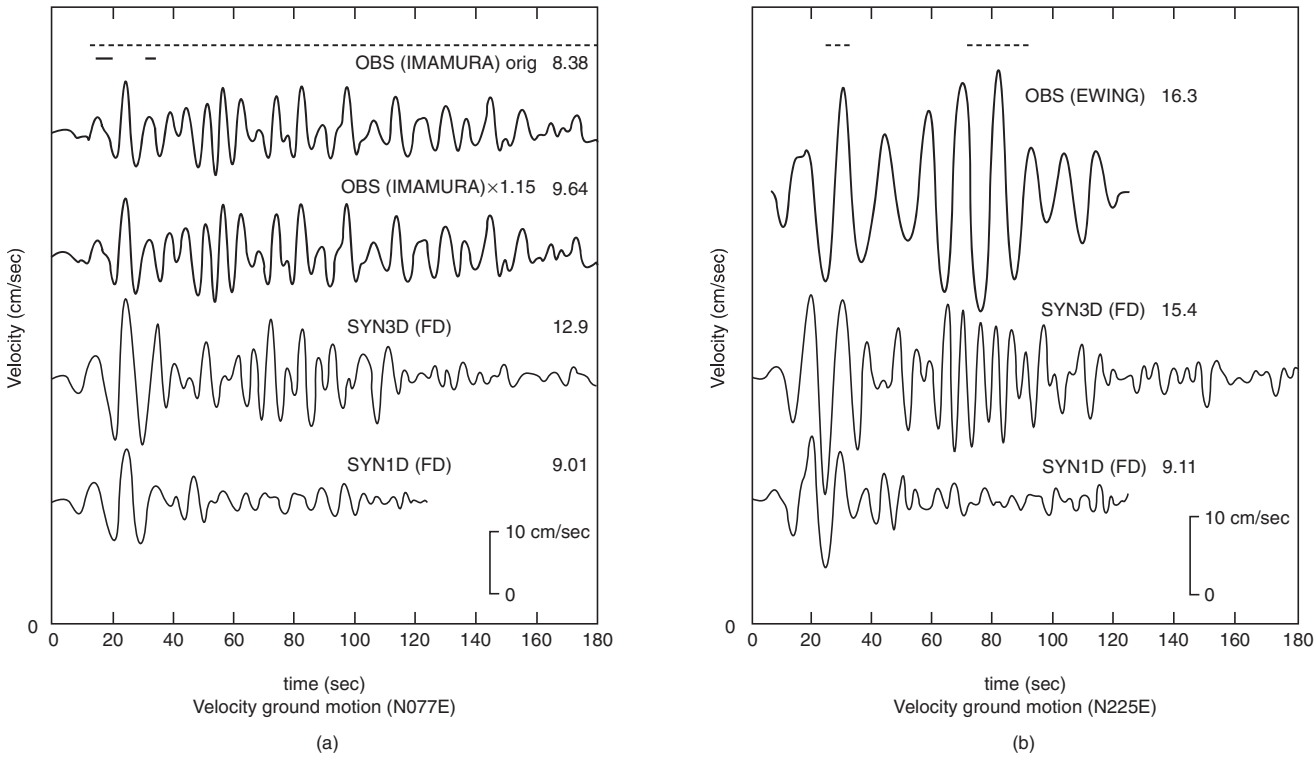

FIGURE 13 Comparison of the restored records observed at Tokyo during the Kanto earthquake of 1923 and the 3-D basin response calculated by Sato *et al*. (1999).

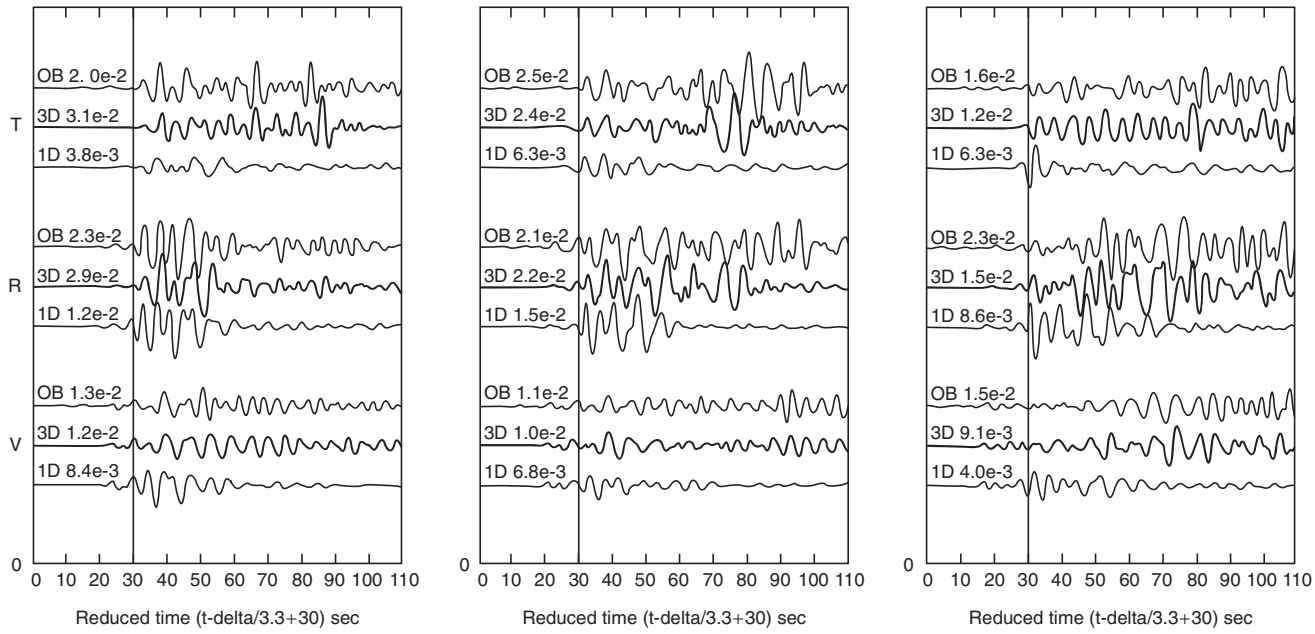

FIGURE 14 Comparison of the observed records used as a calibration event with 1-D and 3-D theoretical calculations by Sato *et al.* (1999).

site effects due to the subsurface structure below (e.g., Steidl *et al*., 1996; Spudich *et al*., 1996) so it may be difficult to distinguish the effects of the subsurface structure and those of the topography from observed site effects, unless we know the subsurface velocity structure of the site in detail. Theoretically speaking, the pure topographic amplification factor will be 2 at most, because constructive interference between two arrivals of different waves, either diffracted waves, surface waves, or body waves, is likely to happen but more than two arrivals with the same phase rarely meet at the same location. Besides, strong topography can be found only in the mountain area, where amplification itself is basically low compared to the basin surface and so practically speaking pure topographic effects are of secondary importance.

3. Empirical Modeling of Site Effects

If we obtain site effects directly from observed data, such an approach is called an empirical modeling approach. In the empirical modeling of site effects we must observe strong or weak ground motions due to one or more earthquakes and analyze data to extract site effects. It seems straightforward to extract site effects from data. It is, only if we have a very good reference site near the target site, as mentioned in the Introduction section. Here, we briefly review two empirical approaches for site-effects studies, namely, a separation method (sometimes called an inversion method) and a method based on coda and microtremors.

3.1 Separation of Source, Path, and Site

Empirical approaches to characterizing site effects have had a long history if we include studies of soil-type-specific amplification factors. Such an approach has been very common for engineering purposes. Over the last fifteen years we have been extracting site-specific empirical amplification factors from many observed data for different sites and different earthquakes. In a pioneering work, Andrews (1986) proposed a method to separate source effect, $S_i(f)$, path effect, $P_{ij}(f)$, and site effect, $G_j(f)$, by a singular value decomposition of the whole data space of observed Fourier spectra, $A_{ij}(f)$. The basic equation of the method is quite simple, as follows:

$$A_{ij}(f) = S_i(f)\, P_{ij}(f)\, G_j(f) \tag{3}$$

where i is a suffix for earthquake and j for site, while f is a frequency. If we assume *S*-wave propagation, $P_{ij}(f)$ could be expressed in terms of a geometrical spreading factor with respect to R_{ij}, the representative distance between a source and a site, and attenuation due to the intrinsic and scattering Q(f) as

$$P_{ij}(f) = R_{ij}^{-1} \exp(-\pi f R_{ij}/\beta Q(f)) \tag{4}$$

where β is the representative *S*-wave velocity of the whole path.

This technique has an important problem we need to note; it requires at least one independent constraint either on source, path, or site factors. Andrews (1986) assumed the logarithm of the sum of all the site factors to be zero, which physically means the average site factor should be a reference. Following Andrews, Iwata and Irikura (1988) used the same technique but a different constraint, in which they assumed any site factors to be

more than 2.0. This physically means that a site with the least site factor among others should be a reference. Since these pioneering studies, many similar studies have followed as strong-motion databases have been expanding in different areas of the world (e.g., Kato *et al*., 1992; Satoh *et al*., 1997; Bonilla *et al*., 1997). We should note that the scheme of the singular value decomposition is equivalent to the first step of the two-step decomposition used in the attenuation analysis for peak ground values (Joyner and Boore, 1981; Fukushima and Tanaka, 1990). Because decomposed source or site effects depend on the constraint, we should always be careful of its appropriateness. In an idealistic situation we can assume one station among all to be site-effect free so that the Fourier spectra at the reference site should consist of only source and path factors. If it is not the case, resultant source factors are directly biased by the site effect at the reference site. Such an example was reported in Kato *et al*. (1992). They used a hard-rock site, which was thought to be a good reference site from its surface *S*-wave velocity of 2.2 km/sec. After the separation, however, they found significant site effect present due to the V-shaped canyon topography around the site. This paper teaches us one important lesson; if we have a common frequency variation in the source (or site) factors for different earthquakes (or sites) we should check the validity of the assumption used as a constraint.

3.2 Microtremor and Coda

There has been a long history of using microtremors to delineate site characteristics. After the pioneering work of Kanai and his colleagues in the 1950s and 1960s in Japan, based on the microtremor data in Tokyo (e.g., Kanai *et al*., 1954), different techniques have been proposed. The latest addition is to take a spectral ratio of the horizontal component with respect to the vertical component (H/V), which was proposed by Nakamura (1989) and is sometimes called Nakamura's technique. Because H/V ratios of microtremors often show similar site characteristics obtained by other independent methods, the H/V method has gained popularity quite rapidly (Lermo and Chavez-Garcia, 1993; Field and Jacob, 1995). As the method becomes widely used, skepticism on its validity as a method for directly obtaining *S*-wave amplification factors has arisen (e.g., Lachet and Bard, 1994; Zhao *et al*., 1997). From array measurements of microtremors, the dominant wave type in the vertical component is found to be a Rayleigh wave (e.g., Horike, 1985; Kawase *et al*., 1998b). A numbers of papers on this topic are found in the proceedings of the second International Symposium on Effects of Surface Geology (Irikura *et al*., 1998); interested readers should refer to them.

Coda, the later part of the seismograms decreasing exponentially, has also been used for a long time for site correction. Physically, coda is considered to be scattered *S* waves in the whole volume between a source and a site, and is used to characterize the scattering property of the volume (e.g., Aki and Chouet, 1975; Tujiura, 1978; Sato, 1984). If the origin of coda is scattered *S* waves, then the local site amplification of coda should be an average of *S*-wave amplification for incident *S* waves with different azimuths and incidence angles and, therefore it could be more stable than that of a direct *S* wave (Chin and Aki, 1991; Kato *et al*., 1995). From the results of studies reviewed here it seems too simplistic to assume that coda consists mainly of *S* waves scattered in the whole path for sites inside a soft sedimentary basin. Most of the previous studies on the site factors from coda draw the frequency limit in the lower frequency end at 1 Hz or higher so that contamination of basin-induced and/or basin-transduced surface waves may not be significant. Yet, physically, we should always expect to have some surface-wave contamination in the later part of the ground motion.

Recently Satoh *et al*. (2001) analyzed the data observed in Sendai, Japan, quite extensively and found that both *P*-coda and *S*-coda at soft soil sites, especially *P*-coda, are strongly contaminated by the basin-induced surface waves. They checked the characteristics of H/V ratios for initial parts of *P* and *S* waves, early coda, late coda, and microtremors for both soft-soil sites and rock or hard-soil sites. H/V ratios of coda are not the same as the direct *P* or *S* wave and are converging rapidly to those of microtremors. They also calculated H/H ratios with respect to the hardest rock site and found that they are varying with time for soft-soil sites but are stable for rock or hard-soil sites. Theoretical simulation based on the *S*-wave structures determined by array measurements of microtremors reveals that H/H ratios of direct *S* wave can be explained well by 1-D responses of the structures for the soft-soil sites and that H/V ratios of coda and microtremors can be explained well by the Rayleigh wave H/V ratios of the same structures. These results suggest that coda and microtremors on soft sediments consist mainly of surface waves so that they have amplification characteristics different from *S* waves.

4. Conclusions

The essential aspects of the site-effect studies are reviewed by focusing mainly on the physical modeling scheme to reproduce wave propagation phenomena in the shallower part of the Earth. The *S*-wave amplification can be characterized by 1-D modeling of soil sediments as a first-order approximation. In addition to that, we sometimes need to consider nonlinear effect and 2-D/3-D basin effect including the basin-induced surface-wave effect and the edge effect. In lower frequency range we need to consider the effect of the basin-transduced surface waves and in higher frequency range we do the focusing effect, as well.

However, no matter what is the most important effect for a specific site of target, the physical modeling scheme for site effect needs a precise model of the actual ground. If the model is strongly biased, then the prediction should also be strongly biased. Thus success of this approach depends on the information of the physical model that we can collect. The better the

model, the better the prediction. To what precision and extent we must explore the underground structure for desired accuracy of prediction is an open question. A simple rule of thumb is that any variation of a structure with the same order of one-quarter wavelength may have non-negligible effect as Eq. (1) implies.

Physical properties of the actual complex structures of the Earth can be obtained by various geological, geophysical, and geotechnical methods, which can be used in the physical modeling scheme. Once a physical model of the whole area of interest is calibrated to actual observation, then such a model of the ground will be a common property of people, on which we can depend forever. From materials we have shown here, it seems appropriate to conclude that physical modeling of the ground is now a realistic and effective approach for practical evaluation/prediction of site effects. Needless to say, any physical models that we create in this manner must be validated with the observed data before we use them for prediction. Otherwise it will be a "castle on the sand." The advantage of the physical modeling approach is that it can predict site amplification for any hypothesized sources that have not yet happened but will happen in the near future.

From an engineering point of view, it seems too rigorous and cumbersome to include site-specific, spectral, or waveform representation of site effects as described here. However, a soil-type-specific approach commonly found in the current seismic codes does not represent the essential part of the site effects and, hence, the resulting engineered structures will be vulnerable to the actual input generated by a strong earthquake close to the site. This is exactly the case of the Hyogo-ken Nanbu, Japan, earthquake of 1995. Most of the damage-concentrated areas in Kobe belong to the moderate-to-stiff soil category in the Japanese code and it was not necessary to consider much amplification. But the damage concentration was created by the edge effect of the deeper structure near the edge of the Osaka basin, as reviewed here. Thus we may need to develop a way to translate site effects evaluated by a physical modeling approach into simple but effective engineering representations for better seismic design of structures.

References

Aki, K. (1988). Local site effects on strong ground motion. In: "Earthquake Engineering and Soil Dynamics II - Recent Advances in Ground Motion Evaluation," pp. 103–155. ASCE.

Aki, K., and B. Chouet (1975). Origin of coda waves: source, attenuation and scattering effects. *J. Geophys. Res.* **80**, 3322–3342.

Aki, K., and K. L. Larner (1970). Surface motion of a layered medium having an irregular interface due to incident plane SH waves. *J. Geophys. Res.* **75**, 933–954.

Aki, K., and P. G. Richards (1980). *Quantitative Seismology*. W. H. Freeman, San Francisco.

Andrews, D. J. (1986). Objective determination of source parameters and similarity of earthquakes of different size. In: "Earthquake Source Mechanics," *AGU Geophys. Monograph* **37**, 259–268.

Archuleta, R. (1998). ESG studies in the United States: Results from borehole arrays. In: "The Effects of Surface Geology on Seismic Motion" (K. Irikura, K. Kudo, H. Okada, and T. Sasatani, Eds.), pp. 3–14. Balkema, Rotterdam.

Bard, P.-Y., and M. Bouchon (1980). Seismic response of sediment-filled valleys, Part 1: The case of incident SH waves. *Bull. Seismol. Soc. Am.* **70**, 1263–1286.

Bard, P-Y., M. Campillo, F. J. Chavez-Garcia, and F. J. Sanchez-Sesma (1988). The Mexico earthquake of September 19, 1985—A theoretical investigation of large- and small-scale amplification effects in the Mexico City Valley. *Earthq. Spectra* **4**, 609–633.

Bonilla, L. F., J. H. Steidl, G. T. Lindley, A. G. Tumarkin, and R. Archuleta (1997). Site amplification in the San Fernando Valley, California: Validity of site effect estimation using the S-wave, coda, and H/V methods. *Bull. Seismol. Soc. Am.* **87**, 710–730.

Boore, D. M. (1972). Finite-difference methods for seismic waves. In: "Methods in Computational Physics" (B.A. Bolt, ed.), Vol. 11, pp. 1–37. Academic Press.

Chavez-Garcia, F. J., and P.-Y. Bard (1994). Site effects in Mexico City eight years after the September 1985 Michoacan earthquake. *Soil Dyn. Earthq. Eng*. **13**, 229–247.

Chin, B. H., and K. Aki (1991). Simultaneous study of the source, path, and site effects on strong motion during the 1989 Loma Prieta earthquake: A preliminary result on pervasive nonlinear site effects. *Bull. Seismol. Soc. Am.* **81**, 1859–1884.

Field, E. H., and K. H. Jacob (1995). A comparison and test of various site response estimation techniques, including three that are not reference-site-dependent. *Bull. Seismol. Soc. Am.* **85**, 1127–1143.

Field, E. H., Y. Zeng, J. G. Anderson, and I. A. Beresnev (1998). Pervasive nonlinear sediment response during the 1994 Northridge earthquake. In: "The Effects of Surface Geology on Seismic Motion" (K. Irikura, K. Kudo, H. Okada, and T. Sasatani, Eds.), pp. 773–778. Balkema, Rotterdam.

Fukushima, Y., and T. Tanaka (1990). A new attenuation relation for peak horizontal acceleration of strong earthquake ground motion in Japan. *Bull. Seismol. Soc. Am.* **80**, 757–783.

Fukutake, K., A. Ohtsuki, M. Sato, and Y. Shamoto (1990). Analysis of saturated dense sand-structure system and comparison with results from shaking table test. *Earthq. Eng. Struct. Dyn.* **19**, 977–992.

Furumura T., and B. L. N. Kennett (1998). On the nature of regional seismic phases-III. The influence of crustal heterogeneity on the wavefield for subduction earthquakes: the 1985 Michoacan and 1995 Copala, Guerrero, Mexico earthquakes. *Geophys. J. Int.* **135**, 1060–1084.

Geli, L., P.-Y. Bard, and B. Jullien (1988). The effect of topography on earthquake ground motion: A review and new results. *Bull. Seismol. Soc. Am.* **78**, 42–63.

Graves, R. W. (1998). Long period 3D finite difference modeling of the Kobe mainshock. In: "The Effects of Surface Geology on Seismic Motion" (K. Irikura, K. Kudo, H. Okada, and T. Sasatani, Eds.), pp. 1339–1345. Balkema, Rotterdam.

Graves, R. W., A. Pitarka, and P. G. Somerville (1998). Ground-motion amplification in the Santa Monica area: effect of shallow basin-edge structure. *Bull. Seismol. Soc. Am.* **88**, 1224–1242.

Hanks, T. C. (1975). Strong ground motion of the San Fernando, California, earthquake: ground displacements. *Bull. Seismol. Soc. Am.* **65**, 193–225.

Hartzell, S., A. Leeds, A. Frankel, and J. Michael (1996). Site response for urban Los Angeles using aftershocks of the Northridge earthquake. *Bull. Seismol. Soc. Am.* **86**, S168–S192.

Haskell, N. A. (1960). Crustal reflection of plane SH waves. *J. Geophys. Res.* **65**, 4147–4150.

Hatayama, K., K. Matsunami, T. Iwata, and K. Irikura (1995). Basin-induced Love waves in the eastern part of the Osaka basin. *J. Phys. Earth* **43**, 131–155.

Hong, T. L., and D. V. Helmberger (1978). Glorified optics and wave propagation in non planar structures. *Bull. Seismol. Soc. Am.* **68**, 1313–1330.

Horike, M. (1985). Inversion of phase velocity of long period microtremors to the S-wave velocity structure down to the basement in urbanized areas. *J. Phys. Earth* **33**, 59–96.

Hudson, D. E. (1972). Local distribution of strong earthquake ground motions. *Bull. Seismol. Soc. Am.* **62**, 1765–1786.

Inoue, T., and T. Miyatake (1997). 3-D simulation of near-field strong ground motion: Basin edge effect derived from rupture directivity. *Geophys. Res. Lett.* **24**, 905–908.

Irikura, K., K. Kudo, H. Okada, and T. Sasatani (Eds.) (1998). The Effects of Surface Geology on Seismic Motion, *Proc. of the Second International Symposium on Effects of Surface Geology on Strong Motions*. Yokohama, Japan, Balkema, Rotterdam.

Iwata T., and K. Irikura (1988). Source parameters of the 1983 Japan Sea earthquake sequence. *J. Phys. Earth* **36**, 155–184.

Joyner, W. D., and D. M. Boore (1981). Peak horizontal acceleration and velocity from strong-motion records including records from the 1979 Imperial Valley, California, earthquake. *Bull. Seismol. Soc. Am.* **71**, 2011–2038.

JWG-ESG (IASPEI/IAEE Joint Working Group on Effects of Surface Geology on Strong Motions) (1992). *Proc. of the First International Symposium on Effects of Surface Geology on Strong Motions*. Odawara, Japan.

Kagawa, T., S. Sawada, and Y. Iwasaki (1992). On the relationship between azimuth dependency of earthquake ground motion and deep basin structure beneath the Osaka plain. *J. Phys. Earth* **40**, 73–83.

Kanai, K., T. Osada, and T. Tanaka (1954). An investigation into the nature of microtremors. *Bull. Earthq. Res. Inst.* **32**, 199–209.

Kato, K., M. Takamura, T. Ikeura, K. Urano, and T. Uetake (1992). Preliminary analysis for evaluation of local site effects from strong motion spectra by an inversion method. *J. Phys. Earth* **40**, 175–191.

Kato, K., K. Aki, and M. Takemura (1995). Site amplification from coda waves: Validation and application to S wave site response. *Bull. Seismol. Soc. Am.* **85**, 467–477.

Kawase, H. (1993). Effects of surface and subsurface irregularities. In: "Earthquakes and Ground Motions", Pert I, Ch.3, Section 3.3, pp. 118–155. Architectural Institute of Japan.

Kawase, H. (1996). The cause of the damage belt in Kobe: "The basin-edge effect," Constructive interference of the direct S-wave with the basin-induced diffracted/Rayleigh waves. *Seism. Res. Lett*. **67**(5), 25–34.

Kawase, H., and K. Aki (1989). A study on the response of a soft basin for incident S, P, and Rayleigh waves with special reference to the long duration observed in Mexico City. *Bull. Seismol. Soc. Am.* **79**, 1361–1382.

Kawase, H., and T. Sato (1992). Simulation analysis of strong motions in the Ashigara Valley considering one- and two-dimensional geological structures. *J. Phys. Earth* **40**, 27–56.

Kawase, H., T. Satoh, and K. Fukutake (1996). Simulation of the borehole records observed at the Port Island in Kobe, Japan, during the Hyogo-ken Nanbu earthquake of 1995. *Proc. of 11th World Conf. on Earthq. Eng.*, Paper No.140.

Kawase, H., S. Matsushima, R. W. Graves, and P. G. Somerville (1998a). Three-dimensional wave propagation analysis of simple two-dimensional basin structures with special reference to "the Basin-Edge Effect." *Zisin (Series-2)* **50**, 431–449 (in Japanese with English abstract).

Kawase, H., T. Satoh, T. Iwata, and K. Irikura (1998b). S-wave velocity structures in the San Fernando and Santa Monica areas. In: "The Effects of Surface Geology on Seismic Motion" (K. Irikura, K. Kudo, H. Okada, and T. Sasatani, Eds.), pp. 733–740. Balkema, Rotterdam.

Kinoshita, S. (1992). Attenuation of shear waves in a sediment. *Proc. of 10th World Conf. on Earthq. Eng.*, pp. 685–690.

Kobayashi, K., F. Amaike, and Y. Abe (1992). Attenuation characteristics of soil deposits and its formulation, *Proc. of International Symposium on the Effects of Surface Geology on Seismic Motion*, **1**, pp. 269–274. Association for Earthquake Disaster Prevention, Japan.

Kudo, K., K. Irikura, and H. Kawase (1992). Effects of surface geology on seismic motion: Introduction to the special issue. *J. Phys. Earth* **40**, 1–4.

Lachet, C., and P.-Y. Bard (1994). Numerical and theoretical investigation on the possibilities and limitations of the Nakamura's technique. *J. Phys. Earth* **84**, 1574–1594.

Lermo, J., and F. J. Chavez-Garcia (1993). Site effect evaluation using spectral ratios with only one station. *Bull. Seismol. Soc. Am.* **83**, 1574–1594.

Lysmer, J., and G. Waas (1972). Shear waves in plain infinite structures. *J. Eng. Mech. Div.* **98**, 85–105. ASCE.

Matsushima, S., and H. Kawase (1998). 3-D wave propagation analysis in Kobe referring to "The basin-edge effect." In: "The Effects of Surface Geology on Seismic Motion" (K. Irikura, K. Kudo, H. Okada, and T. Sasatani, Eds.), pp. 1377–1384. Balkema, Rotterdam.

Nakamura, Y. (1989). A method for dynamic characteristics estimation of subsurface using microtremor on the ground surface. *QR of RTRI* **30**, 25–33.

Pitarka, A., K. Irikura, and T. Iwata (1997). Modeling of ground motion in the Higashinada (Kobe) area for an aftershock of the 1995 January 17 Hyogo-ken Nanbu, Japan earthquake. *Geophys. J. Int.* **131**, 231–239.

Pitarka, A., K. Irikura, T. Iwata, and H. Sekiguchi (1998). Local geological structure effects on ground motion from earthquakes on basin-edge faults. In: "The Effects of Surface Geology on Seismic Motion" (K. Irikura, K. Kudo, H. Okada, and T. Sasatani, Eds.), pp. 901–906. Balkema, Rotterdam.

Sanchez-Sesma, F. J. (1987). Site effects on strong ground motion. *Soil Dyn. Earthq. Eng.* **6**, 124–132.

Sato, H. (1984). Attenuation and envelope formulation of three component seismograms of small local earthquakes in randomly inhomogeneous lithosphere. *J. Geophys. Res.* **89**, 1221–1241.

Sato, T. (1990). Simulation of observed seismograms on sedimentary basin using theoretical seismograms in the period range from 2 sec to 20 sec—Synthesis of seismograms at Kobe and Osaka stations for the 1961 Kita-Mino earthquake, *Proc. of 8th Japan Earthq. Eng. Sym.*, pp. 193–198. Tokyo, Japan (in Japanese).

Sato, T., D. V. Helmberger, P. G. Somerville, R. W. Graves, and C. K. Saikia (1998a). Estimates of regional and local strong motions during the Great 1923 Kanto, Japan, earthquake (M_S8.2), Part 1: Source

estimation of a calibration event and modeling of wave propagation paths. *Bull. Seismol. Soc. Am.* **88**, 183–205.

Sato, T., D. V. Helmberger, P. G. Somerville, R. W. Graves, and C. K. Saikia (1998b). Estimates of regional and local strong motions during the Great 1923 Kanto, Japan, earthquake (M_S 8.2), Part 2: Forward simulation of seismograms using variable-slip rupture models and estimation of near-fault long period ground motions. *Bull. Seismol. Soc. Am.* **88**, 206–227.

Sato, T., R. W. Graves, and P. G. Somerville (1999). 3-D Finite-Difference simulations of long-period strong motions in the Tokyo Metropolitan Area during the 1990 Odawara earthquake (M_J 5.1) and the Great 1923 Kanto earthquake (M_S8.2) in Japan. *Bull. Seismol. Soc. Am.* **89**, 579–607.

Satoh, T., T. Sato, and H. Kawase (1995a). Evaluation of local site effects and their removal from borehole records observed in the Sendai Region, Japan. *Bull. Seismol. Soc. Am.* **85**, 1770–1789.

Satoh, T., T. Sato, and H. Kawase (1995b). Nonlinear behavior of soil sediments identified by using borehole records observed at the Ashigara Valley, Japan. *Bull. Seismol. Soc. Am.* **85**, 1821–1834.

Satoh, T., T. Sato, and H. Kawase (1997). Statistical spectral model of earthquakes in the eastern Tohoku district, Japan, based on the surface and borehole records observed in Sendai. *Bull. Seismol. Soc. Am.* **87**, 446–462.

Satoh, T., M. Fushimi, and Y. Tatsumi (1998). Inversion of nonlinearity of soil sediments using borehole records in Amagasaki. In: "The Effects of Surface Geology on Seismic Motion" (K. Irikura, K. Kudo, H. Okada, and T. Sasatani, Eds.), pp. 823–830. Balkema, Rotterdam.

Satoh, T., H. Kawase, and S. Matsushima (2001). Differences between site characteristics obtained from microtremors, S-wave, P-wave, and codas, *Bull. Seismol. Soc. Am.* **91**, 313–334.

Schnabel, P. B., J. Lysmer, and H. B. Seed (1972). A computer program for earthquake response analysis of horizontally layered sites. *EERC Report 72-12*.

Seale, S. H., and R. Archuleta (1989). Site amplification and attenuation of strong ground motion. *Bull. Seismol. Soc. Am.* **79**, 1673–1696.

Singh, S. K., and M. Ordaz (1993). On the origin of long coda observed in the lake-bed strong-motion records of Mexico City. *Bull. Seismol. Soc. Am.* **83**, 1298–1306.

Spudich, P., M. Hellweg, and W. H. K. Lee (1996). Directional topographic site response at Tarzana observed in aftershocks of the 1994 Northridge, California, earthquake: Implications for mainshock motions. *Bull. Seismol. Soc. Am.* **86**, 192–208.

Steidl, J. H., A. G. Tumarkin, and R. Archuleta (1996). What is a reference site? *Bull. Seismol. Soc. Am.* **86**, 1733–1748.

Takahashi, K., S. Omote, T. Ohta, T. Ikeura, and S. Noda (1988). Observation of earthquake strong-motion with deep borehole—Comparison of seismic motions in the base rock and those on the rock outcrop, *Proc. of 8th World Conf. on Earthq. Eng.* **3**, 181–186.

Takenaka, H., T. Furumura, and H. Fujiwara (1998). Recent developments in numerical methods for ground motion simulation. In: "The Effects of Surface Geology on Seismic Motion" (K. Irikura, K. Kudo, H. Okada, and T. Sasatani, Eds.). Balkema, Rotterdam.

Toriumi, I. (1975). Earthquake characteristics in the Osaka plain. *Proc. of the 4th Japan Earthq. Eng. Sym.* pp. 129–136 (in Japanese).

Toriumi, I., S. Ohba, and N. Murai (1984). Earthquake motion characteristics of Osaka plain. *Proc. of 8th World Conf. on Earthq. Eng.* **2**, 761–768.

Tujiura, M. (1978). Spectral analysis of the coda waves from local earthquakes. *Bull. Earth. Res. Inst.* **53**, 1–48.

Vidale, J. E., and D. V. Helmberger (1988). Elastic finite difference modeling of the 1971 San Fernando, California, earthquake. *Bull. Seismol. Soc. Am.* **78**, 122–141.

Yamanaka, H., K. Seo, and T. Samano (1989). Effects of sedimentary layers on surface-wave propagation. *Bull. Seismol. Soc. Am.* **79**, 631–644.

Zhao, B., M. Horike, Y. Takeuchi, and H. Kawase (1997). Comparison of site-specific response characteristics inferred from seismic motions and microtremors, *Zisin (Series-2)* **50**, 67–87 (in Japanese with English abstract).

62

Use of Engineering Seismology Tools in Ground Shaking Scenarios

Ezio Faccioli
Department of Structural Engineering, Politecnico, Milano, Italy
Vera Pessina
INGV - Instituto Nazionale di Geofisica e Volcanologia, Milan, Italy

1. Introduction: Approaches to the Selection of Scenario Earthquakes

Damage scenario and loss estimation studies for destructive events represent a potentially powerful tool for enhancing the level of earthquake preparedness and for improving disaster prevention policies for densely populated areas in seismic regions. Especially for large and complex urban environments, a fundamental prerequisite for such a task is the realistic estimation of the spatial distribution of the ground-motion severity generated by scenario earthquakes. The recent cases of the 1995 Kobe (Hyogo-ken Nanbu) and 1999 Kocaeli and Duzce (Turkey) events stand out to signal the overwhelming influence that the spatial distribution of ground motions and its close dependence on source characteristics, local geological structure, and soil properties can have on the resulting damage.

A preliminary issue of critical relevance for the construction of damage scenarios is the choice between a deterministic and a probabilistic approach to the representation of ground shaking and to damage estimation. For ease of reference, the two approaches are briefly outlined and discussed below.

The deterministic approach develops a particular earthquake scenario upon which a ground-motion hazard evaluation is based. The scenario consists of the postulated occurrence of an earthquake of a specified size occurring at a specified location, typically a seismically active fault. The standard deterministic approach consists of the following steps:

1. Identification of the locations and characteristics of all significant earthquake sources that might affect the zone of interest, typically a city. The seismic potential is quantified by assigning to each source a significant earthquake that can be the maximum historical event known from that source (Maximum Probable Earthquake, or MPE), or the maximum earthquake that appears capable of occurring under the known tectonic framework (Maximum Credible Earthquake, or MCE). The shortest distance from the source to the sites in the zone of interest is generally assumed, in the absence of other information.
2. Selection of the attenuation relations enabling one to estimate the ground shaking (e.g., in terms of intensity, response spectral ordinates, or Arias intensity) within the zone of interest as a function of earthquake magnitude, source-to-site distance, and local ground conditions.
3. Definition of the controlling earthquake (i.e., the earthquake that is expected to produce the strongest level of shaking). The selection is made comparing, through the attenuation relation, the effects produced at the site by the combination of earthquake distance and magnitude identified at step 1. The resultant earthquake will define the seismic scenario.

However, depending on the historical seismicity of the region, variations with respect to this standard procedure are possible. Thus, it may be desirable to adopt more than one scenario earthquake, for instance, a destructive event (such as the MPE) and a less severe, but damaging, one with a higher likelihood of occurrence.

At the end of the process, the deterministic analysis gives as a result one or more scenarios that represent the worst situations expected, but it does not provide any information about their occurrence in time. In fact, this approach does not predict the likelihood of such occurrences during the lifetime of the

INTERNATIONAL HANDBOOK OF EARTHQUAKE AND ENGINEERING SEISMOLOGY, VOLUME 81B *ISBN: 0-12-440658-0*

TABLE 1 Occurrence Probabilities of Earthquakes Commonly Referred to in Earthquake Engineering

Type of occurrence	Return period[a]	Probability in 50 years
Frequent	43	0.70
Occasional	72	0.50
Rare	475	0.10
Very rare	970	0.05

[a] Based on Poisson occurrence process.

structures that make up the building and infrastructure stock in the zone of interest.

The probabilistic approach is a typical application of Probabilistic Seismic Hazard Analysis (PSHA), whose basic features have been established since the late 1960s (Cornell, 1968). The method has since become a worldwide standard and need not be recapitulated here in detail. It consists of four basic steps, some of which are partly coincident with those of the deterministic approach, namely:

- Seismic source zone identification
- Probabilistic characterization of source zone activity
- Selection of attenuation relation
- Integration over the whole range of magnitudes and distances for each source zone in order to obtain, for each site of interest, the probabilistic hazard values in the form of a cumulative distribution for the ground-motion parameter(s) of interest

A certain degree of combination of the deterministic and probabilistic approaches is also conceivable. For instance, in a zone with a well-documented history of damaging earthquakes one may choose the deterministic scenario, paying some consideration to the relative frequency of past events rather than to the MPE or MCE events. Table 1 may provide some guidance in this respect.

The 50 years reference term in Table 1 can be roughly regarded as the expected engineering lifetime of an ordinary building (this lifetime would increase to about 100 years for a bridge or tunnel, and to 100–150 years for a dam).

At a more sophisticated level, since probabilistic risk studies cover all possible damaging events in a region and estimate the cumulative losses from all of them (e.g., in the form of the annual loss rate), they can help in making an objective preselection of the basic features of the scenario earthquake. For instance, the latter could be the event that occurs on the seismogenic structure (fault or area source) that contributes most to the risk at the chosen return period, and has the magnitude and location contributing most to the loss (McGuire, 1995). Probabilistic ground-motion maps are normally developed on a regional basis for a single "reference" class of ground conditions, e.g., soft rock; one can then multiply such motions by frequency-dependent factors depending on the site conditions. Some of the difficulties inherent in this approach, which is not ideally suited for scenario studies in urban areas with complex geology, have been discussed by Frankel and Safak (1998).

While the two approaches generally point to different requirements on the side of risk analysts and managers (see, e.g., PELEM 1989), the deterministic approach is more intuitive and may be more appealing to local administrators because it assumes the occurrence of a well-defined earthquake (in terms of magnitude and source-to-site distance) that is used as input for all the successive steps of the risk analysis. However, it conceals to some extent the problem that the choice of the appropriate earthquake is a judgmental and not a quantitative issue.

Since the emphasis in this chapter is mainly on the quantification and representation of the effects that potentially control the ground shaking scenario within a limited area of interest, and especially those related to the type and severity of site effects and to the source process, such as the fault rupture geometry and directivity, we assume the deterministic approach as the natural underlying reference.

The practical feasibility of the deterministic approach may in itself be a nonnegligible problem. In many earthquake-prone areas of the world, and typically in most of the Mediterranean region, the seismicity is governed by earthquakes with maximum magnitudes in the 6.5–7.0 range, originating on faults that seldom generate unambiguous co-seismic surface ruptures, and whose geometry is ill-defined. It is consequently difficult to associate a scenario earthquake in such zones with a precisely defined tectonic lineament, as is often done in much of the western United States and Japan. This difficulty, as well as the need to provide ground-motion estimations with tools basically accessible to engineers, supports the use of simple methods. Therefore, in this chapter we shall mostly consider ground-motion representations obtained by combining appropriate attenuation relations of strong-motion parameters with digital geological or geotechnical maps of the study area. The combination is typically performed through Geographic Information System (GIS) technology in raster version. Since the attenuation relations play a central role, the following section is devoted entirely to an overview of them from the viewpoint of the user interested in scenario development.

Concerning the role of the different factors that control scenario ground motions, we devote somewhat more attention to site effects than to source effects, because the former are considered capable of causing stronger deviations with respect to average empirical predictions. Situations in which these predictions are particularly inadequate because of the occurrence of complex site effects, such as on sediment-filled valleys, are dealt with in Section 4.

2. Attenuation Relations for Ground-Motion Parameters: An Overview

The attenuation relations for ground-motion parameters are statistical regressions, either linear or nonlinear, on appropriate sets of recorded data. Since we are not interested here in the

TABLE 2 Distinctive Factors of Attenuation Relations

Ground-motion descriptor	Tectonic regime	Origin of data
• Response spectral ordinates • Macroseismic intensity • Arias intensity • Other	• Shallow earthquakes in active tectonic regions • Stable continental regions • Subduction zones	• Europe • North America • Japan • Worldwide

generation aspects of these relations but rather in their use as engineering tools, the emphasis in this section is mainly on practical application aspects.

Table 2 highlights three general criteria that can be used as a guide in the initial choice of an attenuation relation. The selection of the ground-motion parameter is linked to the scope of the scenario study and is discussed in more detail in the next section. The two other criteria—tectonics and geographical region—should be considered with great care, usually side by side. Geographical origin of data usually entails not only differences of tectonic regime affecting earthquake generation but also different prevailing geological features, different crustal attenuation properties, and to some extent, different characteristics of recording instruments.

A sufficiently general representation of attenuation relations, showing the specific independent physical variables that concur to the ground shaking estimation, has the following additive structure:

$$\log y = f_1(M, r, SD) + f_2(FT) + f_3(S) + \varepsilon \qquad (1)$$

where

y = ground-motion parameter, e.g.: peak ground acceleration (PGA) or velocity; response spectral ordinate (horizontal or vertical) for a prescribed fundamental period T of the oscillator and damping factor; Arias intensity; macroseismic intensity.
M = preferably moment magnitude M_w, or equivalent in appropriate range (e.g., M_S, M_L).
r = source distance; this can be epicentral, hypocentral (r_{hypo}), minimum distance from the fault rupture (r_{rup}), or closest distance to the vertical projection of rupture on the Earth surface; see Abrahamson and Shedlock (1997, their figure 1).
SD = source directivity factor.
FT = fault-type factor.
S = site conditions factor.
ε = random variable, introduced to account for the uncertainty of the prediction, usually assumed to have a normal distribution, with zero mean and standard deviation $\sigma_{\log y}$.

The term $f_1(M, r, SD)$ is the basic form describing the dependence on magnitude, source-to-site distance, and source rupture directivity (SD). For rock sites and y = larger horizontal PGA value (in units of g), two of the most commonly used among such basic forms are

$$f_1(M, r) = -0.038 + 0.216(M_w - 6) - 0.777 \log R$$
$$R = (r^2 + 5.48^2)^{1/2} \qquad \sigma_{\log y} = 0.205 \qquad (2)$$

(Boore *et al.*, 1993) and

$$f_1(M, r) = -1.48 + 0.266 M_S - 0.922 \log R$$
$$R = (r^2 + 3.5^2)^{1/2} \qquad \sigma_{\log y} = 0.25 \qquad (3)$$

(Ambraseys *et al.*, 1996). In both cases, R and r are in kilometers. Equation (2) is based on data from western North America, with moment magnitude M_w ranging between 5.5 and 7.0, and is valid up to 100-km distance, while Eq. (3) is applicable in Europe and the Middle East, with M_S in the 4.0–7.9 range. For $M_w \cong M_S = 7$ the values predicted by Eq. (2) are 1.2 to 2.0 times larger than those obtained with Eq. (3), depending on distance, while for $M_w = 6$ the ratio is 0.4 to 0.6. In Eqs. (2) and (3) attenuation with distance is independent of magnitude. In other relations (e.g., Abrahamson and Silva, 1997), a nonlinear magnitude-dependent factor is introduced in the distance attenuation term that produces faster attenuation of ground-motion amplitude at the smaller magnitudes.

For subduction zone earthquakes, where the distances are generally larger because of the offshore position or the depth of hypocenter, the distance dependence is r_{hypo}^{-1} (Atkinson and Boore, 1997). Other authors (e.g., Anderson, 1997; Youngs *et al.*, 1997) use instead r_{rup}, but r_{hypo} is indeed a good approximation for r_{rup} when the rupture surface is not defined.

The directivity term SD in Eq. (1) contains typically a cosine function of the angle between the direction of rupture propagation and that of waves traveling from the fault to the site. More specifically, in Somerville *et al.* (1997) the SD term is $\cos\theta$ for strike-slip faults and $\cos\phi$ for dip-slip faults, where θ and ϕ are defined as shown in Figure 1. Rupture directivity causes spatial variation in both amplitude and duration of the ground motion. Somerville *et al.* (1997) introduce the directivity term as an additive factor in existing attenuation relations, which account for the magnitude and distance dependence. Thus, using

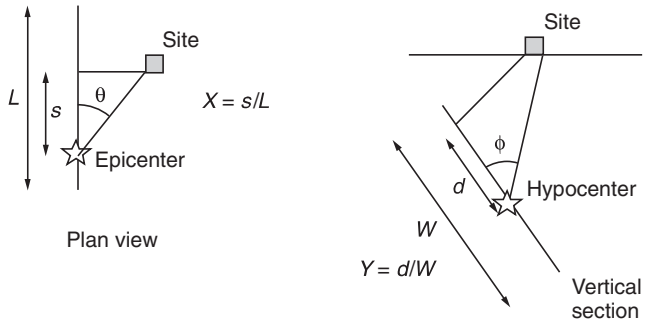

FIGURE 1 Definition of rupture directivity parameters θ and X for strike-slip fault, and ϕ and Y for dip-slip fault (from Somerville *et al.*, 1997).

the Abrahamson and Silva (1997) relation as a reference, the additional directivity term is

$$y = C_1 + C_2 X \cos\theta \qquad \text{for strike-slip faults and } M > 6.5$$

or

$$y = C_1 + C_2 Y \cos\phi \qquad \text{for dip-slip faults and } M > 6.5 \quad (4)$$

where

y = prediction residual of ln(spectral acceleration) at a given oscillator period.
X, Y = along strike and updip distance ratios, shown in Figure 1.
θ, ϕ = angles previously defined.
C_1, C_2 = period-dependent regression coefficients.

The influence of the directivity terms is significant at periods larger than 0.6 sec and increases with period: for a strike-slip fault, at $T = 2$ sec, the directivity effect on amplitude ranges between 0.6 and 1.8 times the average value neglecting directivity (for dip-slip fault the range is 0.8–1.2).

A somewhat different, analytical approach has been adopted to introduce directivity in an attenuation relation for the Arias intensity I_a, with parameters calibrated on strong-motion data from the Mediterranean region (Faccioli, 1983). This relation basically applies for a point source, and for horizontal motion has the form

$$\log I_a = 1.065 M_w - 2 \log r_{hypo} + \log D_a(\theta) - 4.63 \quad (5)$$

where I_a is in m/sec, and r_{hypo} is limited within the 10- to 50-km range. Source directivity is described by the function

$$D_a(\theta) = \frac{3 - m\cos\theta}{(1 - m\cos\theta)(2 - m\cos\theta)^2} \quad (6)$$

where θ is the angle between the direction of rupture propagation and the hypocenter-to-receiver direction, and m (<1) is the ratio between the rupture propagation and the S-wave propagation speeds, generally assumed between 0.7 and 0.85. The effects of directivity are best taken into account by the previous expression in the case of vertical (strike-slip) or steeply inclined (dip-slip) faults and rupture propagation along the strike of the fault.

The fault-type factor on the r.h.s. of Eq. (1), written out more explicitly, is

$$f_2(FT) = F_{\psi 1}(M, T) + HW_{\psi 2}(M, r_{rup}) \quad (7)$$

where $F_{\psi 1}(M, T)$ accounts for the fault style: reverse and thrust faulting generate larger high-frequency spectral ordinates than strike-slip and normal earthquakes. F is the fault-type index: it is 1 for reverse slip, 0.5 for reverse/oblique, and 0 otherwise in Abrahamson and Silva (1997). Boore *et al.* (1997) use instead a single coefficient to discriminate strike-slip earthquakes, reverse-slip ones, and the case of unspecified mechanism; $HW_{\psi 2}(M, r_{rup})$ describes the "overhanging wall" effect in reverse-fault ruptures. One attenuation relation showing this factor is due to Abrahamson and Silva (1997), where HW is equal to 1 for sites on the overhanging-wall side of the fault and 0 otherwise.

The third factor in Eq. (1), $f_3(S)$, quantifies the influence of the soil profile at the site. As a starting point, it is useful to recall the site classification of Boore *et al.* (1993) based on V_{S30}, i.e., the shear-wave velocity averaged in the upper 30 m of soil, reproduced in Table 3. A number of other commonly used descriptions, summarized in Table 4, refer to this classification.

The simplest option one can use in the estimation of response spectral ordinates, discriminating simply between rock and soil, is case I of Table 4, where C_S is a constant regression coefficient

TABLE 3 Site Classification (from Boore *et al.*, 1993)

Soil profile class	V_{S30} [m/sec]
A	>750
B	360–750
C	180–360
D	<180

TABLE 4 Available Options for the Site Factor $f_3(S)$ in Eq. (1)

Case	$f_3(S)$	Parameter values/note		Reference
I	$C_S\, S_S$	$S_S = 0$ for rock, $S_S = 1$ for soil C_S = regression coefficient (const.)		Spudich *et al.* (1999)
		$C_S = \text{a} + \text{b}\ \ln(\text{PGA}_{rock} + \text{c})$		Abrahamson and Silva (1997)
II	$C_a S_a + C_S\, S_S$	Rock	$S_a = 0,\ S_S = 0$	Ambraseys *et al.* (1996)
	where	Stiff soil	$S_a = 1,\ S_S = 0$	Boore *et al.* (1993)
	S_a and S_S, or S_H,	Soft soil	$S_a = 0,\ S_S = 1$	
	describe the soil	Firm/stiff Quat. deposits > 10 m	$S_S = 0,\ S_H = 0$	Campbell (1997)
	classification and/or	Soft rock	$S_S = 1,\ S_H = 0$	
	deposit depth	Hard rock	$S_S = 0,\ S_H = 1$	
	C_a, C_S are	Rock	$S_a = 0,\ S_S = 0$	Sabetta and Pugliese (1996)
	regression coeff.	Shallow alluvium	$S_a = 1,\ S_S = 0$	
		Deep alluvium	$S_a = 0,\ S_S = 1$	
III	$C_S \log(V_{S30})$	V_{S30} values		Bommer *et al.* (1998) Boore *et al.* (1997)

depending on oscillator period (as in Spudich *et al.*, 1999). A considerable refinement, allowing to take into account nonlinearity in soil response, represents C_S as a function of expected PGA on rock (Abrahamson and Silva, 1997). Case II of Table 4 shows three different possibilities of seismic soil classification inspired by the four classes of Table 3; the S_a and S_s factors in this case allow also to take into account the influence of the depth of the soil deposit.

As a step toward a finer spatial resolution in the representation of soil response, one can also describe the site effects as a continuous function of the shear-wave velocity V_{S30} (case III), if known.

Especially for soil category C in Table 3, the magnitude of site effects estimated by the attenuation relations on response spectra strongly depends on the period; this is illustrated in Figure 2, which portrays the variation of the soil amplification factor $y(T;\text{soil})/y(T;\text{rock})$ for the different cases of Table 4. For $T = 0$ amplification is about 1.3, while the largest soil amplification, about 1.7, occurs at T around 1 sec. The amplification factors of the relation by Boore *et al.* (1997) actually coincide with those by Spudich *et al.* (1999). Note the significantly different amplification behavior of shallow soil deposits with respect to deep ones, consistent with the expectations.

Finally, concerning the uncertainty of the predictions, the standard deviation $\sigma_{\log y}$ is the commonly used measure of the data dispersion about the regression mean value. The typical range of $\sigma_{\log y}$ values between 0.2 and 0.3 found in most attenuation relations (for spectral ordinates it may be somewhat larger) means that the standard error band extends between about 0.6 and 1.8 times the predicted mean value.

In reality, in an attenuation relation the standard error depends on two different sources: (1) the statistical uncertainties due to the random scatter of data, and (2) the so-called epistemic uncertainties linked to the model chosen to represent attenuation.

The epistemic aspects of the standard error are difficult to define; we illustrate in Section 3.3 one example comparing alternative methods for the prediction of earthquake ground motion that can provide some quantitative appreciation of the variability to be expected from the use of different models.

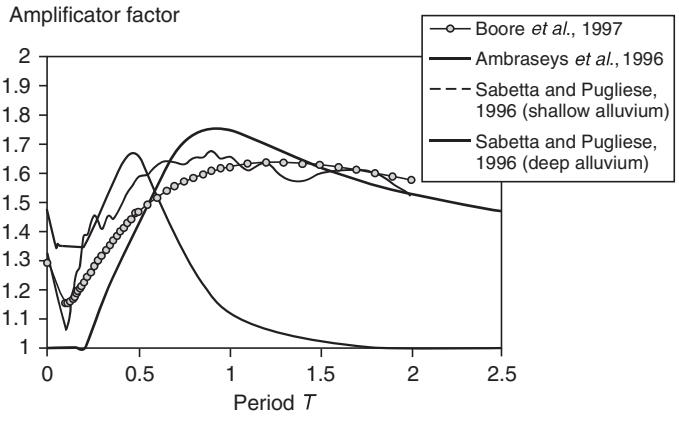

FIGURE 2 Variation with oscillator period of response spectral amplification factors of soft (category C in Table 3) and deep/shallow soil sites with respect to rock sites for different cases in Table 4.

About the random variability of the ground motion, a number of authors (mainly those who use a two-stage regression method) recognize a part of the standard error as due to the random variability of the records of the same event (Boore *et al.*, 1993), and a part collecting all the other (unspecified) components of variability. Other authors, using a random effect model analysis (Abrahamson and Silva, 1997) or a joint regression analysis (Youngs *et al.*, 1997), recognize the same intraevent variability term and, in addition, an earthquake-to-earthquake component of the variability. The total standard error is the square root of the overall variance of the regression.

It was also found (Youngs *et al.*, 1997) that the standard error depends on the magnitude of the earthquake or on the level of shaking (expressed by PGA), especially for PGA (Boore *et al.*, 1997).

3. Selection of Ground-Motion Descriptors

3.1 Ground Motions and Damage Estimation

A basic criterion for the selection of the parameters describing the shaking hazard in earthquake scenario studies is that the higher the damage state, the greater is generally the need for more detailed ground-motion information. Seismic risk scenarios do not usually produce damage predictions at the structure-by-structure level, which may require the knowledge of the full-time history of motion, but make use of some surrogates of it such as peak acceleration, or response spectral ordinates (related to global strength or displacement demand), or even macroseismic intensity. In addition, close to the seismic source, different descriptors of the ground motion may be useful. Some peculiar damage features observed, e.g., in Northridge 1994, especially for steel structures, have been linked to the distinct large-amplitude velocity pulses occurring in the near field. Because it has been found that the response spectrum cannot properly account for the destructiveness of these motions, a new measure of damage potential has been proposed, in the form of the drift demand spectrum (Iwan, 1994). On the other hand, integral measures that directly account for the ground-motion duration, such as the Arias intensity, appear as more suitable indicators of the shaking when geological damage, such as landslides and rockfalls, is of interest. Earthquake scenario maps using Arias intensity are discussed in more detail in Section 3.3.

A detailed discussion on the "best" ground-motion descriptor for earthquake scenarios is beyond the scope of this chapter since, as previously mentioned, the choice also depends on the parameters and methods used to estimate the damage to structures. Traditionally, because of scarcity of strong-motion recordings, macroseismic intensity has been used to quantify ground motion, and damage estimation methodologies were

TABLE 5 Ground Motion Descriptors and Damage Estimation Methods

Type of ground-motion parameter	Vulnerability (V)/damage (d) estimation	Object of estimation
Peak Ground Acceleration (PGA)	Vulnerability from score assignment, damage through empirical correlation e.g., $d = f(V, \text{PGA})$	Building and other structures
Acceleration or Displacement Response Spectrum	ATC–13 methodology, displacement limit state approach (Calvi, 1999; Faccioli *et al*., 1999)	Building structures
Intensity (I_{MM}, I_{MCS}, ...)	Methods based on Damage Probability Matrices (DPM)	Building and other structures
Arias Intensity (I_a)	Empirical correlations, e.g., between I_a and failure displacements (Wilson and Keefer, 1985)	Natural/artificial slopes, ground deformation

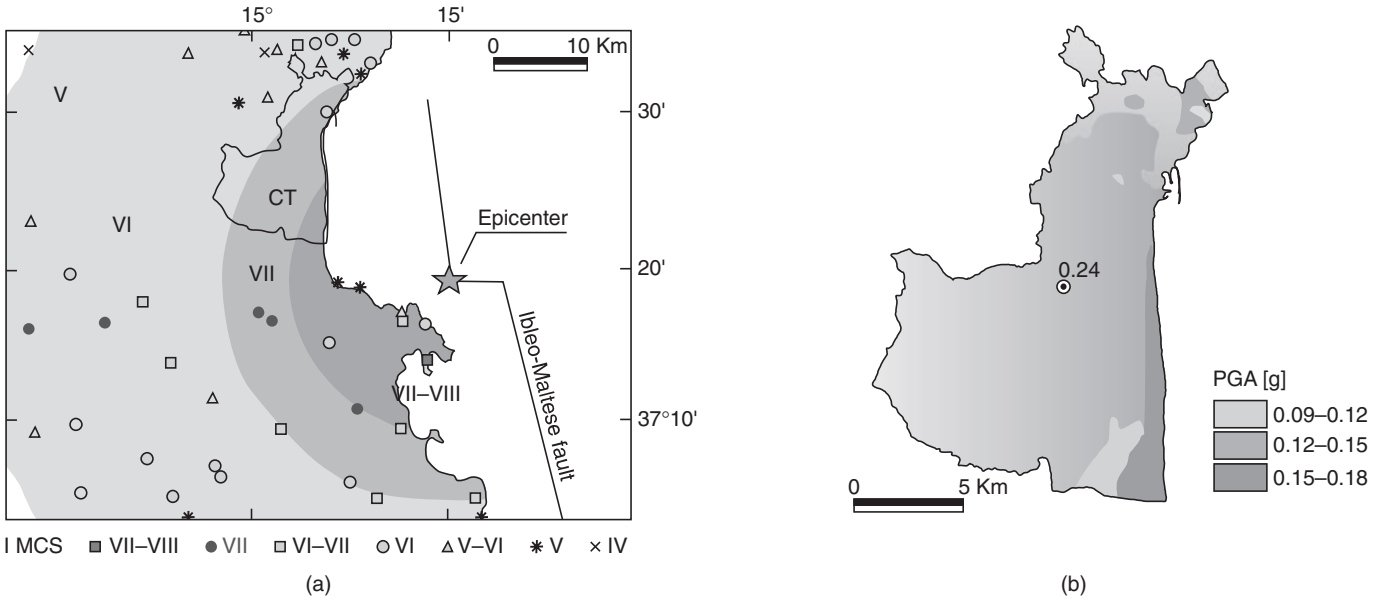

FIGURE 3 (a) Predicted and observed MCS intensities for the M_s 5.8, 1990 earthquake in eastern Sicily, including the Catania municipal area (denoted by CT). Symbols in legend are for observed intensities, while predicted intensities appear in different shades of gray and Latin numerals. (b) PGA values, in g, over the Catania municipal area predicted for the same earthquake using a geotechnical zonation map (see text); shown also is the only recorded PGA value (0.24 g).

predominantly based on this parameter. In recent years, following the vast increase of useful recorded data and the development of reliable numerical methods for simulating ground motions, instrumental measures have been increasingly used as ground-motion descriptors. The damage estimation methods have been updated accordingly, as in the US tool HAZUS (Whitman *et al*., 1997) and in other approaches developed in Europe (e.g., Calvi, 1999; Faccioli *et al*., 1999). In practice, in addition to intensity, peak ground acceleration (PGA) and response spectral ordinates, both in acceleration and displacement, are the parameters presently used in most earthquake scenario studies. For geological damage in hilly areas, as already pointed out, the Arias intensity is a convenient descriptor. Table 5 gives a summary of how these different descriptors of ground-motion severity can be linked to different methods of vulnerability and damage estimation.

Sensitivity considerations linked to the consequences on predicted damage resulting from the assumptions made in the creation of ground shaking maps are discussed in Section 3.4. We illustrate in the following section aspects related to the resolution of ground shaking maps resulting from different descriptors.

3.2 Resolution of Maps Using Different Descriptors: Intensity and PGA

To grasp some implications of using different hazard descriptors in terms of their spatial resolution, the comparison of predictive maps using macroseismic intensity (MCS scale) and PGA is instructive. An example is provided in Figures 3 and 4 for two different events affecting the municipal area of Catania, in eastern Sicily (Italy), which has a present population of about 500,000 and a historical record of destructive earthquakes. The maps in Figure 3 are for a moderate (M_S 5.8) earthquake that occurred in 1990, with maximum MCS intensity I_0 = VII–VIII. The epicenter, shown by a star in Figure 3a, is probably associated with a strike-slip E–W segment of a major N–S trending tectonic

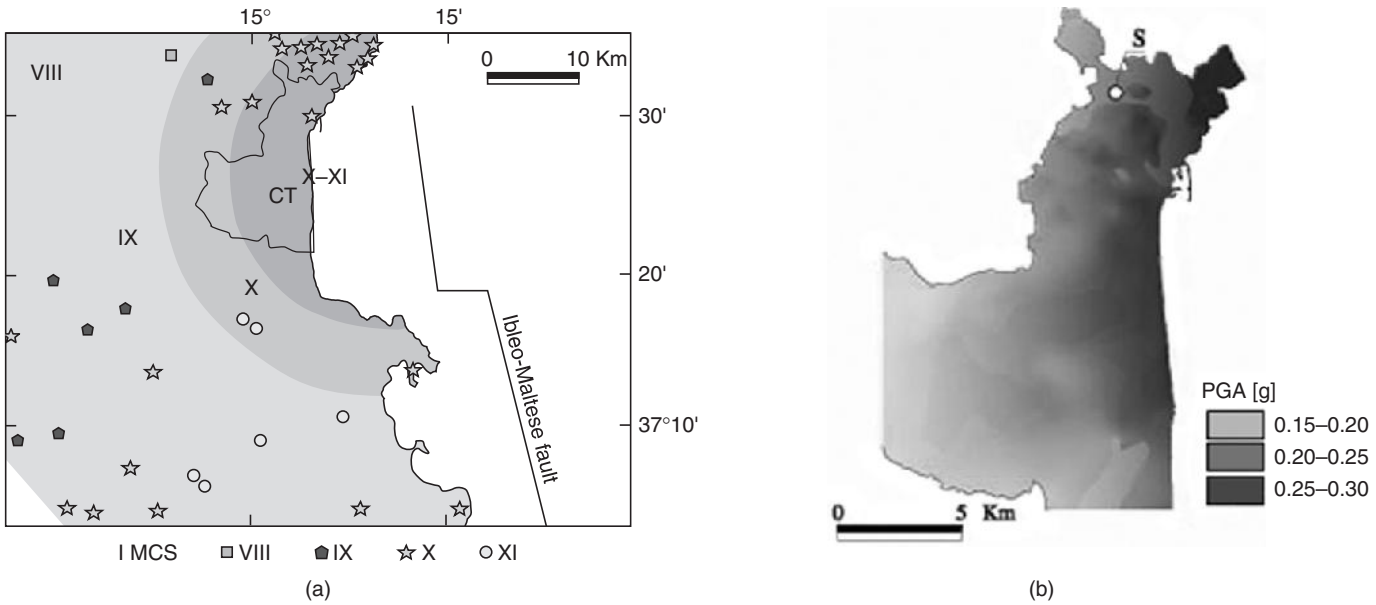

FIGURE 4 (a) As in Figure 3a, but for the $M7+$ event of January 11, 1693. (b) PGA map for Catania, generated assuming a 50-km-long rupture along the Ibleo-Maltese fault shown in Figure 3a. Site S in (b) is studied in the text, Section 4.3.

lineament, known as the Ibleo-Maltese fault (or escarpment). The relatively small size of this event allows us, for present purposes, to represent its source as a point.

The map of Figure 3a has been generated with a "circular" attenuation relation of the form $I = f(I_0, R_0, \text{distance})$ whereby I is predicted to decrease with distance only beyond the radius R_0 of earthquake effects on the built environment, and as such does not explicitly account for site conditions, as in the map of Figure 3a. The map area in this figure extends beyond the actual Catania municipality (labeled CT), to show both predicted and felt intensities in the surrounding region.

Note that the predicted variation across the Catania municipal area exceeds one intensity degree, while it is of one degree (from VII to VI) in the city area proper, which occupies the northern portion of the municipality. The felt intensity in 1990 in Catania was VI.

In contrast to the intensity map, the PGA map of Figure 3b (limited to the Catania municipal area) makes use of a geotechnical zonation in the form of a digital map of V_{S30}. The PGA map itself is generated from an attenuation relation that relies on a large set of European strong-motion data, including most of the significant records from Italian earthquakes, and is of type III in Table 4 as regards quantification of site conditions (Ambraseys, 1995). Thus, the map reflects the difference in near-surface soil properties between the city area proper, where massive and thin lava flows (from the Mt. Etna volcano) prevail, and the central and southern parts of the municipality, where the sediments of the so-called Catania plain predominate. The resolution (pixel size) of the latter map is 40 m, chosen on the basis of the density of available geotechnical borings in some city sections. The PGA values in Figure 3b correspond to the 81-percentile level; an observed value of PGA is shown for comparison in Figure 3b at the only accelerograph recording site in Catania.

Using a geotechnical zonation, as in Figure 3b, evidently introduces small-scale spatial variability in the ground-motion maps. However, in this case the distance attenuation effect predominates and the two maps in Figure 3 can be regarded as roughly equivalent in terms of input to a damage scenario for ordinary buildings, because of the moderate level of the ground motions involved, and also because of the position of the earthquake source with respect to the city.

The difference between the two types of maps, and the advantage of using an instrumental parameter, becomes much more evident if a substantially larger earthquake is considered. In the present example, the obvious candidate as a scenario earthquake is the 1693 event, with an estimated M_s between 7.0 and 7.5. This earthquake claimed over 10,000 victims (out of a total city population of 18,000) in Catania alone (Boschi *et al.*, 1995) and may have ruptured some 70 km of fault length on the Ibleo-Maltese escarpment (Sirovich and Pettenati, 1999). Intensity and PGA maps for this earthquake were constructed using the same attenuation relations as in Figure 3; the results, illustrated in Figure 4, indicate that the two maps can hardly be considered equivalent as an input for scenario damage prediction. The small-scale variability in ground motion introduced by the geotechnical zonation is now such that the local amplification of PGA values could control in certain areas the distribution of heavy damage to some classes of buildings. On the other hand, a hazard map such as that of Figure 4b could only be used as a rough preliminary scenario for emergency operations.

The same comments made on the PGA maps would qualitatively apply to maps of predicted spectral ordinates at periods $T \neq 0$.

3.3 Maps of Arias Intensity

The Arias intensity I_a, being proportional to the integral of the squared acceleration values from a strong-motion record, gives a measure of the energy released at a site by ground shaking. Hence, I_a should be a physically more meaningful parameter than peak acceleration for evaluating the susceptibility to the seismically induced failure of slopes in an area (see, e.g., Harp and Wilson, 1995). Because I_a varies in the far field as the inverse of the source distance squared, one would expect the highest concentration of slope failures to be predicted at close distances from the source. Figure 5 provides an example of the correlation observable in the M 6.9, 1995 Hyogo-ken Nanbu earthquake between I_a values (both predicted and observed) and the occurrence of slides and rockfalls on the slopes of the Rokko Mountains, steeply rising behind the city of Kobe. The predicted I_a values were generated with Eqs. (5) and (6), which account for directivity effects keeping the point source representation. In Figure 5, only the moment release on the Kobe side of the fault rupture (Irikura *et al*., 1996) has been taken into account for the prediction, and the fault geometry proposed by Wald (1996) has been used.

The predictions of I_a in the near field appear reasonable, despite the simplification in the source description and the fact that the effects of surface geology are disregarded. The distribution of real slides is primarily controlled by slope steepness and surface geology, but it is also interesting to note that it clusters in a rather narrow strip aligned with the surface projection of the fault rupture, in agreement with previous studies (Faccioli, 1995).

3.4 Sensitivity Considerations

Sensitivity analyses on the consequences in terms of predicted damage can provide very helpful guidance to the choice of the attenuation relation for a hazard scenario. As a matter of fact, the implications of adopting one attenuation relation in preference to another—giving apparently similar ground-motion predictions—may not be obvious at first sight. We illustrate an example (Pessina, 1999) in which the scenario earthquake is the same considered in Figure 4a and two different attenuation relations were considered for PGA after a preliminary selection. The first ground-motion prediction is precisely the map of Figure 4b, while the second was generated using a relation based on a worldwide set of data recorded in extensional tectonic environments (Spudich *et al*., 1997).

Shown in Figure 6 (top) are the two predicted frequency distributions of PGA across the Catania municipal area, using pixels of 40 × 40 m. Significant differences between the two distributions occur only for PGA > 0.25 g; only a small fraction of area is affected by values exceeding 0.30 g. However, based on fragility curves for masonry buildings in Italy, the limited differences in the PGA distributions are strongly amplified in the

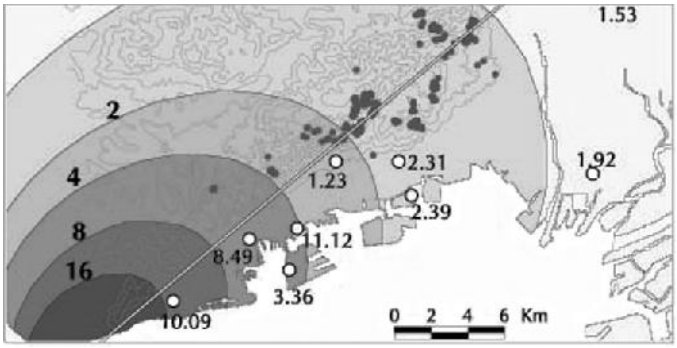

FIGURE 5 Predicted Arias intensities (I_a), shown by different shades of gray (in m/sec), in the Kobe area for the 1995 Hyogo-ken Nanbu earthquake; also shown are observed I_a values at selected strong-motion stations, the sites of landslide and rockfall occurrence (Okimura, 1995), the assumed surface projection of the ruptured fault, and the elevation contours at 100-m intervals.

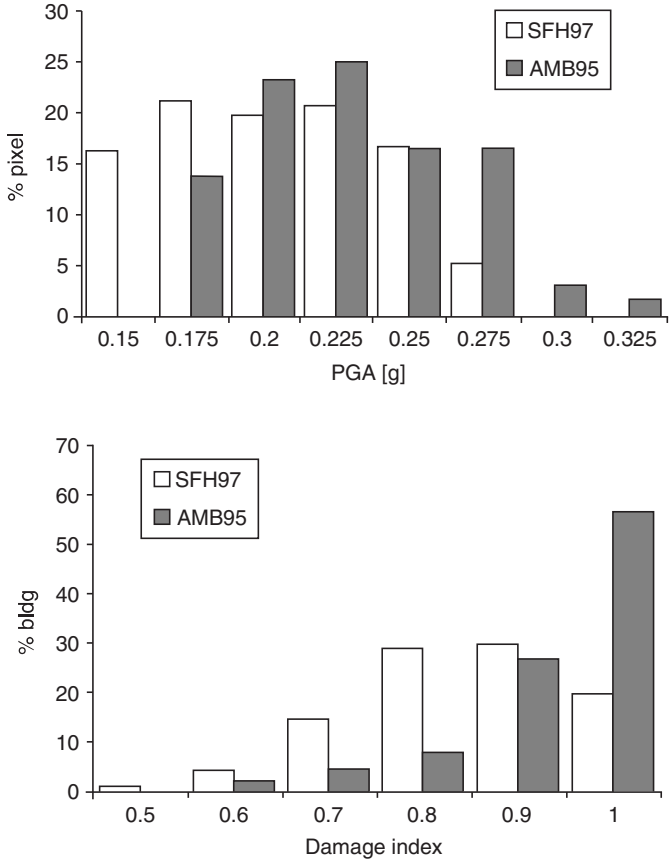

FIGURE 6 Sensitivity of damage predictions for masonry buildings in Catania to the ground motions for the destructive scenario earthquake. *Top*: frequency distributions of PGA in terms of percentage of elementary land cells (pixels) having the same level of ground shaking, predicted with the attenuation relation AMB95 (Ambraseys, 1995) and SFH97 (Spudich *et al.*, 1997). *Bottom*: predicted damage distributions, in percentage of buildings with a given damage index, for the previous two PGA distributions (from Pessina, 1999).

damage predictions. The results, portrayed in Figure 6 (bottom) in the form of mean damage distribution as a function of damage index, show a sharp increase of collapse or high damage incidence when the PGA map of Figure 4b is adopted. This is simply because the latter contains more pixels in the densely built city center where the collapse accelerations assumed for the typical masonry structures in Catania are attained.

4. Source-Related Factors

4.1 Representation of the Source Geometry

If the scenario ground shaking is to be predicted in the near-source range of events with $M > 6.0$, a finite source representation is obviously preferable even if rupture directivity effects may not be important (as is often the case of normal fault earthquakes). However, at larger distances an acceptable ground-motion scenario for $M \sim 7$ events can be estimated with a "circular" attenuation relation, e.g., from the epicenter, provided an appropriate site classification is used to account for average amplification effects. An example is presented in Color Plate 26 for the destructive $M = 6.8$, 1980 Irpinia earthquake in southern Italy.

The PGA map in Color Plate 26 was generated with an attenuation relation widely used in Italy, which separates rock/stiff sites from shallow alluvium sites (Sabetta and Pugliese, 1996; see case II in Table 4 and Fig. 2). A zonation into these two broad soil categories for the region of interest was derived from a digital geological map of Italy (originally at 1:500,000 scale), ignoring the detailed geotechnical characterization available for the accelerograph sites, and the acceleration map was then generated via GIS in raster format. The instrumental epicenter, the surface projection of the rupture area in the form of two adjacent rectangles (slightly simplified from Cocco and Pacor, 1993), and the area enclosed within the intensity IX (MCS) isoseism are also shown in Color Plate 26, together with the accelerograph site locations and the recorded horizontal PGA values. In the bar diagram of Color Plate 26, the observed peak accelerations are compared to the values predicted using both the finite source representation of Color Plate 26 and the distance from the epicenter.

At most accelerograph stations the latter assumption yields slightly better predictions. However, for the earthquake in question none of the acceleration records was obtained near the source, where the differences arising from the different source representation are expected to be large.

A point worth stressing here is that if a finite source is to be introduced for producing ground-motion maps of future earthquakes, its geometry must be assumed *a priori*, and this can prove especially difficult in the case of blind faults. In countries with a long and well-documented historical seismicity record, one can, however, rely on intensity maps of the strongest earthquakes in the region. In the last example, the intensity IX (MCS) isoseism appears to be a reasonable indicator of the size and position of the ruptured area, although some of its features seem well correlated with the presence of sedimentary deposits causing amplification. The determination of the geometry of earthquake sources from macroseismic intensity data is supported by a recent study on Italian earthquakes (Gasperini *et al*., 1999).

4.2 Source Directivity

The 1994 Northridge and 1995 Hyogo-ken Nanbu events have provided, in different ways, strong evidence that the damage distribution occurring in the near-source region of a strong earthquake depends on the energy-focusing effects produced by the directivity of rupture on the rupturing fault. The impact of this evidence has been such that the directivity effects can now be accounted for through appropriate attenuation relations for response spectral ordinates; see Eqs. (1) and (4)–(6). On the other hand, as regards engineering design, the latest versions of building codes have introduced for the highest seismicity zones a classification of earthquake sources (in terms of magnitude and seismic rate) and "near-source factors" that can increase by up to a factor of 2 the ordinates of the design spectrum (ICBO, 1997). For these reasons, we are not dwelling here any further on the influence of directivity on the response spectra.

Unlike the response spectrum, which is rather insensitive to the significant duration of ground motions, the Arias intensity I_a, should be affected to a greater extent by directivity effects because it more closely reflects the influence of duration. A predictive I_a map, which takes directivity into account, generated with Eqs. (5) and (6), has already been shown in Figure 5; this prediction has been compared with that obtained for the same earthquake by an attenuation relation for I_a that disregards directivity (Wilson and Keefer, 1985). The comparison, not shown here, indicates that the residuals at close azimuths from the fault strike are in most cases decreased when Eqs. (5) and (6) are used.

4.3 Empirical vs Synthetic Ground-Motion Predictions

The preferred alternative to the use of empirical relations is obviously represented by numerical simulations based on realistic source representations (including finite dimensions, rupture propagation, etc.), which can be performed by a variety of seismological models and computational methods for wave propagation, and can produce ground-motion synthetics at any site within an area of interest. A recent overview of such methods and their performance has been provided in the context of a recent international prediction experiment (see Irikura *et al*., 1999). Direct modeling is especially useful in parametric studies for the quantification of the uncertainties in the predicted spatial distribution of ground shaking, and of their dependence on the physical parameters of source and propagation path. Because of computational burden and lack of resolution in the crustal

models, these calculations are typically limited to frequencies around 1 Hz, which leaves out a vast range of primary interest for engineering structures. Extension to higher frequencies can be achieved by adding an appropriate random component to the deterministically simulated time histories.

In the aforementioned scenario studies for Catania, in addition to the empirical ground-motion predictions, three different approaches were used to generate acceleration synthetics from the fault geometry and earthquake magnitude assigned to the destructive 1693 earthquake (Fig. 4). The variability of the results yielded by the different approaches at a given point in studies of this nature is an empirical measure of the model-to-model, or epistemic, uncertainty discussed in Section 2. As an illustration, we compare in Figure 7 the acceleration response spectra predicted at a site (S in Fig. 4) located on massive lava flows, at about 15 km source distance. The empirically predicted spectrum, shown in Figure 7 with its standard deviation band, has been generated with attenuation relations based on European data, already mentioned as an example of case II in Table 4 (Ambraseys *et al.*, 1996, labeled ASB96). The curve labeled 2D is the spectrum of a representative synthetic computed at point S by a 2D high-resolution spectral element analysis along a cross section perpendicular to the coastline (Priolo, 1999). This curve roughly matches the mean plus one standard error bound of the empirical prediction up to about 1 sec period. The bump of the 2D synthetic spectrum at longer periods is related to a strong phase reflected at a deep interface; this is a typical example of a feature that would be difficult to predict by empirical relations.

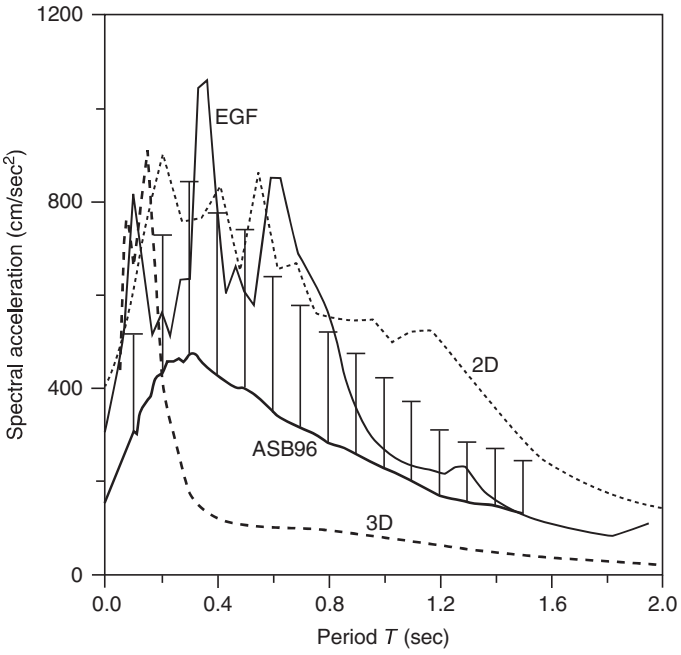

FIGURE 7 Comparison of acceleration response spectra generated at site S of Figure 4, on massive lava flows, by using empirical attenuation relations (ASB96, shown with plus one standard error bars), synthetic from 2D spectral analysis (labeled 2D), synthetic from 3D high-frequency method (labeled 3D), and empirical Green's function summation (labeled EGF).

The curve labeled 3D in Figure 7 is generated by a high-frequency approximation approach for the far-field analytical Green's functions combined with randomly generated models of the rupture process on the fault (Zollo *et al.*, 1997). Because of its computational efficiency, this approach is especially useful for obtaining estimates of the uncertainty in the spatial distribution of ground motions attached to the complexity of the source process, but the lack in intermediate and long period components in the associated spectrum of Figure 7 does not seem compatible with a $M7+$ earthquake at relatively close distance. Because of the high-frequency approximation, the model in question is more suitable for predicting peak ground acceleration than the full response spectra.

An independent assessment of the previous results has been obtained by the empirical Green's function (EGF) method, using a horizontal acceleration component recorded during the previously mentioned 1990 earthquake at a site denoted GRR (PGA $=$ 0.04 g), located on the coast some 50 km north of the epicenter, on thick lava flows from Mt. Etna. GRR is to some extent representative of the ground conditions prevailing in several older sections of Catania, including site S under consideration. However, since S is only about 30 km from the 1990 epicenter, a simple distance geometrical spreading correction was applied to the amplitude of the original record used as EGF.

Taking a record from the 1990 earthquake as EGF for the large 1693 event seems acceptable in view of the probable location of the 1990 epicenter on the Ibleo-Maltese fault. A random summation scheme has been adopted to synthesize the ground motion for the large event, of which one only needs to specify the stress drop (Ordaz *et al.*, 1995). The extended target source area is approximated by a point source, whose rupture duration, however, is in accordance with its dimension. This method was selected in view of the uncertainty on the exact position and dimensions of the 1693 source and of the good results reported for the Mexican earthquakes by Ordaz *et al.* (1995). Also, strong directivity effects are not expected in Catania given its position with respect to the most probable seismogenic fault (Fig. 4). By taking a target seismic moment corresponding to M 7.0, and a stress drop of 100 bar for both the small and the large events, 22 different synthetic acceleration histories were generated, from which an average PGA of 0.28 g is obtained at the Catania site S, with a standard deviation of 0.07 g, in rather good agreement with the value shown on the map of Figure 4. One simulated time history with peak value equal to the sample average was then used to compute the EGF spectrum in Figure 7. Similar comparisons performed at soil sites confirm the indication of Figure 7, i.e., that in first approximation, in the absence of strong directivity effects, the standard error band associated with the empirical prediction is also a realistic measure of the spread of the synthetics generated by different methods, i.e., of the model-to-model uncertainty.

Layer	Material	V_S (m/sec)
1a	Alluvium	150
1b		250
1c		320
2	Marl	500
3	Limestone	1000–1500

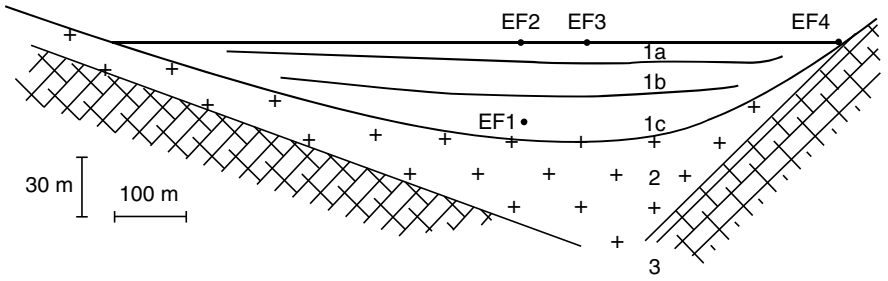

FIGURE 8 SW–NE cross section of alluvium valley at IONIANET test site in Kefalonia Island (Greece); EF1, EF2, EF3, and EF4 are the locations of digital accelerographs, while V_S denotes shear-wave velocity. Right-hand part of figure modified after Psarropoulos and Gazetas (1998).

5. Alternative Tools for the Treatment of Complex Site Effects

The inadequacy of zoning at a purely geotechnical level in the presence of markedly 2D or 3D near-surface configurations, e.g., alluvial valleys or sedimentary basins, has already been mentioned. The quantification of seismic site effects on such configurations can be a challenging task in a scenario investigation, especially if time-consuming numerical simulations are to be avoided for lack of sufficient geological and geophysical data. Of particular concern is the occurrence of 2D/3D resonant response of sediment valleys, which—although thoroughly understood from a theoretical standpoint (see Bard and Bouchon, 1985) and documented by remarkable data for weak-motion earthquakes (e.g., Paolucci *et al.*, 2000)—remains still scarcely supported by strong-motion observations. On the other hand, the main reason for the concern is the possible occurrence of soil response spectral amplification well in excess of the empirical values illustrated in Figure 2 as well as of those provided by 1D response analyses. We illustrate by means of two real case histories the applicability of alternative tools for quantifying 2D site effects: simplified analytical approaches and seismic noise spectra.

5.1 Use of Simplified Analytical Models: The IONIANET Test Site

The first case history stems from strong-motion observations obtained by the IONIANET digital accelerograph network, located on a small sediment valley in Kefalonia Island, in the most seismically active region of Greece. A cross section of the valley with the accelerograph location is shown in Figure 8. The valley, about 0.8 km wide at the test site and 6 km long, is filled with soft-to-medium dense Quaternary sediments (interbedded sand and clay layers) and surrounded by hills of limestone and marl. Geotechnical investigations were limited to two boreholes, one drilled near the rock outcrops at the edges and one in the middle of the valley, which disclosed about 46 m of soil overlying marl.

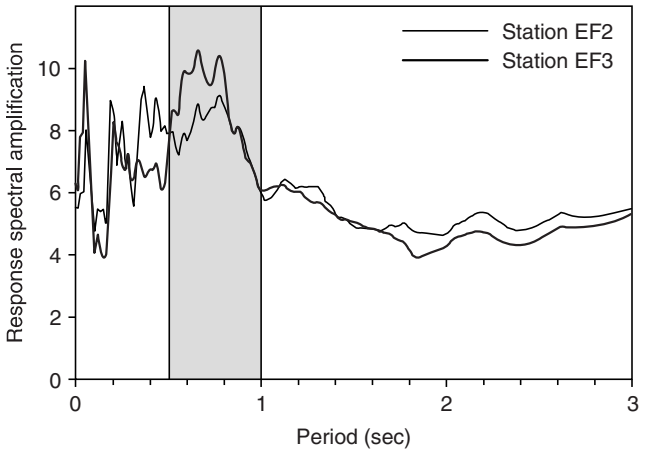

FIGURE 9 Response spectra ratios EF2/EF4 and EF3/EF4 for horizontal motion in the direction normal to the plane of Figure 5, averaged over three earthquakes. Shaded band indicates range of vibration periods where 2D resonance has probably occurred.

The shear-wave velocity values in Figure 8 were estimated from N_{SPT} measurements using empirical correlations.

In 1997 and 1998 IONIANET recorded four moderate earthquakes; three of them, with $4.2 < M < 5.2$, occurred during the same seismic sequence, at 20- to 45-km epicentral distance from the network, with focal depth of 5–7 km. The largest peak accelerations at EF4, on rock, were about 0.05 g, while on soil (at EF2) they reached about 0.22 g during the same event.

Previous analyses of IONIANET data had shown that 2D wave propagation and layering of the valley sediments must be accounted for to explain the amplitudes and duration of the accelerations recorded at EF3 and EF4 (Psarropoulos and Gazetas, 1998). We measure site amplification by the ratio between the response spectra of the soil recordings at EF2 and EF3 and those on rock at EF4, averaged over the three earthquakes. Figure 9 displays the ratios for the horizontal motion parallel to the valley axis. The six- to tenfold spectral amplification occurring up to 1 sec period should be noted in the first place. Particularly at EF3, a broad peak may be noted for vibration periods between about

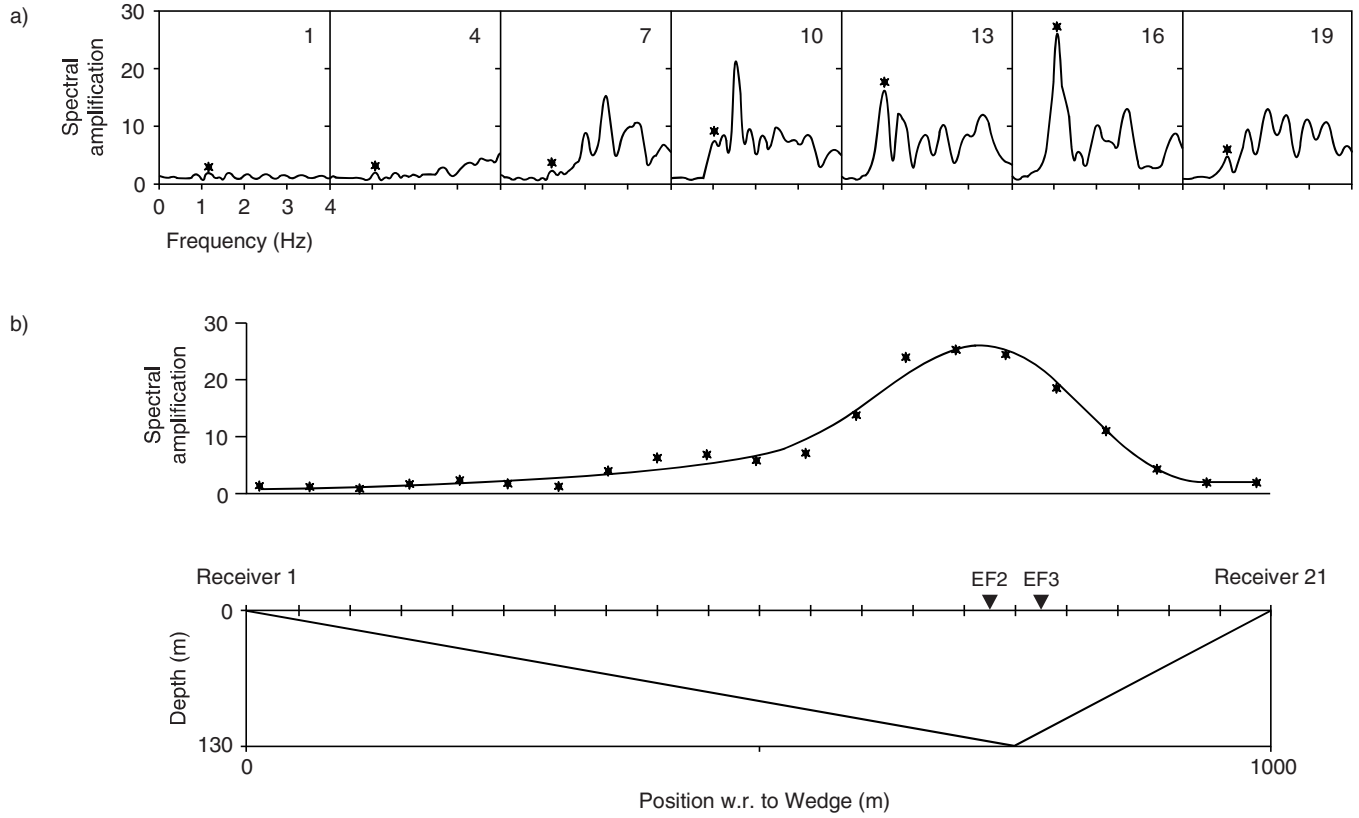

FIGURE 10 (Top) IONIANET site: amplification functions at selected surface receivers for antiplane (*SH*) motion calculated with the simple model of triangular homogeneous valley, shown at bottom. Receivers are numbered 1 to 21, from left to right, and equally spaced. Solid star in amplification plots indicates 2D resonance peak at 1.1 Hz. Receiver 16, exhibiting the highest peak, is between stations EF2 and EF3. Graph in the middle depicts variation of resonant peak amplitude across the valley.

0.5 and 1.0 sec (shaded band in Fig. 9). The observed amplification is substantially higher than the average empirical estimates shown in Figure 2.

To investigate 2D resonance effects as a possible cause of the high amplification observed, a very simple two-dimensional model of the valley was analyzed, consisting of homogeneous soil (with $V_S = 400$ m/sec) and having a triangular shape, shown in Figure 10. The simplicity stems from the fact that for specific values of the edge angles, a nearly exact solution of the problem can be quickly obtained for a vertically propagating plane *SH* wave (Paolucci *et al.*, 1992). The analytical amplification functions calculated with this method at different points across the valley, reproduced in Figure 10, clearly display a resonance peak common to all locations, which becomes very prominent in the zone where the valley sediments are deepest. The resonance peaks are indicated by a star in the figure. The common frequency of this peak is 1.1 Hz, while its amplitude variation across the valley is depicted in the middle graph in Figure 10. Based on well-known studies on the seismic response of valleys (Bard and Bouchon, 1985), the analytical results in Figure 10 are consistent with the fundamental resonant mode for *SH* waves at the frequency of 1.1 Hz (period 0.9 sec). Making due allowance for the approximations in the valley geometry and material properties of the simplified model, we conclude that the amplification peak in the shaded band of Figure 9 is caused by the fact that the three recorded earthquakes have also excited the 2D resonant response of the valley in its fundamental *SH* mode. As a rule of thumb, this example indicates that the 2D amplification effects would require, for the most critical sites, an extra multiplicative factor of 2 to 3 with respect to the predictions of attenuation relations (similar to those of current seismic codes such as UBC97).

In reality, due to the moderate earthquake magnitudes involved, the strongest ground response at the IONIANET site occurred between about 0.1 and 0.3 sec period, and little energy was present in the 0.6–0.9 interval where 2D resonance effects are identified. However, the 2D resonant motion could be strongly excited by higher-magnitude (say $M > 6$) future events, such as have repeatedly occurred in the past in the Ionian Islands. Obviously, nonlinearity of soil response should be considered in this case.

In conclusion, the IONIANET data interpretation indicates that relatively simple analytical or numerical models allowing

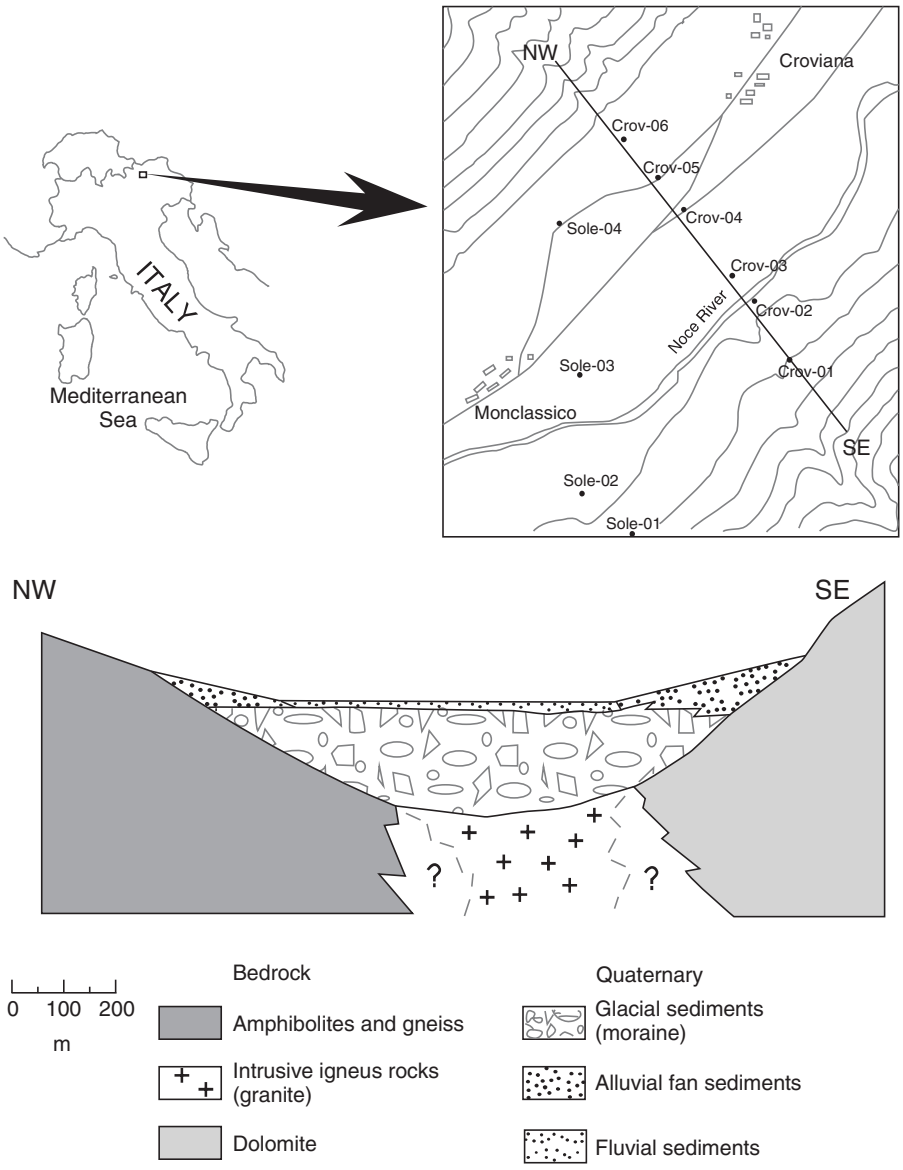

FIGURE 11 Location of the Val di Sole site and indicative vertical cross section of the valley along the NW–SE trace shown on the upper right map.

performance of quick parametric studies are essential for understanding complex site effects and determining their magnitude.

5.2 Use of Seismic Noise Spectral Ratios: The Val di Sole Site

A powerful alternative approach to the identification of resonant response on sedimentary valleys and basins relies on measurements of seismic noise and associated use of single-station, H/V spectral ratios (Nakamura, 1989; Field *et al*., 1995). In fact, several studies show that this method can provide reliable estimates of dominant frequencies of motion, although it tends to underestimate the amplitude of the response when compared with the technique of the classical spectral ratios, it being generally accepted that the H/V ratios give a lower bound of the soil response amplitude for this frequency (see, e.g., Lachet and Bard, 1994).

Thus, to assess the capability of the H/V ratio technique in identifying the basic features of 2D response in a real valley, a second case history follows. The case study refers to a valley (Val di Sole) located in the Italian Alps (Fig. 11). The valley is filled by three types of Quaternary sediments. The oldest are glacial sediments (moraine), while alluvial fans are present on the hillsides of the valley, and the surface materials consist of fine detritic sediments accumulated by the river Noce. A sketch of the structure of the valley, based on observations made close to the study zone, is given in Figure 11. The sediment thickness

is estimated at more than 200 m at the valley center. The alluvial fans have a thickness probably exceeding 50 m at some points, while the river sediments are thinner, probably less than 20 m. The shape ratio (thickness/half-width) of the valley is approximately 0.3.

Ambient noise was measured at 10 sites on the valley (Fig. 11), using a three-component seismometer of 1 sec period. After performing the FFT of the digitized noise recordings, the resulting spectra were smoothed with a sliding window and the spectral H/V ratio for each window and horizontal component was calculated. Finally, the average spectral ratio on both horizontal components was obtained. The resulting H/V spectral ratios are presented in Figure 12.

Apart from site Sole-01, which is located over very thin soil close to the sediment-rock (dolomites) contact, most of the remaining sites show an amplification peak between 1.16 and 1.77 Hz. This peak is maximum at the center of the valley (Crov-04 and Sole-03) and decreases toward the edges, where higher dominant frequencies exist with peaks of lesser amplitude (Crov-06 and Sole-04). These observations are in agreement with findings by Tucker and King (1984) and by Bard and Bouchon (1985) about the characteristics of the 2D response of valleys. Since no *in situ* data are available on the material properties of the sediments, they were estimated from correlations applicable in the same geological context (e.g., Frischknecht *et al*., 1998); Table 6 summarizes the properties used in the models. A 1D dynamic response analysis at valley sites was performed first, based on the cross section of Figure 11. The results (not shown here) indicated that a 1D model does not fit the observations: computed resonance frequencies decrease from the edge toward the center of the valley, where they are lower than the observed one. Additionally, computed peak amplifications decrease from the edges toward the center of the valley, while the observed ones vary in just the opposite sense.

These preliminary analyses indicate that the dynamic ground response in the valley is more complex than in a simple 1D case, and it is possibly related to a 2D resonance condition. Due to the lack of data on the structure of the valley, the occurrence

TABLE 6 Mechanical Properties of the Val di Sole Materials (estimated)

Material	(kg/m^3)	V_P (m/sec)	V_S (m/sec)	Q
Fluvial	2000	1400	200	50
Alluvial fan	2100	1500	250	50
Moraine	2100	2000	700	100
Bedrock	2500	4000	2500	200

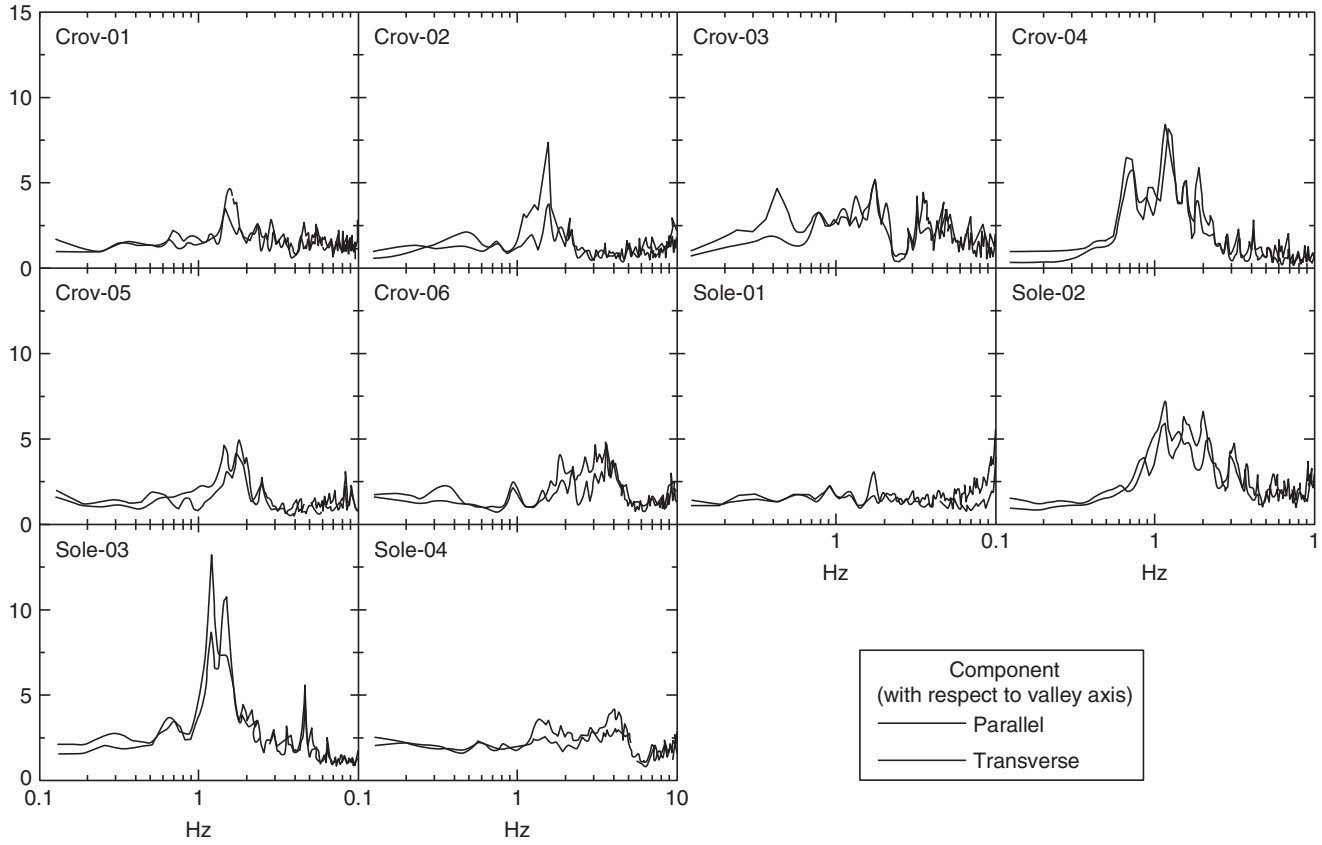

FIGURE 12 H/V spectral ratios of ambient noise measurements taken at the site shown in Figure 11.

of a 2D resonance was investigated first with a simplified method that allows estimation of the fundamental 2D resonance frequency, but not its amplification, through Rayleigh's approximation (Paolucci, 1999). A 2D valley model 1100 m wide was used, consisting of two layers (20 and 190 m thick) embedded in a half-space, with shear velocities equal to those for fluvial, moraine, and bedrock materials, respectively. The resulting 2D resonant frequencies vary between 0.95 and 1.10 Hz, depending on the shape of the model (elliptical, sinusoidal) and type of wave (*SH* or *SV*) used in the analysis. Such values are only slightly lower than those observed in the H/V ratios of noise at the center of the valley (1.16 Hz).

Based on this evidence, a full time-domain 2D analysis was performed next with the hybrid computer code AHNSE (Casadei and Gabellini, 1997), and transfer functions for the surface receivers were obtained. The code can combine spectral elements (Faccioli *et al.*, 1997) and—in the more irregular near-surface domains—finite elements; in 2D, it performs a *P–SV* propagation analysis. High-velocity materials (bedrock and moraine) were modeled with spectral elements while the low-velocity sediments were discretized by finite elements. The grid size was designed to propagate a maximum frequency of 9 Hz. As input motion, a plane Ricker wavelet with 3-Hz peak frequency was used.

To investigate the effect of the shape of the valley, the sediments were considered homogeneous, with properties identical to the moraine. In the frequency domain, Figure 13 compares the numerically computed amplification functions at different positions in the valley with the observed H/V ratios. For this comparison, sites Sole-01 to Sole-04 were projected onto the profile used in the simulation, shown in Figure 11.

The calculated fundamental frequency of resonance of the valley at 1.12 Hz is very evident in Figure 13. At this frequency, the maximum amplification occurs at the center of the valley and is about 2.5 times greater than the sediment/rock seismic impedance ratio (1D amplification); this level decreases toward the edges of the model. Additional evidence of 2D response is the good agreement between H/V ratios and numerical amplification functions at stations Sole-03 and Crov-04 near the valley center, as well as at Sole-02. This rather interesting result suggests that the H/V ratios, in addition to being a reliable tool for determining dominant frequencies of motion, could also be used for amplification estimates, at least for moderate excitation levels.

We may conclude from this second case history that inexpensive methods based on noise measurements are among the tools that can reliably be used to assess the effects of some basic features of ground response on complex geologic configurations.

As an appropriate complement to the previous case histories, in a recent study aimed at estimating a simplified "basin amplification factor" for alluvial valleys, Chávez-García and Faccioli (2000) show that, unlike the 1D site effects considered in current engineering practice, the additional amplification caused by 2D effects may not be safely evaluated using the soil properties in the near-surface layers, such as V_{S30}. As a minimum, some information is necessary also on the bedrock properties, to estimate the velocity contrast with respect to the underlying soft sediments. According to Chávez-García and Faccioli, this contrast is the most significant parameter controlling the severity of 2D effects.

To make complex site effects amenable to relatively simple empirical predictions for scenario studies, the most practical

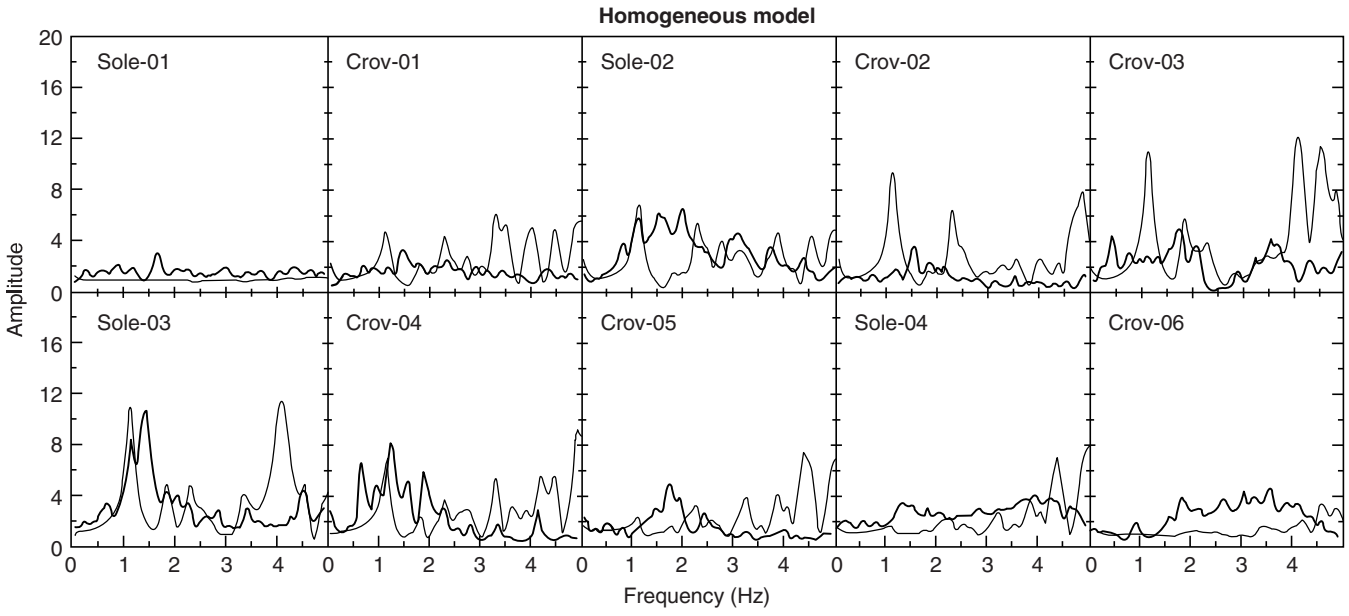

FIGURE 13 Comparison between H/V ratios of ambient noise (thick line) and computed 2D transfer functions (thin line). For this comparison, sites Sole-01 to Sole-04 were projected to profile used in the simulation. *P–SV* components transverse to valley axis are used for H/V ratios.

way is probably to perform regression analyses (incorporating a few simple geometrical and mechanical parameters) on the data already recorded by the dense accelerograph arrays installed on 2D/3D geological configurations around the world. While the use of average basin amplification factors derived from statistical analyses of many numerical simulations and observations could only be used as a rough first approximation in a scenario study where the source–receivers geometry is assigned, some of the general indications contained in the study by Chávez-García and Faccioli may provide useful guidelines, such as the following:

1. 2D effects in alluvial valleys are significant only at periods smaller than the 1D resonance period evaluated at the point where the valley sediments are deepest.
2. For realistic values of the sediment/bedrock velocity ratio (2.5 to 3.5), the basin amplification factor, i.e., the additional amplification factor by which one should multiply the 1D factor, is between 1.5 and 2.5.

6. Closing Remarks

After reviewing, as a basic preliminary step, the issue of a deterministic vs a probabilistic definition of a scenario earthquake, we have summarized the features of the main tool used in the engineering approach to the creation of a ground shaking scenario, namely attenuation relations for ground-motion parameters. Although such relations are discussed also in other chapters of this handbook, we have deemed it indispensable to recall here, from the user's standpoint, some quantitative aspects of the predictions obtained thereby, including the measures of statistical uncertainty.

We have subsequently discussed the selection of hazard descriptors for earthquake scenarios and highlighted some features of typical ground-motion maps generated through GIS technology, using for illustration a few examples from recent studies, notably those for the southern Italian city of Catania. Sensitivity analyses in terms of predicted damage are certainly apt to provide significant guidance on the choice of the tools for predicting ground motion. Also, sophisticated geotechnical zonation maps can be conveniently incorporated to produce ground shaking maps for an area, although they cannot bring into the picture the influence of sedimentary basins and of other nonsurficial geologic structures that are likely to generate complex site amplification effects.

One critical question in scenario studies concerns the extent to which physical factors that are likely to have a strong influence on the spatial distribution of ground motion can be realistically accounted for by the simple approach based on attenuation laws. For the source-related aspects of the problem (such as source finiteness and rupture directivity), the prediction tools made available after the Northridge and Kobe earthquakes can be considered adequate. However, the answer is mostly conditioned by the *a priori* knowledge of the geometry and orientation of the seismogenic structures, highly uncertain in many populated and highly seismic zones of the world. The rational exploitation of historical intensity data in regions with a sufficiently long historical record may be the best way to tackle this problem.

The situation is quite different for soil amplification arising on sediment-filled valleys and basins. Alternative methods for identifying complex site effects and determining their magnitude have been extensively illustrated in a specific section with the support of two real case histories. The quantitative results indicate that, although amplification factors in specific frequency bands can be well beyond the reach of current empirical predictions, some clue is already available on the values of the "basin amplification factors" coming into play in complex geological configurations of this type.

Regarding the relative performance of empirical predictions, and of advanced numerical methods for generating synthetic time histories at any desired location, the available results suggest that the former are probably adequate for most scenario studies using response spectra, in the sense that the model-to-model variability is basically within the standard error band of the empirical predictions.

Acknowledgments

We are grateful to L. Veronese and O. Groaz (Geological survey of the Trento Province administration) who collected the Val di Sole field data, and to J. Delgado (University of Alicante, Spain) who processed the data and performed the associated 2D numerical analyses. The Geological Survey (Servizio Geologico) of Italy provided the 1:500,000 digital geological map of Italy.

References

Abrahamson, N. A., and K. M. Shedlock (1997). Overview. *Seism. Res. Lett.* **68**, 9–23.

Abrahamson, N. A., and W. J. Silva (1997). Empirical response spectral attenuation relations for shallow crustal earthquakes. *Seism. Res. Lett.* **68**, 94–109.

Ambraseys, N. N. (1995). The prediction of earthquake peak ground acceleration in Europe. *Int. J. Earthquake Eng. Struct. Dyn.* **24**, 467–490.

Ambraseys, N. N., K. A. Simpson, and J. J. Bommer (1996). Prediction of horizontal response spectra in Europe. *Int. J. Earthquake Eng. Struct. Dyn.* **25**, 371–400.

Anderson, J. G. (1997). Non parametric description of peak acceleration above a subduction thrust. *Seism. Res. Lett.* **68**, 86–93.

Atkinson, G. M., and D. M. Boore (1997). Some comparison between recent ground-motion relations. *Seism. Res. Lett.* **68**, 24–40.

Bard, P. Y., and M. Bouchon (1985). The two-dimensional resonance of sediment-filled valleys. *Bull. Seism. Soc. Am.* **75**, 519–541.

Bommer, J. J., A. S. Elnashai, G. O. Chlimintzas, and D. Lee (1998). Review and development of response spectra for displacement-based seismic design. *ESEE Research Report N. 98-3*, Civ. Engng. Dept., Imperial College, London.

Boore, D. M., W. B. Joyner, and T. E. Fumal (1993). Estimation of response spectra and peak acceleration for Western North America earthquakes: an internal report. *Open-File Report 93-509*, US Geological Survey, Menlo Park, California.

Boore, D. M., W. B. Joyner, and T. E. Fumal (1997). Equations for estimating horizontal response spectra and peak acceleration for Western North America earthquakes: a summary of recent work. *Seism. Res. Lett.* **68**, 128–153.

Borcherdt, R., L. Lawson, V. Pessina, J. Bouabid, and H. Shah (1995). Applications of Geographic Information System Technology to Seismic Zonation and Earthquake Loss Estimation, State-of-art Paper. *Proc. Fifth Int. Conf. on Seismic Zonation*, Nice, France, III, 1933–1973.

Boschi, E., G. Ferrai, P. Gasperini, E. Guidoboni, G. Smriglio, and G. Valensise (1995). "Catalogo dei forti terremoti in Italia dal 461 a.C. al 1980." ING-SGA, Bologna (Italy), 973 pp. and a CD-ROM.

Calvi, G. M. (1999). A displacement-based approach for vulnerability evaluation of classes of buildings. *J. Earthquake Eng.* **3**, 411–438.

Campbell, K. W. (1997). Empirical near-source attenuation relationships for horizontal and vertical components of peak ground acceleration, peak ground velocity, and pseudo-absolute acceleration response spectra. *Seism. Res. Lett.* **68**, 154–179.

Casadei, F., and E. Gabellini (1997). Implementation of a 3D coupled spectral element/finite element solver for wave propagation and soil structure interaction simulations. *European Commission JRC Institute for Systems, Informatics and Safety Rep. EUR 17730 EN*, Ispra, Italy.

Chávez-García, F., and E. Faccioli (2000). Complex site effects and building codes: making the leap. *J. Seismology* **4**, 23–40.

Cocco, M., and F. Pacor (1993). Space-time evolution of the rupture process from the inversion of strong motion waveforms. *Ann. Geophys.* **36**, 109–130.

Cornell, C. A. (1968). Engineering seismic risk analysis. *Bull. Seism. Soc. Am.* **58**, 1583–1601.

Faccioli, E. (1983). Measures of strong ground motion derived from a stochastic source model. *Soil Dyn. Earthquake Eng*. **2**, 135–149.

Faccioli, E. (1995). Induced hazards: earthquake triggered landslides. State-of-art Paper. *Proc. Fifth Int. Conf. on Seismic Zonation*, Nice, France, III, 1908–1931.

Faccioli, E., F. Maggio, R. Paolucci, and A. Quarteroni (1997). 2D and 3D elastic wave propagation by a pseudo-spectral domain decomposition method. *J. Seismology* **1**, 237–251.

Faccioli, E., V. Pessina, G. M. Calvi, and B. Borzi (1999). A study on damage scenarios for residential buildings in Catania city. *J. Seismology* **3**, 327–343.

Field, E. H., A. C. Clement, V. Aharonian, P. A. Friberg, L. Carroll, T. O. Babaian, S. S. Karapetian, S. M. Hovanessian, and H. A. Abramian (1995). Earthquake site response study in Giumri (formerly Leninakan), Armenia, using ambient noise observations. *Bull. Seism. Soc. Am.* **85**, 349–353.

Frankel, A., and E. Safak (1998). Recent trends and future prospects in seismic hazard analysis. *Proc. Specialty Conf. on Geotechnical Earthq. Engng. and Soil Dynamics*, *ASCE Spec. Technical Publ. No. 75* **I**, 91–115.

Frischknecht, C., M. Gonzenbach, Ph. Rosset, and J. J.Wagner (1998). Estimation of site effects in an alpine valley. A comparison between ground ambient noise response and 2D modeling. *Proc. XI European Conf. on Earthquake Engineering*. Paris, September.

Gasperini, P., F. Bernardini, G. Valensise, and E. Boschi (1999). Defining seismic sources from historical earthquakes felt reports. *Bull. Seism. Soc. Am.* **89**, 94–110.

Harp, E. L., and R. C. Wilson (1995). Shaking intensity thresholds for rock falls and slides: examples from 1987 Whittier Narrows and Superstition Hills earthquake strong-motion records. *Bull. Seism. Soc. Am.* **85**, 1739–1757.

International Conference of Building Officials (ICBO) (1997). Uniform Building Code, Vol. 2, Structural Engineering Design Provisions, Chap. 16, Div. IV. Whittier, California.

Irikura, K., T. Iwata, H. Sekiguchi, and A. Pitarka (1996). Lesson from the 1995 Hyogo-ken Nanbu earthquake: why were such destructive motions generated to buildings? *J. Natural Disaster Sci.* **17**, 99–127.

Irikura, K., K. Kudo, H. Okada, and T. Sasatani, Editors (1999). Simultaneous simulation for Kobe. In: "The Effect of Surface Geology on Seimic Motion," *Proc. 2nd Int. Symp. on the Effects of Surface Geology on Seismic Motion*, Yokohama, December 1998, **3**, 1283–1514.

Iwan, W. (1994). Near-field considerations in specification of seismic design motions for structures. *Proc. 10th European Conf. on Earthq. Engin*., August 28–September 2, Vienna, Austria, **1**, 257–267.

Lachet, C., and P. Y. Bard (1994). Numerical and theoretical investigations on the possibilities and limitations of Nakamura's technique. *J. Phys. Earth* **42**, 377–397.

McGuire, R. (1995). Scenario earthquakes for loss studies based on risk analysis. *Proc. 5th Int. Conf. on Seismic Zonation,* October 17–19, 1995, Nice, France, II, 1325–1333.

Nakamura, Y. (1989). A method for dynamic characteristics estimation of subsurface using microtremor on ground surface. *QR Railway Tech. Res. Inst.* **30**, 25–33.

Okimura, T. (1995). Damage to mountain slopes and embankments in residential areas. Preliminary Report on the Great Hanshin earthquake, Japan. Soc. of Civil Eng., 340–346.

Ordaz, M., J. Arboleda, and S. K. Singh (1995). A scheme of random summation of an empirical Green's function to estimate ground motions from future large earthquakes. *Bull. Seism. Soc. Am.* **85**, 1635–1647.

Paolucci, R., M. M. Suárez, and F. J. Sánchez Sesma (1992). Fast computation of SH seismic response for a class of alluvial valleys. *Bull. Seism. Soc. Am.* **82**, 2075–2086.

Paolucci, R. (1999). Shear resonance frequencies of alluvial valleys by Rayleigh's method. *Earthquake Spectra* **3**, 503–521.

Paolucci, R., E. Faccioli, F. Chiesa, and R. Cotignola (2000). Searching for 2D/3D site response patterns in weak and strong motion array data from different regions. Proc. 6th Int. Conf. on Seismic Zonation, Palm Springs, November 12–15, 2000, CD-Rom edited by EERI, Oakland, California, 6 pp.

PELEM (Panel on Earthquake Loss Estimation Methodology) (1989). Estimating losses from future earthquakes. *Panel Report*, National Academy Press, Washington, D.C.

Perkins, J., and J. Boatwright (1995). On shaky ground. *Association of Bay Area Governments Publication No*. P95001EQK, Oakland, California.

Pessina, V. (1999). Empirical prediction of the ground shaking scenario for the Catania area. *J. Seismology* **3**, 265–277.

Priolo, E. (1999). 2-D spectral element simulation of destructive ground shaking in Catania. *J. Seismology* **3**, 289–309.

Psarropoulos, P., and G. Gazetas (1998). Surface and borehole accelerograms versus spectral element simulation of alluvial basin in Cefalonia. *Proc. 2nd Int. Conf. on Earthquake Geotechnical Engineering,* Lisbon, 157–162.

Sabetta, F., and A. Pugliese (1996). Estimation of response spectra and simulation of nonstationary earthquake ground motions. *Bull. Seism. Soc. Am.* **86**, 337–352.

Sirovich, L., and F. Pettenati (1999). Seismotectonic outline of Eastern Sicily; an evaluation of the available options for the earthquake fault rupture scenario. *J. Seismology* **3**, 213–233.

Somerville, P. G., N. F. Smith, R. W. Graves, and N. A. Abrahamson (1997). Modification of empirical strong ground motion attenuation relations to include the amplitude and duration effects of directivity. *Seism. Res. Lett.* **68**, 199–222.

Spudich, P., J. Fletcher, M. Hellweg, J. Boatwright, C. Sullivan, W. Joyner, T. Hanks, D. Boore, A. McGarr, L. Baker, and A. Lindh (1997). SEA96—A new predictive relation for earthquake ground motion in extensional tectonic regimes. *Seism. Res. Lett.* **68**, 190–198.

Spudich, P., W. B. Joyner, A. G. Lindh, D. M. Boore, B. M. Margaris, and J. B. Fletcher (1999). SEA99—A revised ground motion prediction relation for use in extensional tectonic regimes. *Bull. Seism. Soc. Am.* **89**, 1156–1170.

Tucker, B. E., and J. L. King (1984) Dependence of sediment-filled valley response on the input amplitude and valley properties. *Bull. Seism. Soc. Am.* **74**, 153–165.

Wald, D. (1996). Slip history of the 1995 Kobe, Japan, earthquake, determined from strong motion, teleseismic, and geodetic data. *J. Phys. Earth* **44**, 489–503.

Whitman, R. V., T. Anagnos, C. A. Kircher, H. J. Lagorio, R. S. Lawson, and P. Schneider (1997). Development of a national earthquake loss estimation methodology. *Earthquake Spectra* **13**, 643–661.

Wilson, R., and D. Keefer (1985). Predicting areal limits of earthquake induced landsliding. In: "Evaluating earthquake hazards in the Los Angeles region" (J. Ziony, Ed.), *U.S. Geological Survey Professional Paper 1360*, 317–493.

Youngs, R. R., S. J. Chiou, W. J. Silva, and J. R. Humphrey (1997). Strong ground motion attenuation relationships for subduction zone earthquakes. *Seism. Res. Lett.* **68**, 58–73.

Zollo, A., A. Bobbio, A. Emolo, A. Herrero, and G. De Natale (1997). Modelling of ground acceleration in the near source range: the case of 1976, Friuli earthquake. *J. Seismology* **1**, 305–319.

Editor's Note

Please see Chapter 57 by Anderson for a general discussion of strong-motion seismology.

63

Kyoshin Net (K-NET), Japan

Shigeo Kinoshita
Yokohama City University, Yokohama, Japan

1. Introduction

After the Kobe (Hyogoken-nanbu) earthquake in 1995, the Japanese government decided to increase the number of strong-motion observation stations, to upgrade the observation network, and to release future strong-motion records as soon as possible. The National Research Institute for Earth Science and Disaster Prevention (NIED) of the Science and Technology Agency was given the responsibility to implement the program.

Kyoshin Net (K-NET) is one product resulting from this one-year program. The word *Kyoshin* stands for "Strong" (*Kyo*) "quake" (*shin*). The K-NET is a system that transmits strong-motion data on the Internet, data that are obtained from 1000 observatories deployed all over Japan. The K-NET was constructed on the basis of three policies. The first is to carry out systematic observation. All of the K-NET stations use the same seismograph, K-NET95, and they are all installed at free-field sites. The second is to create a network of uniform spacing. The K-NET consists of observatories having an almost equal station-to-station distance. The third policy is the release of all strong-motion records on the Internet. These easily available data files include the soil structures of all sites, obtained by downhole measurement.

We started to release the K-NET information, including strong-motion data, on June 3, 1996, through our graphical user interface on the World Wide Web. The text home page version of the K-NET Internet site has been available for quicker distribution of K-NET data since April 1, 1997. The Internet capacity in Japan is so poor that users found it impossible to connect to the K-NET Internet site immediately after the occurrence of moderate earthquakes. To resolve this problem, we constructed two new mirror sites and started to release K-NET information through the two new sites beginning on April 1, 1997.

In this article, we report on the hardware and software configurations and the development of the K-NET. The many uses to which K-NET data has been put during the last 6 years indicate that the K-NET information, without any access restrictions, is important not only before and long after a shock, but also immediately after a shock, and that the data provide an effective contribution to earthquake disaster countermeasures.

2. K-NET Instrumentation

2.1 Observation Network

The K-NET consists of 1000 strong-motion observation stations, a control center, and two mirror sites of the control center. Figure 1 shows the distribution of K-NET stations. The average station-to-station distance is about 25 km. This spacing of observation sites is designed to sample the epicentral region of an earthquake with a magnitude of 7 or larger occurring anywhere in Japan.

Each station is installed on a site 3 meters square. It commonly consists of a housing that is made of fiber-reinforced plastic (FRP), a concrete base on which a strong-motion seismograph is installed, facilities for electric power, a telephone line with lightning arresters, and a fence. The housing is designed to withstand snow of a depth of 4 m. Figure 2 shows the layout of a typical observatory. The effects of the concrete base and installation on the recorded motion appear in frequencies exceeding 10 Hz (Ikeura *et al.*, 1999). At sites where the temperature falls to below -20°C, the base is constructed about 80 cm below the ground's surface, as shown in Figure 2. Thus, the K-NET effectively offers a uniform, free-field, strong-motion data set throughout Japan.

The headquarters of the K-NET is the control center in Tsukuba city. The control center fully monitors the seismographs, acquires strong-motion data from the K-NET95 seismograph by telemetry, prepares the database for the strong-motion data files and earthquake catalogs, and releases the strong-motion files on the Internet. The procedure of the retrieval and

INTERNATIONAL HANDBOOK OF EARTHQUAKE AND ENGINEERING SEISMOLOGY, VOLUME 81B *ISBN: 0-12-440658-0*

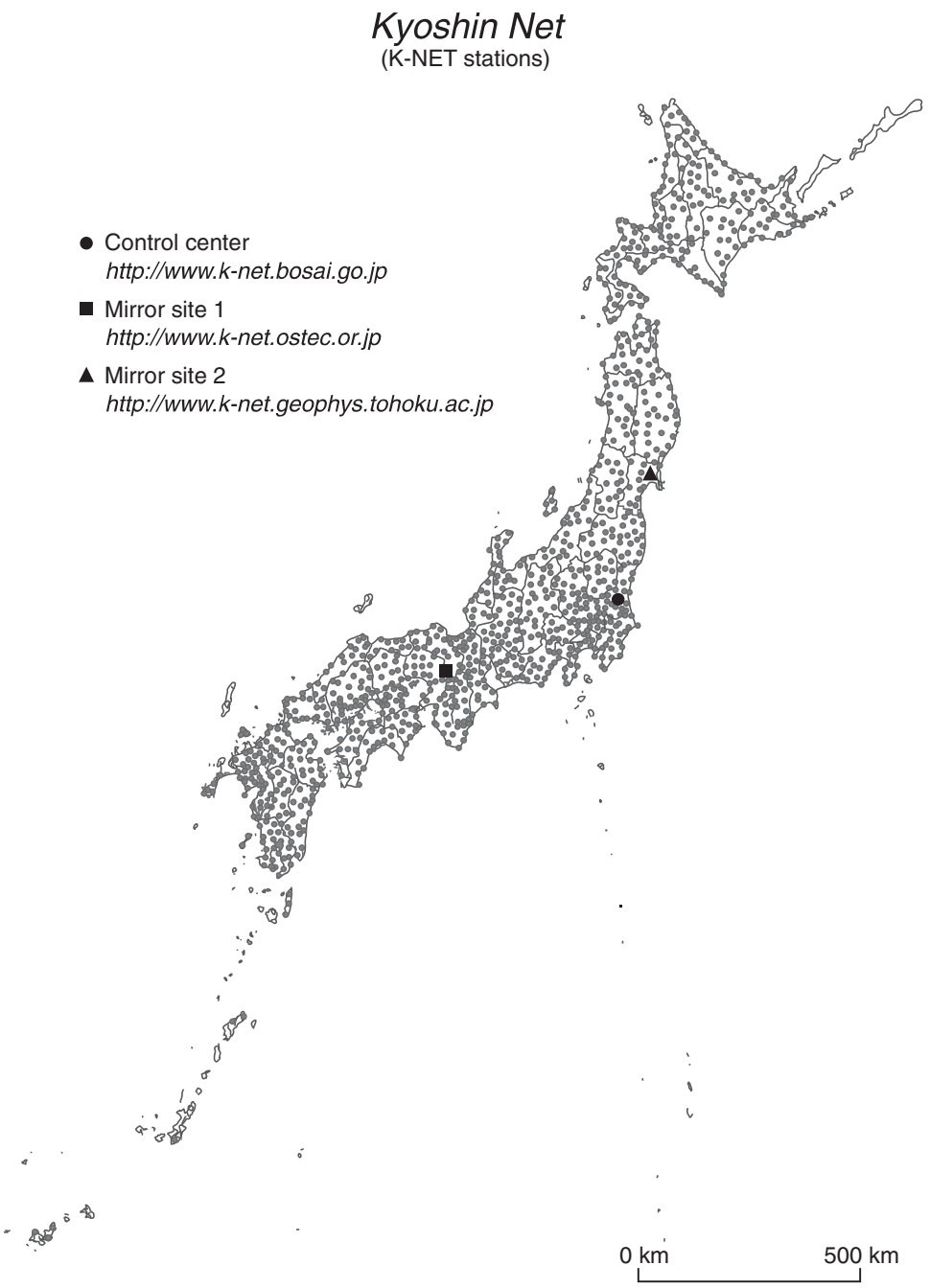

FIGURE 1 Distribution map of the K-NET strong-motion observatories. These 1000 stations, the control center, and two mirror sites comprise the K-NET. Reprinted from Kinoshita (1998) with permission from the Seismological Society of America.

release of data is as follows: When an earthquake occurs, the Japan Meteorological Agency (JMA) promptly determines and releases the source parameters (i.e., the origin time, epicenter location, depth, and magnitude) through a JMA weather satellite, provided that JMA observatories report the JMA intensity to be more than 3. The first task of the control center is to receive the JMA source parameters through an emergency information receiver installed at the center. After receiving this information, the control center automatically estimates the distribution of maximum acceleration by using an empirical function relating maximum acceleration to magnitude and distance (Fukushima and Tanaka, 1990) and then starts to retrieve the strong-motion records on the basis of the estimated maximum acceleration map.

The K-NET95 seismograph has two RS232C ports. The control center usually occupies one of the two ports and communicates with the K-NET95 by a dial-up procedure. The communication rate is automatically determined by the line condition. The maximum data transmission rate is 9600 bits/sec. The

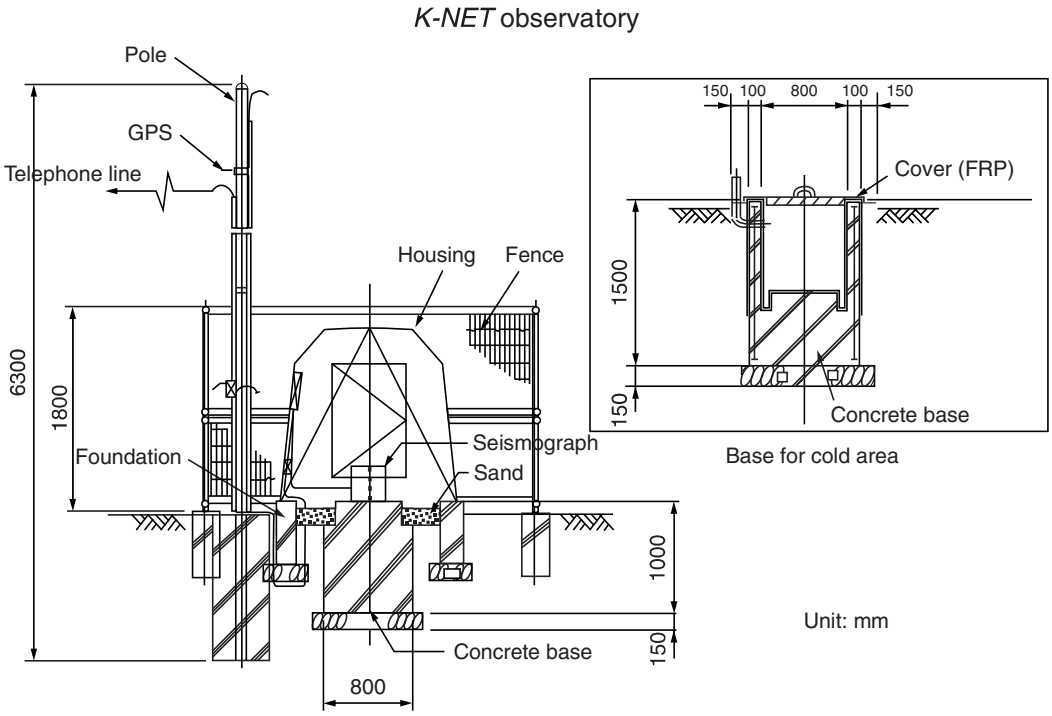

FIGURE 2 Layout of a typical observatory. In cold areas, the seismograph base is constructed beneath the ground's surface. Reprinted from Kinoshita (1998) with permission from the Seismological Society of America.

communication protocol is based on AT commands. After retrieving the strong-motion records obtained by the K-NET95 seismographs, the control center creates strong-motion data files with a common header that includes the JMA prompt source parameters and then creates a database of strong-motion files. Simultaneously, the earthquake catalog database is updated. These databases are maintained on a database server with a memory of 120 GB, which is installed in the control center. Finally, the control center simultaneously sends the strong-motion files to the three WWW servers installed at the control center and the two mirror sites. The servers make strong-motion data files available on the Internet. Usually, the release of K-NET data on the Internet is made within several hours of the occurrence of an earthquake in Japan. For example, in the case of the earthquake of March 16, 1997 ($M = 5.4$), we obtained 209 three-component seismograms and released these data after about 3 hours.

Another important job of the control center is to keep the seismographs in an operational condition. The K-NET95 seismograph continuously maintains a monitor file that has information on the state-of-health of the seismograph. The control center regularly checks these monitor files in order to maintain the K-NET. When the control center finds abnormal data in a monitor file, it orders a specified maintenance company to repair the seismograph.

The other RS232C port of the K-NET95 seismograph is connected to a local government office. The local government may be able to obtain the strong-motion data more quickly than the control center and to retrieve the data from the K-NET95 by visiting the site if AC power is lost or the telephone line is disconnected. This compensates for the control center's dependence on possibly unreliable telephone telemetry.

2.2 Type K-NET95 Seismograph

The strong-motion seismograph, type K-NET95 manufactured by Akashi Co., is an accelerograph with a wide frequency band and dynamic range. This seismograph is similar to a Kinemetrics K2. The K-NET95 has the following specifications.

2.2.1 Sensor

The sensor, type V403BT, is a triaxial, force-balance accelerometer with a natural frequency of 450 Hz and a damping factor of 0.707 (standard values). The output is 3 V/g and the resolution is more than 0.1 mGal.

2.2.2 Recording System

The recording system of the K-NET95 consists of six parts as shown in Figure 3. The amplification of the strong-motion records stored on IC memory is adjusted by the gain of a DC amplifier $G(f)$, where f is frequency in Hz. The analog low-pass filter $F(f)$ is an antialias filter for the A/D converter $C(f)$. This filter consists of a two-stage RC filter with the corner frequencies of 800 kHz and 160 kHz. The A/D converter $C(f)$ is a 24-bit type with a converter clock frequency of 1.6384 MHz. Strictly speaking, this A/D converter consists of a 1-bit sigma-delta modulator and the following digital decimation filter. This digital filter is a linear phase finite impulse response (FIR) filter with

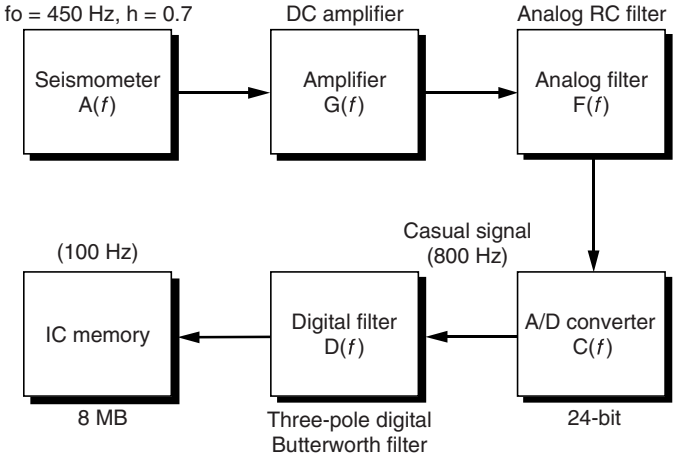

FIGURE 3 Block diagram of the K-NET recording system. The output of the A/D converter retains the causality of ground motion, and the sampling frequency is 800 Hz. The digital decimation filter D(f) converts the sampling frequency from 800 Hz to 100 Hz.

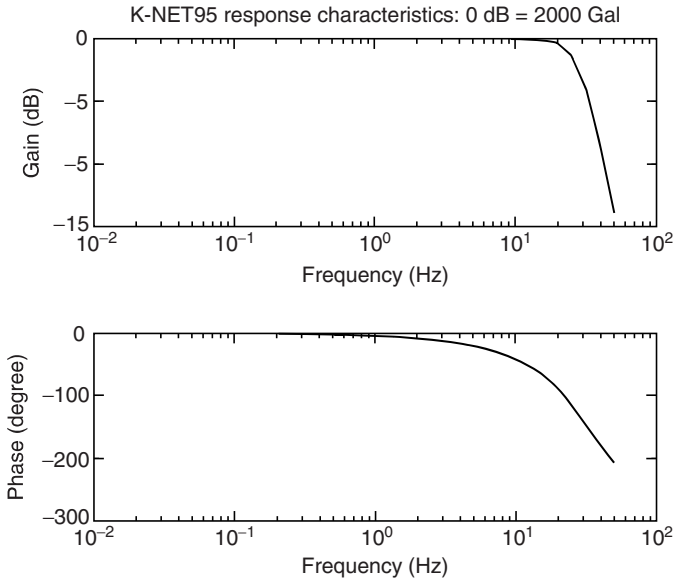

FIGURE 4 Overall frequency characteristics of the K-NET95 strong-motion seismograph.

a tap length of 1.25 ms, and the over sampling ratio is 2048. Thus, the output of C(f) is a signal with a sampling frequency of 800 Hz that retains the causality of the original signal. The digital filter D(f) is also a decimation filter. This filter is a three-pole Butterworth filter with a corner frequency of 30 Hz, and it also decreases the sampling frequency from 800 Hz to 100 Hz. This filter is designed by applying the bilinear transform to an analog Butterworth filter. Finally, the signal with a sampling frequency of 100 Hz is stored in IC memory. A flash memory card with a recording capacity of 8 MB is used for data storage. The maximum available time for recordings is 2.5 h. The maximum measurable acceleration is 2000 Gal. Strong-motion signals stored in the K-NET95 are deleted only by a command from the control center. This means that the K-NET95 keeps the main shock data in case of an earthquake swarm.

Figure 4 shows the overall frequency response characteristics of the K-NET95. The response characteristics are approximately equal to those of a three-pole digital Butterworth filter with a sampling frequency of 800 Hz and a filter corner at 30 Hz. Thus, instrument correction may be easily performed in the Fourier domain. However, it is difficult to execute instrument correction in the time domain because the digital Butterworth filter with a sampling frequency of 100 Hz does not preserve the digital Butterworth characteristics with a sampling frequency of 800 Hz in the frequency range from 30 Hz to 50 Hz. The reason is due to the decimation filter used in the K-NET95 recording system, in which the sampling frequency decreases from 800 Hz to 100 Hz.

2.2.3 Time Code

Timing in the K-NET95 is controlled by using Global Positioning System (GPS) satellite systems. A GPS antenna is installed at each site, and the K-NET95 has a GPS receiver.

2.2.4 Communication

The K-NET95 has two RS-232C communication ports. These ports are connected to modems, and the maximum speed of communication is 9600 bits/sec. Communication is executed using AT commands.

2.2.5 AC and DC Power

The main power for the K-NET95 is 100V AC. The K-NET95 has a battery with a capacity of 24 Ah. This battery is charged by a trickle-charger with a maximum current of 0.5 A at 12 V. Thus, the K-NET95 can function for approximately 24 hours using a fully trickle-charged battery if AC power is lost, because the power consumption of the K-NET95 is approximately 11 VA.

2.2.6 Packaging Case

The packaging case of the K-NET95 is made of FRP and is waterproof to a depth of 3 m. The dimensions are as follows: 180 mm (H), 380 mm (L), and 280 mm (W). The weight of the K-NET95 is approximately 7 kg.

2.2.7 Resolution and Dynamic Range of the K-NET95

The actual performance of the K-NET95 was tested at the factory and at a field test site, station TKN. This test yielded the following results (Kinoshita, 1998).

Figure 5 shows the maximum acceleration amplitude at each frequency, which is calculated from the acceleration power spectral density. The two dotted lines, LNM and HNM, show the USGS low- and high-noise models (Peterson, 1993), respectively. Also, Figure 5 shows the maximum acceleration

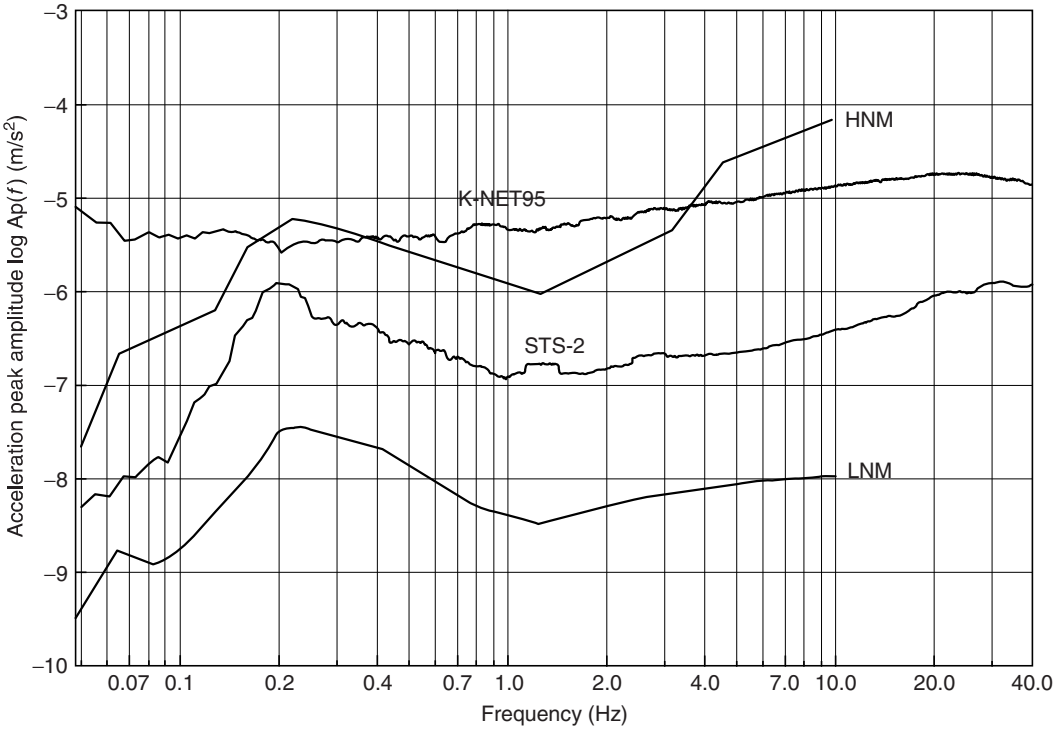

FIGURE 5 Amplitude spectra calculated from the power spectra. The solid line is the acceleration amplitude of a K-NET95. The two dotted lines, LNM and HNM, are the USGS low- and high-noise models, respectively, proposed by Peterson (1993).

amplitude of a UD component microtremor observed from the STS-2 seismometer installed on the same concrete base simultaneously. The K-NET95 and the STS-2 seismometers were installed on the same base. The result obtained from the STS-2 probably represents the actual microtremor at this site, and thus the result obtained by the K-NET95 probably consists almost entirely of instrument noise, due to the resolution amplitude of the K-NET95. This figure shows that the K-NET95 amplitude resolution is approximately 1 mGal throughout the entire frequency band. Thus, in this case, the dynamic range of the K-NET95 is 126 dB because the maximum measurable acceleration is 2000 Gal.

The V403BT negative feedback accelerometer has a test coil for calibrating the K-NET95 seismograph. This calibration is implemented by a command from the control center, and the calibration data are stored in the K-NET95. By retrieving the calibration file by a dial-up procedure, we can check the dynamic range of the K-NET system including transmission lines. This return test is performed every month.

2.2.8 Temperature Sensitivity and Temperature Dependence of the K-NET95 Responses

The K-NET95 functions within a nominal temperature range of −5 to 50°C, according to the specifications. However, in practice, the K-NET95 functions in a temperature range from −20 to 60°C as follows. Temperature sensitivity was measured by using an environment controller throughout a temperature range of from −10 to 50°C. The results showed that the temperature sensitivity of the K-NET95 is about 0.1%. The strong-motion data files available on the Internet include the temperature information at the time of recording, which is written under the heading of memorandum in the header part of the file.

2.2.9 DC Offset

There are two kinds of DC offset in the K-NET95. One is an initial drift, which continues for about 2 days until the internal temperature of the K-NET95 reaches a steady condition. The other is due to environmental temperature changes. After the initial offset, the K-NET95 has a hysteresis loop in the DC offset. This characteristic depends on the temperature transmission of the FRP case of the K-NET95. The average gradient of this loop is about 1 Gal/°C and the K-NET95 kept this value under a forced temperature change test within a temperature range of from −10 to 50°C.

2.2.10 Cross-Axis Sensitivity

The cross-axis sensitivity between the three components of the K-NET95 is measured by using a shake table. During the test, shaking within a frequency range of from 1 to 10 Hz, the cross-axis sensitivity was less than 1%.

3. K-NET Information

The K-NET provides four kinds of data and one software package. These include site information, strong-motion data, a maximum acceleration map, K-NET95 instrument parameters, and utility programs. The control center and the two mirror sites send these data and software across the Internet according to the user's request. The Internet addresses of the control center and the two mirror sites are as follows:

http://www.k-net.bosai.go.jp (control center in Tsukuba city)
http://www.k-net.ostec.co.jp (mirror site 1 in Osaka city)
http://www.k-net.geophys.tohoku.ac.jp (mirror site 2 in Sendai city)

3.1 Site Information

At each K-NET station, the velocity structure beneath the site to a depth of 10 or 20 meters was investigated by downhole measurement. The control center and the two mirror sites provide the location, elevation, address, and soil structure including N-values, bulk density, P- and S-wave structures, and soil profile for each site as part of the station information. Figure 6 shows an example of the site information sent across the Internet.

3.2 Strong-Motion Data

The control center makes three kinds of strong-motion data files available (UNIX, DOS, and ASCII) with a common header that includes the quick source parameters determined by JMA for each event. Users can select from among the three file types on the Internet. The UNIX and DOS files are compressed by gzip and lha compression commands, respectively.

A separate data file is made for each component of each seismogram. The numerical data in each file are raw accelerograms recovered from the K-NET95, without any corrections. The source parameters, origin time, epicenter location, focal depth, and magnitude, written in the header of the data file, are from the preliminary JMA report on the earthquake source. The control center does not release the JMA final source parameters on the Internet.

Since April 1, 1997, users have been able to download all strong-motion data files obtained from a specific event at one time. Such data retrieval is also possible for a set of events selected according to a user's request.

3.3 Maximum Acceleration Map

The map of maximum acceleration with equi-acceleration contour lines will be made after an event when the control center has recovered enough data, usually more than 50 three-component

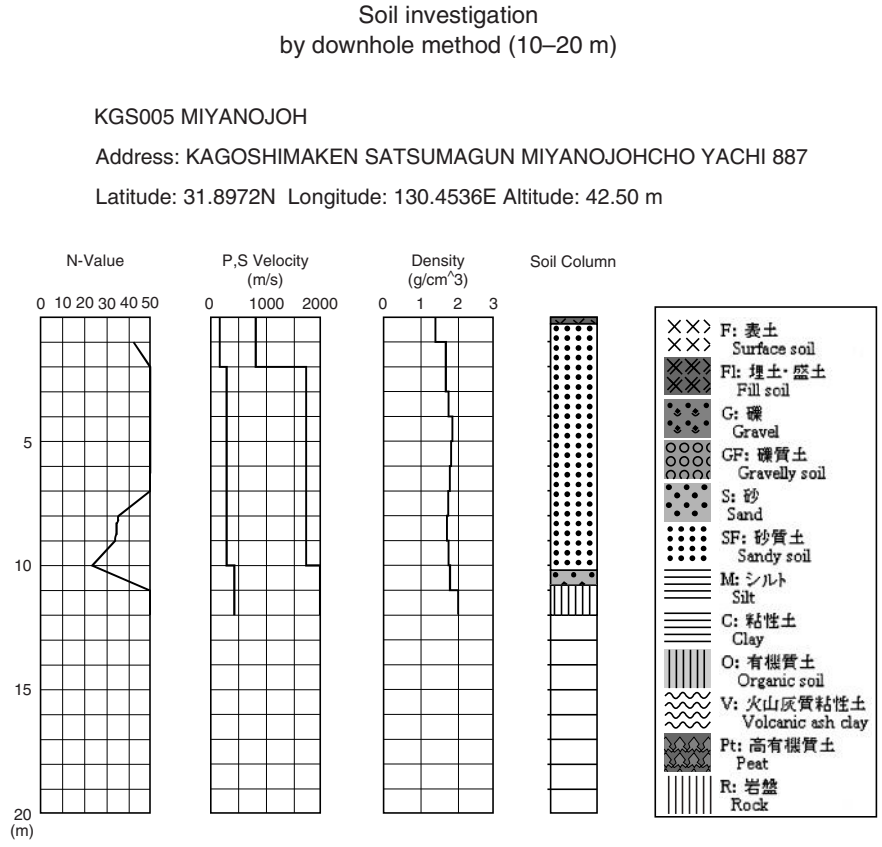

FIGURE 6 An example of site data sent out on the Internet.

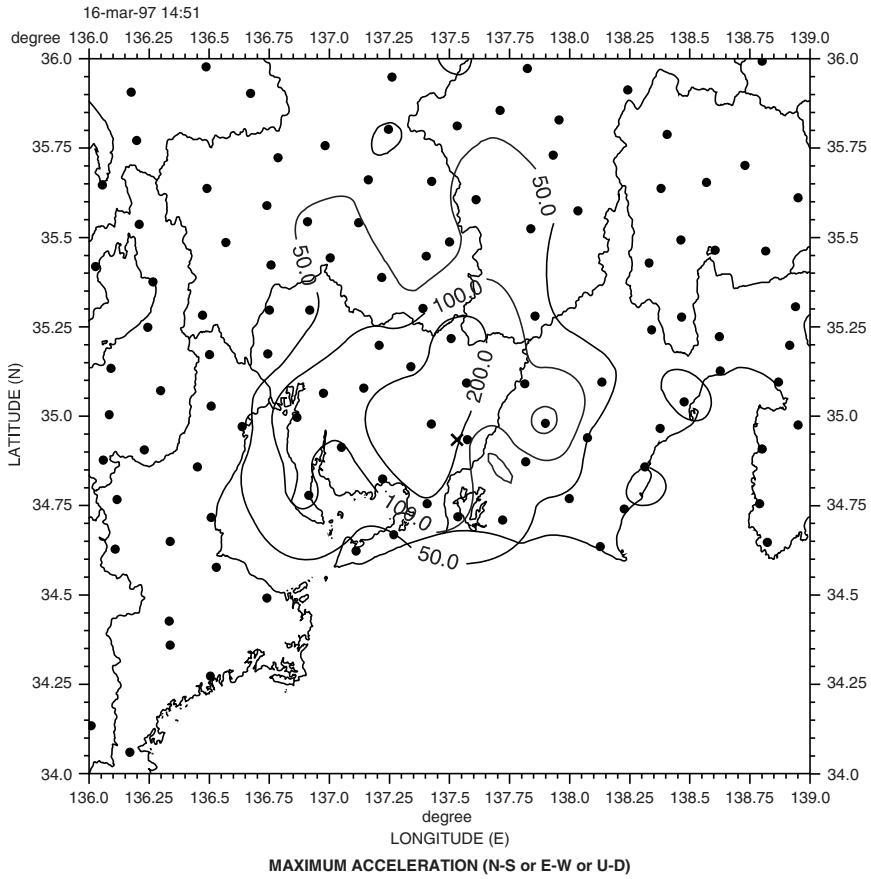

FIGURE 7 An example of a maximum acceleration map sent out on the Internet.

seismograms. The contour lines are smoothed by using Spline interpolation and indicate the center point of strong motion, which may be different from the epicenter of the earthquake. If the control center has not recovered enough data to construct such a map, only the table of maximum acceleration is released.

Figure 7 shows an example of a maximum acceleration map sent out on the Internet. This map was obtained from the Eastern Aichi prefecture earthquake of March 16, 1997 ($M = 5.4$). From such a map, it is possible to interpret the local characteristics of maximum acceleration.

3.4 The K-NET95 Instrument Parameters

The control center provides the information on the K-NET95 seismograph. These are the block diagram, overall frequency characteristics, and specifications, of the seismograph. The detailed information on the K-NET95 seismograph is provided by Kinoshita (1998) and Kinoshita *et al*. (1997).

3.5 Utility Software

In 1997, K-NET released utility software, which runs on Windows 95 or NT, for preliminary studies on the K-NET95 seismograms. The released application programs are applicable to DOS seismogram files, which are retrieved from our Web sites and are able to calculate and plot velocity and displacement seismograms in addition to the original accelerograms. Also, the utility programs can calculate Fourier, power, and response spectra and can implement various filtering functions. Plotting programs for the calculated spectra are included in the utility software. When we plot the three-component K-NET95 seismogram by using the utility program, the program simultaneously provides the value of the JMA intensity at the site.

3.6 Off-line Release of K-NET Information

Since April 1, 1997, individual users have been able to copy the K-NET strong-motion data and other information on to their MO and/or DAT media at the control center and mirror site 2. This is a self-service. We also distributed the strong-motion data obtained in 1996 and 2001 on ten CD-ROMs. Such a service is performed every 6 months.

4. Closing Remarks

From the Kobe earthquake of 1995, we learned that more information on strong motion in a hypocentral area is necessary to investigate the generation of strong earthquake shaking and to assess the degree of a disaster for quick mitigation response.

The K-NET deployed in 1995 to respond to these demands. This network was constructed on the basis of previous seismic networks installed in the United States, Japan, Mexico, the Republic of China, and other countries. The construction cost was US$40,000,000, and the maintenance cost for each year is 5% of the construction cost. Three persons including a computer engineer have been operating this system.

After about 1 year of operation, the K-NET has transmitted one million data files to users on the Internet. This means that the K-NET is responding very well to users' requests. In the future, the K-NET will provide even more useful information as the instruments and network are upgraded. The K-NET will continue to provide even more useful information as the instruments and network are upgraded. For example, K-NET upgraded the Web pages in 2001, in which a concise text of strong-motion entitled, "Fundamentals of strong-motion," was released.

Acknowledgments

The author thanks Makoto Miyamoto and Takao Sakai for the site negotiation of K-NET stations. Dr. Aketo Suzuki administrated the construction of the K-NET observatory. Masayosi Uehara, Toshio Tozawa, and Yasuji Wada built the network system of the K-NET including seismograph installation. I offer them my sincere gratitude for their invaluable assistance.

References

Fukushima, Y., and T. Tanaka (1990). A new attenuation relation for peak horizontal acceleration of strong earthquake ground motion in Japan. *Bull. Seism. Soc. Am.* **80**, 757–783.

Ikeura, T., S. Uchiyama, N. Adachi, T. Yamashita, T. Uetake, and M. Kikuchi (1999). Effects of K-NET seismometer installation conditions on its strong motion records. *Programme and abstracts, PO18, 1999 SSJ fall meeting* (in Japanese).

Kinoshita, S. (1998). Kyoshin net (K-NET). *Seism. Res. Lett.* **69**, 309–332.

Kinoshita, S., M. Uehara, T. Tozawa, Y. Wada, and Y. Ogue (1997). Recording characteristics of the K-NET95 strong-motion accelerograph. *Zishin (Series-2)* **49**, 467–481 (in Japanese with English abstract).

Peterson, J. (1993). Observation and modeling of seismic background noise. *Open-File Report 93-322*, US Geological Survey, Albuquerque, New Mexico.

64

Strong-Motion Instrumentation Programs in Taiwan

T. C. Shin
Central Weather Bureau, Taipei, Taiwan
Y. B. Tsai
National Central University, Chung-li, Taiwan
Y. T. Yeh
Ching Yun Institute of Technology, Jung-Li, Taiwan
C. C. Liu
Institute of Earth Sciences, Academia Sinica, Taipei, Taiwan
Y. M. Wu
Central Weather Bureau, Taipei, Taiwan

1. Introduction

Taiwan is located on the Circum-Pacific seismic belt. On the east side of Taiwan, the Philippine Sea plate subducts beneath the Eurasian plate at the Ryukyu trench, while at the south end of Taiwan, the South China Sea lithosphere subducts eastward under the Philippine Sea plate. The active convergent margin, connecting these two subduction zones, is characterized by rapid crustal deformation, regional-scale crustal faulting, and high seismicity. The densely populated western Taiwan, with high-rise buildings as a consequence of developing economy, is vulnerable to increasing earthquake hazard. Therefore, earthquake research has a high priority in Taiwan and considerable amounts of resources have been devoted to seismic instrumentation in general, and strong-motion instrumentation in particular.

Many disastrous earthquakes have occurred in the past, the most recent one being the 1999 Chi-Chi earthquake (Teng *et al*., 2001). About 2500 people died and 300,000 were left homeless. The importance of strong-motion instrumentation has long been recognized, and we will summarize here the history of the strong-motion instrumentation programs in Taiwan. The earlier instrumentation programs were conducted primarily by the Institute of Earth Sciences, Academia Sinica, and have been mostly research oriented (Tsai, 1997; see also Report of the Institute of Earth Sciences under China (Taipei) in Chapter 79). The later efforts, involving an order-of-magnitude increase in the number of instruments, were conducted primarily by the Central Weather Bureau.

2. Strong-Motion Instrumentation Program by IES

2.1 Strong-Motion Accelerographs Network (SMA)

An islandwide strong-motion network was deployed by the Institute of Earth Sciences (IES), Academia Sinica, beginning in 1974, and by 1983, this network consisted of 72 stations. The instruments used were the standards at that time, i.e., the SMA-1s. The first strong-motion record obtained by this network was in April 1976. The purpose of this network is mainly to study earthquake source, structure responses, attenuation of ground motions, and risk analysis. By 1990, accelerographs of this network increased to 79, as a mix of analog and digital recording units. Most of them were installed on free-field sites, while some were on man-made structures. Most of those free-field stations were installed on the populous plain areas. After 1990, all stations of this network have been continuously upgraded to force-balance accelerometers with 16-bit resolution. Numbers of accelerograph stations on plain areas were reduced, and new stations were installed in the Central Range Mountain

INTERNATIONAL HANDBOOK OF EARTHQUAKE AND ENGINEERING SEISMOLOGY, VOLUME 81B *ISBN: 0-12-440658-0*

of Taiwan. The total number of stations in this network is currently 74. The purpose of the new installation is to study the topographic effects and attenuation behavior of strong motion in the mountainous area (Huang, 2000). Leaders of this project include Y. B. Tsai (1974–1978), C. S. Wang (1979–1980), Y. T. Yeh (1981–1992), and B. S. Huang (1992–present).

2.2 Strong-Motion Accelerograph Array in Taiwan, Phase 1 (SMART-1 Array)

SMART-1 Array was set up in Lotung in 1980 and closed at the end of 1990. This was a cooperative project between the Institute of Earth Sciences, Academia Sinica and University of California, Berkeley. The SMART-1 Array consisted of a central site and accelerographs in three concentric circles, with radii of 200 m, 1 km, and 2 km, respectively. Each circle had 12 evenly spaced sensors. All 43 accelerographs were tied to a common time base, with timing to better than ± 0.01 sec. Each accelerograph consisted of a triaxial force-balance accelerometer, capable of recording ± 2 g, connected to a digital event recorder that uses a magnetic tape cassette for recording. The accelerographs were triggered on either vertical or horizontal acceleration at an adjustable preset threshold. Signals were digitized with a 13-bit resolution at 100 samples per second. Each recorder had a digital preevent memory that stored the output signals from the force-balance accelerometer for approximately 2.5 sec before trigger. Such accelerographs had an obvious advantage of providing synchronous time history of the ground-motion acceleration. Hence, we could perform spatial and temporal correlation across the whole array. The recorded data on digital cassettes were played back at the central laboratory and transferred onto a regular 9-track magnetic tape in ASCII format. During the playback, a seismologist scanned the digital signals displayed on a minicomputer console and made corrections for glitches, gaps, time code errors, and offsets in DC level. A regular magnetic tape containing edited data was available for further analysis only hours after the recording, whereas the analog recording/processing commonly used at that time would take days to digitize and process (Tsai and Bolt, 1983). Many research papers were published using the SMART-1 data (e.g., Loh *et al.*, 1982; Abrahamson, 1988).

2.3 Lotung Large Scale Seismic Test Array (LSST)

The LSST program was set up for evaluating soil-structure interaction effects and backfill effects. These effects are important in seismic design of nuclear reactor facilities. A quarter-scale and a 1/12-scale model of the nuclear reactor containment structure were constructed inside the SMART-1 Array on October 1985. It was closed at the end of 1990, the same time that SMART-1 Array had completed its mission. The LSST program was a joint project between the Taiwan Power Company (Taipower) and the Electric Power Research Institute of USA (EPRI), under the management of H. T. Tang. Under a contract with Taipower, IES installed and maintained the instruments, as well as carried out data collection, reduction, and analysis. In the initial phase, four types of sensors were installed in the fields for data acquisition: the surface accelerometer, the downhole accelerometer, the structural response accelerometer, and the interfacial pressure transducer. These sensors were triaxial type, except the pressure transducer. The output of all accelerometers and pressure gauges was transmitted by hard wire to the central recording unit and was recorded on cassette tapes. These tapes were then processed and transcribed onto 9-track tapes using the ASCII format.

2.4 SMART-2 Array

The SMART-2 strong-motion array was deployed by IES in the northern part of the Longitudinal Valley in Hualien in December 1990, and was fully operational in 1992 (Chiu *et al.*, 1994). It consists of 45 Kinemetrics SSR-1 instruments as surface stations and two sets of downhole subarrays. All sensors used in this array are force-balance accelerometers. This array is designed to study the rupture process of seismic faults and the characteristics of near-source ground motions. Furthermore, the high-quality data from SMART-2 may be used for research in seismology and earthquake engineering (e.g., Huang and Chiu, 1996).

Chiu *et al.* (1995) studied the coherency of ground motions based on the SMART-2 data and compared it with the results of the SMART-1. A comparison of coherency functions for both vertical and horizontal motions from a magnitude 5.5 earthquake recorded by the SMART-2 indicated no significant difference in the range of 1 to 10 Hz for separation distance of 400, 800, and 1500 m.

2.5 Hualien Large Scale Seismic Test Array (HLSST)

Since 1993, EPRI and Taipower have sponsored a dense multiple-element array, the HLSST network, located at the Veteran's Marble Plant of Hualien within the SMART-2 deployment area of northeastern Taiwan. This is an international joint project operated by IES with the objectives of investigating soil-structure interaction behavior during severe earthquakes and verifying the validity of various analysis methods using the strong-motion records. To serve this purpose, a one-quarter-scale cylindrical reactor model and a cylindrical liquid-storage-tank model were constructed in Hualien, a high-seismicity region. The cylindrical liquid-storage-tank model was closed in July 1998.

2.6 Downhole Accelerometer Arrays in the Taipei Basin (DART)

A research project, "Integrated Survey of Subsurface Geology and Engineering Environment of the Taipei Basin," was proposed in early 1990s to collect data for the purposes of engineering construction, groundwater management, ground subsidence

prediction, study of the basin effects of seismic waves, and geological sciences. This project has been sponsored by the Central Geological Survey (CGS), Ministry of Economic Affairs since August 1991. CGS contracted the study of the basin effects on seismic waves to IES, which proposed the DART program, in which one site was installed per year to analyze the variation of seismic waves propagating from the basement to ground surface. Each site includes one free-surface accelerometer and some downhole sensors. These force-balance accelerometers are connected to a PC-based central recording system or a K2 digital recording system with GPS timing and position information.

Wen *et al*. (1995) studied basin effects using a dense strong-motion array in Taipei Basin. Their results showed that site amplification is frequency dependent. They also indicated that both horizontal peak ground acceleration and the spectral ratio in low-frequency band are closely correlated with the geological structure of Taipei Basin.

3. Strong-Motion Instrumentation Program by CWB

In the late 1980s, Y. B. Tsai proposed an extensive strong-motion instrumentation program for the urban areas in Taiwan. Since the Central Weather Bureau has the official responsibility to monitor earthquakes in the Taiwan region, the Taiwan Strong-Motion Instrument Program (TSMIP; see Shin, 1993) was successfully implemented during 1991–1996.

The main goal of this program is to collect high-quality instrumental recordings of strong ground shaking from earthquakes, both at free-field sites and in buildings and bridges. These data are crucial for improving earthquake-resistant design of buildings and bridges and for understanding the earthquake source mechanisms, as well as seismic wave propagation from the source to the site of interest, including local site effects.

Two types of digital strong-motion instruments were deployed throughout Taiwan in this program, with special emphasis in nine metropolitan areas. One type is a digital triaxial accelerograph for recording free-field ground shakings (Liu *et al*., 1999). The other type is a multichannel (32 or 64 channels), central-recording, accelerograph array system for monitoring shaking caused by earthquakes in buildings and other structures (Lee and Shin, 1997). By the end of 2000, a total of 640 free-field accelerographs and 56 structural arrays had been deployed. Locations of the free-field accelerographs are shown in Figure 1, and locations for the building arrays are shown in Figure 2.

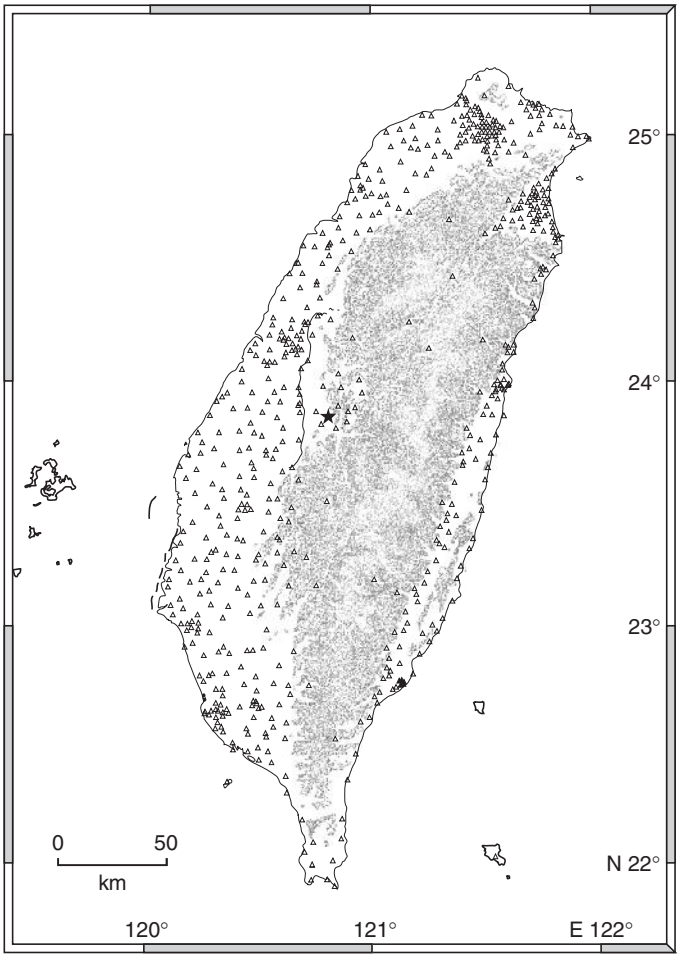

FIGURE 1 Locations of the CWB free-field, three-component, digital accelerograph stations. The star indicates the location of the Chi-Chi earthquake. Surface ruptures extending about 80 km north–south are shown to the left of the epicenter.

4. The Taiwan Rapid Earthquake Information Release System

The desire for seismological observation in real time has long been recognized, and significant advances have been made during the past decade in many countries (Kanamori *et al*., 1997). The idea of an islandwide early earthquake warning system using the existing telemetry in Taiwan was first proposed by T. L. Teng in the early 1990s. The Taiwan Rapid Earthquake Information Release System (RTD) is based on a simple hardware/software design first introduced by Lee *et al*. (1989), and was subsequently improved and refined (Lee, 1994; Lee *et al*., 1996; Shin *et al*., 1996; Teng *et al*., 1997; Wu *et al*., 1997, 1998, 1999). The RTD system consists of 80 telemetered strong-motion accelerographs in Taiwan (Fig. 3). Digital signals are continuously telemetered to the headquarters of the Central Weather Bureau (CWB) in Taipei via 4800-baud leased telephone lines. Each telemetered signal contains three-component seismic data digitized at 50 samples per second and at 16-bit resolution. The full recording range is ± 2 g. The incoming digital data streams are processed by a computer program called XRTPDB (Tottingham and Mayle, 1994). Whenever the prespecified trigger criteria are met, the digital waveforms are stored in memory and are automatically analyzed by a series of programs (Wu *et al.*, 1998).

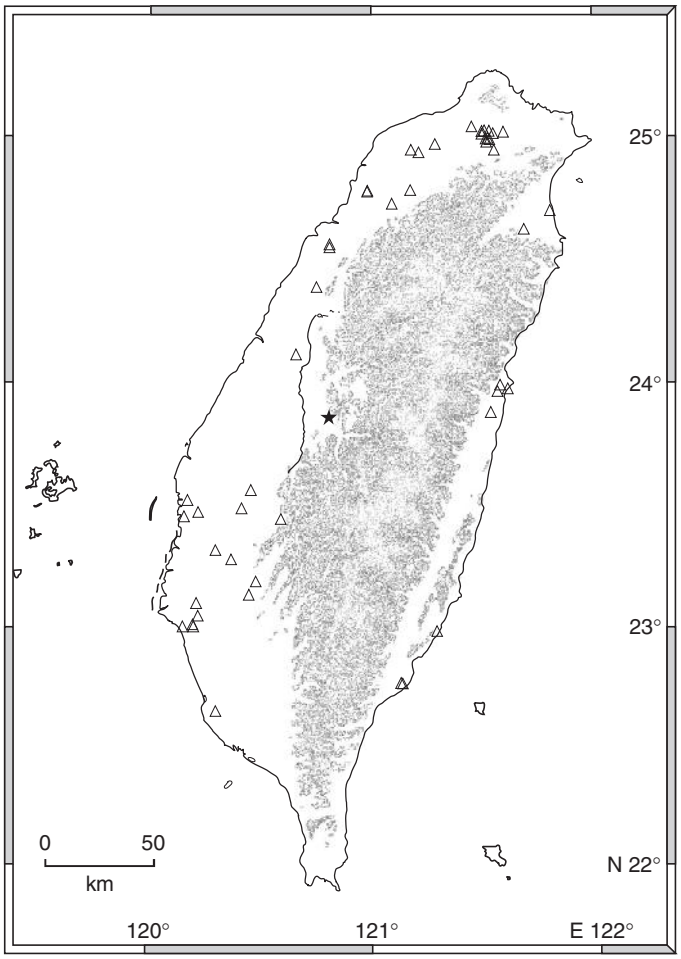

FIGURE 2 Locations of the CWB structural strong-motion arrays in buildings and bridges. The star indicates the location of the Chi-Chi earthquake. Surface ruptures extending about 80 km north–south are shown to the left of the epicenter.

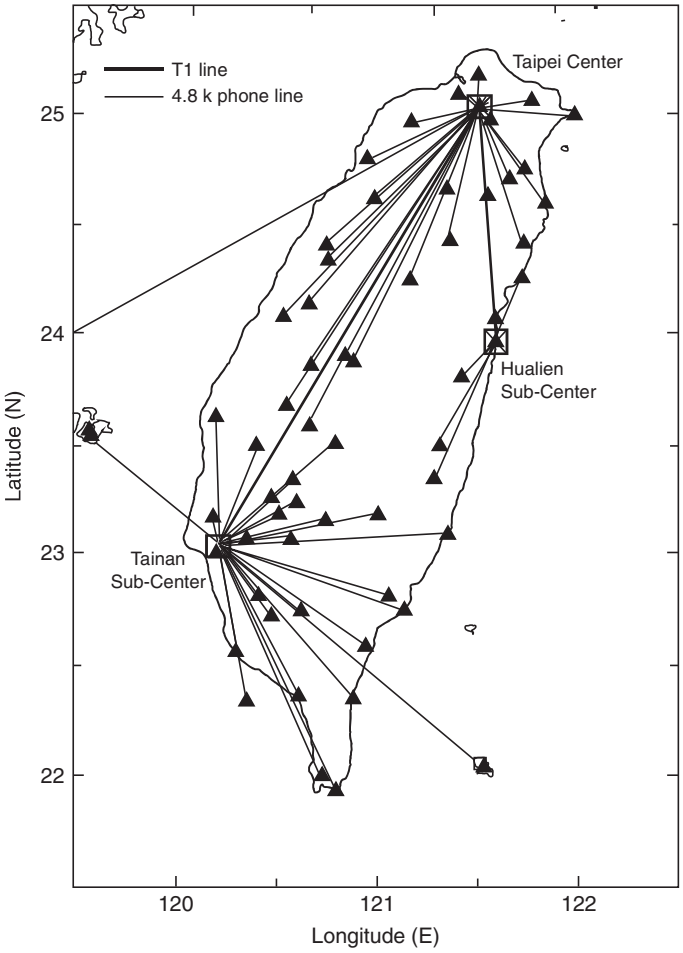

FIGURE 3 Map showing the telemetered stations of the Taiwan Earthquake Rapid Information Release System (RTD).

The results are immediately disseminated to emergency response agencies electronically in four ways, namely, by e-mail, World Wide Web, fax, and a pager system (Fig. 4).

5. The Chi-Chi Earthquake of September 21, 1999

The Chi-Chi earthquake occurred at 1:47 on September 21, 1999 (Taiwan local time) or at 17:47 on September 20, 1999 UTC. It was the largest ($M_w = 7.6$) earthquake to have occurred on land in Taiwan in the 20th century. For the main shock, 441 digital three-component, strong-motion records were successfully retrieved by the Taiwan Central Weather Bureau (CWB) from about 640 accelerographs deployed at the free-field sites. These preliminary strong-motion data from the Chi-Chi main shock were released on December 13, 1999, in the form of a prepublication data CD (Lee *et al*., 1999). During the first 6 hours after the main shock, about 10,000 strong-motion records were recovered, and since then another 20,000 records were obtained. This is by far the best-recorded major earthquake in the world. There are over 60 three-component strong-motion records from within 20 km of the fault ruptures.

A preliminary report of this earthquake is given in Shin *et al.* (2000), and a detailed report of the processed free-field acceleration data is given in Lee *et al*. (2001a). These data are also archived in Lee *et al.* (2001b). Characteristics of the strong ground motion are given by Tsai and Huang (2000). At the time of the earthquake, the Taiwan Rapid Earthquake Information Release System (RTD) automatically determined the location and magnitude for the main shock and prepared a shake map within 102 seconds after the earthquake's origin time. This information was then sent out by a pager-telephone system, by an e-mail server, and by fax. Its performance during the Chi-Chi earthquake and numerous strong aftershocks has been documented in Wu *et al.* (2000).

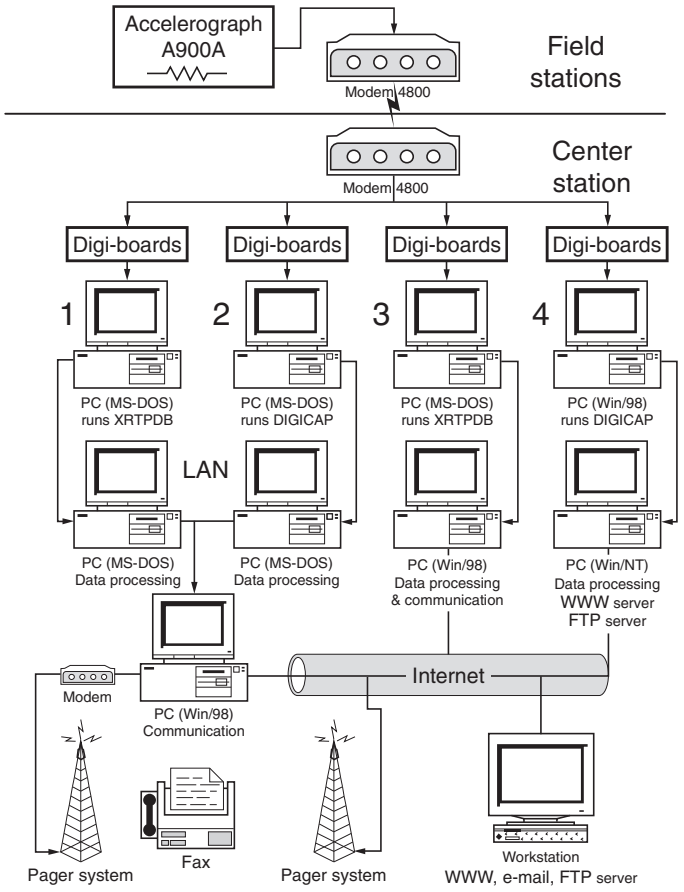

FIGURE 4 A block diagram showing the hardware of the RTD system.

6. Concluding Remarks

The Chi-Chi earthquake clearly demonstrated the usefulness of the extensive strong-motion instrumentation in Taiwan for purposes of emergency response and research in seismology and earthquake engineering. Readers are referred to several special issues and proceedings on the Chi-Chi earthquake (e.g., BERI, 2000; Loh and Liao, 2000; Wang *et al*., 2000; Teng *et al.*, 2001).

Acknowledgments

The strong-motion instrumentation programs in Taiwan would not be possible without the labor of many people. We wish to thank many advisors and collaborators: B. A. Bolt, K. C. Chen, H. C. Chiu, B. S. Huang, G. C. Lee, W. H. K. Lee, K. S. Liu, S. C. Liu, C. H. Loh, S. T. Mau, G. B. Ou, M. S. Sheu, H. T. Tang, T. L. Teng, C. Y. Wang, K. L. Wen, C. F. Wu, F. T. Wu, Y. H. Yeh, and G. K. Yu.

References

Abrahamson, N. A. (1988). Statistical properties of peak ground acceleration recorded by the SMART 1 array. *Bull. Seism. Soc. Am.* **78**, 26–41.

BERI (2000). "Special Issue: The 1999 Chi-Chi, Taiwan earthquake." *Bull. Earthquake Res. Inst. Tokyo Univ.* **75**, Paret 1.

Chiu, H. C., Y. T. Yeh, S. D. Ni, L. Lee, W. S. Liu, C. F. Wen, and C. C. Liu (1994). A new strong-motion array in Taiwan—SMART-2. *Terres. Atmos. Ocean. Sci.* **5**, 443–455.

Chiu, H. C., R. V. Amirbekian, and B. A. Bolt (1995). Transferability of strong ground motion coherency between the SMART1 and SMART2 arrays. *Bull. Seism. Soc. Am.* **85**, 342–348.

Huang, B. S. (2000). Reconstruction of 2-D ground motions. *Geophys. Res. Lett.* **27**, 3025–3028.

Huang, H. C., and H. C. Chiu (1996). Estimation of site amplification from Dahan Downhole recording. *Int. J. Earthquake Eng. Struct. Dyn.* **25**, 319–332.

Kanamori, H., E. Hauksson, and T. Heaton (1997). Real-time seismology and earthquake hazard mitigation. *Nature* **390**, 461–464.

Lee, W. H. K. (Editor) (1994). "Realtime Seismic Data Acquisition and Processing," IASPEI Software Library, Volume 1 (2nd Edition), Seismological Society of America, El Cerrito, CA, (285 pp. and 3 diskettes).

Lee, W. H. K., D. M. Tottingham, and J. O. Ellis (1989). Design and implementation of a PC-based seismic data acquisition, processing, and analysis system. *IASPEI Software Library* **1**, 21–46.

Lee, W. H. K., T. C. Shin, and T. L. Teng (1996). Design and implementation of earthquake early warning systems in Taiwan. *Proc. 11th World Conf. Earthq. Eng., Paper No. 2133*.

Lee, W. H. K., and T. C. Shin (1997). Realtime seismic monitoring of buildings and bridges in Taiwan. In: *Structural Health Monitoring* (F. K. Chang, Ed.), Technomic Pub. Co., Lancaster, PA, 777–787.

Lee, W. H. K., T. C. Shin, K. W. Kuo, and K. C. Chen (1999). CWB Free-Field Strong-Motion Data from the 921 Chi-Chi Earthquake: Volume 1. Digital Acceleration Data, Pre-Publication CD, Central Weather Bureau, Taipei, Taiwan.

Lee, W. H. K., T. C. Shin, K. W. Kuo, K. C. Chen, and C. F. Wu (2001a). CWB Free-Field Strong-Motion Data from the 921 Chi-Chi Earthquake: Processed Acceleration Files on CD-ROM, *Strong-Motion Data Series CD-001*, Central Weather Bureau, Taipei, Taiwan.

Lee, W. H. K., T. C. Shin, K. W. Kuo, K. C. Chen, and C. F. Wu (2001b). Data Files from "CWB Free-Field Strong-Motion Data from the 21 September Chi-Chi, Taiwan, Earthquake," *Bull. Seism. Soc. Am.* **91**, 1390 and CD-ROM.

Liu, K. S., T. C. Shin, and Y. B. Tsai (1999). A free-field strong motion network in Taiwan: TSMIP. *Terres. Atmos. Ocean. Sci.* **10**, 377–396.

Loh, C. H., J. Penzien, and Y. B. Tsai (1982). Engineering analysis of SMART 1 array accelerograms. *Int. J. Earthquake Eng. Struct. Dyn.* **10**, 575–591.

Loh, C. H., and W. I. Liao (Editors) (2000). "Proceedings of International Workshop on Annual Commemoration of Chi-Chi Earthquake," 4 volumes, National Center for Research on Earthquake Engineering, Taipei, Taiwan.

Shin, T. C. (1993). Progress summary of the Taiwan strong-motion instrumentation program. In: "Symposium on the Taiwan Strong-Motion Program," Central Weather Bureau, 1–10.

Shin, T. C. (2000). Some seismological aspects of the 1999 Chi-Chi earthquakes in Taiwan. *Terres. Atmos. Ocean. Sci.* **11**, 555–566.

Shin, T. C., Y. B. Tsai, and Y. M. Wu (1996). Rapid response of large earthquake in Taiwan using a realtime telemetered network of digital accelerographs. *Proc. 11th World Conf. Earthq. Eng., Paper No. 2137*.

Shin, T. C., K. W. Kuo, W. H. K. Lee, T. L. Teng, and Y. B. Tsai (2000). A preliminary report on the 1999 Chi-Chi (Taiwan) earthquake. *Seism. Res. Lett.* **71**, 24–30.

Teng, T. L., Y. M. Wu, T. C. Shin, Y. B. Tsai, and W. H. K. Lee (1997). One minute after: strong motion map, effective epicenter, and effective magnitude. *Bull. Seism. Soc. Am.* **87**, 1209–1219.

Teng, T. L., Y. B. Tsai, and W. H. K. Lee (Editors) (2001). Dedicated Issue on the Chi-Chi (Taiwan) Earthquake of September 20, 1999. *Bull. Seism. Soc. Am.* **91**, 893–1395.

Tottingham, D. M., and A. J. Mayle (1994). User manual for XRTPDB. *IASPEI Software Library* **1** (2nd Edition), 255–263.

Tsai, Y. B. (1997). A brief review of strong motion instrumentation in Taiwan. In: "Vision 2005: An Action Plan for Strong Motion Programs to Mitigate Earthquake Losses in Urbanized Areas," A Workshop held in Monterey, California on April 2–4, 1997.

Tsai, Y. B., and B. A. Bolt (1983). An analysis of horizontal peak ground acceleration and velocity from SMART 1 array date. *Bull. Inst. Earth Sci., Acad. Sinica* **3**, 105–126.

Tsai, Y. B., and M. W. Huang (2000). Strong ground motion characteristics of the Chi-Chi, Taiwan earthquake of September 21, 1999. *Earthquake Eng. & Eng. Seism.* **2**, 1–21.

Wang, C. S., S. K. Hsu, H. Kao, and C. Y. Wang (Editors) (2000). Special Issue on the 1999 Chi-Chi Earthquake in Taiwan. *Terres. Atmos. Ocean. Sci.* **11**, 555–752.

Wen, K. L., H. Y. Peng, L. F. Liu, and T. C. Shin (1995). Basin effects analysis from a dense strong motion observation network. *Int. J. Earthquake Eng. Struct. Dyn.* **24**, 1069–1083

Wu, Y. M., T. C. Shin, C. C. Chen, Y. B. Tsai, W. H. K. Lee, and T. L. Teng (1997). Taiwan rapid earthquake information release system. *Seism. Res. Lett.* **68**, 931–943.

Wu, Y. M., C. C. Chen, J. K. Chung, and T. C. Shin (1998). An automatic phase picker of the real-time acceleration seismic network. *Meteorol. Bull., Central Weather Bureau, Taipei* **42**, 103–117 (in Chinese).

Wu, Y. M., J. K. Chung, T. C. Shin, N. C. Hsia, Y. B. Tsai, W. H. K. Lee, and T. L. Teng (1999). Development of an integrated seismic early warning system in Taiwan—case for Hualien area earthquakes. *Terres. Atmos. Ocean. Sci.* **10**, 719–736.

Wu, Y. M., W. H. K. Lee, C. C. Chen, T. C. Shin, T. L. Teng, and Y. B. Tsai (2000). Performance of the Taiwan Rapid Earthquake Information Release System (RTD) during the 1999 Chi-Chi (Taiwan) earthquake. *Seism. Res. Lett.* **71**, 338–343.